Universität der Bundeswehr München
Fakultät für Luft- und Raumfahrttechnik
Institut für Thermodynamik

Numerical Modelling of Electric Discharges Generated in High-Speed Flows

Dipl.-Ing. Alexander Nekris

Vollständiger Abdruck der von der
Fakultät für Luft- und Raumfahrttechnik
der Universität der Bundeswehr München
zur Erlangung des akademischen Grades eines

Doktor-Ingenieurs (Dr.-Ing.)

genehmigten Dissertation

Vorsitzender:	Prof. Dr.-Ing. habil. Markus Klein
1. Berichterstatter:	Prof. Dr.-Ing. Christian Mundt
2. Berichterstatter:	HDR Dr. Jean-Denis Parisse

Die Dissertation wurde am 19.11.2019 bei der Universität der Bundeswehr München eingereicht und durch die Fakultät für Luft- und Raumfahrttechnik am 13.03.2020 angenommen.

Tag der Prüfung: 07.07.2020

Acknowledgements

My special thanks go to my supervisor at the French-German Research Institute of Saint-Louis (ISL) HDR Dr. Patrick Gnemmi for his patience, his continuous interest, motivation, guidance and support during my doctoral studies. I am grateful for the opportunity to carry out this interesting and versatile work at ISL.

I would also like to express my deepest appreciation and gratitude to my PhD supervisor Prof. Dr.-Ing. Christian Mundt from the Bundeswehr University Munich. I would like to thank Professor Mundt for supervising my dissertation, for his professional support and his personal interest in my work.

I express my warm thanks to HDR Dr. Jean-Denis Parisse from Centre de Recherche de l'École de l'Air (CREA) for his work as second examiner. I am grateful for his valuable advice and the interest he has shown for the present work. I would also like to thank Prof. Dr. habil. Markus Klein from the Bundeswehr University Munich for leading the doctoral process.

My thanks also go to all my colleagues at the French-German Research Institute of Saint-Louis. I have always greatly appreciated the pleasant atmosphere at the institute and would therefore like to thank all the staff. For the preparatory work and for conducting the experiments I wish to acknowledge the following colleagues: Berthold Sauerwein, Christian Rey, Myriam Bastide, Remy Kempf, Robert Bernhard and Jean-Marc Wunderly. In addition, my thanks go to Dr. Hartmut Borchert for evaluating the time-resolving emission spectroscopy experiments and for numerous helpful discussions. Special thanks go to my colleague Christian Rey. This thesis has benefited from his numerous helpful comments. I would like to give my sincere thanks to Dr. Christian Müller for his valuable help during the last part of my studies. I am very grateful for his comments that significantly improved this thesis. I would also like to thank my colleagues Dr. Friedrich Leopold, Dr. Stephan Weidner, Alina Mielke and Christian Franzmann for the stimulating discussions and encouragement throughout the entire work.

The constant encouragement and support from my family throughout the whole time were essential, and I am very grateful for that.

Finally, I would like to thank my wife, Elena, whose patience, help and support have been indispensable throughout all this time. You have supported me in every possible way and have always rebuilt me in difficult phases. I thank you.

Alexander Nekris
July 2020

Abstract

The interest in plasma research and modelling is growing due to its wide range of applications in academia and industry as well as military purposes. This is particularly the case for electric discharges as they can be obtained easily, and thus are one of the most commonly used plasma generation techniques.

The present work combines common electric discharge models with detailed models for nonequilibrium aerothermodynamics and chemical kinetics. These modelling subjects are usually treated separately, and the challenge of combining the two concepts is highly topical. Therefore, in this thesis, the development of a physicochemical model and its subsequent numerical implementation for the simulation of partially ionized high-speed flows in the state of nonequilibrium and in the presence of electric and magnetic fields are carried out. This allows detailed numerical investigations on different types of electric discharges and improves the capabilities to analyse ionized gases in general.

The physicochemical model developed is based on the single-fluid assumption and takes the chemical and thermodynamic nonequilibria in the gas mixture into account. Therefore, the vibrational and electronic excitation of particles are modelled. This allows the use of more sophisticated kinetic mechanisms for high-enthalpy flows, leading to more accurate results for the chemical composition of the plasma, and thus for its thermodynamic and transport properties. Particular attention is paid to the validity of the assumptions and simplifications used in this work. Due to the high complexity of the processes within the nonequilibrium regions near the electrodes and their small dimensions compared to the characteristic length of the system, the modelling of the plasma nonequilibrium layers is simplified.

For the numerical implementation of the physicochemical model the open-source computational fluid dynamics framework OpenFOAM is used. To validate the numerical solver, a three-dimensional arc discharge on the surface of a wedge in a supersonic flow is numerically calculated. The simulation results provide a detailed picture of the physicochemical processes to be investigated. The numerical results show a fair agreement with the experimental measurements and theoretical values. Possibilities for improving prediction accuracy and suggestions for further research are discussed in detail.

Kurzfassung

Aufgrund der vielfältigen Möglichkeiten der Plasmaanwendung in Wissenschaft und Industrie sowie für militärische Zwecke wächst das Interesse an der Erforschung und Modellierung von Plasmen. Dies gilt insbesondere für elektrische Entladungen, da diese eine sehr häufig verwendete Technik zur Erzeugung von Plasma darstellen.

Die vorliegende Arbeit kombiniert bekannte Modelle elektrischer Entladungen mit detaillierten Modellen zur Beschreibung von Nichtgleichgewichtsaerothermodynamik und chemischer Kinetik. Diese Modellierungsgebiete werden im Allgemeinen getrennt voneinander behandelt. Die Kombination der beiden Konzepte ist jedoch notwendig, um die physikochemischen Prozesse im Plasma besser zu verstehen und abbilden zu können. Daher wird in dieser Arbeit ein physikochemisches Modell entwickelt und anschließend numerisch umgesetzt, um Simulationen von teilionisierten Hochgeschwindigkeitsströmungen im Zustand des Nichtgleichgewichtes und in Überlagerung mit elektrischen und magnetischen Feldern durchführen zu können. Dies ermöglicht detaillierte numerische Untersuchungen zu elektrischen Entladungen und erweitert die Möglichkeiten zur Analyse ionisierter Gase.

Das Modell basiert auf der Ein-Fluid-Annahme und berücksichtigt die chemischen und thermischen Nichtgleichgewichtszustände im Gasgemisch. Dazu werden die Vibrationsanregung und die elektronische Anregung von Partikeln im Plasma modelliert. Dies ermöglicht die Verwendung detaillierter kinetischer Mechanismen für Hochenthalpieströmungen und führt zu präziseren Ergebnissen für die chemische Zusammensetzung des Plasmas und damit der thermodynamischen und Transporteigenschaften des Fluids. Besonderes Augenmerk wird auf die Gültigkeit der in dieser Arbeit getroffenen Annahmen und Vereinfachungen gelegt. Aufgrund der hohen Komplexität der Prozesse innerhalb der Nichtgleichgewichtsschichten an den Elektroden und ihrer geringen räumlichen Ausdehnung im Vergleich zur charakteristischen Länge des elektrischen Bogens, werden die Plasmaschichten vereinfacht modelliert.

Die numerische Implementierung des physikochemischen Modells erfolgt mit Hilfe des quelloffenen Softwarepakets für numerische Berechnungen OpenFOAM. Um das in dieser Arbeit entwickelte numerische Lösungsverfahren zu validieren, wird eine dreidimensionale Lichtbogenentladung auf der Oberfläche eines Keils in einer Überschallströmung berechnet. Die Simulationsergebnisse ergeben ein detailliertes Bild der herrschenden physikochemischen Prozesse. Die numerischen Ergebnisse zeigen eine akzeptable Übereinstimmung mit den experimentellen Messungen sowie analytischen Berechnungen. Möglichkeiten zur Verbesserung der Vorhersagegenauigkeit und Vorschläge für weitere Forschungen werden ausführlich erläutert.

Contents

List of Figures

List of Tables

Nomenclature

Roman Symbols

$\mathbf{a}$	acceleration vector	$\mathrm{m} \cdot \mathrm{s}^{-2}$
A	molecular constant of the colliding species	$-$
A_i	coefficients for the equilibrium-constant curve-fit formula	$-$
$\mathbf{A}$	magnetic vector potential	$\mathrm{T} \cdot \mathrm{m}^{-1}$
$\mathbf{A}$	coefficient matrix	
$\mathcal{A}$	pre-exponential factor in the modified Arrhenius equation	$\mathrm{m}^3 \cdot \mathrm{mol}^{-1} \cdot \mathrm{s}^{-1}$
$\mathbf{b}$	source term vector	
B	magnetic-field magnitude	T
$\mathbf{B}$	magnetic field vector	T
c	speed of sound	$\mathrm{m} \cdot \mathrm{s}^{-1}$
c	species mass fraction	$-$
c_v	specific heat capacity at constant volume	$\mathrm{J} \cdot \mathrm{K}^{-1} \cdot \mathrm{kg}^{-1}$
d	distance between the centroids of two discrete elements	m
$\mathbf{d}_{CF}$	vector joining two cell centroids C and F	m
D_{sr}	binary diffusion coefficient between species s and r	$\mathrm{m}^2 \cdot \mathrm{s}^{-1}$
$\mathbf{D}$	electric displacement field vector	$\mathrm{C} \cdot \mathrm{m}^{-2}$
$\mathbf{D}$	deformation rate tensor	s^{-1}
$\mathcal{D}$	effective diffusion coefficient	$\mathrm{m}^2 \cdot \mathrm{s}^{-1}$
e	specific energy	$\mathrm{J} \cdot \mathrm{kg}^{-1}$
$\mathbf{e}$	unit vector of $\mathbf{E}_f$	$-$
E	energy per unit volume	$\mathrm{J} \cdot \mathrm{m}^{-3}$
E	electric field magnitude	$\mathrm{V} \cdot \mathrm{m}^{-1}$
E_1	energy of vibrational excitation from the vibrational quantum number $v = 0$ to $v = 1$	J
$\mathbf{E}$	electric field vector	$\mathrm{v} \cdot \mathrm{m}^{-1}$
$\mathbf{E}_\mathrm{f}$	surface vector collinear with the $\mathbf{d}_\mathrm{CF}$ vector	m^2
$\mathcal{E}$	voltage gradient	$\mathrm{V} \cdot \mathrm{cm}^{-1}$
F_f	mass flux through the face f of a control volume	$\mathrm{kg} \cdot \mathrm{s}^{-1}$
$\mathbf{F}_\mathrm{Lorentz}$	Lorentz force per unit volume	$\mathrm{N} \cdot \mathrm{m}^{-3}$
$\boldsymbol{\mathcal{F}}_\phi$	flux of the transport property ϕ	

g	relative velocity of colliding particles	$\mathrm{m \cdot s^{-1}}$
$(\Delta h_\mathrm{f})^0_s$	specific enthalpy of formation of species s at 0 K	$\mathrm{J \cdot kg^{-1}}$
ΔH^0_f	overall enthalpy of formation of all species at 0 K per unit volume	$\mathrm{J \cdot m^{-3}}$
$\mathbf{H}$	auxiliary field vector	$\mathrm{A \cdot m^{-1}}$
I	electric current	A
$\mathbf{J}$	electric current density vector	$\mathrm{A \cdot m^{-2}}$
k	reaction rate coefficient	$\mathrm{m^3 \cdot kmol^{-1} \cdot s^{-1}}$
K_eq	equilibrium constant	reaction-dependent
l	length	m
ℓ	mean free path	m
$\mathcal{L}$	spatial operator that includes all non-transient terms of a conservation equation	
m	molecular mass	kg
M	collision partner in a chemical reaction	–
M	Mach number	–
$\mathbf{M}$	magnetization vector	$\mathrm{A \cdot m^{-1}}$
$\mathcal{M}$	molar mass	$\mathrm{kg \cdot kmol^{-1}}$
$\overline{\mathcal{M}}$	reduced molar mass between two colliding particles	–
n	number density	$\mathrm{m^{-3}}$
n	mole number	mole
$\mathbf{n}$	outward unit vector normal to the surface S	–
$\mathcal{O}$	truncation error	
p	static pressure	Pa
$\mathbf{P}$	electric polarization vector	$\mathrm{C \cdot m^{-2}}$
$\mathcal{P}$	arc input power per centimetre	$\mathrm{kW \cdot cm^{-1}}$
q^c	charge of a particle	C
$\mathbf{q}$	heat flux vector	$\mathrm{W \cdot m^{-2}}$
Q	partition function	–
Q_C	Gvosdover cross section for Coulomb collisions	$\mathrm{m^2}$
$\dot{Q}$	source term per unit volume	$\mathrm{W \cdot m^{-3}}$
$\dot{Q}_\mathrm{Joule}$	Joule heating per unit volume	$\mathrm{W \cdot m^{-3}}$
$\dot{Q}_\mathrm{rad}$	radiative heat loss per unit volume	$\mathrm{W \cdot m^{-3}}$
r_pc	positive column radius	cm
R	specific gas constant	$\mathrm{J \cdot kg^{-1} \cdot K^{-1}}$
R	quantum mechanical coefficient describing the reflection of electrons from the potential barrier	–
s	ion slip factor	–
S	fraction of the electron current with respect to total electric current	–
S	surface of a control volume	$\mathrm{m^2}$
S_f	surface of the face f of a discrete element	$\mathrm{m^2}$
t	time	s
$\mathbf{t}$	unit vector of $\mathbf{T}_f$	–

T	temperature	K
$\mathbf{T}$	stress tensor	Pa
$\mathbf{T}_f$	surface vector orthogonal to the cell face f	m^2
$\boldsymbol{\mathcal{T}}_\phi$	all transport mechanisms of the transport property ϕ except convection	
u	velocity magnitude	$m \cdot s^{-1}$
$\mathbf{u}$	velocity vector	$m \cdot s^{-1}$
U	voltage drop	V
V	volume of the discrete element	m^3
$\overline{v}_{sr}$	mean relative speed of particles s and r with Maxwellian velocity distribution	$m \cdot s^{-1}$
$\mathbf{V}$	diffusion velocity vector	$m \cdot s^{-1}$
x_T	distance from leading edge to end of transition	m
y_s	molar fraction of species s	–
z_s	number density ratio n_s/n_tot	–

Greek Symbols

α	wedge angle	deg
β	oblique shock angle	deg
β	Hall parameter	–
β_rot	coefficient for the energy exchange between free electrons and rotational energy of molecules	–
γ	specific heat ratio	–
γ	reduced velocity	$m \cdot s^{-1}$
γ_eff	electron-ion emission coefficient in high-pressure electric arcs	–
γ_i	electron-ion emission coefficient for secondary emission	–
Γ_ϕ	diffusion coefficient of the transport variable ϕ	
$\delta\Phi$	work-function decrease due to Schottky effect	eV
$\Delta_{ij}^{(1)}$	defined by Eq. 3.32	$m \cdot s$
$\Delta_{ij}^{(2)}$	defined by Eq. 3.33	$m \cdot s$
ϵ	average energy per particle	J
ϵ_F	Fermi energy of the material	eV
ε	permittivity of material	$F \cdot m^{-1}$
ζ	empirical constant for the continuum-radiation formula	–
ζ	coefficient of the non-orthogonal contribution	–
η	temperature exponent in the modified Arrhenius equation	–
η	efficiency coefficient for Joule heating and Lorentz force	–

θ	deflection angle	deg
θ_{a}	temperature of activation	K
Θ	characteristic temperature	K
κ	spring constant of the harmonic oscillator	$\mathrm{kg} \cdot \mathrm{s}^{-2}$
κ	thermal conductivity	$\mathrm{W} \cdot \mathrm{m}^{-1} \cdot \mathrm{K}^{-1}$
λ	bulk viscosity	$\mathrm{Pa} \cdot \mathrm{s}$
λ_D	Debye length	m
Λ	cut off parameter for the Gvosdover cross section	$-$
μ	dynamic viscosity	$\mathrm{Pa} \cdot \mathrm{s}$
μ	permeability of matter	$\mathrm{H} \cdot \mathrm{m}^{-1}$
μ_e	electron mobility	$\mathrm{m}^2 \cdot \mathrm{V}^{-1} \cdot \mathrm{s}^{-1}$
$\overline{\mu}_{rs}$	reduced mass of two particles of species r and s	kg
$\overline{\nu}$	characteristic electrical conductivity	s^{-1}
ν	stoichiometric mole number of the reactants	$-$
ξ	correction factor for the field emission	$-$
$\Delta\nu$	bandwidth of the spectrum	s^{-1}
σ	electrical conductivity	$\mathrm{S} \cdot \mathrm{m}^{-1}$
σ_{ij}	differential cross section for the $i-j$ pair of particles	m^2
$\pi\overline{\Omega}_{sr}^{(1,1)}$	collision integral for momentum transfer between species s and r	m^2
$\pi\overline{\Omega}_{sr}^{(2,2)}$	collision integral for energy transfer between species s and r	m^2
ρ	mass density	$\mathrm{kg} \cdot \mathrm{m}^{-3}$
ρ^c	total electric charge density per unit volume	$\mathrm{C} \cdot \mathrm{m}^{-3}$
τ	relaxation time	s
$\boldsymbol{\tau}$	viscous stress tensor	Pa
Υ	molar concentration per unit volume	$\mathrm{kmol} \cdot \mathrm{m}^{-3}$
ϕ	any intensive transport property (generic variable)	
Φ	electric potential	V
Φ_0	work function	eV
χ	scattering angle in the centre of mass system	deg
χ_e	electric susceptibility	$-$
χ_m	magnetic susceptibility	$-$
ψ	compressibility	$\mathrm{m}^2 \cdot \mathrm{s}^{-2} \cdot \mathrm{K}^{-2}$
$\tilde{\psi}$	isentropic compression/expansion coefficient	$\mathrm{m}^2 \cdot \mathrm{s}^{-2} \cdot \mathrm{K}^{-2}$
$\psi(r)$	limiter function	$-$
ω	angular frequency of the harmonic oscillator	s^{-1}
ω_e	electron cyclotron frequency	s^{-1}
ω_{ip}	weighting function of the integration point	$-$
ω_{p}	characteristic angular plasma frequency	s^{-1}
$\dot{\omega}_s$	mass production rate of species s	$\mathrm{kg} \cdot \mathrm{m}^{-3} \cdot \mathrm{s}^{-1}$
$\overline{\omega}$	downwind weighting factor (DWF)	

Subscripts

a	anode
ar	anode region
b	backward
b	bond charge
c	characteristic value
c	cathode
cr	cathode region
C	centroid of the discrete element in the middle of the computational molecule
e	electrons
e	electron-electronic
el	electronic excitation
e,tr	translational mode of free electrons
ex	explicit
f	forward
f	free charge
f	face of a control volume
F	centroid of the neighbouring discrete element
F	field emission
hp	heavy particles: neutral atoms, neutral molecules, ions
i	ionic species
im	implicit
int	source term for the system-internal energy exchange
ind	induced field
ip	integration point along a surface of the face of a discrete element
j	species participating in a chemical reaction
Joule	Joule heating effect
m	molecular species
n	total number of species
n	neutral atom
p	polarization
pc	positive column
r	relative
r	species r
r	equilibration
r	arc column radius
rad	radiative heat loss
rn	total number of chemical reactions
rot	rotational
rot-e	rotational-electron exchange
s	species s: N_2, N, N_2^+, N^+, and e
st	static field

tot	total
tr	translational
tr-rot	translational-rotational
tr-e	translational-electron exchange
T	thermoionic emission
TF	thermo-field emission
vib	vibrational
vib-e	vibrational-electron exchange
vib-rot	vibrational-rotational exchange
vib-tr	vibrational-translational exchange
∞	free-stream conditions
2	flow conditions behind the shock wave

Superscripts

a	ambipolar
C	convection
D	diffusion
D	dissociation
e	edge of the boundary layer
eq	equilibrium
I	ionization
IC	initial condition value
n	reaction order
nip(f)	number of integration points along surface f of a discrete element
nip(V)	number of integration points in the volume V of a discrete element
p	polarization
R	rate of change
$^\circ$	value of the last available solution
*	value of the instantaneous solution
$'$	reactants
$''$	products

Abbreviations

BC	boundary conditions
CD	central differencing scheme
CGS	centimetre-gram-second system of units
CFD	computational fluid dynamics
CV	control volume
DC	direct current
DSMC	direct simulation Monte Carlo
DWF	downwind weighting factor

ESU	electrical CGS units
FDM	finite difference method
FEM	finite element method
FVM	finite volume method
HO	higher-order scheme
HR	high resolution scheme
ISL	French-German Research Institute of Saint-Louis
LTE	local thermodynamic equilibrium
MHD	magnetohydrodynamics
MKS	meter-kilogram-second system of units
NLTE	local thermodynamic nonequilibrium (Non-LTE)
ODE	ordinary differential equation
OpenFOAM	Open Field Operation and Manipulation
SIBS	semi-implicit Burlish-Stoer solver
TVD	total variation diminishing
UD	upwind differencing scheme
1-D	one-dimensional
2-D	two-dimensional
3-D	three-dimensional

Constants

e	elementary charge $= 1.60217662 \times 10^{-19}$	C
h	Planck constant $= 6.62607 \times 10^{-34}$	$\mathrm{J \cdot s}$
k_B	Boltzmann constant $= 1.38064 \times 10^{-23}$	$\mathrm{m^2 \cdot kg \cdot s^{-2} \cdot K^{-1}}$
N_A	Avogadro constant $= 6.02214 \times 10^{26}$	$\mathrm{kmol^{-1}}$
$\mathcal{R}$	ideal gas constant $= 8.3144598$	$\mathrm{J \cdot K^{-1} \cdot mol^{-1}}$
ε_0	electric permittivity of free space $= 8.8541878 \times 10^{-12}$	$\mathrm{F \cdot m^{-1}}$
μ_0	permeability of free space $= 4\pi \times 10^{-7}$	$\mathrm{H \cdot m^{-1}}$

Chapter 1

Introduction

1.1 Background and Motivation

Background

The present work arose in the context of a larger project aiming at investigating the applicability of plasma actuators for course correction of high-speed vehicles and projectiles. The change in the projectile trajectory is caused by asymmetries in the surface pressure distribution induced by a gas discharge on the projectile surface during the flight (plasma-flow interaction) [1, 2, 3, 4]. For this purpose, a DC plasma actuator is used, which, on-demand, induces power-controlled electric discharges between the electrodes installed flush with the surface. The free-flight shock tunnel experiment in a supersonic flow shown in Fig. 1.1 demonstrates the functionality of this concept [5, 6].

The original purpose of the present work was to investigate the possibilities for numerical modelling of the gas discharge impact on flow variables around a projectile [7, 8, 9]. Based on this, a numerical solver should be developed. The subsequent numerical simulations should then contribute to a better understanding of the process to be investigated.

However, the problem described above is more related to flight control, for which a relatively simple plasma model would be sufficient to analyse the influence of a high-intensity arc on the flow variables. At the same time, the interest in plasma research and modelling is growing due to its wide range of applications in academia and industry as well as military purposes. For this reason, the scope of the present work has been extended to the development of a more sophisticated numerical solver capable of modelling subsonic and supersonic ionized nonequilibrium gas flows and their response to electric and magnetic fields. This would allow the carrying out of detailed numerical investigations of various types of electric discharges, as well as improving the analysis of ionized gases in general. Based on this, it is possible to investigate which assumptions and simplifications are reasonable for certain electric discharges and which modelling depth is suitable for phenomena to be modelled.

To summarise, the present work deals with the development of a physicochemical

model and its subsequent numerical realization for the simulation of ionized nonequilibrium high-speed gas flows in the presence of electric and magnetic fields, regardless of the area of application of the model.

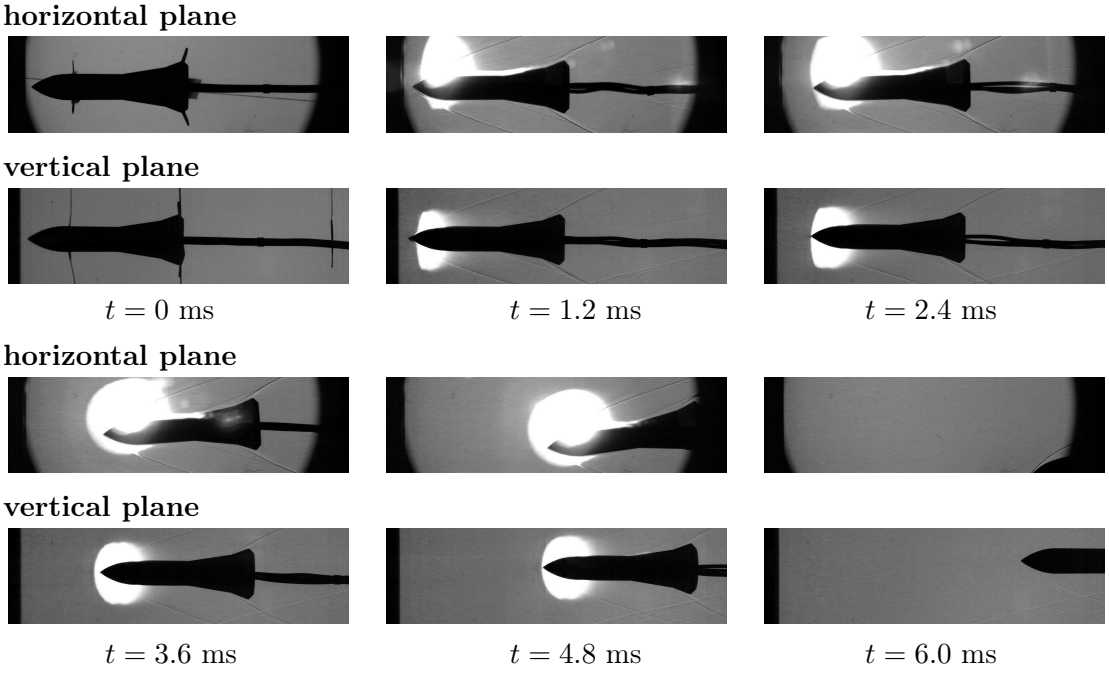

Figure 1.1: Electric discharge generated on a projectile in a nitrogen flow in a free-flight shock-tunnel experiment at $M = 4.5$, $p_\infty = 0.747$ bar, $T_\infty = 272$ K [10].

Motivation

The scope of application of plasmas generated by electric discharges covers a wide range of industrial sectors and research fields. Although the use of gas discharges can be challenging, it is often advantageous over conventional techniques. In the chemical industry, for example, plasmas are used for initiating chemical reactions that are difficult or impossible to induce by applying ordinary chemical mechanisms. A particularly promising technique is the use of gliding arcs generated between two diverging electrodes in a high-speed flow. This technique permits to simultaneously obtain high power levels and high degrees of nonequilibrium of the gas flow. That is, the vibrational or electronic excitation of molecules and atoms would reach high values, while their translational temperature would remain low. By doing so, a selective chemical treatment of reactants can be achieved [11]. Furthermore, plasmas are used in environmental control equipment for treating a wide range of emissions. Also, there exist many applications of electric discharges in the field of material processing like coating, surface modification, and arc welding. Plasmas are also used in aerospace applications, for example in the arc-heated wind tunnels which can be used for ground-based experiments of planetary entry [12]. Moreover, in the last two decades, the interest in studying the effects of electric discharges on subsonic,

supersonic, and, particularly, hypersonic gas flows has increased. This is related to an increasing interest in developing hypersonic flying vehicles as well as ramjet and scramjet engines [13]. There plasma actuators can be used for plasma assisted ignition and combustion (plasma-chemistry interaction) as well as for external and internal flow control (plasma-flow interaction).

Detailed numerical simulations of electric discharges contribute to the understanding of the complex thermochemical and electrodynamic processes in plasmas, as it is often difficult or even impossible to experimentally reproduce and to measure certain phenomena and their interactions under the desired boundary conditions. Furthermore, numerical models allow a separate consideration of different physical effects under simplified conditions, which contributes greatly to the study of individual processes and their impact on the system. Moreover, numerical calculations help to make detailed quantitative statements about the plasma parameters, such as the chemical composition of the gas, the level of vibrational and electronic excitation of different species, the strength of induced magnetic fields and Lorentz forces acting on the ionized gas. Finally, many configurations, geometries, and boundary conditions can be virtually examined and tested utilizing numerical simulations, which is often not possible experimentally.

In some cases, a successful high-quality experiment requires a detailed understanding of the processes to be investigated. In this case, numerical simulation could provide necessary information for carrying out the experiment successfully. For example, a numerical model can be used for obtaining all relevant gas properties of the free jet released from the nozzle exit of an arc-heated wind tunnel. Measuring all gas properties of interest experimentally would be extremely difficult, firstly, because the heating process in the constrictor of an arc heater is complicated and, secondly, due to the strong thermochemical nonequilibrium in the nozzle [12]. For plasma-chemical gas processing numerical simulations can help to find desired plasma parameters at which the chemical process runs optimally. The same applies to plasma assisted ignition and combustion in a high-speed flow, which is especially useful for active control of ramjet and scramjet engines. In general, numerical simulations of ionized high-speed flows can be of great use for investigations of hypersonic flow regimes, for example for the study of nonequilibrium gas-surface interactions [14].

1.2 Objectives

The aim of this project is the development of a numerical solver for the simulation of nonequilibrium electric discharges in high-speed flows with a detailed modelling of the thermochemical processes. The development comprises the following steps:

1. Development of a physicochemical model for a partially ionized high-speed flow in the presence of electric and magnetic fields,
2. Numerical implementation of the model,
3. Solver validation by means of one- and multidimensional analyses.

Development of the Physicochemical Model

The development of the physicochemical model forms the core of this research. The subsequent numerical implementation depends entirely on this work step. The goal is to define a complete physicochemical model consisting of a closed system of governing equations, supplemented by submodels for the calculation of all required chemical, thermodynamic, and transport properties. A precondition for this work step, however, is the preceding definition of a test case, a physicochemical system, which exemplarily represents the field of application of the new solver. A qualitative and quantitative analysis of this system allows the definition of the required modelling depth with all associated assumptions and approximations. This information is then used for the development of the physicochemical model.

As far as the requirements are concerned, the physicochemical model must be able to account for the thermodynamic and chemical nonequilibrium in the system under investigation (test case). In addition, the model must be applicable to both subsonic and supersonic flows and should consider viscous effects in the gas. The turbulence effects are not taken into account for now. Due to the high complexity of the processes within the nonequilibrium regions near the electrodes (plasma sheaths and presheaths) and their small dimensions compared to the characteristic length of the system, the modelling of the plasma nonequilibrium layers is simplified. The breakdown during the ignition of the electric discharge is not modelled. Instead, a simpler method of modelling the ignition is used, in which the gas is heated between the electrodes until ionization begins and the gas becomes a conductor.

Numerical Implementation of the Physicochemical Model

The numerical implementation of the physicochemical model is carried out within the framework of the open-source CFD toolbox foam-extend 4.0, a development branch (a fork) of the open-source CFD platform OpenFOAM (Open Field Operation and Manipulation). The numerical implementation includes two tasks. First, a new OpenFOAM thermophysical model has to be developed, which includes functions for the calculation of all necessary thermodynamic and transport properties of the gas as well as all source terms included in the conservation equations. Second, a new customized OpenFOAM solver has to be set up, which includes all the necessary conservation equations.

Solver Verification and Validation

The verification and validation of the solver consists of two steps. First, the carrying out of a one-dimensional analysis over a temperature range from 2000 to 24,000 K at a pressure of 1 bar. The simulation results obtained are used for the verification of submodels for the transport properties and individual physical processes. Second, performing a transient analysis on a simple three-dimensional (3-D) test case for the validation of the entire physicochemical model by comparing the results with the experimental measurements and data from the literature.

1.3 Thesis Contribution and State of Research

1.3.1 Thesis Contribution

The present work combines common gas discharge models with more sophisticated models for nonequilibrium aerothermodynamics and chemical kinetics. These phenomena are usually treated separately as indicated by Surzhikov [13]: „To date, problems of electrodynamic and physical mechanics of electric discharges have, as a rule, been covered separately from problems of physicochemical kinetics.“ He also states that the challenge of combining the two concepts is highly topical.

Indeed, in most research works in the field of gas-discharge modelling, the modelling depth of chemical kinetics, as well as nonequilibrium thermodynamics, can be increased. In many research projects, local thermodynamic equilibrium (LTE) is assumed for high-pressure gas discharges where the ionized gas is characterized by a single temperature only, which is a simplification. Even if local thermodynamic nonequilibrium (Non-LTE, or NLTE) is taken into account, in most cases, only a two-temperature model is used for calculating thermodynamics. In such a model, the plasma is characterized by two temperatures, namely the translational temperature of free electrons $T_{\mathrm{e,tr}}$, and the temperature of heavy particles (molecules, atoms, and ions) T_{hp}. That is, thermodynamic equilibrium is assumed between all energy modes of heavy particles, meaning the rotational, vibrational, and electronic excitations are in equilibrium with the translational energy: $T_{\mathrm{rot}} = T_{\mathrm{vib}} = T_{\mathrm{el}} = T_{\mathrm{tr}}$. However, in many cases, this assumption is violated, especially in low-density high-speed flows [15]. Consequently, for performing more accurate calculations, such processes as vibrational and electronic excitation must be taken into account. This allows the use of more sophisticated kinetic mechanisms for high-enthalpy flows, leading to more accurate results for the chemical composition of the plasma, and thus for its thermodynamic and transport properties.

1.3.2 State of Research

State of Research in Numerical Gas-Discharge Modelling

Surzhikov [13] provides a detailed overview of several different modelling concepts of electric discharges. In the present research, his work is used as the basic foundation of the knowledge in the field of electric discharge modelling. It must be pointed out that hybrid, kinetic, and stochastic models of gas-discharge processes are beyond the scope of Surzhikov's book. In all computational models discussed there, the plasma is viewed as a continuum. The book deals with both gas and glow discharges with the emphasis on the latter. The computational models discussed are followed by the corresponding simulation examples. For the modelling of glow discharges, Surzhikov presents two classes of models, namely drift-diffusion models and quasi-neutral models with ambipolar diffusion. Most of the examples of glow-discharge models presented are multi-fluid models. As for the gas discharges, which are the subject of the present thesis, Surzhikov provides a detailed description of several

calculation models for different applications and of different modelling depth. All discussed gas-discharge models are one-fluid models and are based on the concept of magnetohydrodynamics (MHD). The discussion includes one-temperature and two-temperature gas-discharge models for plasmas in the state of chemical equilibrium and nonequilibrium.

Nevertheless, Surzhikov's book does not offer the depth of modelling for chemical and thermodynamic processes targeted in the frame of the present thesis. Surzhikov himself points out that the major frame of problems of the physical and chemical kinetics of gas-discharge plasmas is beyond the scope of his book.

The same applies to the work of Mitchner and Kruger [16] where the thermodynamics is limited to a two-temperature plasma and where, in most discussions, chemical equilibrium is assumed. However, this book provides valuable information on developing the fundamental concepts and calculation methods for the study of collision-dominated partially-ionized gas flows in the presence of electric and magnetic fields. Of particular importance for the present work is the discussion in Mitchner and Kruger about the applicability of the so-called MHD approximation and the associated generalized Ohm's law to a physical system to be investigated. The MHD approximation considerably simplifies the Maxwell's equations and thus the electrodynamic part of the model.

Baudry [17] also uses the MHD approximation in his work about 3-D time-dependent modelling of the arc's dynamic behaviour in a DC plasma spray torch. Further assumptions used by Baudry are the quasi-neutrality condition – a requirement for the MHD approximation, the macroscopic description of a plasma, where the plasma is treated as a fluid and the assumption of a laminar and incompressible flow. Analogous to the present thesis, the nonequilibrium plasma sheaths between the plasma column and the electrodes are not modelled in Baudry's work. As far as physicochemical modelling is concerned, the LTE assumption is used in the whole domain of interest. Furthermore, Baudry uses the assumption of chemical equilibrium, where a mixture of argon and hydrogen is treated as a single species.

A similar modelling approach can be found in the work of Blais [18]. This work deals with the development of a numerical model for the deflection of DC transferred arcs using an external magnetic field. The simulations are performed with the CFD finite-volumes commercial code ANSYS Fluent. Also in Blais' work, the assumption of local thermodynamic equilibrium is used and no account is taken of the nonequilibrium electrode layers.

A more detailed modelling of thermodynamic processes can be found in the work of Trelles *et al.* [19]. In the frame of that work, a two-temperature thermal nonequilibrium model is developed and applied to the three-dimensional time-dependent simulation of the flow inside a DC arc plasma torch, typically used in plasma spraying. The authors justify the use of the two-temperature model by stating, that the occurrence of nonequilibrium effects in thermal plasma processes is the rule rather than the exception. They also state that – to their best knowledge – no nonequilibrium model, applied to a 3-D and time-dependent problem, has been reported in the literature yet (as of 2007). Regarding the chemical-kinetic modelling, a four-component chemical

equilibrium model of an argon plasma is used. The authors point out, that chemical nonequilibrium effects could be important in the flow inside plasma torches.

The work of Wendelstorf [20] presents a modelling approach for analysing the overall thermal plasma gas discharge behaviour with the consideration of the nonequilibrium boundary layers (sheath and presheath) in front of the cathode and anode. The model consists of three submodels that are applied to physically different regions. The arc-plasma region and the electrode-solid regions are calculated by separate multidimensional (2-D or 3-D) submodels. The very thin nonequilibrium layers between the electrodes and the plasma are calculated by a further submodel that links the region of the plasma column and the electrode-solid regions by a surface with implemented additional physical processes to be modelled. This layer submodel between the plasma and the solid surface calculates the processes inside the sheath and presheath and transfers plasma and solid surface parameters to new boundary-condition values for the next iteration step [20]. As a result, detailed plasma simulations can be carried out taking into account, for example, such effects as heat conduction within the solid electrodes, electron emission from the cathode surface, the electrical and thermal transition from the electrode surface to the thermal plasma. The mathematical model demonstrated in [20], is more general than the actual numerical implementation, which is two-dimensional and is restricted to stationary DC discharges with cylindrical symmetry. The electrodynamic modelling is based on the MHD approximation. The two-temperature approach is used to separately calculate the temperatures of electrons and heavy particles. Because only monatomic gases (argon, xenon, vaporized mercury) are simulated, the heavy-particle energy includes only the translational and electronic-excitation energy modes, which are considered to be in equilibrium.

From the research works discussed above it becomes clear that the modelling depth of thermochemical processes in the plasma can be increased considerably. Significant progress in the modelling of high-temperature gases has been achieved in the last decades in the field of aerospace research. Thus, calculation models from this field of science are used in the present thesis for detailed modelling of thermodynamics and chemical kinetics.

State of the Art in High-Temperature Gas Dynamics

The work of Chul Park [14] makes a decisive contribution to the development of the physicochemical model in the present work. It provides detailed information on physical phenomena occurring in nonequilibrium chemically reacting flows in the hypersonic regime. This includes, among others, the governing equations of fluid dynamics for a nonequilibrium chemically-reacting flow, formulas for calculating transport properties based on collision integrals, and a detailed definition of thermodynamic properties as well as equilibration models between internal states due to collisional processes.

The thermodynamic model, proposed by Park, is a multitemperature model in which the energy contained in the high-temperature gas is separated into three en-

ergy pools: the translational-rotational, the vibrational, and the electron-electronic energy pool. Consequently, by applying this model to an ionized gas, the fluid is characterized by three temperatures: translational-rotational (T), vibrational (T_{vib}), and electron-electronic temperature (T_{e}). Furthermore, Park delivers a detailed kinetic mechanism for high-temperature air, enabling calculations of chemical nonequilibrium in the fluid flow.

The general modelling strategy used in the present work is based primarily on Park's research. Moreover, several assumptions and simplifications are inherited from Park's work as well. This applies, for example, to the assumption of the thermodynamic equilibrium between the translational and the rotational energy modes of molecules, leading to a common translational-rotational temperature.

The translational-rotational assumption is also used in the work of Jong-Hun Lee [21]. By combining and extending existing theories, Lee delivers basic governing equations for nonequilibrium flows, occurring at flight regimes of aeroassisted orbital transfer vehicles. In addition, Lee provides a complete set of formulas for the calculation of all transport variables. The transport-property models used in the present thesis are mostly taken from Lee's work. They represent a modified version of the models introduced by Yos [22]. The modification consists in extending Yos' models from a one- to a multitemperature approach.

In Yos' work the transport properties are calculated for hydrogen, nitrogen, oxygen, and air for temperatures from 1000 to 30,000 K and for pressures from 1 to 3 bar. The calculation models are based on the Chapman-Enskog theory which gives the transport properties in terms of the so-called collision integrals. Although this work dates back to the 1960s, it has been used for a long time for the calculations of transport variables. For example, Park [14] refers to the transport-property calculation models and corresponding collision-integral data presented by Yos. Also in the report of Gupta *et al.* [23], published in 1990, the results of Yos' work are widely used. For example, the collision cross-sections, required for calculating transport properties, are recomputed in Gupta *et al.* using the same molecular data previously used by Yos. The work of Gupta *et al.* provides a review of reaction rates and thermodynamic and transport properties for an 11-species air model for chemical and thermal nonequilibrium calculations for temperatures up to 30,000 K. Based on previous works, Gupta *et al.* provides more exact formulas for computing the properties of partially ionized air and, also, gives them as curve-fit formulas, which is very convenient for numerical implementations. In this thesis, the research works of Gupta *et al* [23] and Yos [22] are used for the calculation of the collision integrals.

Takahashi *et al.* [12] also uses research work of Gupta *et al.* to evaluate transport properties. The research work of Takahashi *et al.* deals with the effects of radiative heat transfer in the numerical simulations of nonequilibrium flows. The system under investigation is the gas flow inside a constrictor-type arc-heated wind tunnel. The expansion flow in the nozzle section of such a testing facility is in the state of thermodynamic and chemical nonequilibrium. This fact is taken into account in the numerical model. The reaction rate coefficients for chemical reactions are obtained from Park's work [14]. In contrast to Lee [21] and Park [14], Takahashi *et al.* treats

the rotational temperature separately from the translational temperature to take into account the strong nonequilibrium in the arc heaters nozzle. On the other hand, in contrast to the works of Lee and Park, electronic-excitation of molecules and atoms is not taken into account. The authors justify this simplification with a negligibly small contribution of the electronic-excitation energy E_{el} to the overall energy in the system.

The computational model of Takahashi *et al.* provides a complete modelling approach for the energy equilibration between the internal energy modes via energy-exchange models. Some of these models are used in the present work. As far as electrodynamics is concerned, Takahashi *et al.* derives the electric field and the current density, required for the calculation of Joule heating, from the generalized Ohm's law and the potential expression of the charge conservation equation. The calculation of the induced magnetic field and the Lorentz force, however, are not taken into account. The simulated flow is laminar, steady, continuous, and axisymmetric.

The work of Yu *et al.* [24] is devoted to 2-D numerical simulations of inductively coupled plasma flows in the state of thermodynamic and chemical nonequilibrium inside a plasma wind tunnel. As in the research work of Takahashi *et al.*, Yu *et al.* use a four-temperature model for modelling the thermodynamic nonequilibrium and the work of Gupta *et al.* for calculating the collision integrals, required for computing transport properties. Similar to Takahashi *et al.*, the electronic-excitation energy is not taken into account in the thermodynamic modelling. The chemical nonequilibrium is modelled by using a kinetic mechanism for high-temperature nitrogen – the working gas of the plasma wind tunnel. This kinetic mechanism represents a combination of selected chemical reactions, taken from the work of Dunn and Kang [25] and Park [14]. The same mechanism is used in the present research.

Of particular interest for the present work is the work of Casseau [26]. In the frame of Casseau's work, based on the open-source CFD platform OpenFOAM, a solver called *hy2Foam* is developed. This is a two-temperature hypersonic CFD solver developed for simulating flows past high-speed vehicles like they occur during a planetary entry or at a hypersonic flight. According to Casseau, the solver *hy2Foam* aims at providing a foundation for a future hybrid CFD-DSMC code within the OpenFOAM framework. That is, for lower layers of the atmosphere, where the fluid can be treated as a continuum and, consequently, the governing equations of fluid dynamics hold, the *hy2Foam* solver can be used. For simulating low-density flow conditions, appearing at high altitudes, OpenFOAM provides a direct simulation Monte Carlo[1] (DSMC) solver – named *dcmsFoam*. Coupling both methodologies would allow to simulate the full range of regimes from the molecular regime in a rarefied gas at high altitudes to the continuum regime in the lower layers of the atmosphere.

The two-temperature formulation, implemented in *hy2Foam*, is based on the work of Park [14]. There, the electron and electronic excitation energy modes are assumed

[1]DSMC is a technique used for analysing high Knudsen number flows. It emulates the same physics as the Boltzmann equation by following the motions and collisions of a large number of particles [27].

to be in equilibrium with the vibrational energy mode. The same applies to the translational and rotational energy modes. As a result, the fluid is characterized by two temperatures, the translational-rotational and the vibro-electronic temperature [26]. It is worth to mention that there is a multi-vibrational version of *hy2Foam* in which the vibrational-vibrational energy exchange between molecules of different species is taken into account.

Casseau's work has many things in common with the work presented here. There are many similarities in the physicochemical modelling and in both cases, the OpenFOAM platform is used for the numerical realization. The main difference to the present work, however, is that Casseau's work focuses mainly on the development of a numerical tool for simulating flow fields surrounding a reentry vehicle. For this reason, no responses of the partially ionized gas on external electromagnetic fields have been considered.

1.4 Dissertation Overview

The present thesis consists of six chapters. The present chapter – Chapter 1 – provides the motivation, the aims and objectives of the present work as well as some information on the state of research. Chapter 2 deals with the definition of a physicochemical system, exemplarily representing the field of application of the new solver, and subsequent elaboration of the basic concept of the physicochemical model, which is to be implemented numerically. For this purpose, a preliminary analysis of the physicochemical system is carried out, in which all potential assumptions and simplifications are examined for their validity. Based on Chapter 2, a physicochemical model is derived in Chapter 3 for the simulation of ionized nonequilibrium high-speed gas flows in the presence of electric and magnetic fields. The chapter is divided into three sections, one for chemical-kinetic, one for fluid-dynamic and one for electrodynamic modelling. Chapter 4 focuses on the numerical realization of the physicochemical model derived in Chapter 3. The validation of the numerical tool and the subsequent discussion of the simulation results of the system under investigation are presented in Chapter 5. The last chapter – Chapter 6 – summarises the work, draws conclusions from the numerical results and gives suggestions for future work.

Chapter 2

Physicochemical System under Investigation

The development of the physicochemical model requires the definition and evaluation of a test case - a physicochemical system that exemplarily represents the field of application of the new solver. This system must be kept simple, while retaining the most physical effects of interest.

This chapter opens with the definition of a suitable test case of an electric discharge in a supersonic flow in Sec. 2.1. Subsequently, the defined physicochemical system is analysed by first determining in Sec. 2.2 the type of the discharge under investigation as well as its structure and physical properties. Subsequently, in Sec. 2.3, the system is studied from the view point of aerothermodynamics and chemical kinetics. During this process, the physicochemical system is analysed to obtain information about what assumptions and simplifications can be used to construct the physicochemical model as simple as possible, while retaining the physical and chemical effects of interest. Based on the information obtained, a modelling concept is then derived in Sec. 2.4.

2.1 Definition of the Physicochemical System

The physicochemical system under investigation consists of an aerodynamic model and a plasma actuator embedded in this model. Both systems are described below.

2.1.1 Aerodynamic Model

For the test case geometry, a wedge with a length of 250 mm, a width of 120 mm and an angle of 30° with a sharp leading edge is selected. On one of wedge's surfaces a possibility for installation of the actuator's electrodes and pressure transducers is provided (see Fig. 2.1, left). The experiments are carried out in the high-enthalpy shock tunnel STA of the French-German Research Institute of Saint-Louis (ISL). The wedge is mounted in the measurement section without angle of attack at a distance of 10 mm from the nozzle exit (see Fig. 2.1, right).

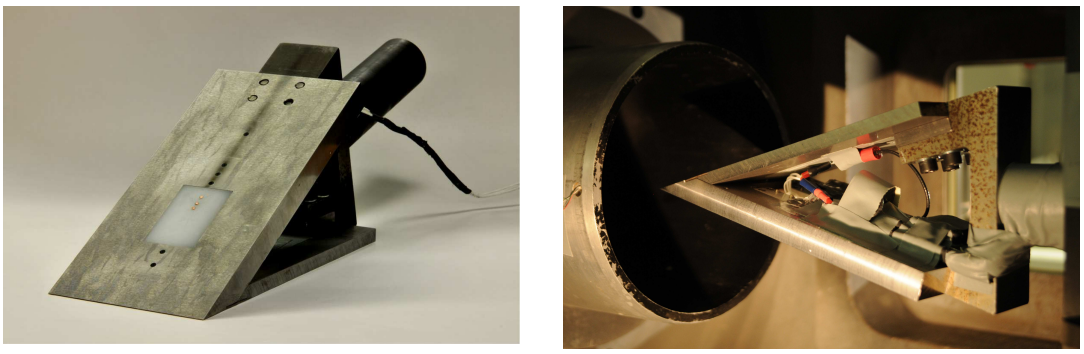

Figure 2.1: Aerodynamic model of a wedge mounted in the measurement section of the shock tunnel.

The electric discharge is generated on the surface of the wedge in a high-speed nitrogen flow between the electrodes installed flush with the surface in an electrically insulating plate (see Fig. 2.2).

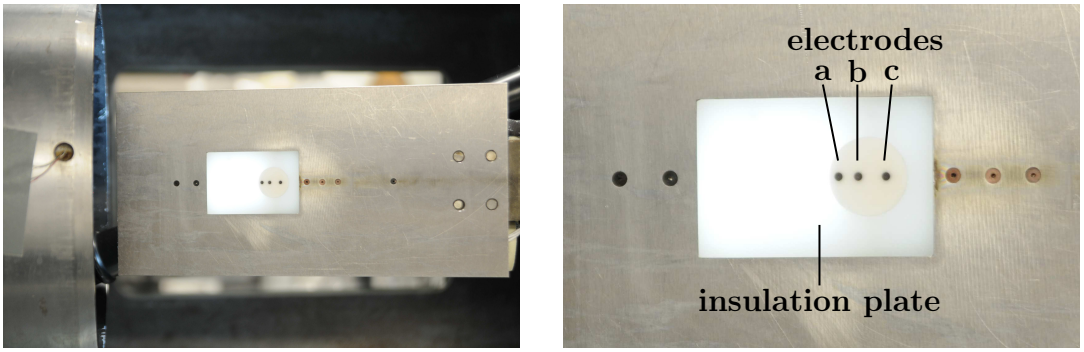

Figure 2.2: Wedge surface with the electrodes embedded in an insulating plate.

After the membranes of the shock tunnel burst, the nitrogen is expanded and accelerated in the nozzle forming a quasi-steady high-speed flow past the wedge of a duration of 3 to 4 ms (Fig. 2.3) [10]. During this period of time, the gas discharge is

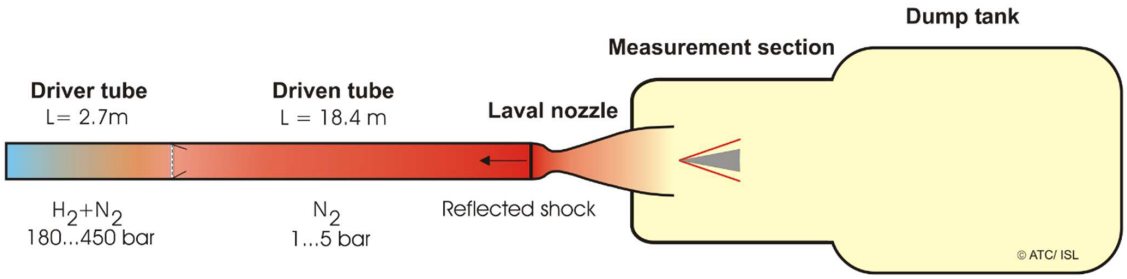

Figure 2.3: Schematic of the shock tunnel.

generated and experimental measurements are conducted. A typical operation time of electric discharges analysed in the present work is between 1 and 3 ms.

The free-stream conditions of the high-speed flow are as follows: $p_\infty = 0.34$ bar, $T_\infty = 234$ K, and $u_\infty = 1452.44\ \mathrm{m \cdot s^{-1}}$, corresponding to conditions at approximately 8 km of altitude. At these conditions, an oblique shock wave, attached to the nose of the wedge, occurs, as shown in the image sequence in Fig. 2.4.

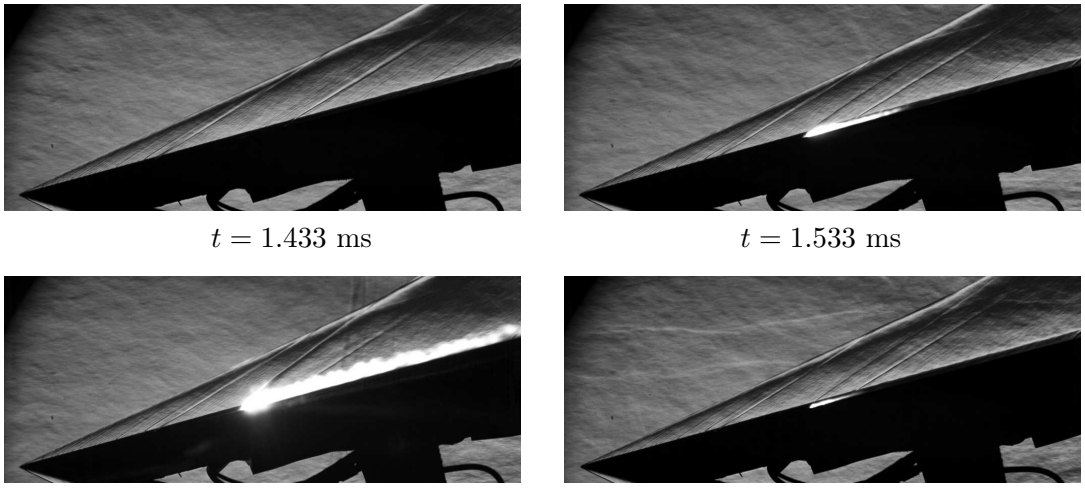

$t = 1.433$ ms $t = 1.533$ ms

$t = 2.0$ ms $t = 3.2$ ms

Figure 2.4: Electric discharge generated on a wedge in a nitrogen flow in a shock-tunnel experiment at: $M = 4.6$, $p_\infty = 0.34$ bar, $T_\infty = 234$ K.

The wave angle[1] β can be calculated by using the so called θ-β-M relation [28]:

$$tan(\alpha) = 2cot(\beta)\frac{M_\infty^2 sin^2(\beta) - 1}{M_\infty^2\,(\gamma + cos(2\beta)) + 2}\ , \tag{2.1}$$

where θ denotes the deflection angle which is of 15°, since the wedge angle amounts to 30° and the angle of attack is 0°. The quantity γ denotes the specific heat ratio. The free-stream Mach number is calculated by [15]:

$$M_\infty = \frac{u_\infty}{c}\ , \tag{2.2}$$

where the speed of sound is given as [15]:

$$c = \left(\gamma \frac{\mathcal{R} T_\infty}{\mathcal{M}}\right)^{1/2}\ . \tag{2.3}$$

At a free-stream flow temperature of $T_\infty = 234$ K, the specific heat ratio of nitrogen is estimated at $\gamma = 1.4$. The ideal gas constant is given in $\mathrm{J \cdot K^{-1} \cdot mol^{-1}}$ and amounts to $\mathcal{R} = 8.3144598$. The molar mass of nitrogen has a value of $\mathcal{M}_{N_2} = 0.028\ \mathrm{kg \cdot mol^{-1}}$. By inserting the free-stream conditions into Eqs. 2.1 - 2.3, the following values are

[1] The wave angle is the angle between the shock wave and the upstream-flow direction [28]

obtained: $c = 311.81\ \mathrm{m \cdot s^{-1}}$, $M_\infty = 4.65$, and $\beta = 25.1°$. The density ρ_∞ can be calculated via the ideal gas law as follows:

$$\rho_\infty = \frac{p_\infty \mathcal{M}_{\mathrm{N_2}}}{T_\infty \mathcal{R}} = 0.4893\ \mathrm{kg \cdot m^{-3}}\ .$$

With the above calculated data, it is possible to determine the flow conditions behind the shock wave (indicated by the subscript 2) where the electric discharge is ignited. The Mach number behind the oblique shock, M_2, is calculated by [28]:

$$(M_2)^2 sin^2(\beta - \alpha) = \frac{(\gamma - 1)M_\infty^2 sin^2(\beta) + 2}{2\gamma M_\infty^2 sin^2(\beta) - (\gamma - 1)}\ . \tag{2.4}$$

The obtained value amounts to $M_2 = 3.318$. The thermodynamic conditions behind the oblique shock wave can be calculated with the following relations [28]:

$$\frac{\rho_2}{\rho_\infty} = \frac{(\gamma + 1)M_{\mathrm{n},\infty}^2}{2 + (\gamma - 1)M_{\mathrm{n},\infty}^2}\ , \tag{2.5}$$

$$\frac{p_2}{p_\infty} = 1 + \frac{2\gamma}{\gamma + 1}(M_{\mathrm{n},\infty}^2 - 1)\ , \tag{2.6}$$

$$\frac{T_2}{T_\infty} = \frac{p_2}{p_\infty}\frac{\rho_\infty}{\rho_2}\ , \tag{2.7}$$

where the Mach number normal to the shock wave is given as: $M_{\mathrm{n},\infty} = M_\infty sin(\beta)$ [28]. The obtained conditions amount to: $p_2 = 1.4866$ bar, $T_2 = 389.43$ K, $c_2 = 402.36\ \mathrm{m \cdot s^{-1}}$, $\rho_2 = 1.2855\ \mathrm{kg \cdot m^{-3}}$ and $u_2 = 1335\ \mathrm{m \cdot s^{-1}}$.

2.1.2 Electric Discharge Actuator

Operation Principle of the Electric Discharge Actuator

As shown in Fig. 2.2, the DC plasma actuator has three electrodes a, b, and c. Actually, these are two pairs of electrodes, namely a - b and b - c, which belong to two different systems forming the actuator. The anode a and the shared cathode b belong to the high-voltage low-energy activating system – called discharge trigger. This system is used to ignite the electric arc. The shared cathode b and the anode c are the electrode pair of the low-voltage high-energy plasma generator for providing the energy necessary for the gas discharge operation [10].

The ignition process of the actuator is shown schematically in Fig. 2.5. The high-voltage low-energy activating system generates a high-voltage pulse in the kilovolts range at the a - b - electrode pair. This causes an electrical breakdown, leading to the ionization of a small gas volume between the electrodes. This step is called in Fig. 2.5 as preionization. The preionized gas volume is advected and stretched by the gas flow until it finally passes over the b - c - electrode pair. At that moment, the electrical circuit of the low-voltage high-energy plasma generator closes. The gas

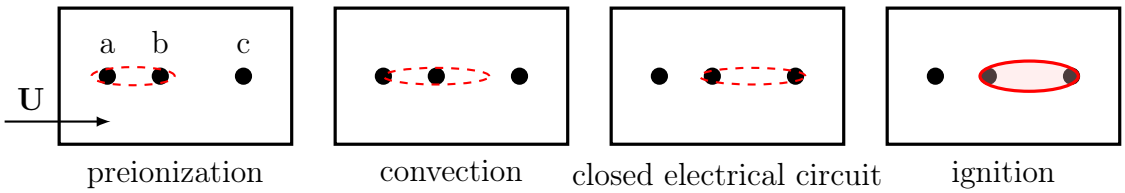

Figure 2.5: Schematic representation of the ignition process of the plasma actuator.

discharge ignites and electric current begins to flow between the electrodes through the ionized gas resulting in a self-sustained electric arc.

In the present work, copper electrodes embedded in an insulating polyamide plate are used for experiments (see Fig. 2.6, left). The electrodes have a radius of 1.0 mm. The distance between the centre lines of the electrodes of the a - b pair amounts to 5 mm and of the b - c pair to 7 mm. That is, the shortest distance between the electrode edges of the b - c pair is 5 mm. This distance is essential for the intensity of the discharge, since it is inversely proportional to the electric field strength.

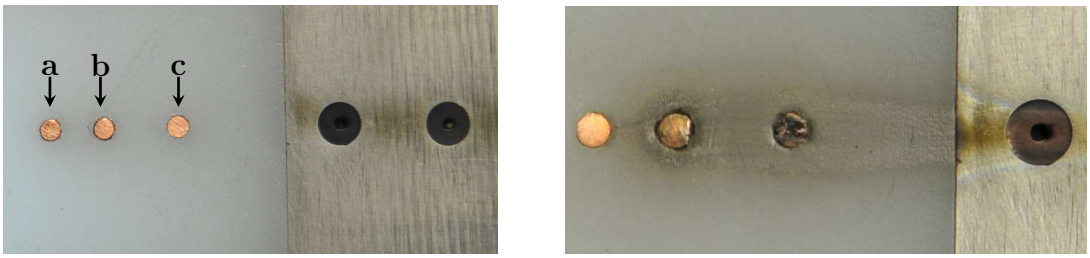

Figure 2.6: Copper electrodes in a polyamide plate.

Consequences of the Electrode Erosion

In Fig. 2.6 on the right, the state of the electrodes after several experiments is shown. A clear electrode surface erosion can be recognized which is limited to the right edge of the electrode b and is distributed over the entire surface of the electrode c.

This is a clear disadvantage of copper electrodes in the study of a pure nitrogen plasma, since contamination by copper vapour could significantly alter the transport properties of the plasma. This is demonstrated in the work of Shayler and Fang [29] where the transport properties of a copper-nitrogen mixture are calculated for temperatures between 2000 and 28,000 K and pressures from 1 to 10 bar (see Fig. 2.7). The results show that for temperatures in the range of approximately 12,000 to 16,000 K, the presence of copper vapour would not significantly affect the transport properties of the nitrogen plasma. At lower temperatures, however, even a low concentration of copper would significantly enhance plasmas transport properties.

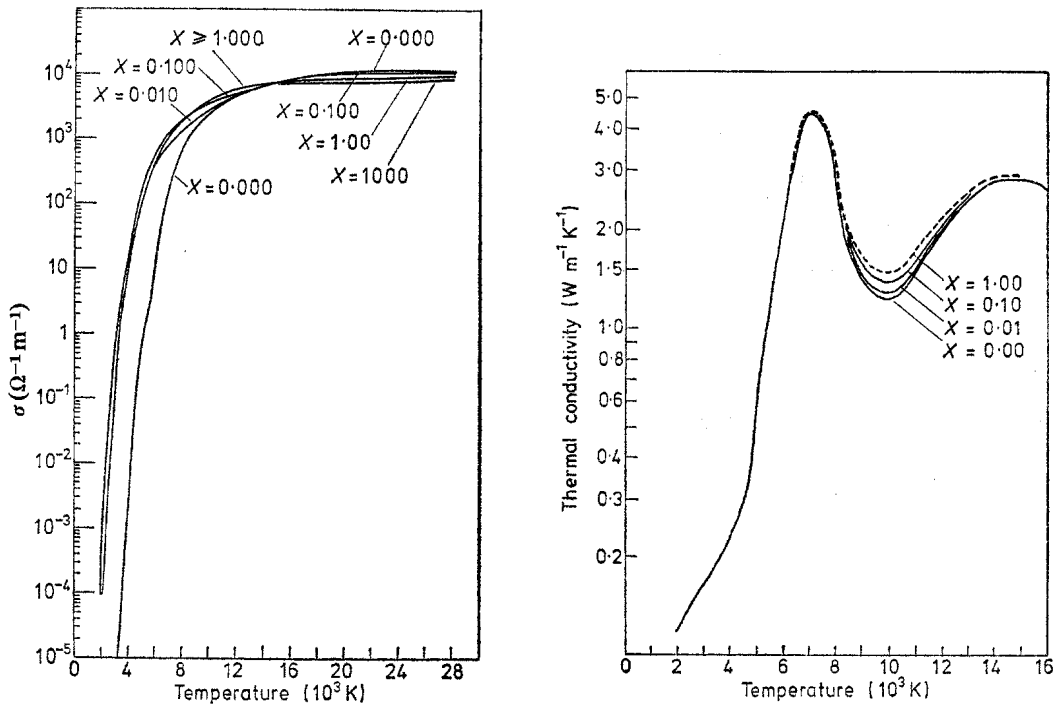

Figure 2.7: Electrical and total thermal conductivities of copper-nitrogen mixture at 1 bar as a function of number density ratio (here denoted by X) [29].

Operation Conditions of the Plasma Actuator

In the present work, a gas discharge with a constant input power of 10 kW is analysed. To achieve this in an experiment, the power supply is regulated during the operational time by a current controller which holds the current at values in the range of 70 to 90 A. Under these conditions, a voltage in the range of 120 - 140 V arises at the main electrodes b and c.

Regarding the geometry and configuration it can be stated that the gas discharge under investigation is stabilized from one side by the wall and from other sides by the stream flow. Magnetic stabilization should play a rather minor role, since only self-induced magnetic fields occur that are rather weak.

Based on all the information given above the system under investigation can be schematically represented as shown in Fig. 2.8.

2.2 Analysis of the Electric Discharge

Based on the information obtained in Sec. 2.1 a theoretical analysis of the electric discharge to be modelled is now undertaken. In the following, first the theoretical background regarding the classification of gas discharges is given. Afterwards, the subregions of a typical gas discharge and their basic physical features are examined.

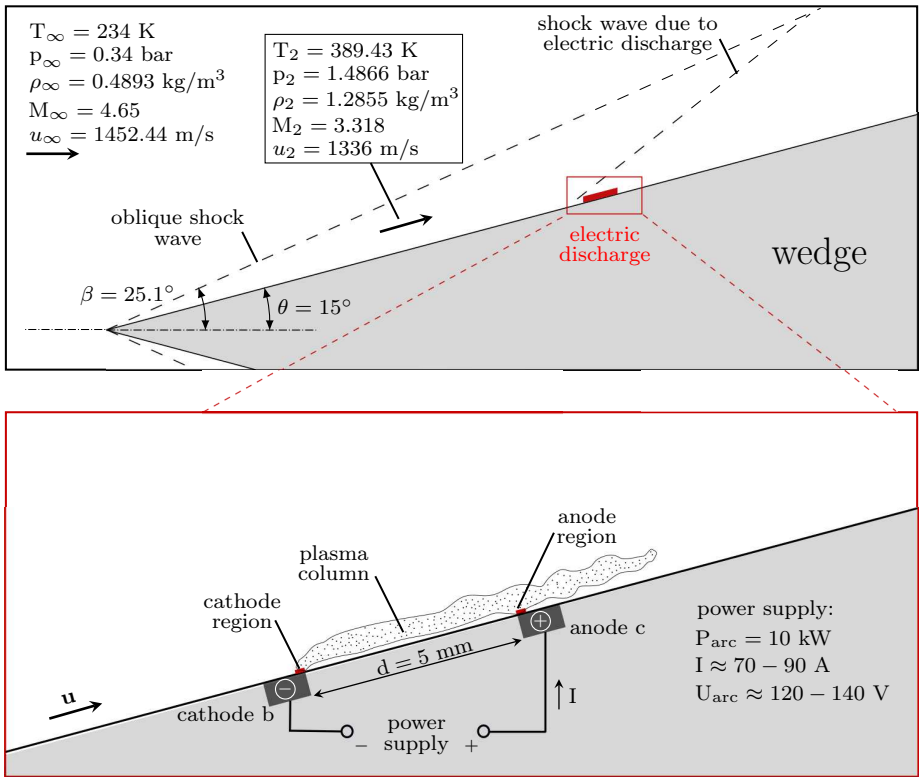

Figure 2.8: Schematic representation of the physical system under investigation.

2.2.1 Classification of the Electric Discharge

Classification through the Voltage-Current Characteristics

According to Hoyaux [30], electric discharges can be subdivided according to their voltage-current characteristic into three major classes with the corresponding transitions as follows: dark discharges (also called Townsend discharges), glow discharges, and arc discharges (see Fig. 2.9).

The current threshold for the transition from a glow to an arc discharge lies approximately between 0.1 and 1 A [30]. The electrode voltage drops during the transition from a glow to a gas discharge from several hundreds to a few tens of volts.

Classification via the Operating Pressure Level

For electric arcs, a further distinction can be made between high-pressure and low-pressure arc discharges, wherein the threshold for the transition from low- to high-pressure discharge class is at approximately 0.1 bar [30, 11].

In high-pressure arcs, the translational temperature of free electrons and heavy particles (ions and neutrals) and the temperatures that characterize the excitation of different internal energy modes of atoms and molecules are relatively close together. This assumption is often called local thermodynamic equilibrium (LTE). In the case of low-pressure arcs, the translational temperature of free electrons considerably exceeds

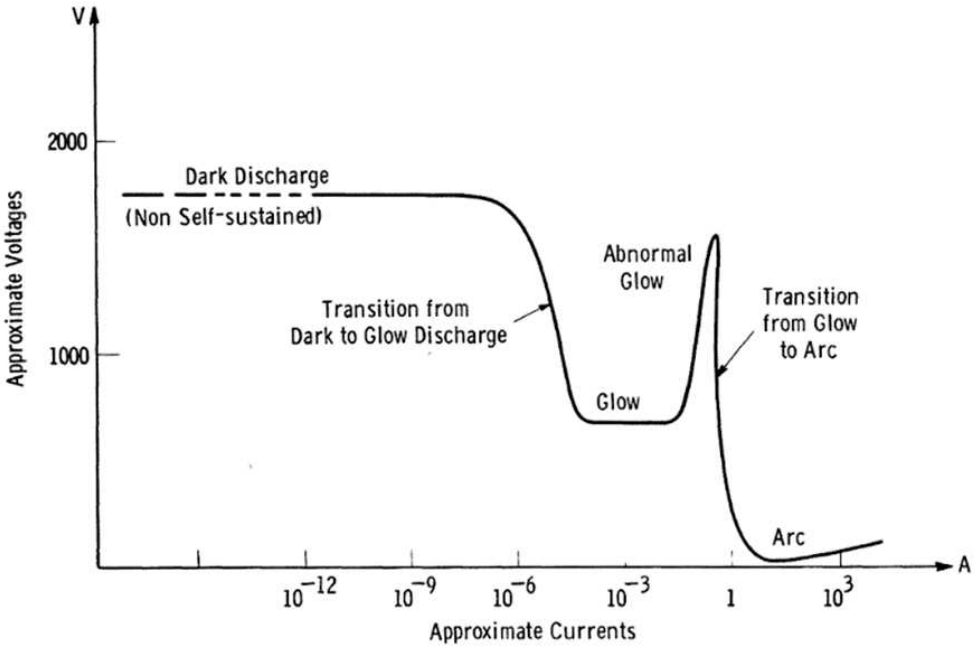

Figure 2.9: Approximate voltage-current characteristic of an electric discharge with electrodes free from tips or edges [30].

the temperature of heavy particles, reaching temperature ratios of two orders of magnitude. This behaviour results from a relatively large mean free path[2] of free electrons and from a large amount of energy, received from the external electric field [30]. That is, in a diluted plasma, free electrons experience a longer acceleration time between the successive collisions with heavy particles than in a denser plasma. In such a case, the LTE assumption is violated and the plasma is said to be in the state of local thermodynamic nonequilibrium (NLTE-sate).

Distinction between Thermal and Nonthermal Discharges

In the context of the concept of local thermal equilibrium, a further classification of electric discharges is often made, namely between thermal and nonthermal discharges. A glow discharge is considered a typical example of a nonthermal discharge. Such systems can operate very far from the thermodynamic equilibrium and are characterized by a high selectivity with respect to the plasma-chemical reactions [11]. An arc discharge, on the other hand, is considered a traditional example of a thermal discharge. In contrast to glow discharges, these discharges are usually powerful, easy to sustain, and can operate close to LTE. However, at lower pressures, but still above the threshold of 0.1 bar, the LTE assumption may be violated.

In summary it can be stated, that arc discharges can be both thermal and nonthermal, depending on operation conditions. Typical ranges of thermal and nonthermal arc discharge parameters are depicted in Tab. 2.1 [11].

[2]The average distance travelled by a particle between successive collisions [16, 31]

Table 2.1: Typical ranges of thermal and nonthermal arc discharge plasma parameters [11].

Discharge plasma parameter	Thermal arc discharge	Nonthermal arc discharge
Gas pressure	$0.1 - 100$ bar	$1 \times 10^{-6} - 0.1$ bar
Arc current	$30 - 30 \times 10^3$ A	$1 - 30$ A
Cathode current density	$10^7 - 10^{11}$ A $\cdot$ m^{-2}	$10^6 - 10^8$ A $\cdot$ m^{-2}
Voltage	$10 - 100$ V	$10 - 100$ V
Power per unit length	> 100 kW $\cdot$ m^{-1}	< 100 kW $\cdot$ m^{-1}
Electron density	$10^{21} - 10^{25}$ m^{-3}	$10^{20} - 10^{21}$ m^{-3}
Gas temperature	$> 10{,}000$ K	$300 - 6000$ K
Electron temperature	$> 10{,}000$ K	$2000 - 20{,}000$ K

Classification of the Gas Discharge under Investigation

Based on the information given above, the gas discharge under investigation can be classified as follows:

- The electric discharge to be analysed belongs, with its amperage of $70 - 90$ A and a voltage of $120 - 140$ V, rather to the arc-discharge class.
- In the system under investigation the static pressure behind the shock wave amounts to 1.4866 bar, which means that the gas discharge to be modelled is a high-pressure arc.
- Based on the operating conditions given in Fig. 2.8, the system under investigation may be assigned to the class of thermal gas discharges. However, because the discharge is generated in a supersonic flow and on a cold wall, a local deviation from the LTE assumption may occur.

2.2.2 Structure of an Arc Discharge

General Description of the Structure of an Arc Discharge

An electric arc can be divided into three regions: cathodic region, positive column, and anodic region [30]. Since the system to be modelled is a surface discharge, a wall region can also be distinguished and should be mentioned.

The most convenient way to describe the structure and the properties of a gas discharge is by means of a simply shaped axially-symmetrical uniform arc, whose plasma channel is not affected by the presence of a wall or any externally imposed gas flow. As a further simplification, it is assumed that the electrodes, in contrast to the system under investigation, are facing each other. The description of the arc structure is carried out in the following by using the schematic representation of a free-burning linear arc in Fig. 2.10. This illustration is prepared using the works of Fridman and Kennedy [11], Wendelstorf [20], Zhukov and Zasypkin [32], and Surzhikov [13].

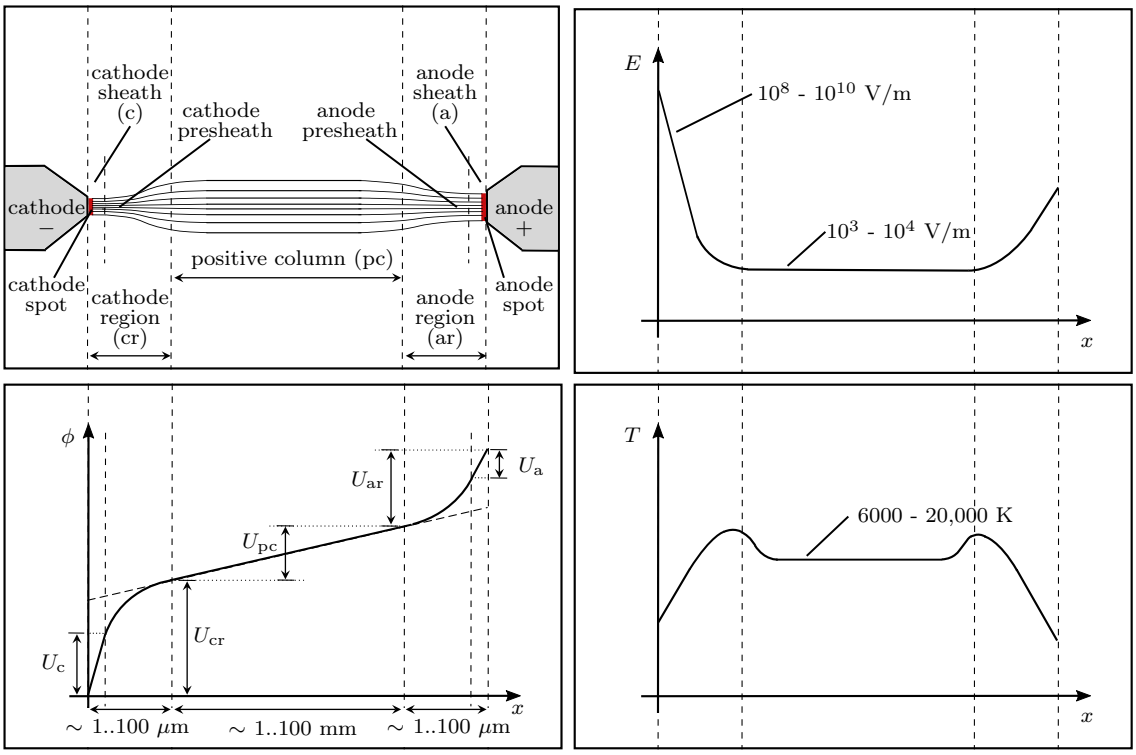

Figure 2.10: Schematic representation of a free-burning linear arc with corresponding spatial distribution of the electric potential ϕ, electric field magnitude E, and gas temperature T.

The positive column represents the largest part of the arc, the length of which may vary between a few millimetres and a few centimetres, depending on the distance between the electrodes. In the cathode and anode regions, the cathodic and anodic boundary layers can be identified, which provide the transition from the solid-electrode surface to the plasma. Each of these layers consists of a sheath and a presheath (see Fig. 2.10) [20]. The length of the cathode and anode layers in high-pressure arcs is of the order of magnitude of $1 - 100$ μm and is inversely proportional to the gas density and pressure [11]. This length corresponds to the order of several mean free path lengths, ℓ, of the particles in the plasma [32].

Distribution of Arc Properties over the Discharge Length

The division of the arc into three regions allows to divide the total voltage drop over the discharge into the voltage drop over the cathodic region U_{cr}, the positive column U_{pc}, and the anodic region U_{ar} (see Fig. 2.10). Due to the ambiguity of the terms "electrode region" and "electrode layer", the definition of the cathodic and anodic voltage drops, U_{c} and U_{a}, is more difficult, although these terms are often used [30].

The cathodic and anodic voltage drops cause peaks in the electric field in the vicinity of the cathode and anode (see Fig. 2.10). The potential drop in the major part of the positive column, on the other hand, is often considered to be more or

less linear. Thus, in the central part of the positive column the electric field remains approximately of the same magnitude almost over the entire length of the discharge.

For simple analysis, the temperature profile over the positive column is often assumed to be nearly constant. The temperature values range from several thousands to a few tenths of thousand of Kelvin (see Fig. 2.10), depending on operating conditions. However, at the constricted ends of the discharge, due to electric field peaks and consequently a more intensive Joule heating, temperature peaks emerge. By further approaching the electrodes, the temperature drops to the level of the electrode surface temperature, which is much lower than in the positive column [11].

Positive Column

The positive column represents a long homogeneous region of the electric arc, consisting of quasineutral plasma ($n_e \approx n_i$). The main part of the discharge power is released there [11, 30]. The discharge column can be constricted at both ends and is separated from the electrodes by the cathode and anode regions (see Fig. 2.10).

The electric current in the positive column is provided almost completely by the electrons due to their high mobility compared to ions [11]. This means that the fraction of the electron current S of the total electric current has almost the value of one: $J_{\text{tot}} \approx J_e$, and hence $J_e \gg J_i$. This can be proved for the system under investigation by comparing the velocity of free electrons $\mathbf{V}_e$ with the velocity of ions $\mathbf{V}_i$. Supposing that the gas temperature in the positive column amounts to $T = 12{,}000$ K, it can be assumed that nitrogen is almost completely dissociated and thus consists mostly of neutral and ionized atoms and free electrons. By assuming that no significant pressure and concentration gradients of electrons and ions occur inside the positive column, the only significant driving force of electrons and ions is the external electric field. Thus, their drift velocities can be calculated as follows:

$$\mathbf{V}_e = -n_e \mu_e \mathbf{E} \quad \text{and} \quad \mathbf{V}_i = n_i \mu_i \mathbf{E} \ , \tag{2.8}$$

where the electron and ion mobilities are given as [16]:

$$\mu_e = \frac{e}{\overline{\mu}_{ehp} \overline{\nu}_{ehp}} \quad \text{and} \quad \mu_i = \frac{e}{\overline{\mu}_{in} \overline{\nu}_{in}} \ . \tag{2.9}$$

The elementary charge e amounts to $1.60217662 \times 10^{-19}$ C. The reduced mass of species s and r is defined as [16]:

$$\overline{\mu}_{sr} = \frac{m_s m_r}{(m_s + m_r)} \ . \tag{2.10}$$

For the reduced mass of electrons (e) and heavy particles (hp) it can be assumed that: $\overline{\mu}_{ehp} \approx m_e$, since $m_e + m_{ehp} \approx m_{hp}$. For the reduced mass of ions (i) and neutral atoms (n) it may be assumed that $\overline{\mu}_{in} = m_{\text{N}}/2$, where the mass of nitrogen atoms $m_{\text{N}} = 2.3259 \times 10^{-26}$ kg. The collision frequencies of electrons with heavy particles $\overline{\nu}_{ehp}$, as well as of ions with neutral atoms $\overline{\nu}_{in}$, are calculated in Sec. 2.3.2. For a nitrogen plasma at $T = 12{,}000$ K and a pressure of 1 bar these values are

approximately as follows: $\overline{\nu}_{ehp} \approx 3.0 \times 10^{11}$ s^{-1} and $\overline{\nu}_{in} \approx 4.7 \times 10^{9}$ s^{-1}. Substituting these quantities into Eq. 2.9 yields the following mobilities: $\mu_e \approx 0.58$ m$^2 \cdot$ V$^{-1} \cdot$ s^{-1} and $\mu_i \approx 0.0029$ m$^2 \cdot$ V$^{-1} \cdot$ s^{-1}. Due to quasineutrality of plasma ($n_e \approx n_i$) from Eq. 2.8 it becomes evident that for confirming the above statement it is sufficient to compare the mobilities only. Since $\mu_e \gg \mu_i$, it can be stated that $J_e \gg J_i$.

Cathode Region

The cathode region is divided into a cathode layer, consisting of a sheath and a presheath, and a near-cathode plasma constriction zone. All these subregions are characterized by different physics [33].

Looking from the cathode surface towards the positive column, the sheath – also called space charge layer – forms the first subregion. This is a narrow, positively charged, collisionless layer, in the non-LTE state [30]. The positive charge results from the accumulation of ions on the cathode surface due to the ion drift towards the cathode caused by the electric field. This leads to a high ion particle density in the vicinity of the cathode surface ($n_i > n_e$) and, consequently, to a breakdown of quasineutrality in the sheath. In high-pressure arcs the thickness of the sheath is of the order of the Debye length λ_D approx. $\sim$ 10 nm. Most of the cathode voltage drop takes place in the sheath having values between 10 and 20 V depending on the cathode material [11]. Due to the extremely short length of the sheath, this voltage drop generates a strong electric field in the immediate vicinity of the cathode surface, which is the order of $10^8 - 10^{10}$ V $\cdot$ m^{-1} [32]. As a result, the ions generated in the adjacent presheath are accelerated in the sheath towards the cathode. This results in ion bombardment of the cathode surface, leading to a heating of the cathode. Heat radiation from the positive column is a further contribution to the temperature increase of the cathode surface. Both high surface temperature and strong electric field activate different electron emission mechanisms from the cathode's surface, which are discussed in detail in Appendix A [11, 33]. The fraction of the electron current in a high-pressure arc, generated by cathode emission mechanisms, is of $S \approx 0.7 - 0.9$ [11]. That is, between 70 % and 90 % of the arc electron current is generated in the sheath: $J_e = S \cdot J_{\text{tot}}$. The remaining 10 % to 30 % of the total electric current J_{tot} result from the flux of positive ions towards the cathode surface.

The presheath, also known as ionization zone, is a longer quasineutral layer of the order of thickness of several mean free path lengths ℓ of plasma particles, corresponding to ~ 100 μm. This layer is located between the sheath and the constricted zone of the positive column and is responsible for the formation of positive ions due to electron-impact ionization of neutral particles [34, 30]. Thus, one of the major functions of the presheath is to provide a sufficient number density of ions, necessary for the cathode heating [11]. Due to the electron-impact ionization and the resulting electron avalanche, the electron current fraction in the presheath grows from $S \approx 0.7 - 0.9$ to almost unity in the positive column [11].

The last subregion of the cathode region is the near-cathode plasma constriction zone. It forms a transition from the cathode layer to the plasma column. Because of

its strongly contracted cross section, this zone is characterized by significantly higher electric field and temperature compared to the positive column.

Another feature of the cathode region is the so-called cathode spot through which the arc discharge is connected to the cathode surface. The cathode spot is formed when the energy flux to the cathode does not suffice to heat up the entire cathode surface to temperature values necessary for activating electron-emission mechanisms. Instead, the entire electrical current of the electric arc is transmitted to the cathode through a small surface fraction [11]. Depending on electrodynamic effects, cathode material and geometry as well as surface heterogeneities, the cathode spot may appear in different configurations. It can appear as a single and relatively large contact surface (diffuse spot), a small hot spot, or even as several microspots [20]. Moreover, cathode spots have a tendency to move on the cathode surface [30].

It is worth to mention, that in high-pressure arcs the cathodic surface acts as a heat sink. This property is not limited to the cathode spot only, but concerns the entire cathode surface [30]. Additional energy removal occurs at cathodes with low melting temperature, like copper or silver, due to melting, sputtering, and evaporation of the cathode material under the cathode spot.

From Fig. 2.6 it can be seen that in the system under investigation the erosion takes place at the right edge of the cathode, because it is closest to the anode. It is assumed that the hot spot is likely to be smaller than the entire eroded zone. Consequently, it probably moves during the discharge or appears as several microspots.

Anode Region

The structure of the anode region is analogous to the cathode region [33], where a nonequilibrium layer can be identified, consisting of an anodic sheath and a presheath [20]. Depending on the anode geometry and configuration, the anode-region cross section may be contracted towards the anode surface and thus may form a near-anode plasma constriction zone.

According to Benilov [33], the voltage drop in the anode sheath is considerably lower than in the cathode sheath layer and may even have negative values under certain circumstances. It occurs because the electrons attracted by the positively charged anode form a negative space charge near their surface, which in turn repels the ions leading to a voltage drop in the anode sheath. At high arc currents, this voltage drop can have values of approximately the ionization potential [11]. Depending on the arc geometry, an additional voltage drop may occur when the discharge column is constricted at the anode. This additional voltage drop sometimes exceeds the voltage drop in the sheath by a factor of two [11].

The anode spots usually occur in high-pressure discharges on relatively small and inhomogeneous anodes, having current densities of approx. 10^5 to 10^7 $\mathrm{A} \cdot m^{-2}$ [11]. The high electric field in the immediate vicinity of the anode, resulting from the anodic voltage drop, causes a bombardment of the anode surface by electrons. This effect together with the heat radiation coming from the arc, leads to the anode heating. As a result, the anode temperature increases above the boiling point of the

electrode material, leading to the erosion beneath the anode spot [30]. In Fig. 2.6, it can be seen that almost the entire anode surface is eroded. This is probably to the heat radiation from the positive column which is stretched by the high-speed flow over the anode. An additional energy input could be received from the anodic spot.

Wall Region

The wall surface in the system under investigation is made of polyamide, meaning that no current is flowing from the plasma to the wall or vice versa. Such an insulating wall is called "inert" wall [30]. Similar to the electrodes, a sheath (space charge layer) and a quasineutral presheath are formed on an inert wall [11, 30]. The sheath has a thickness of the order of the Debye length and thus can be considered as collisionless, whereas the thickness of presheath is several times larger. Formation of the sheath takes place because the electrons have a faster thermal velocity than the much heavier and hence less mobile ions. Thus, the electrons travel much faster towards the wall and are able to stick to its surface, leaving the near-wall zone to the ions [11]. As a result, a positively charged sheath is created over the wall [30]. More information on this topic can be found, for example, in the book of Fridman and Kennedy [11].

For the present work, it is only important that all the effects occurring in the wall region are more relevant to low-pressure arcs. In high-pressure arcs, these processes are completely superseded by the function of the wall as a heat sink [30]. Since the system to be investigated represents a high-pressure arc, it is assumed that the physical phenomena in the sheath and presheath of the wall are also completely superimposed by the cooling effects on the wall.

2.3 Analysis of the Aerothermodynamic System

From the thermo- and fluid dynamic perspective, it can be stated that the physical system to be modelled is a gaseous, supersonic, high-temperature fluid flow, which is partially ionized at certain locations (here between the electrodes and somewhat downstream) and hence electrically conductive. The ionized fluid is subject to electric and magnetic fields and therefore responds to them with certain physical effects.

In the following, the physicochemical system under investigation is analysed from the view point of aerothermodynamics in order to determine the necessary modelling depth. For this purpose, the characteristic scales of space and time of the physicochemical system are compared with spatial and temporal scales of several separate physical and chemical processes, occurring in the system [13].

2.3.1 Characteristic Values of the System

Characteristic Electric Field

The voltage drop over the entire discharge amounts to 130 V. This is the approximate average value measured at the power supply terminals during a gas discharge with

constant input power of 10 kW. By assuming an overall voltage drop over the cathode and anode layers of $U_{\mathrm{cr}} + U_{\mathrm{ar}} \approx 30$ V, the voltage drop over the positive column becomes $U_{\mathrm{pc}} \approx 100$ V. The shortest distance between the electrodes amounts to 5 mm. Thus, for the electric-field magnitude along the shortest field lines between the electrodes the following value is obtained: $100\ \mathrm{V}/5\ \mathrm{mm} = 2 \times 10^4\ \mathrm{V \cdot m^{-1}}$. This value is taken as the characteristic value of the electric-field magnitude E_{c}.

Characteristic Length

As the characteristic length of the system the radius of the arc column is selected, since the strongest gradients of the arc properties occur there. However, even stronger gradients may occur outside the plasma column in the cathode and anode regions.

To estimate the arc radius, the report of Wells [35] is used in which a detailed study of axially-symmetrical uniform arc columns is given. Wells defines the radial limit of an arc column as the radius from which the electrical conductivity becomes so small that it is essentially negligible. For nitrogen plasmas at atmospheric pressures, the electrical conductivity becomes negligibly small at temperatures below 5000 K, which is why Wells chooses this temperature as the peripheral temperature of the arc column T_{R}. Further, he demonstrates that with increasing voltage gradient per centimetre $\mathcal{E}$ and a constant input power per centimetre $\mathcal{P}$, the radius of an axially-symmetric positive column r_{pc} tends to approach a specific value. Wells calculates that for a gas discharge with $\mathcal{P} = 10\ \mathrm{kW \cdot cm^{-1}}$, the arc radius approaches a value of ≈ 0.00175 m for $\mathcal{E} > 40\ \mathrm{V \cdot cm^{-1}}$. In the present study, $\mathcal{E} \approx 200\ \mathrm{V \cdot cm^{-1}}$ and the input power per centimetre amounts to $20\ \mathrm{kW \cdot cm^{-1}}$, since $\mathcal{P} = P_{\mathrm{arc}}/d$ and $P_{\mathrm{arc}} = 10$ kW. It is therefore assumed that r_{pc} approaches an even smaller value due to a higher voltage gradients prevailing in the gas discharge to be modelled. In addition, the system under investigation is a surface discharge in a supersonic flow which is stretched and pressed against the surface by the gas flow. This could lead to a further reduction of the radius. Consequently, such a gas discharge is not radially symmetric. Therefore, the average arc column radius and thus the systems characteristic length of $r_{\mathrm{pc}} = l_{\mathrm{c}} = 1 \times 10^{-3}$ m are used in the present work.

Characteristic Temperature

In his work, Wells [35] uses arc-column similarity parameters previously defined by Lord [36] and confirms their validity by numerical calculations. Of particular interest to the present work is the so-called current parameter $I\mathcal{E}^{-1}r_{\mathrm{pc}}^{-2}$ and it can be shown that it is a function of the centre-line temperature of the arc column T_0.

The value of the arc current I is given in Sec. 2.1.2 and is in the range of approximately $70 - 90$ A. By inserting the above-mentioned values for the system to be examined, the following value is obtained for the current parameter:

$$\frac{I}{\mathcal{E}\ r_{\mathrm{pc}}^2} = \frac{80\ \mathrm{A}}{200\ \mathrm{V \cdot cm^{-1}}\,(0.1\ \mathrm{cm})^2} = 40\ \mathrm{A \cdot V^{-1} \cdot cm^{-1}}\ . \tag{2.11}$$

Fig. 2.11 shows the variation of current parameter with the centre-line temperature T_0 for nitrogen arcs at $p = 1$ bar. From this diagram a value of $T_0 \approx 12{,}000$ K can be read out for the system to be examined. This value is considered to be the characteristic temperature of the positive column. However, due to the electric field peaks at the electrode edges, higher temperatures are expected there.

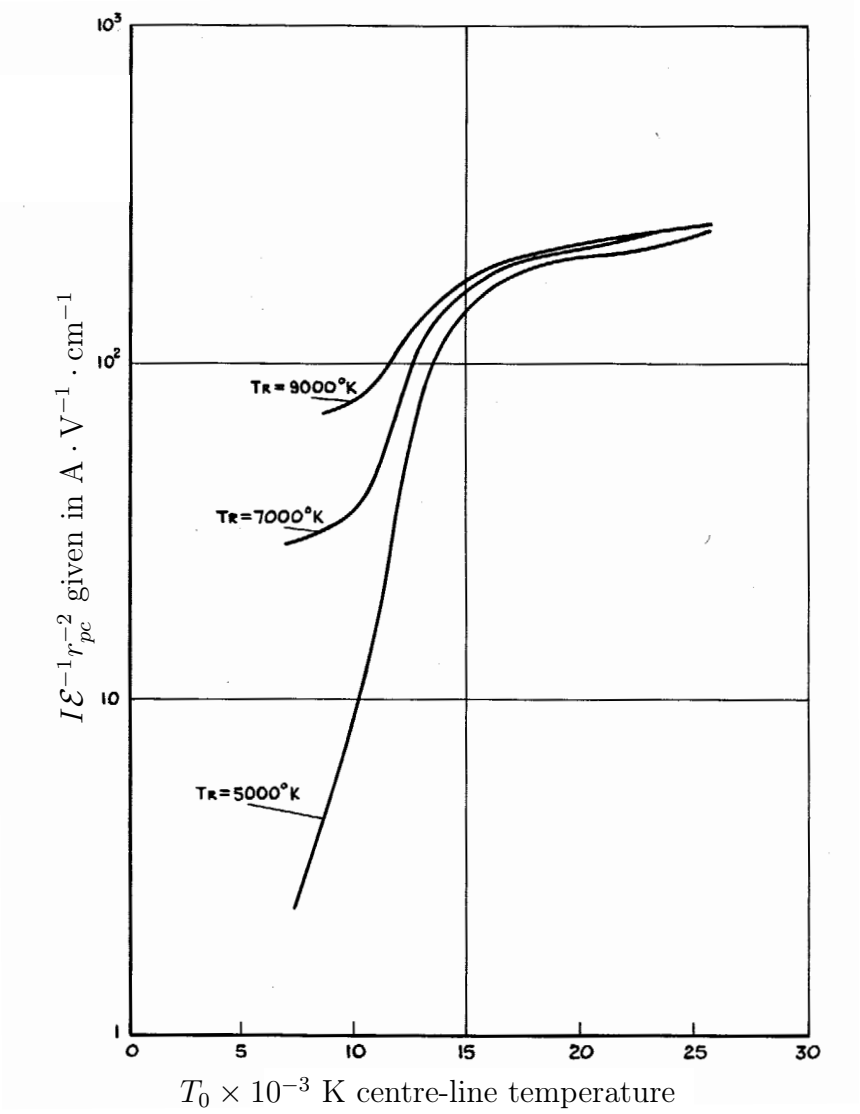

Figure 2.11: Variation of current parameter $I\mathcal{E}^{-1}r_{\mathrm{pc}}^{-2}$ given in A · V^{-1} · cm^{-1} with the centre-line temperature for arcs in nitrogen at atmospheric pressure (T_{R} is the peripheral temperature of the arc column) [35].

Characteristic Velocity

The fluid flow velocity behind the shock amounts to 1336 m · s^{-1}. It is assumed that the gas discharge protrudes beyond the boundary layer and is therefore located

partly in the boundary layer and partially in the free-stream flow. For this reason, for the characteristic velocity magnitude u_c a flow speed of 1000 $m \cdot s^{-1}$ is assumed.

Characteristic Time

After ignition, the gas discharge is operated at a constant input power of 10 kW and thus is considered to be in a steady state. For steady-state conditions the characteristic time t_c can be calculated as follows: $t_c = l_c/u_c = 1 \times 10^{-6}$ s [16].

Characteristic Electrical Conductivity

The value of the characteristic electrical conductivity σ_c for nitrogen at $T_c = 12{,}000$ K is taken from the work of Yos [22] and amounts to 4.4×10^3 $S \cdot m^{-1}$.

Characteristic Magnetic Field

The estimation of induced magnetic field magnitude is carried out by using the integral form of Ampère's law for a constant current I, meaning that the Maxwell's correction term can be neglected (magnetostatic case):

$$\oint_S \mathbf{B}\, d\mathbf{s} = \mu_0 I \ . \tag{2.12}$$

Eq. 2.12 states that the integral of induced magnetic field around a loop is proportional to the electric current passing through the surface enclosed by this loop. The diameter of the positive column is estimated at $\approx 2l_c = 2 \times 10^{-3}$ m. The integral of the magnetic field around the arc column is: $s = 2l_c\pi = 0.00628$ m. Thus, the induced magnetic field magnitude can be estimated by: $B = \mu_0 I/s$. At a current of 80 A, the magnetic field magnitude becomes $B_c \approx 0.016$ T. By moving away from the positive column this value would steadily decrease.

Characteristic Values of the Physicochemical System

All characteristic values of the system under investigation are listed in Tab. 2.2.

Table 2.2: Characteristic values of the system under investigation.

l_c	u_c	t_c	T_c	σ_c	E_c	I_c	B_c
1×10^{-3}	1×10^3	1×10^{-6}	1.2×10^4	4.4×10^3	2×10^4	80	1.6×10^{-2}
m	$m \cdot s^{-1}$	s	K	$S \cdot m^{-1}$	$V \cdot m^{-1}$	A	T

2.3.2 Continuum Assumption

One of the requirements for the physicochemical model is its applicability to gas flows at conditions, prevailing in lower layers of atmosphere. At these conditions, the

matter may be sufficiently dense for using the so-called continuum description, where the gas is considered on the macroscopic level and is treated as a fluid [15]. The continuum description is not valid for low-density flows in which the molecules are widely spaced. In such cases, the matter is considered as a conglomerate of particles and therefore methods from kinetic theory must be used for calculations [15].

Conditions for the Continuum Assumption

According to Mitchner and Kruger [16], a plasma can be considered as a continuum if it is a collision dominated plasma. This assumption is subject to the following two conditions:

1. In a collision dominated plasma, the mean free paths ℓ for all constituents are much smaller than the characteristic length scale for macroscopic change: $\ell_s \ll l_\mathrm{c}$.
2. The characteristic time scale for macroscopic change must be much larger than the time of collision intervals: $t_\mathrm{c} \gg \overline{\nu}_s^{-1}$.

The quantity $\overline{\nu}_s$ is the average collision frequency between particles of species s and all other particles in the gas mixture [16].

To examine, whether the first condition applies, often the Knudsen number[3] is used. According to Anderson [15], the continuum assumption holds at Knudsen numbers of $Kn < 0.03$. The Knudsen number is defined as follows [15]:

$$Kn = \frac{\ell_s}{l_\mathrm{c}} \ . \tag{2.13}$$

The mean free path of the species s may be written as [16]:

$$\ell_s = \frac{1}{\sum\limits_{r=1}^{n} \left[\left(m_s / \overline{\mu}_{sr} \right)^{1/2} n_r \pi \overline{\Omega}_{sr}^{(1,1)} \right]} \ , \tag{2.14}$$

where the quantity $\pi\overline{\Omega}_{sr}^{(1,1)}$ denotes the weighted average of the collision cross section for the momentum transfer between species s and r (also known as momentum transfer collision integral). The upper bound n of summation in Eq. 2.14 denotes the total number of species in the gas mixture. The quantity $\overline{\mu}_{sr}$ is the reduced mass of species s and r, defined in Eq. 2.10.

For verifying the second condition for its validity, the averaged momentum transfer collision frequencies $\overline{\nu}_s$ of each species s with all other species are required. They can be calculated by the expression [16]:

$$\overline{\nu}_s = \sum_{\substack{r=1 \\ r \neq s}}^{n} n_r \overline{v}_{sr} \pi \overline{\Omega}_{sr}^{(1,1)} \ , \tag{2.15}$$

[3]The Knudsen number (Kn) is a dimensionless number which is defined as the ratio of the mean free path of a particle to the characteristic length scale for macroscopic change [16].

where $\overline{v}_{sr}$ denotes the mean relative speed between particles s and r with Maxwellian velocity distribution and is defined as [16]:

$$\overline{v}_{sr} = \left(\frac{8 k_\mathrm{B} T}{\pi \overline{\mu}_{sr}} \right)^{1/2} \quad . \tag{2.16}$$

With the help of Eqs. 2.13 - 2.16, the numerical analysis is now conducted to verify the applicability of the continuum description for the system under investigation.

Continuum Assumption: Verification of the First Condition

Since most data for a nitrogen plasma in the literature are given for an atmospheric pressure, a pressure of $p = 1$ bar is assumed for this numerical analysis. The number densities of the nitrogen-plasma constituents are taken from the report of Pflanz and ter Horst [37]. According to these data, at $T = T_\mathrm{c} = 12{,}000$ K the nitrogen plasma is almost completely dissociated and partially ionized, consisting mainly of N, N^+, and e. The number densities are: $n_\mathrm{N} \approx 4.6 \times 10^{23}$ m^{-3} and $n_{\mathrm{N}^+} = n_e \approx 6.5 \times 10^{22}$ m^{-3}. The molecular masses of the nitrogen atoms, their atomic ions, and the electrons amount to: $m_\mathrm{N} \approx m_{\mathrm{N}^+} = 2.3259 \times 10^{-26}$ kg and $m_e = 9.109 \times 10^{-31}$ kg, respectively. The averaged momentum transfer collision integrals of plasma constituents at $T =$ 12,000 K are taken from Yos [22] and shown in Tab. 2.3, where Q_C denotes the Gvosdover cross section for Coulomb collisions.

By inserting the given data into Eqs. 2.13 - 2.16, following mean free paths and Knudsen numbers are calculated for each plasma constituent:

- $\ell_e = 1.01 \times 10^{-6}$ m and $Kn_e = 0.00101$,
- $\ell_\mathrm{N} = 1.31 \times 10^{-6}$ m and $Kn_\mathrm{N} = 0.00131$,
- $\ell_{\mathrm{N}^+} = 4.72 \times 10^{-7}$ m and $Kn_{\mathrm{N}^+} = 0.000472$.

All calculated mean free path values are much smaller than the characteristic length value of $l_\mathrm{c} = 1 \times 10^{-3}$ m. Thus, the first condition, $\ell_s \ll l_\mathrm{c}$, for a collision dominated plasma is met. By calculating the Knudsen number for each species individually, the conditions of required minimum value of $Kn = 0.03$ are met as well.

Table 2.3: Averaged momentum transfer collision integrals given in m^2 for a nitrogen plasma at $T = 12{,}000$ K [22].

Q_C	$\pi\overline{\Omega}_{ee}^{(1,1)}$	$\pi\overline{\Omega}_{e\mathrm{N}}^{(1,1)}$	$\pi\overline{\Omega}_{e\mathrm{N}^+}^{(1,1)}$	$\pi\overline{\Omega}_{\mathrm{NN}}^{(1,1)}$	$\pi\overline{\Omega}_{\mathrm{NN}^+}^{(1,1)}$	$\pi\overline{\Omega}_{\mathrm{N}^+\mathrm{N}^+}^{(1,1)}$
8×10^{-18}	$0.8 Q_\mathrm{C}$	5×10^{-20}	$0.8 Q_\mathrm{C}$	9.3×10^{-19}	1.7×10^{-18}	$0.8 Q_\mathrm{C}$

Continuum Assumption: Verification of the Second Condition

The results for the collision frequencies and collision intervals (reciprocal values of the collision frequencies) are as follows:

- $\overline{\nu}_e = \overline{\nu}_{ee} + \overline{\nu}_{e\mathrm{N}} + \overline{\nu}_{e\mathrm{N}^+} = 4.05 \times 10^{11}\ \mathrm{s}^{-1} + 1.56 \times 10^{10}\ \mathrm{s}^{-1} + 2.86 \times 10^{11}\ \mathrm{s}^{-1}$ $= 7.06 \times 10^{11}\ \mathrm{s}^{-1}$ and $\overline{\nu}_e^{-1} = 1.41 \times 10^{-12}$ s,
- $\overline{\nu}_\mathrm{N} = \overline{\nu}_{\mathrm{N}e} + \overline{\nu}_{\mathrm{NN}} + \overline{\nu}_{\mathrm{NN}^+} = 2.2 \times 10^{9}\ \mathrm{s}^{-1} + 6.63 \times 10^{8}\ \mathrm{s}^{-1} + 2.56 \times 10^{9}\ \mathrm{s}^{-1}$ $= 5.42 \times 10^{9}\ \mathrm{s}^{-1}$ and $\overline{\nu}_\mathrm{N}^{-1} = 1.84 \times 10^{-10}$ s,
- $\overline{\nu}_{\mathrm{N}^+} = \overline{\nu}_{\mathrm{N}^+e} + \overline{\nu}_{\mathrm{N}^+\mathrm{N}} + \overline{\nu}_{\mathrm{N}^+\mathrm{N}^+} = 2.86 \times 10^{11}\ \mathrm{s}^{-1} + 4.69 \times 10^{9}\ \mathrm{s}^{-1} + 2.53 \times 10^{9}\ \mathrm{s}^{-1}$ $= 2.93 \times 10^{11}\ \mathrm{s}^{-1}$ and $\overline{\nu}_{\mathrm{N}^+}^{-1} = 3.41 \times 10^{-12}$ s.

All collision interval values are much smaller than the characteristic time value t_c. That is, the second condition, $t_\mathrm{c} \gg \overline{\nu}_s^{-1}$, is met and the plasma under investigation is a collision dominated plasma for which the continuum description holds.

Continuum Assumption Verification for the Free-Stream Flow

In conclusion, the same numerical analysis is performed for the "cold" nitrogen gas flow at $T_\infty = 234$ K and $p_\infty = 0.34$ bar. In this way, it is examined, whether the continuum assumption also applies to the free-stream flow. The number density n_{N_2}, required in Eq. 2.15, is calculated by the formula:

$$n = \rho \frac{N_\mathrm{A}}{\mathcal{M}}\ , \tag{2.17}$$

where the Avogadro constant amounts to $N_\mathrm{A} \approx 6.02214 \times 10^{26}\ \mathrm{kmol}^{-1}$, the molar mass of molecular nitrogen has a value of $\mathcal{M}_{\mathrm{N}_2} = 28\ \mathrm{kg \cdot kmol}^{-1}$, and the density of nitrogen at 0.34 bar is $\rho_\infty = 0.48930\ \mathrm{kg \cdot m}^{-3}$.

By inserting these values into the equation above, the number-density value results at $n_{\mathrm{N}_2} = 1.05 \times 10^{25}\ \mathrm{m}^{-3}$. The value of $\pi\overline{\Omega}^{(1,1)}_{\mathrm{N}_2\mathrm{N}_2}$ at $T_\infty = 234$ K is estimated at $\approx 4 \times 10^{-19}\ \mathrm{m}^2$. By using Eqs. 2.13 - 2.16, the following values are obtained for the free-stream conditions: $Kn = 1.68 \times 10^{-4} \ll 0.03$ and $t_\mathrm{c} \gg \overline{\nu}^{-1} = 4.0 \times 10^{-10}$ s. Thus, the continuum assumption also holds for the free-stream flow.

2.3.3 Laminar-Flow Assumption

In the following, it is investigated whether the flow in the vicinity of the electrodes is laminar or turbulent. Thus, the key question is whether the transition from a laminar to a turbulent flow takes place in front of the electrodes or behind them – further downstream. In the latter case, the flow next to the electrodes would be laminar and the laminar flow assumption would hold.

The distance between the leading edge of the wedge and the first electrode is ≈ 0.1 m. The transition point x_T, which gives the location of the transition region, can be calculated by using the transition Reynolds number[4] Re_T as follows [15]:

$$x_\mathrm{T} = \frac{Re_\mathrm{T}\ \mu^\mathrm{e}}{\rho^\mathrm{e} u^\mathrm{e}}\ , \tag{2.18}$$

[4]The Reynolds number Re is the dimensionless quantity which gives the ratio of internal forces to viscous forces within a fluid: $Re_\mathrm{T} = \rho u x_\mathrm{T}/\mu$, where x_T is the distance from the leading edge to the end of transition.

where the superscript e denotes the conditions at the edge of the boundary layer. These values correspond to the values behind the oblique shock wave (see Fig. 2.8) which are as follows: $\mu_2 \approx 2 \times 10^{-5}$ Pa·s, $u_2 \approx 1336$ m·s^{-1}, and $\rho_2 \approx 1.2855$ kg·m^{-3}.

According to Anderson [15], no theory yet exists for the prediction of Re_{T}. However, for many conditions empirically derived equations exist. In the work of Hopkins, Jillie, and Sorensen [38], several semiempirical methods derived by Deem and Murphy for estimating the end of boundary-layer transition are presented. They are derived for flat-plate wind-tunnel models with supersonic leading edges at an angle of attack of 0°. Since the experiments, conducted in the frame of this work, are carried out in a shock tunnel, these methods seem to be appropriate. For a zero leading-edge bluntness, Deem and Murphy derived the following formula for the transition Reynolds number prediction [38]:

$$Re_{\mathrm{T},0} = 1 \times 10^6 + 0.36 \times 10^6 \left| M_\infty - 3 \right|^{3/2} \ , \tag{2.19}$$

where M_∞ is the free-stream Mach number. Since the system under investigation is not a flat plate but a wedge with 0°-angle of attack, the Mach number behind the shock M_2 must be used instead M_∞ in Eq. 2.19. By substituting M_2 into Eq. 2.19, the transition Reynolds number becomes $Re_{\mathrm{T},0} = 1.06478 \times 10^6$.

It must be pointed out that Eq. 2.19 is derived based on a free-stream unit Reynolds number of $Re_\infty^{\mathrm{unit}} = 3 \times 10^5$ inch$^{-1} \approx 1.18 \times 10^7$ m^{-1}. The value of $Re_\infty^{\mathrm{unit}}$ in the shock tunnel used for experiments amounts under given conditions to $\approx 5.12 \times 10^7$ m^{-1}. The variation of the transition Reynolds number with unit Reynolds number can be calculated as follows [38]:

$$log_{10}\left(Re_{\mathrm{T}}\right) = C_1 + 0.4 \; log_{10}\left(Re_\infty^{\mathrm{unit}}\right) \ , \tag{2.20}$$

where C_1 is a quantity that depends on such variables like: flat-plate sweep angle, bluntness, and the unit Reynolds number. The unit Reynolds number in Eq. 2.20 must be given in inch^{-1}. For a zero leading-edge bluntness and a zero flat-plate sweep angle the expression for the calculation of C_1 reduces to:

$$C_1 = log_{10}\left(Re_{\mathrm{T},0}\right) - 2.19 \ . \tag{2.21}$$

The complete version of the formula given Eq. 2.21 can be found in [38].

By inserting Eq. 2.21 into Eq. 2.20, the transition Reynolds number for $Re_\infty^{\mathrm{unit}} \approx 5.12 \times 10^7$ m^{-1} becomes $Re_{\mathrm{T},0} = 1.9176 \times 10^6$. When inserting this value into Eq. 2.18, the distance between the leading edge and the transition point becomes $x_{\mathrm{T}} = 0.02232$ m, which is less than the distance between the leading edge and the first electrode (0.1 m).

Nevertheless, in the frame of this work the flow is assumed to be laminar due to time constrains and a tremendous complexity of plasma turbulence. The turbulence modelling will therefore be subject of future research activities.

2.3.4 One-Fluid Approximation

In general, the calculation model for a partially ionized gas can be constructed in two ways: as a one-fluid model and as a multi-fluid model.

The idea behind a multi-fluid model arises from the fact that in the presence of electromagnetic fields differently charged particles respond with different motions [39]. If the continuum description holds and the plasma is considered as fluid, then the different behaviour of charged particles can be taken into account by recognizing each differently charged species as a separate fluid that interacts with other fluids made up of other species [16]. In this assumption each fluid is represented by an individual set of mass and momentum conservation equations which are supplemented by additional source terms. These source terms are used for modelling interactions between different species as well as their response to the electromagnetic fields, like frictional drag forces due to collisions between different species or Lorentz forces. More information on multi-fluid approaches can be found in Surzhikov [13].

For the phenomena with large spatial scales, where plasma is considered to be neutral and collision dominated, the so-called one-fluid assumption may be used. This is a simplification of the multi-fluid assumption discussed above. In this assumption, the mass conservation in the fluid is described by only one equation. Furthermore, mass-averaged velocity $\mathbf{u}$ can be introduced, where the momenta are averaged over all plasma constituents [39]:

$$\mathbf{u} = \sum_{s=1}^{n} m_s n_s \mathbf{u}_s / \sum_{s=1}^{n} m_s n_s \ . \tag{2.22}$$

By summing up over all momentum equations of all species, a single set momentum conservation equations can be obtained [40]. That is, the fluid is described by a single set of mass and momentum conservation equations and is referred to as a one-fluid approximation.

The assumption of a mass-averaged velocity, where $\mathbf{u} \approx \mathbf{u}_s$, is to be enjoyed with caution in cases in which electrons are accelerated between the collisions with heavy particles to high velocities by strong external electromagnetic fields [40]. This may apply in particular to those plasmas in which free electrons have a large mean free path, that is, in rather dilute gases.

2.3.5 Perfect Gas Assumption

Anderson [15] defines perfect gas as a gas, where intermolecular forces are negligible. This assumption holds for gases at pressures $p < 10$ bar and temperatures $T > 300$ K. In the system under investigation, pressure values behind the shock are ≥ 1.4 bar. The temperature behind the shock ranges from 389 K in the free-stream flow to $\sim 10^4$ K in the gas discharge. That is, the fluid under investigation is assumed to be a mixture of perfect gases.

In addition, it is assumed that the gas is thermally perfect in which, unlike calorically perfect gases, the specific heat capacities are not constant, but functions of temperature and chemical composition. This is due to the fact that vibrational and electronic excitations of molecules and atoms grow in importance with increasing gas temperature [15]. Both forms of energy contribute non linearly to the specific heat capacity.

2.3.6 Chemical Nonequilibrium Assumption

The investigated system is a chemically reacting mixture. To take this into account, the liquid is regarded as a multi-species gas in which the composition of the species can change as a result of ongoing chemical reactions.

All processes in a gas, such as chemical reactions or vibrational and electronic excitations, take place due to radiative interactions and collisions between gas constituents [15]. It must be taken into account that collision processes in the gas occur with a certain intensity, depending on factors such as gas temperature and particle densities. Therefore, it takes some time for the system to reach chemical equilibrium [15]. If the time scales of chemical reactions are longer than the characteristic time scale of the system, then a chemical nonequilibrium must be assumed [15]. In this case, the concentrations of plasma constituents, $c_1, c_2, ..., c_n$, depend not only on the thermodynamic state of the fluid, but also on time. The gas composition, in turn, affects the gas properties.

To examine, whether the system is in the state of chemical nonequilibrium, the Damköhler number[5] is often used. For a system in chemical equilibrium, the Damköhler number has to be larger than unity ($Da \gg 1$). According to Scott [41], in continuous-flow reactors for a conversion of more than 90 % the Damköhler number has to be larger than 10. The Damköhler number is defined as follows [14, 42]:

$$Da = \frac{t_\mathrm{c}}{t_\mathrm{r}} = k\ n^{(n-1)} t_\mathrm{c}\ , \tag{2.23}$$

where k is the reaction rate coefficient and the superscript n is the reaction order.

At 9000 K, the molecular nitrogen is almost completely dissociated [15]. It is therefore assumed that at $T_\mathrm{c} = 12{,}000$ K the collisional-ionization reaction $\mathrm{N} + e \rightleftarrows \mathrm{N}^+ + e + e$ is rather the one to be investigated. When running forward, this reaction represents a second order reaction, hence the superscript $n - 1$ in Eq. 2.23 becomes unity. The number density of atomic nitrogen at $T_\mathrm{c} = 12{,}000$ K is $n_\mathrm{N} \approx 4.6 \times 10^{23} \mathrm{m}^{-3}$ [37]. The equation for the forward reaction rate constant k_f is taken from Park [14] and is for 12,000 K as follows:

$$k_\mathrm{f} = 2.5 \times 10^{33} T^{-3.82} exp\left[-\frac{168{,}200}{T}\right] = 5.34 \times 10^{11}\ \ \mathrm{cm}^3 \cdot \mathrm{mol}^{-1} \cdot \mathrm{s}^{-1} \tag{2.24}$$

Dividing k_f by the Avogadro constant N_A and bringing it into the MKS units yields: $k_\mathrm{f} = 8.87 \times 10^{-19}\ \mathrm{m}^3 \cdot \mathrm{s}^{-1}$. By inserting the above values in Eq. 2.23 yields $Da = 0.408$. Therefore, chemical nonequilibrium must be assumed for the system.

2.3.7 Assumption of Separable Internal Modes

In accordance with Park [14], for three major molecular species in air (N_2, O_2, and NO) the assumption of separable modes is approximately valid. For this assumption

[5] The Damköhler number (Da) is a dimensionless number defined as the ratio of the available flow residence time (characteristic time) to the time required for equilibration [14]. It can give a quick estimate of the degree of conversion that can be achieved in continuous-flow reactors [41].

to apply, molecules must be considered as rigid rotators and their vibrational motion is assumed to be harmonic. This assumption allows the separation of the internal energy of a molecule into four different energy modes, namely the translational, rotational, vibrational and electronic-excitation mode. For atoms, the electronic-excitation mode can also be characterized separately from the translational mode. Detailed information on the subject of separable modes can be found in Park [14].

2.3.8 Thermal Nonequilibrium Assumption

In the system to be investigated, the area between the electrodes is exposed to a strong energy input due to Joule heating. Free electrons are accelerated by the electric field after each collision with heavy particles. These collisions not only increase the translational energy of the heavy particles, but also increase their vibrational, rotational and electronic excitations. When entering or leaving the high-temperature zone, the gas needs some time to balance its thermodynamic properties, since a certain number of collisions are necessary to reach equilibrium. Therefore, it is assumed that the temperatures of individual energy modes may deviate locally [15].

The Damköhler number is now used to investigate whether the energy exchange between different energy modes is fast enough for the LTE assumption. For this purpose, instead of the equilibration time t_r in Eq. 2.23, the relaxation time τ of each equilibration process is set in relation to the characteristic time.

Translational-Vibrational Relaxation

The translational-vibrational relaxation time $\tau_{\text{tr-vib}}$ for the equilibration between heavy particles and vibrating molecules is calculated by using the work of Millikan and White [43], which is given as:

$$\tau_{\text{tr-vib}} = \frac{1}{p\ (\text{bar})} exp\left[A\left(T^{-1/3} - 0.015\overline{\mathcal{M}}^{1/4}\right) - 18.42\right] \ . \tag{2.25}$$

The molecular constant of the colliding species A and the reduced molecular weight between the two colliding particles, $\overline{\mathcal{M}}$, for a nitrogen system are 220 and 14, respectively [43]. So far, the characteristic temperature of $T_\mathrm{c} = 12{,}000$ K has been used. But at this temperature the molecular nitrogen is almost completely dissociated. Therefore, a lower temperature is used in this particular calculation. At a temperature of $T = 6000$ K and a pressure value of $p = 1$ bar $\tau_{\text{tr-vib}}$ is approx. 3.0×10^{-6} s. This value is larger than the characteristic time $t_\mathrm{c} = 1 \times 10^{-6}$ s, which means that the Damköhler number for this thermodynamic process is smaller than unity. Therefore, in the low-temperature regions, like in the vicinity of the wall or at the arc column periphery, vibrational nonequilibrium may occur.

Electron-Impact Vibrational Relaxation

The electron-impact vibrational relaxation time $\tau_{\text{vib-e}}$ is calculated by using the empirical curve-fit formulas derived by Lee [44]. Since nitrogen molecules are also involved

in this process, a lower temperature of $T = 6000$ K is also used here for the calculation. For the electron temperature range of 1000 K $\leq T_\mathrm{e} \leq$ 7000 K the electron-impact vibrational relaxation time is given by [44]:

$$log_{10}\left(\tau_{\text{vib-e}} p_e \text{ (bar)}\right) = 3.91\left(log_{10} T_\mathrm{e}\right)^2 - 30.36\left(log_{10} T_\mathrm{e}\right) + 48.90 \ . \tag{2.26}$$

The electron pressure can be calculated by the formula: $p_e = k_\mathrm{B} n_e T_\mathrm{e}$. At $T = 6000$ K the number density of the electrons has a value of approximately 3.3×10^{19} m^{-3} [37]. By inserting these values into Eq. 2.26, the electron-impact vibrational relaxation time yields $\tau_{\text{vib-e}} \approx 1.34 \times 10^{-6}$ s. This value is higher than the characteristic time t_c, that is at $T = 6000$ K the Damköhler number is smaller than unity. Therefore, in cooler regions, for the electron-impact vibrational relaxation process the system is considered to be in the state of nonequilibrium.

Translational Energy Exchange between Electrons and Heavy Particles

The rate of the energy exchange between the translational energy of free electrons and the translational energy of heavy particles is defined by Park [14] as follows:

$$\dot{Q}_{\text{tr-e}} = \frac{3}{2} n_e k_\mathrm{B}\left(T - T_\mathrm{e}\right) \sum_{\substack{s=1 \\ s \neq \mathrm{e}}}^{n} \frac{2m_e}{m_s} \overline{\nu}_{e,s} \ . \tag{2.27}$$

By introducing this equation, Park refers to the calculations done by Morse [45] where this energy exchange rate is defined as:

$$\frac{\partial}{\partial t}\left(\frac{3}{2} k_\mathrm{B} T_1\right) = \frac{1}{\tau_{\text{tr-e}}}\left(\frac{3}{2} k_\mathrm{B}\left(T_2 - T_1\right) + \frac{1}{2} m_2 \left|\Delta \mathbf{u}\right|^2\right) \ . \tag{2.28}$$

The term $\left|\Delta \mathbf{u}\right|^2 = 0$ due to the one-fluid approximation used in the frame of this work. This expression is similar to the general relaxation equation given as [15]:

$$\frac{de}{dt} = \frac{\left(e^{\mathrm{eq}} - e\right)}{\tau} \ , \tag{2.29}$$

which is used in this work for modelling equilibration processes. Thus, the relaxation time of the translational energy exchange between electrons and heavy particles $\tau_{\text{tr-e}}$ (Morse refers to it as a relaxation coefficient) may be defined as follows:

$$\frac{1}{\tau_{\text{tr-e}}} = \sum_{\substack{s=1 \\ s \neq e}}^{n} \frac{2m_e}{m_s} \overline{\nu}_{e,s} \ . \tag{2.30}$$

According to [37], at $T = 12{,}000$ K the nitrogen plasma consists mainly of N, N^+, and e. Consequently, $m_s \approx m_\mathrm{N} = 2.3259 \times 10^{-26}$ kg for all heavy species. The mass of an electron amounts to $m_e = 9.109 \times 10^{-31}$ kg. The collision frequency between the electrons and heavy particles at $T = 12{,}000$ K is: $\overline{\nu}_{e\mathrm{N}} + \overline{\nu}_{e\mathrm{N}^+} = 3.016 \times 10^{11}$ s^{-1}

(see Sec. 2.3.2). By substituting these values into Eq. 2.30, the relaxation time of $\tau_{\text{tr-e}} \approx 4.24 \times 10^{-8}$ s is obtained. This value is considerably below the characteristic time value, that is, the Damköhler number is much greater than unity and the process under investigation is considered to be in the state of equilibrium.

However, the relaxation time $\tau_{\text{tr-e}}$ increases dramatically for lower temperature regions. To demonstrate this, the calculation of $\tau_{\text{tr-e}}$ is carried out again for $T = 6000$ K. According to [35, 37], the number densities n_{N_2}, n_{N}, $n_{\text{N}_2^+}$, and n_{N^+} at 6000 K and $p = 1$ bar are approximately: 1×10^{24} m^{-3}, 2.5×10^{23} m^{-3}, 1.1×10^{19} m^{-3}, and 2.2×10^{19} m^{-3}, respectively. The corresponding averaged momentum transfer collision integrals at $T = 6000$ K are taken from Yos [22] and shown in Tab. 2.4. By using the above listed data together with Eqs. 2.13 - 2.16, the value of relaxation time at $T = 6000$ K amounts to $\tau_{\text{tr-e}} \approx 4.18 \times 10^{-7}$ s. This yields a Damköhler number of 2.39. This value, although greater than one, is below the value of 10 necessary for a conversion of more than 90 %. For this reason, a nonequilibrium is assumed for the thermalisation between heavy particles and electrons in colder arc regions. Apart from this, the physicochemical model should also be applicable to systems in which the thermodynamic nonequilibrium is more likely to appear (e.g. electric discharges in diluted gases).

Table 2.4: Averaged momentum transfer collision integrals in m^2 in a nitrogen plasma at $T = 6000$ K [22].

Q_{C}	$\pi\overline{\Omega}^{(1,1)}_{e\text{N}}$	$\pi\overline{\Omega}^{(1,1)}_{e\text{N}^+}$	$\pi\overline{\Omega}^{(1,1)}_{e\text{N}_2}$	$\pi\overline{\Omega}^{(1,1)}_{e\text{N}_2^+}$
5×10^{-17}	5×10^{-20}	$0.8Q_{\text{C}}$	1×10^{-19}	$0.8Q_{\text{C}}$

Thermal Nonequilibrium Assumption: Conclusion

From the above analysis, it can be seen that at 12,000 K the Damköhler number for the equilibration between the translational energies of heavy particles and electrons is much larger than unity. However, at temperatures below 6000 K the state of nonequilibrium gradually begins. Furthermore, at 6000 K the Damköhler numbers for electron-impact vibrational relaxation and the translational-vibrational relaxation the values are slightly below the value of one. It might therefore be assumed that LTE occurs somewhere between 6000 K and 12,000 K.

2.3.9 Assumption of Translational-Rotational Temperature

In the present work it is assumed that the translation and rotation temperatures are equal ($T = T_{\text{tr}} = T_{\text{rot}}$). This assumption is adopted from Park [14] and it states that both rotational and translational energy modes can be merged into one energy pool characterized by one translational-rotational temperature T. This assumption implies a very fast relaxation of a possible rotational nonequilibrium with the translational mode. Since under certain conditions a rotational nonequilibrium may occur, this assumption should be used with caution.

2.3.10 Assumption of Electron-Electronic Temperature

In his work, Park [14] states that electronic excitation of atoms and molecules takes place mostly as a result of collisions with free electrons. Park assumes that the energy contained in the translational mode of free electrons and the energy of electronic excitation of heavy particles can be characterized by a single temperature: $T_\mathrm{e} = T_\mathrm{e,tr} = T_\mathrm{el}$. That implies a very fast equilibration between these two energy modes. Such an assumption might be useful for calculating high-temperature gas dynamics in processes, where free electrons are not exposed to external electric fields. Park's work, for example, deals with aerodynamics in nonequilibrium hypersonic flow regimes. In the work presented here, however, the energy-exchange chain starts with the energy of free electrons accelerated by an external electric field. These electrons then transfer their energy to heavy particles through equilibration processes. That is, the temperature of free electrons $T_\mathrm{e,tr}$ would be possibly higher, than the electronic-excitation temperature T_el. Nevertheless, the assumption of a common electron-electronic temperature is used in this work due to time constrains. The separate treatment of both energy modes will therefore be subject of future research activities. A further discussion is needed on this issue.

It is worth to mention that in some research works the energy contained in the electronic-excitation mode is neglected, on the justification that its contribution is negligibly small. The impact of this simplification is now examined.

To simplify the calculation, the nitrogen is assumed to be in thermochemical equilibrium. As previously estimated, at $T = 12{,}000$ K the nitrogen plasma consists mainly of N, N^+, and e, with the following number densities: $n_\mathrm{N} \approx 4.6 \times 10^{23}$ m^{-3} and $n_{\mathrm{N}^+} = n_e \approx 6.5 \times 10^{22}$ m^{-3}. The electronic-excitation energy per cubic meter is calculated as follows:

$$E_\mathrm{el} = \sum_{\substack{s=1 \\ s\neq e}}^{n} \rho c_s R_s \frac{\epsilon_{\mathrm{el},s}(T)}{k_\mathrm{B}} = \sum_{\substack{s=1 \\ s\neq e}}^{n} k_\mathrm{B} \epsilon_{\mathrm{el},s}(T) \ .$$

The values of $\epsilon_{\mathrm{el},s}$ are calculated using Park [14] and Scalabrin [46]. The translational energy of free electrons is obtained by:

$$E_\mathrm{e,tr} = \frac{3}{2} \rho c_e R_e T = \frac{3}{2} k_\mathrm{B} n_e T \ .$$

The calculation delivers the following values: $E_\mathrm{el,N} \approx 43469.8$ J $\cdot$ m^{-3}, $E_{\mathrm{el,N}^+} \approx 1811.4$ J $\cdot$ m^{-3}, and $E_\mathrm{e,tr} \approx 16150$ J $\cdot$ m^{-3}. This shows that the electronic-excitation energy makes up a greater part of the common electron-electronic energy pool at 12,000 K and thus is taken into account in the present work.

2.3.11 Multitemperature Approach

The calculation of the species composition in the plasma requires the knowledge of the reaction rates of the ongoing chemical reactions. The reaction rate of each

chemical reaction is a function of temperature and concentration of reactants and products. The system under investigation is assumed to be in a state of thermodynamic nonequilibrium at the periphery of the arc column and in the electrode regions. That is, the temperatures of different energy modes may significantly depart from each other ($T_{\mathrm{vib}} \neq T_{\mathrm{e}} \neq T$). Vibrationally highly excited molecules (at high T_{vib}) dissociate more easily than those of lower excitation levels because they require less collisions with other particles. Consequently, T_{vib} must be included into the calculation of reaction rates of molecular dissociation. By following this strategy, it becomes clear that for reaction mechanisms such as electron-impact dissociation or ionization, the electron-electronic temperature T_{e} must be taken for the calculation.

Summing up, it can be stated that for an accurate calculation of the species composition of a nonequilibrium system, the multitemperature approach should be used for calculating reaction rates, where all three temperatures: T, T_{vib}, and T_{e}, are taken into account in the reaction-rate calculations.

2.3.12 Harmonic Oscillator Model

According to Park [14], for the vibrational excitation of diatomic molecules near the potential minimum all potential curves can be approximated roughly by a parabola. That is, for lower vibrational energy levels the energy contained in the molecular vibration of diatomic molecules can be calculated by means of the harmonic-oscillator model. However, this concept must be used with caution, because in reality all molecules are anharmonic oscillators [15]. This anharmonic behaviour is particularly noticeable at higher vibrational energy levels. For more information see Park [14].

In the frame of this work, the concept of harmonic oscillator is used for the calculation of the vibrational energy content in the gas. By means of statistical thermodynamics the vibrational energy per molecule is derived as follows [15]:

$$\epsilon_{\mathrm{vib}} = k_{\mathrm{B}} T^2 \frac{d}{dT} \left[ln \left(Q_{\mathrm{vib}} \right) \right] \ , \tag{2.31}$$

where Q_{vib} is the vibrational partition function of a molecule. For a rotationless harmonic oscillator, Q_{vib} is such that [14]:

$$Q_{\mathrm{vib}} = \frac{1}{1 - exp\left[-E_1/(k_{\mathrm{B}} T) \right]} \ , \tag{2.32}$$

where E_1 denotes the energy of vibrational excitation from the vibrational quantum number $v = 0$ to $v = 1$. From the quantum mechanics it is known that $E_1 = hf = h\omega/2\pi$, where h denotes the Planck constant. For a harmonic oscillator the angular frequency is calculated by: $\omega = (\kappa/\overline{\mu})^{1/2}$, where κ denotes the spring constant of the harmonic oscillator and $\overline{\mu}$ the reduced (equivalent) mass of two nuclei, defined in Eq. 2.10 [14]. By combining Eqs. 2.31 and 2.32 and evaluating the temperature derivative, the average vibrational energy per molecule is calculated as follows [14]:

$$\epsilon_{\mathrm{vib}} = \frac{E_1}{exp\left[E_1/(k_{\mathrm{B}} T) \right] - 1} \ . \tag{2.33}$$

Again, the harmonic oscillator assumption is a good approximation for the first few vibrational energy levels only. However, Lee [21] assumes that the contribution of the vibrational energy of molecules at higher energy levels is negligible due to the low concentration of those molecules. For this reason the harmonic oscillator model is used in the frame of this work. Whether this statement is sufficiently precise for the system under investigation will remain the subject of future investigations.

2.3.13 Quasineutrality Condition

On a macroscopic level a partially ionized gas can be considered as quasineutral. The quasineutrality condition is defined as follows [39]:

$$\rho^{\mathrm{c}} = \sum_{s=1}^{n} n_s q_s \simeq 0 \ , \tag{2.34}$$

where ρ^{c} is the charge density in $\mathrm{C} \cdot \mathrm{m}^{-3}$. Eq. 2.34 states that on a macroscopic level in a given volume of plasma the electron and ion number densities are approximately equal ($n_e \approx n_i$). It happens, because electrostatic forces between electrically charged particles in the gas do not allow noticeable charge accumulations or separations to occur [16, 40]. However, on a microscopic level a deviation from the quasineutrality can take place. The size of such a non-neutrality region has an extent of the order of a Debye length λ_D [40]. Therefore, λ_D indicates the scale length of plasma quasineutrality [39, 47]. That is, over distances much larger than the Debye length plasma is quasineutral [47]. The Debye length may be calculated as follows [16]:

$$\lambda_D \equiv \sqrt{\frac{T_{\mathrm{e}} k_{\mathrm{B}} \varepsilon_0}{e^2 n_e}} \simeq 69.0 \sqrt{\frac{T_{\mathrm{e}}}{n_e}} \ . \tag{2.35}$$

For an electron temperature $T_{\mathrm{e}} = T_{\mathrm{c}} = 12{,}000$ K and the electron number density of $n_e \approx 6.5 \times 10^{22}$ m^3 the Debye length is $\approx 2.96 \times 10^{-8}$ m. According to Mitchner and Kruger [16], the model in Eq. 2.35 is valid only when the number of electrons in a sphere of a radius of λ_D is large. This can be examined via the condition [16]:

$$\frac{4}{3} \pi \lambda_D^3 n_e \gg 1 \ , \tag{2.36}$$

where a sphere of a radius of λ_D is multiplied with the electron number density. By using already calculated values Eq. 2.36 yields: $6.62 \gg 1$. That is, the model used for the Debye length calculation reaches its limits of applicability. But even already for a sphere with the radius of $3 \times \lambda_D$ the number of electrons would increase from 6,62 to 186. For this reason the model demonstrated in Eq. 2.35 is considered to be valid for the present calculation.

Mitchner and Kruger [16] state that if the Debye length is small compared to other macroscopic lengths of importance, the assumption of quasineutrality can be made. They suggest to compare λ_D with electron mean free path, which is already calculated for the verification of continuum assumption and has a value of $\ell_e = 1.01 \times 10^{-6}$ m.

The Debye length is of about a factor of 34 smaller than the electron mean free path and thus the condition $\ell_e \gg \lambda_D$ is fulfilled. Furthermore, according to Callen [39], plasmas that are larger than a Debye length in size, are often said to be quasineutral. By comparing the characteristic length $l_c = 1 \times 10^{-3}$ m with λ_D, it is evident that the condition $l_c \gg \lambda_D$ is also met. In the present work, the quasineutrality condition is used as the basis for further assumptions discussed below.

2.3.14 Assumption of Ambipolar Diffusion

In an ionized gas, the diffusion of electrons and ions cannot be considered independent from each other. When an electron pressure gradient exists, the much lighter and consequently more mobile electrons will move away from the zone of higher electron pressure [21, 11]. The much heavier ions are less mobile and thus cannot diffuse as fast as the electrons. That is, the diffusion coefficient of electrons exceeds by several orders of magnitude the diffusion coefficient of ions [30]. At the microscopic level, this leads to a zone of charge separation, resulting in electric polarization fields between fast electrons and much slower ions [11]. Due to these polarization fields, the motion of electrons is restrained and the motion of ions is accelerated [13]. In this way, the motions of electrons and ions are linked to each other and can be described as a collective motion, meaning that electrons and ions move as a group. This is the concept of the ambipolar diffusion which is often used for collision-dominated and quasineutral plasmas. Since the plasma under investigation fulfils both requirements, the diffusion of charged particles can be considered as ambipolar. However, this concept does not account for the effects on the drift diffusion of charged particles generated by the voltage drop on the electrodes. More information on this subject can be found in Mitchner and Kruger [16] and Fridman and Kennedy [11].

2.3.15 MHD Approximation

For collision-dominated and conductive gases, for which the quasineutrality and continuum assumptions apply, the so-called magnetohydrodynamics (MHD) approximation can be used. The MHD approximation allows it to considerably simplify the system of Maxwell's equations and the Ohm's law. In this assumption, the electrically conductive media are regarded as continua. This is the difference to classical plasma physics where the ionized gas is not recognized as a fluid but as consisting of particles of various kinds [48].

The MHD approximation is discussed in detail and verified for the system under investigation in Sec. 3.3.3. At this point, it is enough to mention that this assumption is used in the present work for modelling.

2.3.16 Magnetostatic Approximation

In the system under investigation, direct current is used to operate the gas discharge. According to Griffiths [49], steady currents produce magnetic fields that are constant

in time. It is therefore assumed that the induced magnetic field surrounding the positive column is static. This assumption is called magnetostatics and represents a suitable approximation even for fluctuating currents, provided that the current alternates very slowly compared to the system's characteristic time. The verification of this assumption is presented in Sec. 3.3.4.

2.4 General Modelling Concept

2.4.1 Definition of General Modelling Concept

Summary of Assumptions used in the Physicochemical Model

The following assumptions and simplifications were discussed in Sec. 2.3:

- continuum assumption,
- laminar-flow assumption,
- one-fluid approximation,
- perfect gas assumption,
- chemical nonequilibrium assumption,
- assumption of separable internal modes,
- thermal nonequilibrium assumption,
- assumption of translational-rotational temperature,
- assumption of electron-electronic temperature,
- multitemperature approach,
- harmonic oscillator model,
- quasineutrality condition,
- assumption of ambipolar diffusion,
- MHD approximation,
- magnetostatic approximation.

Impact of Assumptions on the Modelling Concept

The continuum assumption is fundamental to the whole physicochemical model. It allows to use the governing equations of fluid dynamics. Furthermore, due to laminar-flow assumption, turbulence modelling is not considered in this work. In addition, the one-fluid approximation allows to describe the whole gas mixture by a single set of mass and momentum conservation equations.

The system under investigation is a multi-species flow in the state of chemical nonequilibrium. This fact is taken into account by supplementing the fluid-dynamical model with species conservation equations in which the species production and destruction due to ongoing chemical reactions are modelled by additional source terms.

The assumption of separable modes allows to distinguish between individual energy modes contained in the internal energy of the gas. It allows the consideration of the thermodynamic nonequilibrium in the physicochemical system. Further, by applying the assumptions of translational-rotational and electron-electronic temperatures, the number of energy modes can be reduced from five to three. That is, three separate energy conservations equations are needed for the calculation of thermodynamic processes in the physicochemical system. The vibrational- and electron-electronic-energy equations are used for obtaining T_{vib} and T_{e}. The translational-rotational temperature T is calculated by solving the total energy conservation equation and, subsequently, subtracting all energy modes from it except $E_{\mathrm{tr-rot}}$.

The perfect-gas assumption allows to correlate the state variables of the gas mixture (density, temperature, pressure) by two perfect-gas equations of state: one for the electron pressure p_e and one for the total pressure p.

The fluid under consideration is a partially ionized and thus electrically conducting gas which is subject to electric and magnetic fields. Such a fluid behaves differently than a neutral fluid, because it responds to electrical and magnetic fields with certain physical phenomena. To take this into account the fluid-dynamical model is modified in two ways. First, additional source terms are included in the conservation equations for modelling the action of electric and magnetic fields on the ionized gas [16]. These are the Joule heating $\dot{Q}_{\mathrm{Joule}}$ and the Lorentz force $\mathbf{F}_{\mathrm{Lorentz}}$. Second, the calculation of the transport properties of the fluid must be set up for an ionized gas. In the present work, it specifically concerns the diffusion coefficients of charged particles for which the concept of ambipolar diffusion is used.

The calculation of $\dot{Q}_{\mathrm{Joule}}$ and $\mathbf{F}_{\mathrm{Lorentz}}$ requires the information about the spatial distribution of the electric and magnetic fields $\mathbf{E}$ and $\mathbf{B}$, as well as information about the electrical current density $\mathbf{J}$ in the system. These data are obtained by solving Maxwell's equations, which are considerably simplified. First, the set of Maxwell's equations is simplified by applying the concept of the so-called MHD approximation. Then, a further appreciable simplification is achieved through the magnetostatic approximation. As a result, the total number of electrodynamic model equations decreased significantly. Finally, the simplified set of Maxwell's equations is expressed in its potential form, where the calculation of electromagnetic fields is based on solving the electric potential Φ and the magnetic vector potential $\mathbf{A}$.

Modelling Concept

The fluid flow in the system under investigation is characterized by following variables: p, p_e, ρ, $\mathbf{u} = (u_x, u_y, u_z)^T$, T, T_{vib}, T_{e}, and species concentrations c_1, c_2, ..., c_n. These are $9+n$ variables, where n denotes the total number of species in the system. All these variables are calculated by means of the thermo-fluid dynamic module that

forms the core of the physicochemical model (see Fig. 2.12). The thermo-fluid dynamic module consists of $7 + n$ conservation equations, plus two additional perfect-gas equations of state for calculating p and p_e.

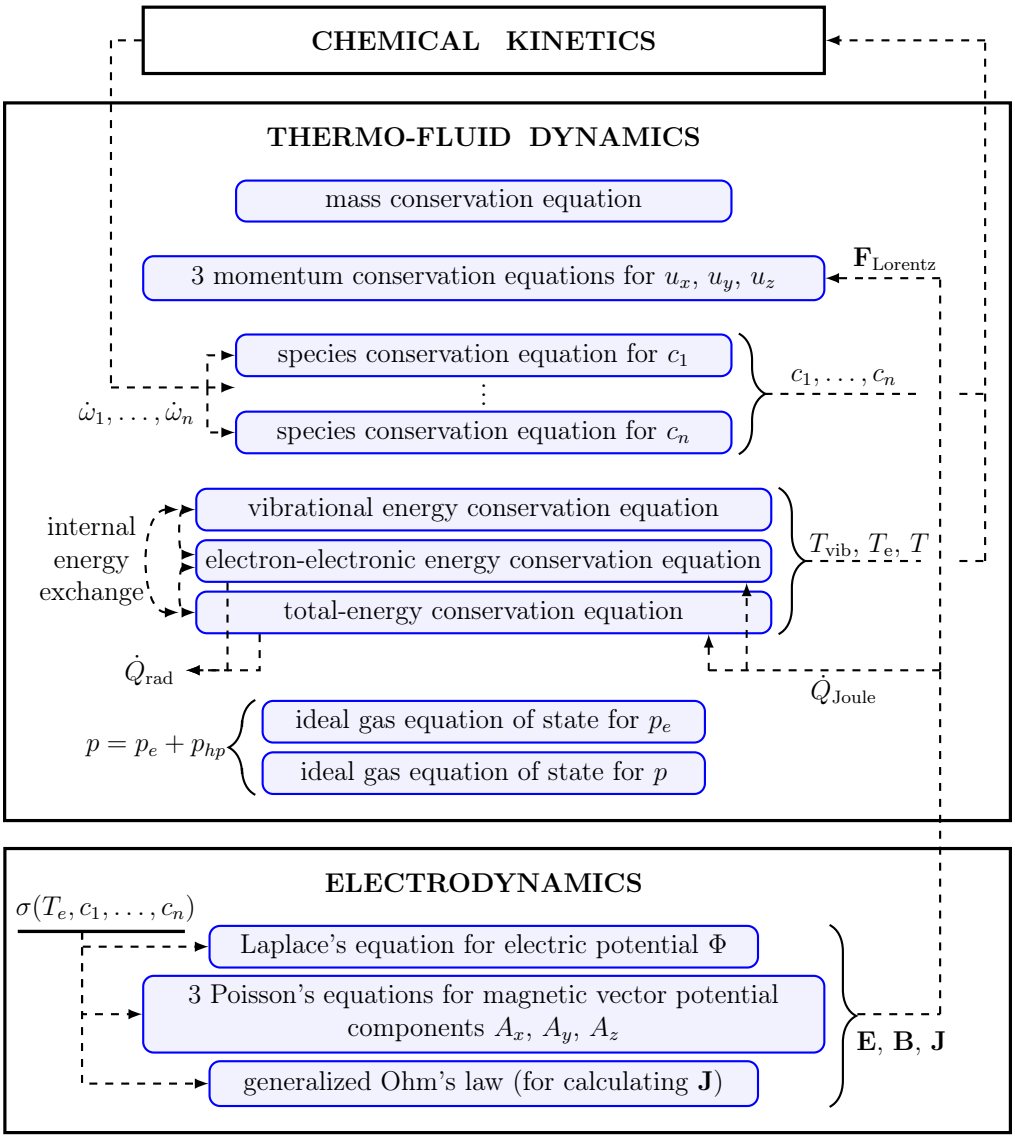

Figure 2.12: Schematic representation of the basic concept.

All three energy conservation equations for calculating T, T_{vib}, and T_{e}, are coupled by additional source terms, representing the internal-energy exchange due to equilibration processes between different energy modes (see Fig. 2.12). The energy exchange between the system and the environment is represented in the present work by two processes, namely the energy gain through the Joule heating effect $\dot{Q}_{\text{Joule}}$ and the energy loss via radiation $\dot{Q}_{\text{rad}}$.

The task of the chemical kinetics module consists in providing information on

the species production and destruction due to ongoing chemical reactions in the gas mixture via source terms for mass production rates: $\dot{\omega}_1$, $\dot{\omega}_2$ ..., and $\dot{\omega}_n$ (given in $\mathrm{kg \cdot m^{-3} \cdot s^{-1}}$). For the calculation of these terms, the chemical kinetics module, in turn, needs the information about the instantaneous species concentrations c_1, c_2 ..., and c_n, as well as temperatures T, T_{vib}, and T_{e} (see Fig. 2.12). This results in a mutual coupling between the fluid dynamics and the chemical modules.

The calculation of the fields **E**, **B** and **J**, required for computing $\dot{Q}_{\mathrm{Joule}}$ and $\mathbf{F}_{\mathrm{Lorent}z}$, is carried out by the electrodynamics module (see Fig. 2.12). The electrodynamics module forms a closed equation system consisting of one Laplace equation for the calculation of the scalar field Φ and three Poisson equations for the calculation of the vector field **A**. The electric current density **J** is calculated based on the generalized Ohm's law. The electrodynamic module requires information about the temporal and spatial distribution of electrical conductivity in the arc discharge σ, which is a function of c_1, c_2 ..., c_n, and T_{e}. This creates a mutual coupling between fluid dynamics and electrodynamics modules explained in more detail in Sec. 3.3.6.

2.4.2 Arc Ignition Modelling

In the frame of this work, the preionization process depicted in Fig. 2.5 is not considered. Therefore, the anode a is not taken into account in the modelling. The arc ignition is modelled by locally heating up the gas between the electrodes b and c via an additional source term in the energy conservation equation until the ionization begins and the gas becomes a conductor. As a result, the electrical circuit closes and the electric arc goes over into a self-sustaining operation mode.

2.4.3 Pollution of Plasma by Electrode Material

An appreciable contamination of nitrogen by copper is assumed due to the significant erosion of the electrode material (see Fig. 2.6). However, the characteristic temperature of the system is in the range of $T_{\mathrm{c}} = 12{,}000$ K, which is why the copper contamination should not significantly affect the transport properties of the plasma in the core of the arc column (see Fig. 2.7). However, this assumption should be treated with caution, because in colder peripheral zones of the arc column the presence of copper vapour might significantly affect the transport properties of the nitrogen plasma. Due to missing data for copper vapour, pure nitrogen plasma is modelled in the present work.

2.4.4 Wall Modelling

In the present work, no information is available about the temperature profile on the wedge surface during the gas discharge. At the beginning of the shock-tunnel experiment, the surface of the wedge is at room temperature (293.15 K). Therefore, the surface acts as a strong heat sink during discharge, which is why the assumption of an adiabatic wall would be rather invalid. From the tempering colours that occur

on the metallic part of the wedge surface after a discharge, it can be seen that the assumption of room temperature on the wall is also unfavourable. These tempering colours are recognizable in Fig. 2.6 on the right. The blue and grey colours indicate that the wall temperature in this area was over 600 K. It can be assumed that in the areas closer to the arc-column centre-line, the wall temperatures during the discharge are even higher. For this reason and due to missing information, a maximum temperature of 1000 K is used as a boundary condition for the wall modelling. This simple assumption should be replaced by a more accurate model.

2.4.5 Modelling of Near-Electrode Nonequilibrium Layers

Dimensions of the Near-Electrode Layers

The thickness of the cathodic sheath is of the order of the Debye length λ_D. In Sec. 2.3.13, a value of 2.96×10^{-8} m has been determined for λ_D for the system under investigation. The thickness of the cathodic presheath is of the order of several mean free path lengths for which values between 4.72×10^{-7} m and 1.01×10^{-6} m were determined in Sec. 2.3.2. That is, in the analysed physicochemical system, the thickness of the cathodic presheath is approximately in the order of several microns, giving a total thickness of the cathodic nonequilibrium layer of the order of $\sim 1...10$ μm. As far as the near-anode layer is concerned, it is assumed that the sheath and presheath thicknesses are of the same order of magnitude as in the cathodic layer.

Modelling Concept of the Near-Electrode Layers

Due to the high complexity of the processes within the near-electrode layers (sheath and presheath) and their small dimensions compared to the characteristic length of the system, the cathode and anode layers are not modelled in the present work. Consequently, neither electron emission processes nor electrode erosion are modelled. That is, the electrode layers are skipped and the modelling domain at the electrode surfaces begins directly with the constricted zones of the positive column. Consequently, the gas conditions prevailing in the constricted zones represent the electrode-surface boundary conditions.

It is essential to mention that in the present work no drift diffusion of electrons and ions between the electrodes, caused by external electric and magnetic fields, is modelled. Instead, only the species concentrations of the gas constituents are considered (one-fluid assumption). The composition of the gas and, consequently, its ionization degree are dictated by the gas temperatures: T, T_{vib}, and T_{e}. This approach eliminates the need of modelling the electron emission from the cathode.

The fraction of the electron current S with respect to the total electric current grows over the thickness of the cathodic layer from ≈ 0.8 at the electrode surface to approximately 1 in the constricted part of the positive column. This means that the electric current density in the modelled area consists almost exclusively of the electron current density: $\mathbf{J} \approx \mathbf{J}_e$. For the ion current, it is assumed that: $\mathbf{J}_i \approx 0$.

2.4.6 Joule Heat Efficiency

Later in Sec. 3.3.2 it will be shown that the induction current may be neglected for the system under investigation. In this way, Ohm's law for the calculation the electric current density can be reduced to: $\mathbf{J} = \sigma\mathbf{E}$. Thus, the energy input into the gas by the Joule-heating effect may be estimated by the following simplified expression:

$$\dot{Q}_{\text{Joule}} = \mathbf{J} \cdot \mathbf{E} \approx \sigma E^2 \ . \tag{2.37}$$

However, there are several factors that reduce the effectiveness of the Joule heating, which is why an efficiency coefficient η is introduced as follows: $\dot{Q}_{\text{Joule}} = \eta\,(\mathbf{J} \cdot \mathbf{E})$. The value of η is usually in the range of $\eta \sim 0.1 - 0.9$, depending on the physical system [13]. According to Takahashi *et al.* [12], η takes into account losses due to voltage drop on the electrodes and heat losses on the electrode surface.

In the following, an attempt is made to estimate the value of η for the system under investigation. The typical characteristic value of the cathodic voltage drop for a copper electrode in a high-pressure arc amounts to 18 V [11]. The voltage drop in the anodic sheath is of a value of about the ionization potential, which is 7.72 eV for copper. Additional anodic voltage drop occurs due to the arc channel constriction in the anode region, which may sometimes exceed the anodic-sheath voltage drop by a factor of two [11]. In the following, it is assumed that the total voltage drop over the electrode layers amounts to 30 V. In this work, an electric-potential difference at the electrodes of 130 V is assumed. Thus, the voltage drop over the positive column is of 100 V. For an electrode distance of $d = 5$ mm, a simple estimation ($E \approx \Delta\Phi/d$) yields for the voltage drops of 130 V and of 100 V electric field magnitudes of 26,000 $\text{V} \cdot \text{m}^{-1}$ and 20,000 $\text{V} \cdot \text{m}^{-1}$, respectively. For a simple estimation of Joule heating, Eq. 2.37 is now used. By assuming a characteristic electrical conductivity of $\sigma_{\text{c}} = 4.4 \times 10^3\ \text{S} \cdot \text{m}^{-1}$, Eq. 2.37 yields for a voltage drop of 130 V a heat power of $\dot{Q}_{\text{Joule}} = 2.974 \times 10^{12}\ \text{W} \cdot \text{m}^{-3}$ and for 100 V a heat power of $\dot{Q}_{\text{Joule}} = 1.760 \times 10^{12}\ \text{W} \cdot \text{m}^{-3}$. As a result, the consideration of the voltage drops at the electrodes leads to a reduction of the heat input power down to 59.17 % ($\eta = 0.5917$).

A further reduction of the heat input power efficiency could result from the heat losses on the electrodes due to such effects, like sputtering and evaporation of the electrode material and heat radiation from the electrode surface. The individual contributions of these effects to the efficiency reduction were not investigated. However, it is clear that the value of η would be further reduced by these energy sinks. In the present work the value of $\eta = 0.5$ is used. Whether this value is accurate enough for the physical system to be modelled, remains the subject of future investigations.

Chapter 3

Physicochemical Model

The purpose of this chapter is to define a physicochemical model describing electric discharges in supersonic gas flows. The system under investigation is a multi-physical system that involves chemical kinetics, thermo-fluid dynamics, and electrodynamics. Therefore, the physicochemical model is divided into three blocks, which are discussed separately. Sec. 3.1 describes the chemical kinetics modelling. In Sec. 3.2 the thermo-fluid dynamics modelling is discussed. Sec. 3.3 is devoted to the electrodynamics modelling. The chapter ends with closing remarks given in Sec. 3.4.

3.1 Chemical Kinetics Modelling

The aim of this section is to set up a model for calculating the mass production rates of chemical species: $\dot{\omega}_1$, $\dot{\omega}_2$ ..., and $\dot{\omega}_n$. The equations used herein originate from the field of chemical kinetics – a domain of physical chemistry.

3.1.1 Kinetic Mechanism for High-Temperature Nitrogen

The fluid to be examined is a high-temperature nitrogen. In the frame of this work, only singly charged and positive ions are taken into account. Therefore, the gas mixture includes the following five species: N_2, N, N_2^+, N^+ and e.

Since a temperature of 12,000 K is expected in the centre line of the arc column, no doubly- or triply-charged ions (N^{++} and N^{+++}) have to be considered for this arc region. However, near the electrode edges in the constricted zones of the positive column much higher temperatures are expected, especially at the cathode. From a temperature of over 25,000 K, the production of N^{++} becomes noticeable, as exemplified in Fig. 3.1, and will affect the properties of the gas. In addition, the required second ionization energy would be extracted from the gas, leading to the cooling of the plasma at the electrode edges. It is therefore important to include the production of N^{++} in the kinetic mechanism for intensive high-pressure arc discharges. However, it is extremely difficult to obtain all necessary data. For this reason, doubly-charged ions are not included in the present work for now.

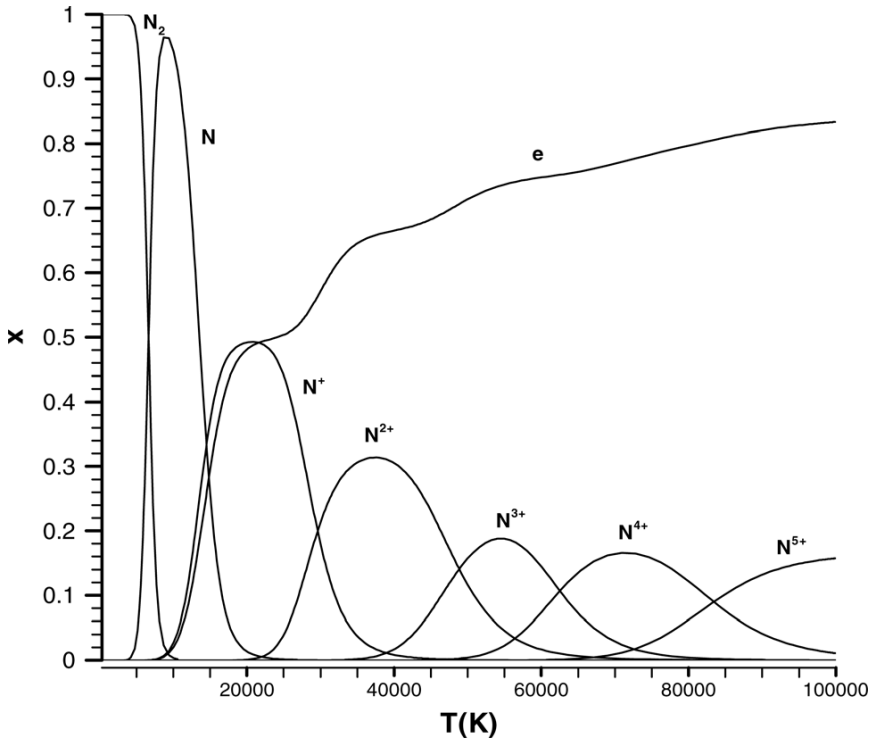

Figure 3.1: Mole fractions X of nitrogen species versus temperature at atmospheric pressure [50].

The kinetic mechanism for the ionized nitrogen used in this work consists of eight chemical reactions shown in Tab. 3.1. This kinetic mechanism is taken from Yu *et al.* [24]. It represents a combination of selected chemical reactions for high-temperature nitrogen, taken from the work of Dunn and Kang [25] and the work of Park [14]. Both works provide data for kinetic mechanisms of high-temperature air.

Table 3.1: Kinetic mechanism for high-temperature nitrogen* [24].

r	Reactants		Products	T_f	T_b	$\mathcal{A}$	η	θ_a	Ref.
1	$N_2 + N_2$	$\rightleftharpoons$	$N + N + N_2$	$\sqrt{TT_\mathrm{vib}}$	T	4.700×10^{17}	-0.50	113,200	[25]
2	$N_2 + N$	$\rightleftharpoons$	$N + N + N$	$\sqrt{TT_\mathrm{vib}}$	T	4.085×10^{22}	-1.50	113,200	[25]
3	$N_2 + N_2^+$	$\rightleftharpoons$	$N + N + N_2^+$	$\sqrt{TT_\mathrm{vib}}$	T	7.000×10^{21}	-1.60	113,200	[14]
4	$N_2 + N^+$	$\rightleftharpoons$	$N + N + N^+$	$\sqrt{TT_\mathrm{vib}}$	T	3.000×10^{22}	-1.60	113,200	[14]
5	$N + N$	$\rightleftharpoons$	$N_2^+ + e$	T	T_e	1.400×10^{13}	0.00	67,800	[25]
6	$N_2 + e$	$\rightleftharpoons$	$N + N + e$	T_e	$\sqrt{TT_\mathrm{e}}$	3.000×10^{24}	-1.60	113,200	[14]
7	$N + e$	$\rightleftharpoons$	$N^+ + e + e$	T_e	T_e	1.100×10^{32}	-3.14	169,000	[25]
8	$N_2 + N^+$	$\rightleftharpoons$	$N_2^+ + N$	$\sqrt{TT_\mathrm{vib}}$	$\sqrt{TT_\mathrm{vib}}$	2.020×10^{11}	0.81	13,000	[25]

* Forward rate coefficients k_f calculated by using these data, have the unit of $\mathrm{cm}^3 \cdot \mathrm{mol}^{-1} \cdot \mathrm{s}^{-1}$. The temperature of activation θ_a is calculated as follows: $\theta_\mathrm{a} = E_\mathrm{a}/\mathcal{R}$, where E_a is the activation energy, given in $\mathrm{cal} \cdot \mathrm{mol}^{-1}$ and $\mathcal{R}$ is the ideal gas constant in $\mathrm{cal} \cdot \mathrm{mol}^{-1} \cdot \mathrm{K}^{-1}$.

All reactions shown in Tab. 3.1 are written in their endothermic direction, meaning they absorb energy to proceed from left to right. In the field of aerospace, this is a common way to write a chemical reaction equation [14]. This convention makes it possible to clearly define the forward and the backward direction of the reaction, namely the endothermic direction is the forward direction. Furthermore, all reactions are binary, that is, they take place as a result of collisions between two particles. Reactions $r = 1 - 4$ represent thermal dissociation of N_2 by collisions with N_2, N, N_2^+, and N^+. Reaction $r = 5$ represents the process of associative ionization. The reverse reaction would be the dissociative recombination. Reactions $r = 6$ and $r = 7$ are the electron-impact dissociation and the electron-impact ionization, respectively. Reaction $r = 8$ is a charge-exchange reaction between molecular and atomic nitrogen.

3.1.2 Species Production Rates

Production Rate Calculation

The mass production rate of species s, which has the units of $\mathrm{kg} \cdot \mathrm{m}^{-3} \cdot \mathrm{s}^{-1}$, can be written as a product of the reaction rate $d\Upsilon_s/dt$, given in $\mathrm{kmol} \cdot \mathrm{m}^{-3} \cdot \mathrm{s}^{-1}$, and the molar mass $\mathcal{M}_s$, given in $\mathrm{kg} \cdot \mathrm{kmol}^{-1}$:

$$\dot{\omega}_s = \frac{d\rho_s}{dt} = \frac{d\Upsilon_s}{dt}\mathcal{M}_s \ . \tag{3.1}$$

The molar concentration per unit volume Υ_s has a unit of $\mathrm{kmol} \cdot \mathrm{m}^{-3}$. The values of molar mass $\mathcal{M}_s$ for all species in the system are given in Appendix B in Tab. B.3.

A general equation for the calculation of the forward reaction rate is given by [15]:

$$\left(\frac{d\Upsilon_s}{dt}\right)_{\mathrm{f}} = (\nu_s'' - \nu_s')\, k_f \prod_{j=1}^{n} \Upsilon_j^{\nu_j'} \ , \tag{3.2}$$

where the quantities ν_s' and ν_s'' denote the stoichiometric mole numbers of the reactants and products, respectively. The subscript j in Eq. 3.2 denotes all species participating in the reaction. The constant of proportionality k_f is the forward reaction rate constant. The backward reaction rate is given by [15]:

$$\left(\frac{d\Upsilon_s}{dt}\right)_{\mathrm{b}} = -\,(\nu_s'' - \nu_s')\, k_b \prod_{j=1}^{n} \Upsilon_j^{\nu_j''} \ . \tag{3.3}$$

where k_b is the backward reaction rate constant. The net reaction rate is the combination of forward and backward reaction rates:

$$\frac{d\Upsilon_s}{dt} = (\nu_s'' - \nu_s') \left[k_\mathrm{f} \prod_{j=1}^{n} \Upsilon_j^{\nu_j'} - k_\mathrm{b} \prod_{j=1}^{n} \Upsilon_j^{\nu_j''} \right] \ . \tag{3.4}$$

As an example, the reaction for thermal dissociation of molecular nitrogen ($N_2 + M \rightleftharpoons 2N + M$) is now considered, where M denotes the collision partner (e.g. M = N

for reaction $r = 2$ in Tab. 3.1). In this particular reaction mechanism, the subscript j stands for the species N_2, N, and M. The stoichiometric mole numbers have the following values: $\nu'_{N_2} = 1$, $\nu'_N = 0$, $\nu'_M = 1$, $\nu''_{N_2} = 0$, $\nu''_N = 2$, and $\nu''_M = 1$. The forward and backward reaction rates for the formation of atomic nitrogen N can be calculated as:

$$\left(\frac{d\Upsilon_N}{dt}\right)_f = 2k_f\Upsilon_{N_2}\Upsilon_M \quad \text{and} \quad \left(\frac{d\Upsilon_N}{dt}\right)_b = -2k_b\Upsilon_N^2\Upsilon_M \ .$$

The net reaction rate for N is then calculated as follows:

$$\frac{d\Upsilon_N}{dt} = 2\left[k_f\Upsilon_{N_2}\Upsilon_M - k_b\Upsilon_N^2\Upsilon_M\right] \ .$$

By summing up Eq. 3.4 over all chemical reactions occurring in the system under investigation and substituting it into Eq. 3.1, the equation for the net production rate of chemical species s is obtained by [24]:

$$\dot{\omega}_s = \mathcal{M}_s \sum_{r=1}^{nr} \left\{ \left(\nu''_{s,r} - \nu'_{s,r}\right) \left[k_{f,r} \prod_{j=1}^{n} \left(\frac{\rho_j}{\mathcal{M}_j}\right)^{\nu'_{j,r}} - k_{b,r} \prod_{j=1}^{n} \left(\frac{\rho_j}{\mathcal{M}_j}\right)^{\nu''_{j,r}} \right] \right\} \ . \tag{3.5}$$

The molar concentrations per unit volume Υ_j are replaced by $\rho_j/\mathcal{M}_j$. The stoichiometric mole numbers of the reactants and products $\nu'_{s,r}$ and $\nu''_{s,r}$ are dictated by the chemical equations shown in Eq. 3.2. The partial densities ρ_j are obtained from the species concentration equations, which are a part of the fluid-dynamical model, discussed in Sec. 3.2. The only unknown values to be determined yet are the reaction rate constants k_f and k_b.

Reaction Rate Constants

The values of the forward reaction rate constant k_f are generally found experimentally and may be expressed by means of the modified form of Arrhenius' equation [15]:

$$k_f(T_f) = \mathcal{A}T_f^{\eta} exp\left(-\frac{\theta_a}{T_f}\right) \ . \tag{3.6}$$

The values of the constants $\mathcal{A}$ and η and of the temperature of activation θ_a are given in Tab. 3.1 for each reaction r. A forward reaction rate constant k_f, obtained by Eq. 3.6, has a unit of $cm^3 \cdot mol^{-1} \cdot s^{-1}$. In the present work, however, the MKS system of units is used. Furthermore, kilomoles are used instead of moles. Therefore, the value of k_f after the calculation by Eq. 3.6 has to be converted to the required units by multiplying it by a conversion factor of 1×10^{-3}.

The backward reaction rate constant can be obtained by using the equilibrium constant K_{eq} as follows [14]:

$$k_b(T_b) = \frac{k_f(T_b)}{K_{eq}(T_b)} \ . \tag{3.7}$$

The equilibrium constant is calculated via a curve-fit formula taken from Park [14]:

$$K_{\mathrm{eq}}(T_{\mathrm{b}}) = exp\left[A_1\left(\frac{T_{\mathrm{b}}}{10{,}000}\right) + A_2 + A_3 ln\left(\frac{10{,}000}{T_{\mathrm{b}}}\right) + A_4\left(\frac{10{,}000}{T_{\mathrm{b}}}\right) + A_5\left(\frac{10{,}000}{T_{\mathrm{b}}}\right)^2\right] . \tag{3.8}$$

For reactions $r = 1 - 7$ the values of A_i are taken from Park [14]. For the reaction $r = 8$ no data are available in Park's work. Therefore, for this reaction the data from Gupta *et al.* [23] are taken and adapted to the curve-fit formula given in Eq. 3.8. The curve-fit coefficients A_i are depicted in Appendix B in Tab. B.1. All data given in Tab. B.1 are valid only for fluids in which the total number density $n \geq 10^{24}\mathrm{m}^{-3}$. The curve-fit coefficients for more diluted gases can be found in Park [14] and Gupta *et al.* [23]. The number density of the gas to be analysed is higher than 10^{24} m^{-3} for all temperature and pressure ranges of interest.

It is important to mention that the equilibrium constant may be dimensionless or non-dimensionless depending on the reaction. K_{eq} for dissociation reactions of the form $\mathrm{AB} \rightleftharpoons \mathrm{A} + \mathrm{B}$, for example, can be written as follows [14]:

$$K_{\mathrm{eq}} = \frac{\Upsilon_{\mathrm{A}}\Upsilon_{\mathrm{B}}}{\Upsilon_{\mathrm{m}}} . \tag{3.9}$$

In this case, when using the CGS system of units, the equilibrium constant has the unit $\mathrm{mol} \cdot \mathrm{cm}^{-3}$ and has to be converted into $\mathrm{kmol} \cdot \mathrm{m}^{-3}$ (unit used in the present work) by multiplying it by the conversion factor of 1000. This concerns reactions 1, 2, 3, 4, 6, and 7 in Tab. 3.1. For the reactions 5 and 8, however, K_{eq} is dimensionless.

The quantities $k_{\mathrm{f}}(T_{\mathrm{f}})$, $k_{\mathrm{b}}(T_{\mathrm{b}})$, and $K_{\mathrm{eq}}(T_{\mathrm{b}})$ are functions of temperature only, where T_{f} and T_{b} may be different for forward- and backward-reaction directions and may also be different for different reactions. This is due to the fact that the system under investigation is considered to be locally in thermal nonequilibrium. That is, temperatures T, T_{vib}, and T_{e} may diverge from each other. To take this into account, the kinetic mechanism in Tab. 3.1 is based on the multitemperature approach, where the nonequilibrium between different energy modes is respected by using geometrically averaged temperatures $\sqrt{TT_{\mathrm{vib}}}$ and $\sqrt{TT_{\mathrm{e}}}$ as well as T and T_{e}.

It is worth to mention, that if the system under investigation reaches thermal equilibrium, all temperatures become equal ($T_{\mathrm{e}} = T_{\mathrm{vib}} = T$) and the kinetic mechanism of chemical reactions becomes a function of one temperature only.

3.2 Fluid-Dynamics Modelling

3.2.1 Governing Equations of Fluid Dynamics

Mass and Momentum Conservation Equations

The mass conservation equation – often called the continuity equation – states that mass can be neither created nor destroyed [28]. The global mass conservation equa-

tion is given in its conservative form and in terms of vector notation by [14]:

$$\frac{\partial \rho}{\partial t} + \boldsymbol{\nabla} \cdot (\rho \mathbf{u}) = 0 \ . \tag{3.10}$$

The momentum conservation equation is expressed in its conservative form and in terms of vector notation as follows [14]:

$$\frac{\partial (\rho \mathbf{u})}{\partial t} + \boldsymbol{\nabla} \cdot (\rho \mathbf{u} \otimes \mathbf{u}) = \boldsymbol{\nabla} \cdot \boldsymbol{T} + \mathbf{F}_{\text{Lorentz}} \ . \tag{3.11}$$

The momentum conservation equation is a vector equation, based on the Newton's second law: $\boldsymbol{F} = m\boldsymbol{a}$. Basically, it states that force is equal to the time rate of change of momentum [28]. Forces acting on an infinitesimally small control volume of fluid, can be divided into surface and body forces [51]. In Eq. 3.11, the Lorentz force $\mathbf{F}_{\text{Lorentz}}$ represents a body force. The stress tensor $\boldsymbol{T}$ represents the surface forces. For compressible Newtonian fluids it is defined as:

$$\boldsymbol{T} = -p\boldsymbol{I} + \underbrace{\lambda \left(\boldsymbol{\nabla} \cdot \mathbf{u}\right) \boldsymbol{I} + 2\mu \boldsymbol{D}}_{\substack{\text{viscous part} \\ \text{of the stress tensor} = \boldsymbol{\tau}}} \ , \tag{3.12}$$

where $\boldsymbol{I}$ denotes the identity tensor. When applying the Stokes hypothesis, the bulk viscosity becomes [15]: $\lambda = -\mu\frac{2}{3}$. Further, the deformation rate tensor is given such that [52]: $\boldsymbol{D} = \frac{1}{2}\left[\boldsymbol{\nabla} \otimes \mathbf{u} + (\boldsymbol{\nabla} \otimes \mathbf{u})^{\mathrm{T}}\right]$, where $\otimes$ is the dyadic product. Hence, the viscous part of the stress tensor can be written as:

$$\boldsymbol{\tau} = -\mu\frac{2}{3}\underbrace{tr\left((\boldsymbol{\nabla} \otimes \mathbf{u})^{T}\right)}_{(\boldsymbol{\nabla} \cdot \mathbf{u})} \boldsymbol{I} + \mu \boldsymbol{\nabla} \otimes \mathbf{u} + \mu \left(\boldsymbol{\nabla} \otimes \mathbf{u}\right)^{\mathrm{T}} \ , \tag{3.13}$$

where tr is the trace of a matrix. Furthermore, it can be shown that: $\boldsymbol{\nabla} \cdot (-p\boldsymbol{I}) = -\boldsymbol{\nabla} p$. Hence, the momentum conservation equation may be written as follows:

$$\frac{\partial (\rho \mathbf{u})}{\partial t} + \boldsymbol{\nabla} \cdot (\rho \mathbf{u} \otimes \mathbf{u}) = -\boldsymbol{\nabla} p + \boldsymbol{\nabla} \cdot \boldsymbol{\tau} + \mathbf{F}_{\text{Lorentz}} \ . \tag{3.14}$$

Species Conservation Equation

The species conservation equation is defined in terms of species mass fractions $c_s = \rho_s/\rho$ such that [14]:

$$\frac{\partial (\rho c_s)}{\partial t} + \boldsymbol{\nabla} \cdot (\rho c_s \mathbf{u}) = -\boldsymbol{\nabla} \cdot (\rho \mathbf{V}_s c_s) + \dot{\omega}_s \ , \tag{3.15}$$

where $\dot{\omega}_s$ is the rate of creation or extinction of species s as a result of chemical reactions and $\mathbf{V}_s$ is the diffusion velocity of species s. The species conservation equation is solved for each species in the system with the following requirements [15]:

$$\sum_{s=1}^{sn} \rho_s = \rho \quad \text{or} \quad \sum_{s=1}^{sn} c_s = 1 \ . \tag{3.16}$$

Energy Conservation Equations

An energy conservation equation is based on the first law of thermodynamics, stating that the energy can neither be created nor destroyed – it only changes the form [28]. In the following, all energy conservation equations are defined in terms of energy per cubic meter ($\mathrm{J}\cdot\mathrm{m}^{-3}$). Thus, the relation to the specific energy e is given as: $E = \rho e$.

The energy conservation equation for the energy contained in the vibrational mode is such that [14]:

$$\frac{\partial E_{\mathrm{vib}}}{\partial t} + \boldsymbol{\nabla}\cdot(\mathbf{u}E_{\mathrm{vib}}) = -\boldsymbol{\nabla}\cdot\mathbf{q}_{\mathrm{vib}} + \left(\frac{\partial E_{\mathrm{vib}}}{\partial t}\right)_{\mathrm{int}} , \tag{3.17}$$

where $\mathbf{q}_{\mathrm{vib}}$ denotes the heat flux vector due to the diffusion of the vibrational energy. The source term $(\partial E_{\mathrm{vib}}/\partial t)_{\mathrm{int}}$ denotes the rate of change of vibrational energy due to internal energy exchange with other energy modes.

The electron-electronic energy conservation equation is expressed by [14]:

$$\frac{\partial E_{\mathrm{e}}}{\partial t} + \boldsymbol{\nabla}\cdot[\mathbf{u}(E_{\mathrm{e}} + p_e)] = -\boldsymbol{\nabla}\cdot\mathbf{q}_{\mathrm{e}} + \left(\frac{\partial E_{\mathrm{e}}}{\partial t}\right)_{\mathrm{int}} + \dot{Q}_{\mathrm{Joule}} - \dot{Q}_{\mathrm{rad}} , \tag{3.18}$$

where $\mathbf{q}_{\mathrm{e}}$ denotes the heat flux vector due to the diffusion of the electron-electronic energy. The source term $(\partial E_{\mathrm{e}}/\partial t)_{\mathrm{int}}$ denotes the rate of change of electron-electronic energy due to internal energy exchange with other energy modes. The source terms $\dot{Q}_{\mathrm{Joule}}$ and $\dot{Q}_{\mathrm{rad}}$ represent the energy gain due to Joule heating effect and the energy loss due to radiation, respectively.

The energy conservation equation for the overall energy E can be written as [14]:

$$\frac{\partial E}{\partial t} + \boldsymbol{\nabla}\cdot[\mathbf{u}(E + p)] = -\boldsymbol{\nabla}\cdot\mathbf{q} + \boldsymbol{\nabla}\cdot(\boldsymbol{\tau}\cdot\mathbf{u}) + \dot{Q}_{\mathrm{Joule}} - \dot{Q}_{\mathrm{rad}} + \mathbf{u}\cdot\mathbf{F}_{\mathrm{Lorentz}} , \tag{3.19}$$

where the quantity $\mathbf{q}$ denotes the total heat flux vector.

In present research, the work done on the fluid due to the Lorentz force ($\mathbf{u}\cdot\mathbf{F}_{\mathrm{Lorentz}}$) in Eq. 3.19 is neglected because of its insignificant contribution. This can easily be shown by comparing the contribution of $\dot{Q}_{\mathrm{Joule}}$ with $\mathbf{u}\cdot\mathbf{F}_{\mathrm{Lorentz}}$. Using the characteristic values of the system under investigation shown in Tab. 2.2, the Joule heating can be estimated as follows: $\dot{Q}_{\mathrm{Joule}} = \eta\,(\mathbf{J}\cdot\mathbf{E}) \approx \eta\sigma_c E_c^2 = 8.8\times10^{11}\ \mathrm{W}\cdot\mathrm{m}^{-3}$. The work due to the body force $\mathbf{F}_{\mathrm{Lorentz}}$ is: $\mathbf{u}\cdot\mathbf{F}_{\mathrm{Lorentz}} \approx u_c\eta\sigma_c E_c B_c = 7.0\times10^{8}\ \mathrm{W}\cdot\mathrm{m}^{-3}$, that is by 3 orders of magnitude lower than the Joule heating.

Equations of State

The ideal gas law is used for calculating the electron gas pressure p_e and the overall pressure p:

$$p_e = n_e k_{\mathrm{B}} T_{\mathrm{e}} , \tag{3.20}$$

$$p = \sum_{\substack{s=1\\ s\neq e}}^{n} \rho c_s \frac{\mathcal{R}}{\mathcal{M}_s} T + p_e . \tag{3.21}$$

Concluding Remarks

Additional submodels are required to calculate unknown variables and source terms contained in the equations introduced above. Firstly, the relations between the energies E_{vib}, E_{e} and E and the corresponding temperatures T_{vib}, T_{e} and T must be established. This issue is discussed in Sec. 3.2.2. Secondly, additional models are needed for the calculation of the yet unknown viscosity μ as well as heat fluxes $\mathbf{q}_{\mathrm{vib}}$, $\mathbf{q}_{\mathrm{e}}$ and $\mathbf{q}$ and the diffusion velocities $\mathbf{V}_s$ (see Sec. 3.2.3). Finally, following source terms must be defined: $\mathbf{F}_{\mathrm{Lorentz}}$, $\dot{Q}_{\mathrm{Joule}}$, $\dot{Q}_{\mathrm{rad}}$, $\left(\partial E_{\mathrm{vib}}/\partial t\right)_{\mathrm{int}}$ and $\left(\partial E_{\mathrm{e}}/\partial t\right)_{\mathrm{int}}$. This is the subject of Sec. 3.2.5. The source terms $\dot{\omega}_1$, ..., $\dot{\omega}_n$ are already defined in Sec. 3.1.

3.2.2 Thermodynamic Properties

The connection between the temperatures (T, T_{e}, T_{vib}) and the specific energies ($e_{\mathrm{tr-rot}}$, e_{e}, e_{vib}) is defined via the following caloric equation of state [23]:

$$de = c_v(T)dT \ , \tag{3.22}$$

where c_v denotes the specific heat at constant volume.

In the following, models used in the present work for the calculation of energies and the associated specific heat capacities are presented.

Vibrational Temperature

The vibrational temperature characterizes the amount of energy contained in the vibrational energy mode. In this work the model of a rotationless harmonic oscillator is used for the calculation of the vibrational energy of diatomic molecules. The overall vibrational energy contained in the system may be calculated as follows [15]:

$$E_{\mathrm{vib}} = \sum_{s=m} n_s \epsilon_{\mathrm{vib},s} = \sum_{s=m} \rho c_s R_s \frac{\epsilon_{\mathrm{vib},s}}{k_{\mathrm{B}}} = \rho e_{\mathrm{vib}} \ , \tag{3.23}$$

where $\epsilon_{\mathrm{vib},s}$ denotes the average vibrational energy per molecule of species s and e_{vib} is the specific vibrational energy in $\mathrm{J} \cdot \mathrm{kg}^{-1}$ [14]. The calculation of ϵ_{vib} is already derived in Sec. 2.3 (see Eq. 2.33). By introducing the characteristic vibrational temperature $\Theta_{\mathrm{vib}} = E_1/k_{\mathrm{B}}$ and substituting Eq. 2.33 in Eq. 3.23 the vibrational energy per unit mass may be modelled as follows:

$$e_{\mathrm{vib}} = \frac{1}{\rho} \sum_{s=m} n_s k_{\mathrm{B}} \frac{\Theta_{\mathrm{vib},s}}{exp\left(\Theta_{\mathrm{vib},s}/T_{\mathrm{vib}}\right) - 1} = \sum_{s=m} c_s R_s \frac{\Theta_{\mathrm{vib},s}}{exp\left(\Theta_{\mathrm{vib},s}/T_{\mathrm{vib}}\right) - 1} \ , \tag{3.24}$$

where the summation is taken over all molecular species m contained in the system. For N_2 the value of $\Theta_{\mathrm{vib,N_2}}$ is taken from Park [14] and amounts to 3393 K. The same Θ_{vib} is assumed for the molecular nitrogen ion N_2^+. The vibrational specific heat at constant volume in $\mathrm{J} \cdot \mathrm{kg}^{-1} \cdot \mathrm{K}^{-1}$ is calculated as follows:

$$c_{v,\mathrm{vib}} = \sum_{s=m} c_s R_s \frac{\left(\Theta_{\mathrm{vib},s}/T_{\mathrm{vib}}\right)^2 exp\left(\Theta_{\mathrm{vib},s}/T_{\mathrm{vib}}\right)}{\left(exp\left(\Theta_{\mathrm{vib},s}/T_{\mathrm{vib}}\right) - 1\right)^2} \ . \tag{3.25}$$

Electron-Electronic Temperature

The electron-electronic energy is defined as [14]:

$$E_{\mathrm{e}} = \rho e_{\mathrm{e}} = \frac{3}{2}\rho c_e R_e T_{\mathrm{e}} + \sum_{\substack{s=1 \\ s\neq e}}^{n} \rho c_s R_s \frac{\epsilon_{\mathrm{el},s}}{k_{\mathrm{B}}} \ . \tag{3.26}$$

The first part of Eq. 3.26 provides the energy contained in the translational mode of free electrons. The second part yields the electronic excitation of atoms and molecules. Both parts are functions of electron-electronic temperature T_{e}. The electronic excitation energy per atom or molecule is modelled as follows [46]:

$$\epsilon_{\mathrm{el},s} = k_{\mathrm{B}} \frac{\sum_{i=1}^{\infty} g_{i,s}\Theta_{\mathrm{el},i,s} exp\left(-\Theta_{\mathrm{el},i,s}/T_{\mathrm{e}}\right)}{\sum_{i=0}^{\infty} g_{i,s} exp\left(-\Theta_{\mathrm{el},i,s}/T_{\mathrm{e}}\right)} \ . \tag{3.27}$$

The quantities $\Theta_{\mathrm{el},i}$ and g_i are the characteristic electronic temperature and the degeneracy of the i-th energy level, respectively. In this work the first seven excited electronic levels are considered. The values of $\Theta_{\mathrm{el},i}$ and g_i are given in Appendix B in Tab. B.2. The electron-electronic specific heat at constant volume is given by [46]:

$$c_{v,\mathrm{e}} = c_{v,\mathrm{el}} + c_{v,\mathrm{e,tr}} = \sum_{\substack{s=1 \\ s\neq e}}^{n} c_s R_s \left\{ \frac{\sum_{i=1}^{\infty} g_{i,s} \left(\Theta_{\mathrm{el},i,s}/T_{\mathrm{e}}\right)^2 exp\left(-\Theta_{\mathrm{el},i,s}/T_{\mathrm{e}}\right)}{\sum_{i=0}^{\infty} g_{i,s} exp\left(-\Theta_{\mathrm{el},i,s}/T_{\mathrm{e}}\right)} \right.$$
$$\left. - \frac{\left[\sum_{i=1}^{\infty} g_{i,s}\Theta_{\mathrm{el},i,s} exp\left(-\Theta_{\mathrm{el},i,s}/T_{\mathrm{e}}\right)\right]\left[\sum_{i=0}^{\infty} g_{i,s}\left(\Theta_{\mathrm{el},i,s}/T_{\mathrm{e}}^2\right) exp\left(-\Theta_{\mathrm{el},i,s}/T_{\mathrm{e}}\right)\right]}{\left[\sum_{i=0}^{\infty} g_{i,s} exp\left(-\Theta_{\mathrm{el},i,s}/T_{\mathrm{e}}\right)\right]^2} \right\}$$
$$+ \underbrace{\frac{3}{2} c_{\mathrm{e}} R_{\mathrm{e}}}_{c_{v,\mathrm{e,tr}}} \ . \tag{3.28}$$

Translational-Rotational Temperature

The energy contained in the translational-rotational mode $E_{\mathrm{tr-rot}}$ may be modelled as follows [14]:

$$E_{\mathrm{tr-rot}} = \rho e_{\mathrm{tr}} + \rho e_{\mathrm{rot}} = \sum_{\substack{s=1 \\ s\neq e}}^{n} \frac{3}{2}\rho c_s R_s T + \sum_{s=m} \rho c_s R_s T \ . \tag{3.29}$$

The translational-rotational specific heat at constant volume is given by:

$$c_{\mathrm{tr-rot}} = c_{\mathrm{tr}} + c_{\mathrm{rot}} = \sum_{\substack{s=1 \\ s\neq e}}^{n} \frac{3}{2} c_s R_s + \sum_{s=m} c_s R_s \ . \tag{3.30}$$

The total energy E is given such that [14]:

$$E = E_{\mathrm{vib}} + E_{\mathrm{e}} + E_{\mathrm{tr-rot}} + \sum_{s=1}^{n} \rho c_s (\Delta h_{\mathrm{f}})_s^0 + \frac{1}{2}\rho |\mathbf{u}|^2 \ \ , \tag{3.31}$$

where $(\Delta h_\mathrm{f})_s^0$ denotes the enthalpy of formation (heat of formation) of species s at 0 K. The values of $(\Delta h_\mathrm{f})_s^0$ are taken from the report of the Glenn Research Center [53] and are depicted in Appendix B in Tab. B.4 in $\mathrm{J \cdot kmol^{-1}}$. That is, for using $(\Delta h_\mathrm{f})_s^0$ in Eq. 3.31, the values must be transformed into $\mathrm{J \cdot m^{-3}}$ by multiplying them with a corresponding $\mathcal{M}_s$. The energy contained in the translational-rotational mode $E_\mathrm{tr-rot}$ is governed by solving the total energy equation Eq. 3.19 and subtracting all other energy parts from the total energy. Afterwards, the translational-rotational temperature T is calculated by means of Eqs. 3.30 and 3.22.

In the total energy conservation equation, Eq. 3.31, enthalpies of formation h_f^0 at 0 K are used instead of internal energies of formation at absolute zero e_f^0. This is the usual practice where it is assumed that: $h_\mathrm{f}^0 \approx e_\mathrm{f}^0$. Since $\Delta E = \Delta H - p\Delta V$ this is a reasonable assumption for solids and liquids, for which $p\Delta V \approx 0$. For gases that behave like an ideal gas, the term $p\Delta V$ can be replaced by $\Delta n \mathcal{R} T$, where Δn represents the change in the number of moles at 0 K during the formation of the species [54]. Here it could be suggested that $\Delta n \mathcal{R} T$ would disappear or at least become negligibly small when T approaches 0 K. But even if $p\Delta V \neq 0$, the calculation would still be correct, since all thermodynamic and gas dynamic problems are about changes of enthalpy and internal energy and not about their absolute values [15].

3.2.3 Transport Properties and Fluxes

The calculation models for transport properties used in this work are derived from the Chapman-Enskog theory, which results from solving the Boltzmann equation by assuming that the velocity distribution function of the particles is close to Maxwellian distribution [55, 21]. More information on the Chapman-Enskog theory can be found e.g. in Chapman and Cowling [55]. This theory was developed by both, Chapman and Enskog independently and delivers formulas for calculating transport properties of neutral-gas mixtures in the state of thermodynamic equilibrium [56, 16].

In his work, Yos [22] uses the Chapman-Enskog theory for deriving formulas for the transport properties of nitrogen, hydrogen, oxygen, and air, for temperatures from 1000 to 30,000 K and pressures from 1 to 30 bar. Lee [21] extended Yos's formulas to the multi-temperature approach by using the translational temperature T for the Maxwellian velocity distribution of the heavy particles, whereas T_e is taken for the electron gas. The same approach can also be found in the transport property formulas presented in the work of Gupta *et al.* [23]. In the present work, the models of Yos, Lee, and Gupta *et al.* are used for the calculation of transport properties. The work of Sutton and Gnoffo [57] is used for the calculation of the diffusion fluxes.

All equations for the transport properties are based on two variables, namely $\Delta_{ij}^{(1)}(T)$ and $\Delta_{ij}^{(2)}(T)$. They give information about the dynamics of two-particle interactions leading to a momentum or energy transfer between species i and j. The two-particle momentum transfer is defined by [14]:

$$\Delta_{ij}^{(1)}(T) = \frac{8}{3}\left(\frac{2 m_i m_j}{\pi k_\mathrm{B} T (m_i + m_j)}\right)^{1/2} \pi \overline{\Omega}_{ij}^{(1,1)} \,, \tag{3.32}$$

where $\pi\overline{\Omega}_{ij}^{(1,1)}$ denotes the collision integral for momentum transfer between species i and j [14]. The energy transfer is given by [14]:

$$\Delta_{ij}^{(2)}(T) = \frac{16}{5}\left(\frac{2m_i m_j}{\pi k_\mathrm{B} T(m_i+m_j)}\right)^{1/2}\pi\overline{\Omega}_{ij}^{(2,2)} \ , \tag{3.33}$$

where $\pi\overline{\Omega}_{ij}^{(2,2)}$ is the collision integral for the energy transfer between species i and j. Again, for collision processes with free electrons T_e is used in $\Delta_{ij}^{(1)}(T)$ and $\Delta_{ij}^{(2)}(T)$ and for those involving heavy particles only the temperature T is taken.

The collision integrals $\pi\overline{\Omega}_{ij}^{(1,1)}$ and $\pi\overline{\Omega}_{ij}^{(2,2)}$, sometimes referred to as weighted averages of the collision cross sections for momentum and energy transfer, play the crucial role in the physicochemical model because all transport properties are linearly related to them. They are treated separately in Sec. 3.2.4.

Viscosity

The viscosity of the gas mixture is calculated as follows [21]:

$$\mu = \sum_{\substack{s=1\\ s\neq e}}^{n}\left(m_s y_s \Bigg/ \left[\sum_{\substack{r=1\\ r\neq e}}^{n} y_r\Delta_{sr}^{(2)}(T) + y_e\Delta_{se}^{(2)}(T_\mathrm{e})\right]\right) + \left(\frac{m_e y_e}{\sum\limits_{r=1}^{n} y_r\Delta_{er}^{(2)}(T_\mathrm{e})}\right) \ . \tag{3.34}$$

Effective Diffusion Coefficient

The effective diffusion coefficient for a neutral particle is obtained as follows [21]:

$$\mathcal{D}_s = \frac{1-y_s}{\sum\limits_{\substack{r=1\\ r\neq s}}^{n} {}^{y_r}\!/_{D_{sr}}} \ . \tag{3.35}$$

The quantity D_{sr} denotes the binary diffusion coefficient of an $s-r$ pair of heavy particles and is given by [21]:

$$D_{sr} = \frac{k_\mathrm{B}T}{p\Delta_{sr}^{(1)}(T)} \ . \tag{3.36}$$

The binary diffusion coefficient between electrons and neutrals is defined as [21]:

$$D_{er} = \frac{k_\mathrm{B}T_\mathrm{e}}{p\Delta_{er}^{(1)}(T_\mathrm{e})} \ , \tag{3.37}$$

where the electron temperature T_e is used for the calculation.

As for the diffusion of ionic species, it is recalled that for the system under investigation the concept of ambipolar diffusion is used. The ambipolar diffusion coefficient of ions may be defined as follows [16, 21]:

$$\mathcal{D}_i^\mathrm{a} = 2\mathcal{D}_i \ , \tag{3.38}$$

where $\mathcal{D}_i$ denotes the effective diffusion coefficient of the ionic species. The calculation of the effective diffusion coefficients for individual ions $\mathcal{D}_i$ is rather expensive, since it includes the calculation of the charge separation effects. Therefore, Lee suggests the following simplification: $\mathcal{D}_i = \mathcal{D}_s$. Here, $\mathcal{D}_s$ is the effective diffusion coefficient of the ionic species ($s = i$) in absence of electric fields and is calculated by Eq. 3.35.

For the calculation of the effective diffusion coefficient of electrons, Lee suggests an assumption that the mass averaged diffusion velocity of all ionic species is equal to the diffusion velocity of electrons. Thus, $\mathcal{D}_e$ may be expressed as follows [21]:

$$\mathcal{D}_e = \frac{m_e \sum_{s=i} \mathcal{D}_s^{\mathrm{a}} y_s}{\sum_{s=i} m_s y_s} \ . \tag{3.39}$$

However, such a simplification does not guarantee the quasineutrality. In order to preserve quasineutrality, the diffusion term must include an additional term, which, in the case of nonuniformity in number densities of ions and electrons (charge separation), would calculate polarization fields and the resulting restoring forces.

Thermal Conductivity

The electron thermal conductivity is given as [21, 23]:

$$\kappa_{\mathrm{e,tr}} = \frac{15}{4} k_{\mathrm{B}} \frac{y_e}{\sum_{\substack{r=1 \\ r \neq e}}^{n} 1.45 y_r \Delta_{er}^{(2)}(T) + y_e \Delta_{ee}^{(2)}(T_{\mathrm{e}})} \ . \tag{3.40}$$

According to Park [14], only a fraction of the heat flux $\kappa_{\mathrm{e,tr}} \boldsymbol{\nabla} T_{\mathrm{e}}$ is transmitted to the electron gas. Therefore, the electron thermal conductivity due to collisions between the electrons only has to be reformulated as follows [21]:

$$\kappa'_{\mathrm{e,tr}} = \kappa_{\mathrm{e,tr}} \left(\frac{y_e \Delta_{ee}^{(2)}(T_{\mathrm{e}})}{\sum_{r=1}^{n} y_r \Delta_{er}^{(2)}(T_{\mathrm{e}})} \right) \ . \tag{3.41}$$

The thermal conductivity due to electronic excitation is such that [23]:

$$\kappa_{\mathrm{el}} = k_{\mathrm{B}} \sum_{\substack{s=1 \\ s \neq e}}^{n} \left(y_s \left(\frac{c_{v,\mathrm{el},s}}{R_s} \right) \Bigg/ \left[\sum_{\substack{r=1 \\ r \neq e}}^{n} y_r \Delta_{sr}^{(1)}(T) + y_e \Delta_{se}^{(1)}(T_{\mathrm{e}}) \right] \right) \ . \tag{3.42}$$

The vibrational thermal conductivity is given as [21]:

$$\kappa_{\mathrm{vib}} = k_{\mathrm{B}} \sum_{s=m} \left(y_s \left(\frac{c_{v,\mathrm{vib},s}}{R_s} \right) \Bigg/ \left[\sum_{\substack{r=1 \\ r \neq e}}^{n} y_r \Delta_{sr}^{(1)}(T) + y_e \Delta_{se}^{(1)}(T_{\mathrm{e}}) \right] \right) \ , \tag{3.43}$$

where the contribution of molecule-molecule collisions to the overall vibrational thermal conductivity is calculated as follows [21]:

$$\kappa'_{\mathrm{vib}} = \kappa_{\mathrm{vib}} \sum_{s=m} \left(\sum_{r=m} y_r \Delta^{(2)}_{sr}(T) \Bigg/ \left[\sum_{\substack{r=1 \\ r\neq e}}^{n} y_r \Delta^{(2)}_{sr}(T) + y_r \Delta^{(2)}_{se}(T_{\mathrm{e}}) \right] \right) \ , \tag{3.44}$$

The translational thermal conductivity is calculated by the following expression [21]:

$$\kappa_{\mathrm{tr}} = \frac{15}{4} k_{\mathrm{B}} \sum_{\substack{s=1 \\ r\neq e}}^{n} \left(y_s \Bigg/ \left[\sum_{\substack{r=1 \\ r\neq e}}^{n} \alpha_{sr} y_r \Delta^{(2)}_{sr}(T) + 3.54 y_e \Delta^{(2)}_{se}(T_{\mathrm{e}}) \right] \right) \ , \tag{3.45}$$

where the factor α_{sr} is given by [21]:

$$\alpha_{sr} = 1 + \frac{\left[1 - (m_s/m_r)\right] \left[0.45 - 2.54\,(m_s/m_r)\right]}{\left[1 + (m_s/m_r)\right]^2} \ . \tag{3.46}$$

The rotational thermal conductivity is defined by the following equation [21]:

$$\kappa_{\mathrm{rot}} = k_{\mathrm{B}} \sum_{s=m} \left(y_s \left(\frac{c_{v,\mathrm{rot},s}}{R_s} \right) \Bigg/ \left[\sum_{\substack{r=1 \\ r\neq e}}^{n} y_r \Delta^{(1)}_{sr}(T) + y_e \Delta^{(1)}_{se}(T_{\mathrm{e}}) \right] \right) \ . \tag{3.47}$$

Electrical Conductivity

The equation for calculating the electrical conductivity is taken from Yos [22] and is modified in the present work by using the temperature T_{e} instead of T:

$$\sigma = \frac{e^2}{k_{\mathrm{B}} T_{\mathrm{e}}} \left(y_{\mathrm{e}} \Bigg/ \left[\sum_{\substack{s=1 \\ s\neq \mathrm{e}}}^{n} y_s \Delta^{(1)}_{\mathrm{e}s}(T_{\mathrm{e}}) \right] \right) \ , \tag{3.48}$$

where the quantity e denotes the elementary charge.

Diffusion Velocity

The diffusion velocity is required for the calculation of diffusion fluxes ($\rho \mathbf{V}_s c_s$) in the species conservation equations and heat fluxes ($\mathbf{q}_{\mathrm{e}}$, $\mathbf{q}_{\mathrm{vib}}$, $\mathbf{q}$) in the energy conservation equations.

According to Sutton and Gnoffo [57], for an approximate calculation of the multi-component diffusion fluxes the following expression is often used:

$$\rho \mathbf{V}_s c_s = -\rho \mathcal{D}_s \boldsymbol{\nabla} c_s \ . \tag{3.49}$$

Sutton and Gnoffo state that by using the approximate equation, Eq. 3.49, the requirement of the diffusion mass fluxes summing to zero is not guaranteed. For this reason, a corrected form of the approximate equation is used in the present work, which ensures that the sum of diffusion mass fluxes yields zero [26, 57]:

$$\mathbf{V}_s = -\frac{1}{c_s}\mathcal{D}_s \boldsymbol{\nabla} c_s + \sum_{\substack{r=1 \\ r\neq e}}^{n} \mathcal{D}_r \boldsymbol{\nabla} c_r \ , \tag{3.50}$$

where for neutral species $\mathcal{D}_s$ is calculated by means of Eq. 3.35. For ions $\mathcal{D}_s = 2\mathcal{D}_i$ and electrons $\mathcal{D}_s = \mathcal{D}_e$, calculated by Eqs. 3.38 and 3.39, respectively.

Heat Fluxes

The heat flux vector $\mathbf{q}_\mathrm{e}$ represents the flux of energy contained in the electron-electronic energy mode and consists of three components [21, 14]:

$$\mathbf{q}_\mathrm{e} = -\kappa'_{\mathrm{e,tr}} \boldsymbol{\nabla} T_\mathrm{e} - \kappa_\mathrm{el} \boldsymbol{\nabla} T_\mathrm{e} + \sum_{\substack{s=1 \\ s\neq e}}^{n} \rho c_s \mathbf{V}_s e_{e,s} \ . \tag{3.51}$$

The first component in Eq. 3.51 arises due to elastic collisions between free electrons. The second component results from the electronic excitation of heavy particles. The third term represents the species diffusion due to concentration gradients.

The heat flux vector $\mathbf{q}_\mathrm{vib}$ represents the flux of energy contained in the vibrational energy mode and it consists of two parts [21, 14]:

$$\mathbf{q}_\mathrm{vib} = -\kappa'_\mathrm{vib} \boldsymbol{\nabla} T_\mathrm{vib} + \sum_{s=m} \rho c_s \mathbf{V}_s e_{\mathrm{vib},s} \ . \tag{3.52}$$

The first component in Eq. 3.52 arises due to molecular collisions, whereas the second component models the heat flux due to molecular diffusion.

The vector $\mathbf{q}$ represents the overall energy flux [21]:

$$\mathbf{q} = -\kappa_{\mathrm{e,tr}} \boldsymbol{\nabla} T_\mathrm{e} - \kappa_\mathrm{el} \boldsymbol{\nabla} T_\mathrm{e} - \kappa_\mathrm{vib} \boldsymbol{\nabla} T_\mathrm{vib} - \kappa \boldsymbol{\nabla} T + \sum_{s=1}^{n} \rho c_s \mathbf{V}_s e_s \ , \tag{3.53}$$

where $e_s = e_{s,\mathrm{tr-rot}} + e_{s,\mathrm{vib}} + e_{s,\mathrm{e}} + (\Delta h_\mathrm{f})^0_s$. The quantity κ denotes the translational-rotational thermal conductivity and is defined as: $\kappa = \kappa_\mathrm{tr} + \kappa_\mathrm{rot}$.

3.2.4 Collision Integrals

According to Yos [22], the collision integrals $\pi\overline{\Omega}^{(1,1)}_{ij}$ and $\pi\overline{\Omega}^{(2,2)}_{ij}$ have the physical significance of effective cross sections between molecules of species i and j. In mathematical terms, the collision integrals are described as weighted averages of the collision cross sections as follows [22]:

$$\pi\overline{\Omega}^{(l,s)}_{ij} = \frac{\int_0^\infty \int_0^\pi exp\left(-\gamma^2\right) \gamma^{2s+3} \left(1 - cos^l\chi\right) 4\pi\sigma_{ij} sin\chi d\chi d\gamma}{\int_0^\infty \int_0^\pi exp\left(-\gamma^2\right) \gamma^{2s+3} \left(1 - cos^l\chi\right) sin\chi d\chi d\gamma} \ , \tag{3.54}$$

where the reduced velocity γ is given by:

$$\gamma = g\left(\frac{m_i m_j}{2(m_i+m_j)k_{\mathrm{B}}T}\right)^{1/2} . \tag{3.55}$$

The quantity g is the relative velocity of the colliding particles, σ_{ij} denotes the differential cross section for the *i*-*j* pair of particles, and χ is the scattering angle in the centre of mass of the system [22].

In the present work collisions between neutral particles as well as neutral-ion and neutral-electron collisions are calculated by means of the curve-fit formulae provided by Gupta *et al.* [23]. For the calculation of collision integrals Gupta *et al.* utilise cross sections previously used by Yos [22]. The curve-fit functions are [23]:

$$\pi\overline{\Omega}_{ij}^{(1,1)} = \left[exp\left(D_{\overline{\Omega}_{ij}^{(1,1)}}\right)\right] T^{\left[A_{\overline{\Omega}_{ij}^{(1,1)}} ln(T)^2 + B_{\overline{\Omega}_{ij}^{(1,1)}} ln(T) + C_{\overline{\Omega}_{ij}^{(1,1)}}\right]} , \tag{3.56}$$

$$\pi\overline{\Omega}_{ij}^{(2,2)} = \left[exp\left(D_{\overline{\Omega}_{ij}^{(2,2)}}\right)\right] T^{\left[A_{\overline{\Omega}_{ij}^{(2,2)}} ln(T)^2 + B_{\overline{\Omega}_{ij}^{(2,2)}} ln(T) + C_{\overline{\Omega}_{ij}^{(2,2)}}\right]} . \tag{3.57}$$

The values of the curve-fit coefficients A, B, C and D for the calculation of $\pi\overline{\Omega}_{ij}^{(1,1)}$ are given in Appendix B in Tab. B.5 and for $\pi\overline{\Omega}_{ij}^{(2,2)}$ in Tab. B.6. For all calculated collision integrals the symmetrical equality applies, meaning $(ij) = (ji)$. In order to convert $\pi\overline{\Omega}_{ij}^{(1,1)}$ and $\pi\overline{\Omega}_{ij}^{(2,2)}$ calculated by Eqs. 3.56 and 3.57 into MKS units, the obtained values must be multiplied by a factor of 1×10^{-20}.

In the frame of the present work, the system is assumed to be in the state of thermal nonequilibrium. For this reason, temperature T_{e} is used in Eqs. 3.56 and 3.57 instead of T for collisions with electrons.

For the calculation of collision integrals $\pi\overline{\Omega}_{ij}^{(1,1)}$ and $\pi\overline{\Omega}_{ij}^{(2,2)}$ for Coulomb collisions the work of Yos [22] is used. The calculation requires the Gvosdover cross section, Q_{C}, which is defined as follows [22]:

$$Q_{\mathrm{C}} = \left(\frac{e^2}{k_{\mathrm{B}}T}\right)^2 ln\Lambda = 3.22 \times 10^{-6}\frac{log_{10}\Lambda^2}{T^2} , \tag{3.58}$$

where the cut-off parameter Λ is calculated by:

$$\Lambda^2 = \frac{9\left(k_{\mathrm{B}}T\right)^3}{4\pi e^6 n_e} + \frac{16\left(k_{\mathrm{B}}T\right)^2}{e^4 n_e^{2/3}} . \tag{3.59}$$

Then the Coulomb collision integrals are calculated using the following formulae [22]:

$$\begin{aligned}
\pi\overline{\Omega}_{e-e}^{(1,1)} &= 0.80Q_{\mathrm{C}} , & \pi\overline{\Omega}_{1-1}^{(2,2)} &= 0.30Q_{\mathrm{C}} ,\\
\pi\overline{\Omega}_{e-e}^{(2,2)} &= 0.75Q_{\mathrm{C}} , & \pi\overline{\Omega}_{e-1}^{(1,1)} &= 0.80Q_{\mathrm{C}} ,\\
\pi\overline{\Omega}_{1-1}^{(1,1)} &= 0.80Q_{\mathrm{C}} , & \pi\overline{\Omega}_{e-1}^{(2,2)} &= 0.75Q_{\mathrm{C}} ,
\end{aligned}$$

where the subscript 1 indicates singly charged ions. In this way the collision integrals for the following species pairs can be determined:

$$e - e \ , \ e - \mathrm{N}_2^+ \ , \ e - \mathrm{N}^+ \ , \ \mathrm{N}_2^+ - \mathrm{N}_2^+ \ , \ \mathrm{N}_2^+ - \mathrm{N}^+ \ , \ \mathrm{N}^+ - \mathrm{N}^+ \ .$$

Since the system is assumed to be in the state of thermal nonequilibrium, temperature T is used in Eqs. 3.58 and 3.59 for collisions between ions, whereas T_e is utilized for ion-electron and electron-electron collisions.

Eqs. 3.58 and 3.59 are given in CGS units where for the elementary charge e electrostatic CGS units (ESU) are used and hence $e = 4.803 \times 10^{-10}$ esu.

3.2.5 Energy Exchange Models

General Information on Energy Exchange

Particular attention must be paid to the overall energy balance in the system under investigation. Fig. 3.2 shows a schematic diagram of the overall energy balance, where the system boundaries are indicated by solid lines.

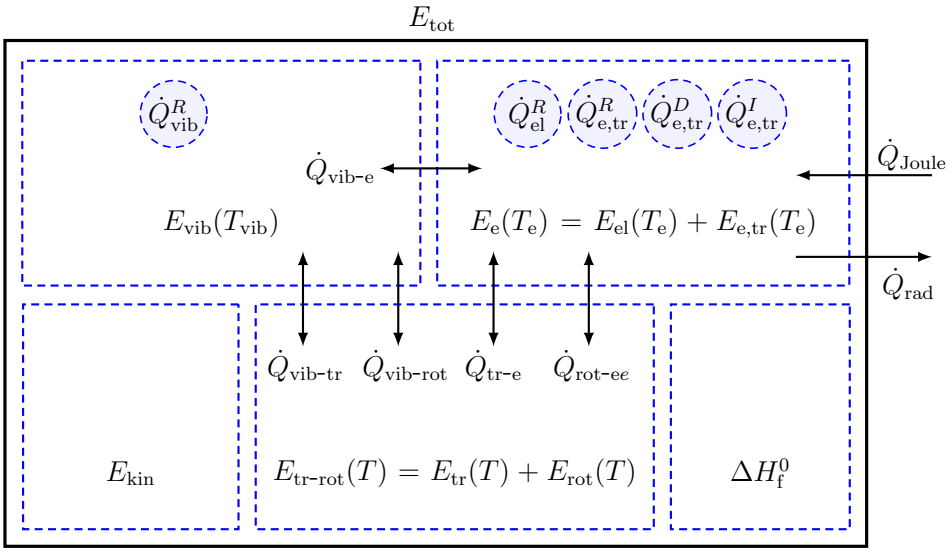

Figure 3.2: Schematic representation of the internal energy exchange between different energy modes in the system.

The set of governing equations, described in Sec. 3.2.1, includes three energy conservation equations. For modelling the system-internal energy exchange, the electron-electronic and the vibrational energy conservation equations are supplemented by additional source terms $\left(\frac{\partial E_\mathrm{e}}{\partial t}\right)_\mathrm{int}$ and $\left(\frac{\partial E_\mathrm{vib}}{\partial t}\right)_\mathrm{int}$, respectively. The total energy equation does not require any consideration of internal energy exchange, since it calculates the whole energy in the system. However, the energy exchange with the surroundings

must be considered in the total energy equation as well as in the electron-electronic energy equation, since the electron-electronic energy mode is the one that exchanges the energy with the surroundings via $\dot{Q}_{\text{Joule}}$ and $\dot{Q}_{\text{rad}}$ (see Fig. 3.2).

As shown Fig. 3.2, the total energy E consists of five different energy parts:

- E_{vib} – energy contained in the vibrational energy mode,
- E_{e} – energy contained in the electron-electronic energy mode,
- E_{kin} – kinetic energy contained in the fluid due to its macroscopic motion relative to some reference frame,
- $E_{\text{tr-rot}}$ – energy contained in the translational-rotational energy mode,
- ΔH_{f}^{0} – overall enthalpy of formation of all species in the system at $T = 0$ K.

Energy Exchange with the Surroundings

Both processes, the Joule heating effect and the energy loss through radiation, are modelled as unidirectional processes. The Joule-heating source term, defined as $\dot{Q}_{\text{Joule}} = \eta\,(\mathbf{J} \cdot \mathbf{E})$, is discussed in detail in Sec. 3.3.6.

The heat losses due to radiation are modelled by using the continuum radiation formula of Yos [22]:

$$\dot{Q}_{\text{rad}} = \zeta \frac{64\pi^{3/2} e^6 p^2 \Delta\nu}{3\sqrt{6}\; m_e^{3/2} c^3 \left(k_{\text{B}} T_{\text{e}}\right)^{5/2}} y_e \sum_{\substack{s=1 \\ s\neq e}}^{n} y_s Z_s^2 \;, \tag{3.60}$$

where $\zeta = 3$ is an empirical constant introduced to make the correspondence between the calculated values of the total radiated power $\dot{Q}_{\text{rad}}$ and the experimentally measured values as good as possible. The quantities h and c denote the Planck's constant and the speed of light, respectively. The value Z_s denotes the charged state of ions (e.g. +1 for singly- and +2 for doubly-charged ions). The bandwidth of the spectrum $\Delta\nu$ is assumed to be equal to the width of the blackbody distribution: $\Delta\nu_{\text{B}} = 4k_{\text{B}}T_{\text{e}}/h$ [22]. Molecular-band and atomic-line radiations are not included in the calculation in Eq. 3.60. In addition, the absorption effects are neglected in Yos' formula, that is, the assumption of an optically thin plasma[1] is used. It should be noted that all values and constants in Eq. 3.60 are in CGS units, except the pressure p, which is in bar. Furthermore, it must be pointed out that T_{e} is used in Eq. 3.60 in the frame of this work, instead of originally proposed temperature T.

As already mentioned, the presence of N^{++} in the plasma is noticeable above 25,000 K. At a temperature above 30,000 K and at atmospheric pressure, the number density of N^{++} would even exceed that of N^{+}. However, the production of N^{++} is not included in this work. In order to take into account the effects of N^{++} at high temperatures on the radiation losses, the charge state Z_s of N^{+} in Eq. 3.60 is switched over from +1 to +2 at a temperature above 35,000 K.

[1] Wells [35] states that: "if the plasma is defined as optically thin, all energy radiated from within the plasma escapes without being re-absorbed within the plasma column."

System-Internal Energy Exchange

The internal energy exchange models can be divided into two groups:

1. equilibration processes between the energy modes,
2. energy sources and sinks due to species production and destruction.

Equilibration Processes between Energy modes

The equilibration processes between the energy modes are calculated by using the works of Park [14], Lee [44], and Millikan and White [43]. All these processes are indicated with arrows in Fig. 3.2 and modelled as bidirectional processes, meaning they may run in both directions between the energy modes.

For the calculation of the time rate of change of vibrational energy due to collisions with heavy particles the general relaxation equation (Eq. 2.29) is used. By using Eq. 2.29, the vibrational-translational relaxation source term can be written as [14]:

$$\dot{Q}_{\text{vib-tr}} = \sum_{s=m} \frac{E_{\text{vib}}(T) - E_{\text{vib}}(T_{\text{vib}})}{\tau_{\text{vib-tr}}} \ , \tag{3.61}$$

where the hypothetical equilibrium vibrational energy $E_{\text{vib}}(T)$ is evaluated by solving Eq. 3.24 for the translational-rotational temperature T. The vibrational-translational relaxation time $\tau_{\text{vib-tr}}$ for molecular species m is calculated as follows [26]:

$$\tau_{m,\text{vib-tr}} = \frac{\sum\limits_{\substack{s=1 \\ s\neq e}}^{n} y_s}{\sum\limits_{\substack{s=1 \\ s\neq e}}^{n} y_s / \left(\tau_{ms}^{\text{MW}} + \tau_{ms}^{\text{P}}\right)} \ , \tag{3.62}$$

where τ^{MW} denotes the vibrational-translational relaxation time proposed by Millikan and White [43] and τ^{P} is the correction suggested by Park [58]. The Millikan and White formula is given such that:

$$\tau_{ms}^{\text{MW}} = \frac{1}{p} exp\left[A_{ms}\left(T^{-1/3} - 0.015\overline{\mathcal{M}}_{ms}^{1/4}\right) - 18.42\right] \ , \tag{3.63}$$

where p is in bar. The quantity $\overline{\mathcal{M}}$ is the reduced molecular weight between the two colliding particles r and s given as:

$$\overline{\mathcal{M}}_{rs} = \frac{\mathcal{M}_s \mathcal{M}_r}{(\mathcal{M}_s + \mathcal{M}_r)} \ . \tag{3.64}$$

The constant A_{ms} is proportional to the characteristic temperature Θ, to the reduced mass of the colliding pair $\overline{\mu}$, and to the length parameter l such that: $A \sim \overline{\mu}^{2/3}\theta^{2/3}l^{2/3}$. According to the data given in [43], for nitrogen $A = 220$ and $\overline{\mathcal{M}} = 14$. Eq. 3.63 gives a good approximation of the experimental data for temperatures below 5000 K. For

higher temperatures, however, it delivers lower values than experimentally measured [14]. That is why Park suggests to correct $\tau_{\text{vib-tr}}$ by adding the collision limited relaxation time τ^P given as [58]:

$$\tau_{ms}^{\text{P}} = \left(n_{\text{tot}} \left[\frac{8 k_{\text{B}} T}{\pi \overline{\mu}_{ms}} \right]^{1/2} \sigma_v \right)^{-1} \quad . \tag{3.65}$$

The quantity n_{tot} denotes the total number density of colliding particles. The value of σ_v can be obtained as follows [58]:

$$\sigma_v = \sigma_v' \left(50{,}000/T \right)^2 \quad , \tag{3.66}$$

where σ_v' is the limiting cross section whose values for N_2, O_2, and NO are chosen to be 3×10^{-21} m^2.

The general relaxation equation is also used for the calculation of the electron-impact vibrational relaxation [14]:

$$\dot{Q}_{\text{vib-e}} = \sum_{s=m} \frac{E_{\text{vib}}(T_{\text{e}}) - E_{\text{vib}}(T_{\text{vib}})}{\langle \tau_s \rangle_{\text{vib-e}}} \quad , \tag{3.67}$$

where the hypothetical equilibrium vibrational energy $E_{\text{vib}}(T_{\text{e}})$ is evaluated by solving Eq. 3.24 for the electron-electronic temperature T_{e}. The electron-impact vibrational relaxation time $\tau_{\text{vib-e}}$ is calculated by the following two empirical formulas of Lee [44]:

$$\begin{aligned} log_{10} \left(p_e \tau_{\text{vib-e}} \right) = 3.91 \left(log_{10} T_{\text{e}} \right)^2 - 30.36 \left(log_{10} T_{\text{e}} \right) + 48.90 \\ \text{for} \;\; 1000 \; K \leqslant T_{\text{e}} \leqslant 7000 \; K \; , \end{aligned} \tag{3.68}$$

$$\begin{aligned} log_{10} \left(p_e \tau_{\text{vib-e}} \right) = 1.3 \left(log_{10} T_{\text{e}} \right)^2 - 9.09 \left(log_{10} T_e \right) + 5.58 \\ \text{for} \;\; 7000 \; K \leqslant T_{\text{e}} \leqslant 50{,}000 \; K \; . \end{aligned} \tag{3.69}$$

It is important to mention that the electron pressure p_e is given in in bar.

The energy exchange due to vibrational-rotational relaxation is calculated by [12]:

$$\dot{Q}_{\text{vib-rot}} = \sum_{s=m} 0.4 \frac{E_{\text{vib}}(T_{\text{rot}}) - E_{\text{vib}}(T_{\text{vib}})}{\tau_{\text{vib-rot}}} = 0.4 \dot{Q}_{\text{vib-tr}} \; , \tag{3.70}$$

where $T_{\text{rot}} = T$ and the relaxation time $\tau_{\text{vib-rot}} = \tau_{\text{vib-tr}}$. The hypothetical equilibrium energy $E_{\text{vib}}(T_{\text{rot}})$ is evaluated by solving Eq. 3.24 for the translational-rotational temperature T.

The elastic energy transfer between electrons and heavy particles is calculated as [14, 45]:

$$\dot{Q}_{\text{tr-e}} = \sum_{s \neq e} n_e \frac{2 m_e}{m_s} \nu_{e,s} \frac{3}{2} k_{\text{B}} \left(T - T_{\text{e}} \right) \quad , \tag{3.71}$$

where $\nu_{e,s}$ denotes the collision frequency between free electrons and heavy particles of species s. This equation couples translational energy of free electrons with the energy contained in the translational mode of heavy particles.

The coupling between the rotational energy mode and the translational energy of free electrons is given by [12]:

$$\dot{Q}_{\text{rot-e}} = \sum_{s=m} n_e \frac{2m_e}{m_s} \beta_{\text{rot},s} \nu_{e,s} \frac{3}{2} k_{\text{B}} \left(T_{\text{rot}} - T_{\text{e}}\right) \ , \tag{3.72}$$

where the coefficient $\beta_{\text{rot},s}$ is assumed to be of the same value for all heavy species and amounts to $\beta_{\text{rot},s} = 10$ [12].

The collision frequencies $\nu_{e,s}$ between electrons and heavy particles are calculated by the expression [16]:

$$\overline{\nu}_{se} = \sum_{\substack{s=1 \\ s\neq e}}^{n} n_s \overline{v}_{se} \pi \overline{\Omega}_{se}^{(1,1)} \ , \tag{3.73}$$

where $\overline{v}_{se}$ denotes the mean relative speed of particles with Maxwellian velocity distribution defined as [16]:

$$\overline{v}_{se} = \left(\frac{8 k_{\text{B}} T}{\pi \overline{\mu}_{se}}\right)^{1/2} \ . \tag{3.74}$$

Energy Sources and Sinks due to Species Production and Destruction

The energy sources and sinks due to species production and destruction in the system are indicated in Fig. 3.2 by dashed circles. These processes also represent a system-internal energy exchange, because the removal of energy from one energy mode may appear as energy gain in another energy mode.

The dissociation of molecular species caused by collisions with other particles leads to a removal of energy from the vibrational mode [14]. The opposite happens when the recombination of two or more atoms to a molecule takes place. This rate of change of energy density E_{vib} is given by [14]:

$$\dot{Q}_{\text{vib}}^{\text{R}} = \sum_{s=m} E_{s,\text{vib}}(T_{\text{vib}}) \dot{\omega}_s \ , \tag{3.75}$$

where the superscript R stands for rate of change.

The rate of change of energy density contained in the electronic excitation of species $E_{s,\text{el}}$ is defined as [14]:

$$\dot{Q}_{\text{el}}^{\text{R}} = \sum_{\substack{s=1 \\ s\neq e}}^{n} E_{s,\text{el}}(T_{\text{e}}) \dot{\omega}_s \ . \tag{3.76}$$

Just like in the case of $\dot{Q}_{\text{vib}}^{\text{R}}$, this process also takes place, because the species composition in the gas undergoes changes due to ongoing chemical reactions. Park [14] explains this process by stating that any species produced as a result of chemical reaction is already electronically excited.

The gain or loss in translational energy of free electrons $E_{\mathrm{e,tr}}$ due to ongoing ionization and recombination is calculated as follows:

$$\dot{Q}^{\mathrm{R}}_{\mathrm{e,tr}} = E_{\mathrm{e,tr}}(T)\dot{\omega}_e \quad \text{for} \quad \dot{\omega}_e > 0 \quad \text{, and} \quad \dot{Q}^{\mathrm{R}}_{\mathrm{e,tr}} = E_{\mathrm{e,tr}}(T_{\mathrm{e}})\dot{\omega}_e \quad \text{for} \quad \dot{\omega}_e < 0 \ . \tag{3.77}$$

It must be noted that when new electrons occur due to ionization, they are born with a finite energy density, which is a function of the translational-rotational temperature ($E_{\mathrm{e,tr}}(T)$). However, when the amount of electron gas decreases due to recombination, the electrons are already accelerated by the external electric field and thus the energy to be extracted is a function of electron-electronic temperature: $E_{\mathrm{e,tr}}(T_{\mathrm{e}})$.

When a neutral particle is ionized as a result of collisions with free electrons, the ionization energy E^{I} is extracted from the electron gas. Thus, the rate of change of E_{e} due to ionization process, forming the ionic species s, is given as [14]:

$$\dot{Q}^{\mathrm{I}}_{\mathrm{e,tr}} = -\sum_{s=i} E^{\mathrm{I}}_s \dot{\omega}^{\mathrm{I}}_s \ , \tag{3.78}$$

where the superscript I stands for the ionization. The source term $\dot{\omega}^{\mathrm{I}}_s$ represents the rate of change of mass of species s due to ionization by electron collisions only. In the kinetic mechanism in Tab. 3.1 this process is represented by the endothermic reaction direction of the reaction $r = 7$. The ionization energy for ionizing the atomic nitrogen amounts to $E^{\mathrm{I}}_{\mathrm{N^+}} = 1.00083 \times 10^8 \ \mathrm{J \cdot kg^{-1}}$.

Likewise, during a molecular dissociation due to collisions with free electrons, the dissociation energy E^{D} is extracted from the electron gas. This process is described by the following equation [14]:

$$\dot{Q}^{\mathrm{D}}_{\mathrm{e,tr}} = -\sum_{s=m} E^{\mathrm{D}}_s \dot{\omega}^{\mathrm{D}}_s \ , \tag{3.79}$$

where the superscript D stands for dissociation. Here, only the rate of change of mass due to dissociation is taken into account, meaning the association of atoms to a molecule is not considered in $\dot{\omega}^{\mathrm{D}}_s$. The dissociation energy of nitrogen amounts to $E^{\mathrm{D}}_{\mathrm{N_2}} = 3.374512386 \times 10^7 \ \mathrm{J \cdot kg^{-1}}$. In the system under investigation the dissociation of nitrogen due to electron impacts is represented in Tab. 3.1 by the endothermic reaction direction of the reaction $r = 6$.

Assignment of Individual Energy Exchange Processes to Energy Conservation Equations

The individual processes of the internal energy exchange are assigned to the corresponding energy conservation equations as follows [14, 12]:

- the rate of change of vibrational energy due to internal energy exchange:

$$\left(\frac{\partial E_{\mathrm{vib}}}{\partial t}\right)_{\mathrm{int}} = \dot{Q}_{\mathrm{vib\text{-}tr}} + \dot{Q}_{\mathrm{vib\text{-}rot}} + \dot{Q}_{\mathrm{vib\text{-}e}} + \dot{Q}^{\mathrm{R}}_{\mathrm{vib}} \ , \tag{3.80}$$

- the rate of change of electron-electronic energy due to internal energy exchange:

$$\left(\frac{\partial E_{\mathrm{e}}}{\partial t}\right)_{\mathrm{int}} = \dot{Q}_{\mathrm{rot\text{-}tr}} + \dot{Q}_{\mathrm{tr\text{-}e}} - \dot{Q}_{\mathrm{vib\text{-}e}} + \dot{Q}^{\mathrm{R}}_{\mathrm{el}} + \dot{Q}^{\mathrm{R}}_{\mathrm{e,tr}} + \dot{Q}^{\mathrm{D}}_{\mathrm{e,tr}} + \dot{Q}^{\mathrm{I}}_{\mathrm{e,tr}} \ . \tag{3.81}$$

3.3 Electrodynamic Modelling

In the frame of this work, the response of the partially ionized fluid to the electromagnetic fields is represented via the Joule heating $\dot{Q}_{\text{Joule}}$ and the Lorentz force $\mathbf{F}_{\text{Lorentz}}$. Both physical phenomena significantly influence the system under investigation and are the last two quantities that still need to be calculated to close the system of governing equations described in Sec. 3.2.1.

Three additional vector fields are introduced to the physical model in order to obtain the two unknown $\dot{Q}_{\text{Joule}}$ and $\mathbf{F}_{\text{Lorentz}}$, namely the electric field $\mathbf{E}$, the magnetic field $\mathbf{B}$, and the current density $\mathbf{J}$. $\mathbf{E}$ and $\mathbf{B}$ are governed by solving the Maxwell's equations described in Sec. 3.3.1. The current density $\mathbf{J}$ is calculated by means of the generalized Ohm's law discussed in Sec. 3.3.2. The electrodynamic modelling is significantly simplified by means of the MHD approximation, the magnetostatic approximation and the potential formulation of Maxwell's equations.

3.3.1 Maxwell's Equations

Common Form of Maxwell's Equations and Force Law

The system of Maxwell's equations together with the force law represent the entire theoretical content of classical electrodynamics [49]. These equations describe how electric charges and currents in vacuum or continuum are related to electromagnetic fields. The Maxwell's equations in their differential form are given as follows [49]:

$$\boldsymbol{\nabla} \cdot \mathbf{E} = \frac{1}{\varepsilon_0}\rho^{\text{c}} \qquad \text{Gauss's law,} \tag{3.82}$$

$$\boldsymbol{\nabla} \cdot \mathbf{B} = 0 \qquad \text{no name,} \tag{3.83}$$

$$\boldsymbol{\nabla} \times \mathbf{E} = -\frac{\partial \mathbf{B}}{\partial t} \qquad \text{Faraday's law,} \tag{3.84}$$

$$\boldsymbol{\nabla} \times \mathbf{B} = \mu_0 \mathbf{J} + \mu_0 \varepsilon_0 \frac{\partial \mathbf{E}}{\partial t} \qquad \text{Ampère's law with Maxwell's correction.} \tag{3.85}$$

The force law describes a force on a charged particle which is moving with velocity $\mathbf{u}$ and is subject to electric and magnetic fields. When charged particles are summarized over a unit volume, the volumetric-force law can be written in terms of charge density ρ^{c}, given in $\text{C} \cdot \text{m}^{-3}$, as follows [59]:

$$\mathbf{F} = \rho^{\text{c}} \left(\mathbf{E} + \mathbf{u} \times \mathbf{B} \right) = \rho^{\text{c}} \mathbf{E} + \mathbf{J} \times \mathbf{B} \; . \tag{3.86}$$

The Gauss's law in Eq. 3.82 states that the flux of the electric field $\mathbf{E}$ through a closed surface is proportional to the charge inside the volume surrounded by this surface [49]. A corresponding law for the magnetic field $\mathbf{B}$ is shown in Eq. 3.83. It states that the flux of the magnetic field through a closed surface is zero, meaning that there exist no magnetic charges (monopoles) [49].

The Faraday's law in Eq. 3.84 states that a temporally changing flux of the magnetic field induces electric vortex fields.

The Ampère's law in Eq. 3.85 states that an electrical current induces a magnetic field. The second term on the right hand side of Eq. 3.85 is called displacement current. It was not included in the original form of Ampère's law and was introduced by Maxwell in order to take into account the effect of nonsteady currents. For steady currents (magnetostatic case) the Maxwell's term becomes zero.

The charge conservation equation is taken into account in Maxwell's equations automatically and is defined as follows [49]:

$$\boldsymbol{\nabla} \cdot \mathbf{J} = -\frac{\partial \rho^{\mathrm{c}}}{\partial t} \ . \tag{3.87}$$

It can be derived from the Ampère's law by applying the divergence operator to it.

The total electric field $\mathbf{E}$ can be decomposed into the electrostatic field $\mathbf{E}_{\mathrm{st}}$ and the electric field $\mathbf{E}_{\mathrm{ind}}$ induced due to the change of the magnetic field [59]:

$$\mathbf{E} = \mathbf{E}_{\mathrm{st}} + \mathbf{E}_{\mathrm{ind}} \ . \tag{3.88}$$

In the system under investigation $\mathbf{E}_{\mathrm{st}}$ arises due to the voltage drop on the electrodes. Taking into account this fact, Gauss's law together with Faraday's law give the following information about these two fields [59]:

$$\boldsymbol{\nabla} \cdot \mathbf{E}_{\mathrm{st}} = \frac{1}{\varepsilon_0} \rho^{\mathrm{c}} \ \text{ and } \ \boldsymbol{\nabla} \times \mathbf{E}_{\mathrm{st}} = 0 \ , \tag{3.89}$$

which means that the electrostatic field is the one which arises due to electric charges and is irrotational. For the induced electric field, the following applies [59]:

$$\boldsymbol{\nabla} \cdot \mathbf{E}_{\mathrm{ind}} = 0 \ \text{ and } \ \boldsymbol{\nabla} \times \mathbf{E}_{\mathrm{ind}} = -\frac{\partial \mathbf{B}}{\partial t} \ , \tag{3.90}$$

meaning that the induced electric vortex field has zero divergence. However, this field is the one that arises due to a temporally changing flux of the magnetic field and thus has a finite curl [59]. The Faraday's law reduces to $\boldsymbol{\nabla} \times \mathbf{E} = 0$ in the static case, meaning when $\mathbf{B}$ remains constant over time [49].

The magnetic field $\mathbf{B}$ includes both the imposed and the induced magnetic fields. In the system under investigation no external magnetic field is imposed, thus only the induced magnetic field is considered.

Maxwell's Equations in Matter

When the electromagnetic field penetrates matter, electric and magnetic polarizations occur, causing so called bound charges and currents in the substance. In the usual form of Maxwell's equations given in Eqs. 3.82 - 3.85, these bound charges and currents are not distinguished from free charges and currents. However, in a physical system, only free charges and currents can be controlled directly. That's why a more

convenient form of Maxwell's equations is usually used for calculations in matter, where a distinction between bound and free charges and currents is made [49].

For bringing Maxwell's equations into this more convenient form, only Gauss's and Ampère's laws, depicted in Eqs. 3.82 and 3.85, have to be modified, while Eqs. 3.83 and 3.84 remain unchanged [49]:

$$\boldsymbol{\nabla} \cdot \mathbf{D} = \rho_{\mathrm{f}}^{\mathrm{c}} \qquad \text{Gauss's law,} \tag{3.91}$$

$$\boldsymbol{\nabla} \times \mathbf{H} = \mathbf{J}_{\mathrm{f}} + \frac{\partial \mathbf{D}}{\partial t} \qquad \text{Ampère's law with Maxwell's correction.} \tag{3.92}$$

The electric displacement $\mathbf{D}$ in Eq. 3.91 is a vector field and is defined as [49]:

$$\mathbf{D} = \varepsilon \mathbf{E} = \varepsilon_0 \underbrace{(1 + \chi_e)}_{\varepsilon_{\mathrm{r}}} \mathbf{E} = \varepsilon_0 \varepsilon_{\mathrm{r}} \mathbf{E} = \varepsilon_0 \mathbf{E} + \underbrace{\varepsilon_0 \chi_e \mathbf{E}}_{\mathbf{P}} = \varepsilon_0 \mathbf{E} + \mathbf{P} \ . \tag{3.93}$$

The constant ε_0 in Eq. 3.93 is electric permittivity of free space which has a value of $\varepsilon_0 = 8.854187817... \times 10^{-12}\ \mathrm{F \cdot m^{-1}}$. The relative permittivity ε_{r}, also known as dielectric constant, is dimensionless and gives a ratio between the electric permittivity of the material ε and the permittivity of free space: $(\varepsilon_{\mathrm{r}} = \varepsilon/\varepsilon_0)$. The relative permittivity is related to the electric susceptibility χ_e as it shown in Eq. 3.93. The electric polarization $\mathbf{P}$ is a vector field and defines the dipole moment per unit volume of the polarized material. The polarization is induced by the external electric field $\mathbf{E}$ which lines up each atomic or molecular dipoles in the material along the electric-field lines [49]. By applying Eq. 3.93 on Eq. 3.91 the Gauss's law can be rewritten as:

$$\underbrace{\boldsymbol{\nabla} \cdot \varepsilon_0 \mathbf{E}}_{\rho^{\mathrm{c}}} + \underbrace{\boldsymbol{\nabla} \cdot \mathbf{P}}_{-\rho_{\mathrm{b}}^{\mathrm{c}}} = \rho_{\mathrm{f}}^{\mathrm{c}} \ , \tag{3.94}$$

where ρ^{c}, $\rho_{\mathrm{b}}^{\mathrm{c}}$, and $\rho_{\mathrm{f}}^{\mathrm{c}}$ denote total, bound and free charge densities, respectively.

Analogically to the electric displacement $\mathbf{D}$ in Eq. 3.93, the auxiliary field $\mathbf{H}$ is introduced to Ampère's law in Eq. 3.92 which permits to distinguish bound from free current ($\mathbf{J}_{\mathrm{b}}$ from $\mathbf{J}_{\mathrm{f}}$) in the physical system. The relationship between the magnetic field $\mathbf{B}$ and the auxiliary field $\mathbf{H}$ is given as follows [49]:

$$\mathbf{B} = \mu \mathbf{H} = \mu_0 \underbrace{(1 + \chi_m)}_{\mu_{\mathrm{r}}} \mathbf{H} = \mu_0 \mu_{\mathrm{r}} \mathbf{H} = \mu_0 \mathbf{H} + \mu_0 \underbrace{\chi_m \mathbf{H}}_{\mathbf{M}} = \mu_0 \mathbf{H} + \mu_0 \mathbf{M} \ , \tag{3.95}$$

hence the auxiliary field is defined as [49]:

$$\mathbf{H} = \frac{1}{\mu_0} \mathbf{B} - \mathbf{M} \ . \tag{3.96}$$

The magnetization $\mathbf{M}$ in Eq. 3.96 is a vector field and is analogous to the polarization $\mathbf{P}$ in Eq. 3.93. The permeability of free space μ_0 is a constant of a value of: $\mu_0 = 4\pi \times 10^{-7}\ \mathrm{H \cdot m^{-1}}$ [49]. The magnetic susceptibility χ_m is substance-dependent and gives the value of the relative permeability μ_{r} and thus the value of the permeability

of the substance defined as: $\mu = \mu_0 \mu_\mathrm{r}$. A relation between Eq. 3.85 and Eq. 3.92 can be established by substituting Eqs. 3.93 and 3.95 into Eq. 3.85 and dividing by μ_0:

$$\boldsymbol{\nabla} \times \mathbf{H} = \mathbf{J} - \underbrace{\boldsymbol{\nabla} \times \mathbf{M}}_{\mathbf{J}_\mathrm{b}} - \underbrace{\frac{\partial \mathbf{P}}{\partial t}}_{\mathbf{J}_\mathrm{p}} + \frac{\partial \mathbf{D}}{\partial t} \ , \tag{3.97}$$

whereby the free current $\mathbf{J}_\mathrm{f}$ is calculated by subtracting bound current and polarization current from total current: $\mathbf{J}_\mathrm{f} = \mathbf{J} - \mathbf{J}_\mathrm{b} - \mathbf{J}_\mathrm{p}$.

Neglecting Matter-Polarization Effects

The relative permittivity in vacuum is $\varepsilon_\mathrm{r} = 1$, meaning that in vacuum $\varepsilon = \varepsilon_0$, which is not the case in the presence of matter. The relative permittivity of gases is very low compared to ε_r of solids and liquids. As an example, the value of ε_r for nitrogen at 1 bar and 293.15 K is $\varepsilon_\mathrm{r} = 1.00055$ and for hydrogen $\varepsilon_\mathrm{r} = 1.00025$. The relative permittivity of water on the other hand is $\varepsilon_\mathrm{r} = 80.1$ [49]. Under the assumption that in gases $\varepsilon_\mathrm{r} \approx 1$, the electric susceptibility χ_e becomes zero and consequently $\varepsilon \approx \varepsilon_0$.

Analogous to the electrical susceptibility, the magnetic susceptibility χ_m in gases is very low. For example, the susceptibility of nitrogen at 0.781 bar and 293.15 K is $\chi_m = -5.06 \times 10^{-9}$ and the one of oxygen at 1 bar and 293.15 K is $\chi_m = 1.9 \times 10^{-6}$ [49]. Under the assumption that in gases the magnetic susceptibility $\chi_m \approx 0$ the relative permeability becomes $\mu_\mathrm{r} \approx 1$ and consequently $\mu \approx \mu_0$.

By applying the above assumptions to Eqs. 3.93 and 3.97, the polarization $\mathbf{P}$ and the magnetization $\mathbf{M}$ become zero. As a result, the following applies to the electric displacement and the magnetic field: $\mathbf{D} = \varepsilon_0 \mathbf{E}$ and $\mathbf{B} = \mu_0 \mathbf{H}$. Consequently, the bound charge density $\rho_\mathrm{b}^\mathrm{c}$ in Eq. 3.94 becomes zero and thus the total charge density becomes $\rho^\mathrm{c} = \rho_\mathrm{f}^\mathrm{c}$. As a direct consequence of $\mathbf{M}$ being zero, the bound current $\mathbf{J}_\mathrm{b}$ also becomes zero. Furthermore, due to the assumption that $\varepsilon_0 \approx \varepsilon$ and $\mathbf{P} = 0$, the polarization current $\mathbf{J}_\mathrm{p}$ becomes zero too.

The assumptions $\varepsilon \approx \varepsilon_0$ and $\mu \approx \mu_0$ have the consequence that the Gauss's law in Eq. 3.91 can be left in its traditional form shown in Eq. 3.82, with the constraint that the matter is not polarized and thus $\rho^\mathrm{c} = \rho_\mathrm{f}^\mathrm{c}$. Likewise, Eqs. 3.85 and 3.92 become identical with the restriction that $\mathbf{J} = \mathbf{J}_\mathrm{f}$.

3.3.2 Generalized Ohm's Law

General Information on Generalized Ohm's Law

According to Mitchner and Kruger [16], the generalized Ohm's law describes how a current flows in a conducting fluid in response to electric and magnetic fields. This form of Ohm's law is used together with the so-called MHD approximation for calculations in partially ionized gases. The generalized Ohm's law can be derived by establishing a set of momentum conservation equations for electrons, ions, and neutral particles. It is worth to mention that the fore law shown in Eq. 3.86 emerges as the electromagnetic body force term in these momentum conservation equations

and thus lies behind the Ohm's law. By adding all momentum equations together and eliminating several terms via appropriate assumptions the generalized Ohm's law for partially ionized gases is obtained [16]:

$$\mathbf{J} = \sigma \left(\mathbf{E} + \mathbf{u} \times \mathbf{B} + \frac{1}{n_e e} \boldsymbol{\nabla} p_e - \frac{B}{n_e e} \mathbf{J} \times \mathbf{b} \right) - s\mathbf{b} \times (\mathbf{J} \times \mathbf{b}) \ . \tag{3.98}$$

In this form, it applies to most conditions of interest involving collision-dominated plasmas [16]. The derivation of Eq. 3.98 is extensively described in Mitchner and Kruger [16]. The vector $\mathbf{b}$ is defined as: $\mathbf{b} = \mathbf{B}/B$ where B is the magnitude of the magnetic field. The quantity s denotes the ion slip factor. The electrical conductivity σ is often estimated by the so-called mean free path formula such that [16]:

$$\sigma = \mu_e n_e e = \frac{n_e e^2}{m_e \overline{\nu}_{ehp}} \ , \tag{3.99}$$

where the electron mobility μ_e is given as [16]:

$$\mu_e = \frac{e}{m_e \overline{\nu}_{ehp}} \ . \tag{3.100}$$

The quantity $\overline{\nu}_{ehp}$ is the average electron heavy-particle collision frequency. According to Mitchner and Kruger [16], the method of calculating σ given in Eq. 3.99 is generally accurate within a factor of two or three. In this work, a more advanced method for the calculation of σ is used (see Eq. 3.48). However, Eq. 3.99 is normally used to verify the applicability of the generalized Ohm's Law to the system under investigation. By using Eqs. 3.99 and 3.100, Eq. 3.98 can be rewritten as follows:

$$\mathbf{J} = \underbrace{\sigma \left(\mathbf{E} + \mathbf{u} \times \mathbf{B} \right)}_{\text{electromagnetic term}} + \underbrace{\mu_e \boldsymbol{\nabla} p_e}_{\substack{\text{electron-} \\ \text{pressure term}}} - \underbrace{\beta_e \mathbf{J} \times \mathbf{b}}_{\text{Hall term}} - \underbrace{s\mathbf{b} \times (\mathbf{J} \times \mathbf{b})}_{\text{ion-slip term}} \ . \tag{3.101}$$

The electron Hall parameter β_e is given such that [16]:

$$\beta_e = \frac{\sigma}{e n_e} B = \frac{\omega_e}{\overline{\nu}_{ehp}} \ , \tag{3.102}$$

where the electron cyclotron frequency is given as [16]:

$$\omega_e = \frac{e \ B}{m_e} \ . \tag{3.103}$$

The average electron heavy-particle collision frequency is composed of electron-ion and electron-neutral collision frequencies as follows: $\overline{\nu}_{ehp} = \overline{\nu}_{ei} + \overline{\nu}_{en}$. The electron-electron collisions would also interrupt the gyrations of electrons, but by definition $\overline{\nu}_{ee}$ is not included in the average electron heavy-particle collision frequency. This affects the interpretation of β_e by at most a factor of two [16].

Later in this section, it is proved that the last three terms on the right hand side of Eq. 3.101 can be neglected, reducing the generalized Ohm's law to the following expression:

$$\mathbf{J} = \sigma \left(\mathbf{E} + \mathbf{u} \times \mathbf{B} \right) \ . \tag{3.104}$$

Applicability of Generalized Ohm's Law

The first two conditions that a system must fulfil in order to be able to use the generalized Ohm's law for the calculation of **J** are the continuum description and the quasineutrality condition. Both assumptions are examined for their validity in Sec. 2.3 and hold for the system under investigation.

The third condition implies that the characteristic time t_c for the macroscopic change is sufficiently large such that [16]:

$$t_\mathrm{c} \gg \frac{\overline{\nu}_{ehp}}{\omega_\mathrm{p}^2} \ , \tag{3.105}$$

where the characteristic angular plasma frequency is given by the expression:

$$\omega_\mathrm{p}^2 = \left(\frac{n\ e^2}{\varepsilon_0 m_e} \right) \ . \tag{3.106}$$

The values of $\overline{\nu}_{ehp}$ at $T_\mathrm{c} = 12{,}000$ K are already calculated for the validation of the continuum assumption in Sec. 2.3.2 and amount to: $\overline{\nu}_{ehp} \approx 3.0 \times 10^{11}$ s^{-1}. The total number density n at $\overline{\nu}_{ehp}$ is taken from [37] and is $n \approx 5.9 \times 10^{23}$ m^{-3}. This results in the following value for the plasma frequency: $\omega_\mathrm{p}^2 = 1.875 \times 10^{27}$ s^{-1}. For the condition in Eq. 3.105, the following inequality results: $1.0 \times 10^{-6} \gg 1.60 \times 10^{-16}$. Thus, this condition is considered to be valid.

The fourth condition for the generalized Ohm's law to be applicable is [16]:

$$t_\mathrm{c} \gg \overline{\nu}_{ehp}^{-1} \ , \tag{3.107}$$

which is clearly fulfilled since $\overline{\nu}_{ehp}^{-1}$ is approximately 3.33×10^{-12} s which is much smaller than the characteristic time ($t_\mathrm{c} = 1.0 \times 10^{-6}$ s).

The last condition that must be satisfied is [16]:

$$t_\mathrm{c} \gg \left(\overline{\nu}_{in} + \overline{\nu}_{ni} \right)^{-1} \ . \tag{3.108}$$

The values of $\overline{\nu}_{\mathrm{NN^+}}$ and $\overline{\nu}_{\mathrm{N^+N}}$ are already calculated in Sec. 2.3.2 and for $T_\mathrm{c} = 12{,}000$ K they amount to: 6.63×10^8 s^{-1} and 4.69×10^9 s^{-1}. From Eq. 3.108, it follows: $1.0 \times 10^{-6} \gg 1.87 \times 10^{-10}$. Thus, all conditions are satisfied and the generalized Ohm's law is applicable for the system under investigation.

Neglecting the Electron-Pressure Term

The second term on the right hand side of Eq. 3.101 is the electron-pressure term. It defines the current density due to electron pressure gradient. It can be set in relation to the current density caused by the electrostatic field $\mathbf{E}_\mathrm{st}$. The electron pressure can be calculated as follows: $p_e = n_e k_\mathrm{B} T_\mathrm{e}$. This results in the following ratio [13]:

$$\frac{\mu_e \boldsymbol{\nabla} p_e}{\sigma \mathbf{E}_\mathrm{st}} = \frac{\boldsymbol{\nabla} p_e}{n_e e \mathbf{E}_\mathrm{st}} \sim \frac{n_e k_\mathrm{B} T_\mathrm{e}}{l_\mathrm{c} n_e e E_\mathrm{st}} = \frac{k_\mathrm{B} T_\mathrm{e}}{l_\mathrm{c} e E_\mathrm{st}} \ . \tag{3.109}$$

By assuming for both E_st and T_e the characteristic values given in Tab. 2.2, the ratio value amounts to 0.0517, which is much less than unity. Therefore, the electron pressure term is neglected in the present work.

Neglecting the Hall Term

The Hall current flows in the direction perpendicular to both the electric and magnetic fields [16]. In a system in which no exterior magnetic fields are imposed and only induced magnetic fields occur, this current can be neglected if the electron Hall parameter β_e is much less than unity. For the estimation of β_e the characteristic value of the induced magnetic field magnitude is used:

$$\beta_e = \frac{e\ B_\mathrm{c}}{m_e \overline{\nu}_{ehp}} \approx 0.00937\ , \tag{3.110}$$

which is much less than unity. From the definition of the Hall parameter it is clear that the magnetic field induction should be rather high to have an appreciable effect on the dynamics of the gas discharge [13]. Thus, the Hall term can be neglected.

Neglecting the Ion-Slip Term

The ion-slip factor s in the ion slip term is defined as follows [16]:

$$s = \left(\frac{\rho_n}{\rho}\right)^2 \beta_e \beta_i\ , \tag{3.111}$$

where β_e is already estimated above. The ion Hall parameter is given by:

$$\beta_i = \frac{e\ B_\mathrm{c}}{\overline{\mu}_{in} \overline{\nu}_{in}}\ . \tag{3.112}$$

At $T_\mathrm{c} = 12{,}000\ K$ the nitrogen plasma consists mostly of N and N^+ and thus the reduced mass amounts to $\overline{\mu}_{in} \approx \frac{1}{2} m_\mathrm{N} = 1.16 \times 10^{-26}\ kg$. The value of $\overline{\nu}_{\mathrm{N^+N}}$ is estimated at $6.63 \times 10^8\ \mathrm{s}^{-1}$. By using these values, the ion Hall parameter is estimated at: $\beta_i = 3.32 \times 10^{-4}$. The ratio $(\rho_n/\rho)^2$ is calculated by using the ideal gas law and the number densities $n_\mathrm{N}^+ = 6.5 \times 10^{22}\ \mathrm{m}^{-3}$ and $n_\mathrm{N} = 4.6 \times 10^{23}\ \mathrm{m}^{-3}$ and amounts to approximately ≈ 0.76. By inserting all these values into Eq. 3.111, the ion-slip factor s is estimated at 2.36×10^{-6}, which is much less than unity and thus the ion-slip term is neglected.

Significance of the Induction Current

Finally, it should be investigated whether the induction current which occurs due to the movement of the conductive fluid in an induced magnetic field ($\mathbf{J} = \sigma\,(\mathbf{u} \times \mathbf{B})$), is significant compared to the current generated by the electrostatic field ($\mathbf{J} = \sigma \mathbf{E}_{st}$). The ratio of both currents results in:

$$\frac{\sigma\,(\mathbf{u} \times \mathbf{B})}{\sigma \mathbf{E}_\mathrm{st}} \sim \frac{u_\mathrm{c} B_\mathrm{c}}{E_\mathrm{c}} = 0.008\ . \tag{3.113}$$

That is, the current arising due to electrostatic field is much larger and thus the induced current may be neglected for the system under investigation:

$$\mathbf{J} = \sigma \mathbf{E} + \underbrace{\sigma\,(\mathbf{u} \times \mathbf{B})}_{\approx 0} \approx \sigma \mathbf{E}\ , \tag{3.114}$$

which is basically the form of the Ohm's law for stationary conductors.

3.3.3 Verification of the MHD Approximation

In this work, the so-called MHD approximation is used to simplify the Maxwell's equations. The use of this approximation presumes the applicability of the generalized Ohm's law, which is proved in Sec. 3.3.2.

The assumption of quasineutrality ($\rho^{\mathrm{c}} \simeq 0$) allows to simplify of the Gauss's law and the charge conservation equation to the following expressions [16]:

$$\boldsymbol{\nabla} \cdot \mathbf{E} = 0 \quad \text{and} \quad \boldsymbol{\nabla} \cdot \mathbf{J} = 0 \ . \tag{3.115}$$

This is due to the fact that in a volume of a radius much larger than the Debye length, the positive and negative charges cancel each other, making the fluid in this volume behaving as neutral matter.

Now it should be investigated if it is possible to neglect the displacement current compared to the conduction current. Using the assumption $\varepsilon \approx \varepsilon_0$, the displacement current $\partial\mathbf{D}/\partial t$ in Eq. 3.92 becomes $\varepsilon_0 \partial\mathbf{E}/\partial t$, that is, identical to the traditional form of the Ampère's law in Eq. 3.85. The ratio of the displacement current to the conduction current $\mathbf{J} = \sigma\mathbf{E}$ which occurs due to the electrostatic field, becomes [16]:

$$\frac{\partial\mathbf{D}/\partial t}{\mathbf{J}} = \varepsilon_0 \frac{\partial\mathbf{E}/\partial t}{\sigma\mathbf{E}} \sim \frac{\varepsilon_0 E_{\mathrm{c}}}{t_{\mathrm{c}} \sigma E_{\mathrm{c}}} = \frac{\varepsilon_0}{t_{\mathrm{c}}\sigma} \ . \tag{3.116}$$

Hence, the displacement current may be neglected if the following restriction applies:

$$t_{\mathrm{c}} \gg \frac{\varepsilon_0}{\sigma} \ . \tag{3.117}$$

When the so-called mean free path formula (see Eq. 3.99) is used for the calculation of σ, the above condition may be rewritten as:

$$t_{\mathrm{c}} \gg \frac{\overline{\nu}_{ehp}}{\omega_{\mathrm{p}}^2} \ , \tag{3.118}$$

which is the same condition as in Eq. 3.105 used for validating the applicability of the generalized Ohm's law. It has already been proven that this condition applies and the displacement current can be neglected, reducing the Ampère's law to [16]:

$$\boldsymbol{\nabla} \times \mathbf{B} = \mu_0 \mathbf{J} \ . \tag{3.119}$$

The MHD approximation and the use of the simplified generalized Ohm's law lead to the following set of simplified Maxwell's equations:

$$\boldsymbol{\nabla} \cdot \mathbf{E} = 0 \qquad \text{Gauss's law,} \tag{3.120}$$

$$\boldsymbol{\nabla} \cdot \mathbf{B} = 0 \qquad \text{no name,} \tag{3.121}$$

$$\boldsymbol{\nabla} \times \mathbf{E} = -\frac{\partial\mathbf{B}}{\partial t} \qquad \text{Faraday's law,} \tag{3.122}$$

$$\boldsymbol{\nabla} \times \mathbf{B} = \mu_0 \mathbf{J} \qquad \text{Ampère's law,} \tag{3.123}$$

$$\boldsymbol{\nabla} \cdot \mathbf{J} = 0 \qquad \text{charge conservation,} \tag{3.124}$$

$$\mathbf{J} = \sigma\mathbf{E} \qquad \text{Ohm's law.} \tag{3.125}$$

3.3.4 Verification of the Magnetostatic Approximation

In the system under investigation direct current is used to sustain the gas discharge. According to Griffiths [49], steady currents produce magnetic fields that are constant in time. Thus, the induced magnetic field is static in the area surrounding the current-carrying fluid region. This assumption is called magnetostatics and represents a suitable approximation even for fluctuating currents, provided that the current varies very slowly with time. As a consequence, the term $-\frac{\partial \mathbf{B}}{\partial t}$ in the Faraday's law can be neglected and this law reduces to:

$$\boldsymbol{\nabla} \times \mathbf{E} = 0 \ . \tag{3.126}$$

Actually, the term $-\frac{\partial \mathbf{B}}{\partial t}$ represents the only remaining coupling between electric and magnetic fields in Eqs. 3.120 - 3.123, since the displacement current in the Ampère's law is already neglected. By neglecting $-\frac{\partial \mathbf{B}}{\partial t}$, the Maxwell's equations of electrostatics become completely decoupled from the Maxwell's equations of magnetostatics [49]:

$$\boldsymbol{\nabla} \times \mathbf{E} = 0 \ , \quad \boldsymbol{\nabla} \cdot \mathbf{E} = \underbrace{\rho^{\mathrm{c}}/\varepsilon_0}_{\text{here} \approx 0} \quad \text{-Maxwell's equations of electrostatics;} \tag{3.127}$$

$$\boldsymbol{\nabla} \times \mathbf{B} = \mu_0 \mathbf{J} \ , \quad \boldsymbol{\nabla} \cdot \mathbf{B} = 0 \qquad \text{-Maxwell's equations of magnetostatics.} \tag{3.128}$$

Thus, for the given physical system only four equations would suffice to obtain the electromagnetic fields and the current density, namely:

$$\boldsymbol{\nabla} \cdot \mathbf{B} = 0 \ , \quad \boldsymbol{\nabla} \times \mathbf{B} = \mu_0 \mathbf{J} \ , \quad \boldsymbol{\nabla} \cdot \mathbf{J} = 0 \ , \quad \mathbf{J} = \sigma \mathbf{E} \ . \tag{3.129}$$

In the following, the applicability of the magnetostatic assumption for the system under investigation is verified. For this, it is assumed that the induced magnetic field alternate with the characteristic time t_{c}. According to Eqs. 3.89 and 3.90, only the induced electric field $\mathbf{E}_{\mathrm{ind}}$ arises due to changing magnetic field $\mathbf{B}$. The magnitude of the externally imposed electrostatic field $\mathbf{E}_{\mathrm{st}}$ is given by E_{c}. The magnitude of the induced magnetic field is B_c (see Tab. 2.2). By using the Faraday's law, the approximate value of $\mathbf{E}_{\mathrm{ind}}$ may be obtained by:

$$\frac{E_{\mathrm{ind}}}{l_{\mathrm{c}}} \sim -\frac{B_{\mathrm{c}}}{t_{\mathrm{c}}} \ \text{ and thus } \ |E_{\mathrm{ind}}| \sim \frac{B_{\mathrm{c}} l_{\mathrm{c}}}{t_{\mathrm{c}}} \ . \tag{3.130}$$

The comparison of the induced and electrostatic electric fields yields:

$$\frac{B_{\mathrm{c}} l_{\mathrm{c}}}{t_{\mathrm{c}} E_{\mathrm{c}}} = 0.002 \ , \tag{3.131}$$

which means that the temporal fluctuations of $\mathbf{B}$ have to be rather fast to have an appreciable effect on the dynamics of the physical system under investigation.

3.3.5 Potential Expression

The number of Maxwell's equations shown in Eqs. 3.120 - 3.123 can be reduced by representing electromagnetic fields in terms of electromagnetic potentials.

Electric and Magnetic Potentials

The electric field $\mathbf{E}$ can be expressed in terms of a scalar potential as follows [49]:

$$\mathbf{E} = -\boldsymbol{\nabla}\Phi \ , \tag{3.132}$$

where the minus sign is purely conventional. In this way, the vector quantity $\mathbf{E}$ reduces to a scalar quantity Φ called the electric potential.

The magnetic field $\mathbf{B}$ can be represented by a vector potential as follows [49]:

$$\mathbf{B} = \boldsymbol{\nabla} \times \mathbf{A} \ . \tag{3.133}$$

It is important to mention that although the divergence of $\mathbf{B}$ is always zero, the curl of the electric field $\mathbf{E}$ is non-zero in the original (unreduced) version of the Faraday's law (see Eq. 3.122). That is, for systems in which the magnetic induction in the Faraday's law cannot be neglected, the potential expression shown in Eq. 3.132 is not applicable. Instead, the following potential expression must be used for the electric field:

$$\mathbf{E} = -\boldsymbol{\nabla}\Phi - \frac{\partial \mathbf{A}}{\partial t} \ .$$

More information on the potential expression can be found in Griffiths [49].

Potential Expression of Maxwell's Equations

Since the curl of a gradient of a scalar field is always zero ($\boldsymbol{\nabla} \times (\boldsymbol{\nabla}\Phi) = 0$), the Gauss's law in Eq. 3.120 is automatically fulfilled. Likewise, since the divergence of a curl is always zero, the potential formulation of $\mathbf{B}$ automatically satisfies Eq. 3.121. Furthermore, the Gauss's law can now be replaced by the charge conservation equation given in Eq. 3.124, since the electric field and the current density are directly related to each other by the Ohm's law (see Eq. 3.125). Thus, only the Ampère's law and the charge conservation equation have to be brought into the potential form.

The charge conservation equation is brought into the potential form by replacing the current density $\mathbf{J}$ with the help of the Ohm's law by $\sigma\mathbf{E}$. In the next step, the electric field is expressed in terms of a scalar potential, leading to the following Laplace's equation:

$$\boldsymbol{\nabla} \cdot (\sigma \boldsymbol{\nabla}\phi) = 0 \ . \tag{3.134}$$

The same procedure is used to replace the current density in the Ampère's law. Additionally, by replacing $\mathbf{B}$ through the magnetic vector potential given in Eq. 3.133, the following expression is obtained for the Ampère's law [49]:

$$\boldsymbol{\nabla} \times \mathbf{B} = \boldsymbol{\nabla} \times (\boldsymbol{\nabla} \times \mathbf{A}) = \boldsymbol{\nabla} (\boldsymbol{\nabla} \cdot \mathbf{A}) - \boldsymbol{\nabla}^2 \mathbf{A} = \mu_0 \sigma \boldsymbol{\nabla}\phi \ . \tag{3.135}$$

It is mathematically possible to add to the magnetic potential any function whose curl vanishes without affecting $\mathbf{B}$. By using this rule, the term $\boldsymbol{\nabla} (\boldsymbol{\nabla} \cdot \mathbf{A})$ in Eq. 3.135 can be eliminated and the Ampère's law becomes [49]:

$$\boldsymbol{\nabla}^2 \mathbf{A} = \sigma \mu_0 \boldsymbol{\nabla}\phi \ , \tag{3.136}$$

which has a form of a Poisson's equation. Both Eq. 3.134 and Eq. 3.136 satisfy all electromagnetic equations of the MHD model given by Eqs. 3.120 - 3.124. That is, the equation system reduces to equations for solving the four variables A_x, A_y, A_z and Φ. This is a significant reduction in the number of equations compared to the electromagnetic equations of the MHD model described in Sec. 3.3.4. The equations are accomplished by the Ohm's law, given in Eq. 3.125. The electric and magnetic fields **E** and **B** are obtained by Eq. 3.132 and Eq. 3.133, respectively.

3.3.6 Joule Heating and Lorentz Force

Joule Heating

The Joule heating is evaluated by the following formula [13]:

$$\dot{Q}_{\text{Joule}} = \eta \left(\mathbf{J} \cdot \mathbf{E} \right) \ , \tag{3.137}$$

where η is the efficiency coefficient of the Joule-heating effect. This source term is included in the electron-electronic energy conservation equation (Eq. 3.18). Therefore, it directly influences the electron-electronic energy E_{e} and thus the temperature T_{e}. Via the system-internal energy exchange, the impact of $\dot{Q}_{\text{Joule}}$ on E_{e} is transmitted to E_{vib} and $E_{\text{tr-rot}}$. In this way, the Joule heating impacts on all three temperatures: T_{e}, T_{vib} and T. This process is marked with the number 1 in Fig. 3.3 where the coupling between the fluid dynamics and the electrodynamics via the Joule heating is represented schematically. Changes in temperatures are reflected in mass production rates

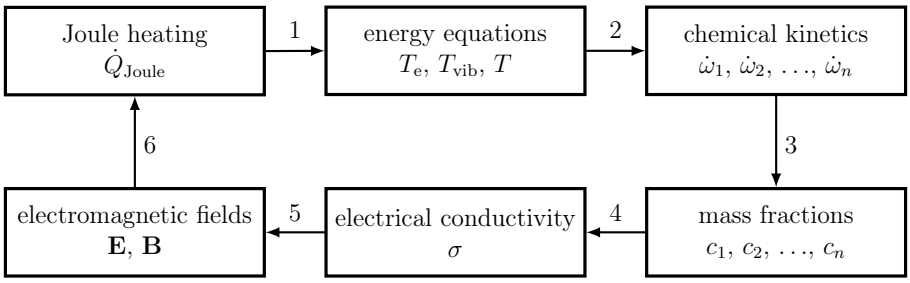

Figure 3.3: Coupling between electromagnetic fields and thermodynamic properties.

and, therefore, also in the mass concentrations of plasma constituents (Fig. 3.3, steps 2 and 3). Since the electrical conductivity σ of the gas is a function of the species composition and of T_{e}, σ would change as well. Since σ is included in the calculation of **E** and **B**, there is a mutual coupling between the electromagnetic fields and the thermodynamic properties of the system, because changes in the electromagnetic fields are reflected in the intensity of $\dot{Q}_{\text{Joule}}$ (steps 4, 5, and 6).

Lorentz Force

By using Eqs. 3.86 and 3.88, the force law can be written as [49]:

$$\mathbf{F} = \rho^{\mathrm{c}}\mathbf{E}_{\mathrm{st}} + \rho^{\mathrm{c}}\mathbf{E}_{\mathrm{ind}} + \mathbf{J} \times \mathbf{B} \ . \tag{3.138}$$

The first term $\rho^{\mathrm{c}}\mathbf{E}_{\mathrm{st}}$ represents the electrostatic force, also known as Coulomb force. The second term $\rho^{\mathrm{c}}\mathbf{E}_{\mathrm{ind}}$ arises due to a time-varying magnetic field. The third term $\rho^{\mathrm{c}}\mathbf{u}^{\mathrm{c}} \times \mathbf{B} = \mathbf{J} \times \mathbf{B}$ arises due to the motion of a conducting fluid in a magnetic field and is called Lorentz force [59].

The system under investigation is a DC discharge where a steady arc current can be assumed. A constant current induces a constant magnetic field and thus the term $\rho^{\mathrm{c}}\mathbf{E}_{\mathrm{ind}}$ can be neglected.

Furthermore, the Coulomb force has a negligible effect on the fluid motion. This can be demonstrated by comparing the Coulomb force with the inertial force necessary for a uniform deceleration of the fluid element with the volume V from a velocity magnitude u_{c} to 0 $\mathrm{m \cdot s^{-1}}$. The electrostatic and the inertial forces can be defined as follows: $\mathbf{F}_{\mathrm{Coulomb}} = \rho^{\mathrm{c}}\mathbf{E}_{\mathrm{st}}V$ and $\mathbf{F}_{\mathrm{inertial}} = \rho\mathbf{a}V \sim \rho V u_{\mathrm{c}}^2/2l_{\mathrm{c}}$, where $\mathbf{a}$ is the acceleration in $\mathrm{m \cdot s^{-2}}$ and u_{c} is the magnitude of the characteristic velocity of the fluid. The charge density ρ^{c} is estimated by using the Gauss's law in Eq. 3.82 as follows: $\rho^{\mathrm{c}} = \varepsilon_0 \boldsymbol{\nabla} \cdot \mathbf{E} \sim \varepsilon_0 E_{\mathrm{c}}/l_{\mathrm{c}}$. The characteristic values are given in Tab. 2.2 and the density of nitrogen at 1 bar and $T = T_{\mathrm{c}}$ is $\rho \approx 0.05$ $\mathrm{kg \cdot m^{-3}}$. The following value is obtained when putting both forces into a ratio [13]:

$$\frac{\mathbf{F}_{\mathrm{Coulomb}}}{\mathbf{F}_{\mathrm{inertial}}} \sim \frac{2\varepsilon_0 E_{\mathrm{c}}^2}{\rho u_{\mathrm{c}}^2} \approx 3.54 \times 10^{-8} \ . \tag{3.139}$$

Thus, the contribution of the Coulomb force is negligible. An analogous calculation is performed in the following for the Lorentz force:

$$\frac{\mathbf{F}_{\mathrm{Lorentz}}}{\mathbf{F}_{\mathrm{inertial}}} \sim \frac{2\sigma_{\mathrm{c}} E_{\mathrm{c}} B_{\mathrm{c}} l_{\mathrm{c}}}{\rho u_{\mathrm{c}}^2} \approx 5.63 \times 10^{-2} \ . \tag{3.140}$$

It can be seen, that the Lorentz force also has a rather minor effect on the free-stream flow. However, it is larger by several magnitudes than the Coulomb force. Thus, the Lorentz force completely dominates the force law.

Since the induced magnetic field depends on the current density and the current density in turn is a function of the electrostatic field (see Eq. 3.125), it seems to make sense to multiply the Lorentz force by the efficiency coefficient η:

$$\mathbf{F} \approx \mathbf{F}_{\mathrm{Lorentz}} = \eta \left(\mathbf{J} \times \mathbf{B} \right) \ . \tag{3.141}$$

The inertial force in the boundary layer is lower due to a lower velocity. Therefore, the Lorentz force could play a role there. For this reason, in the present work the Lorentz force is included in the momentum conservation equation Eq. 3.14.

3.4 Closing Remarks

The physicochemical model presented in this chapter is complete and can be used directly in the form it is presented. All equation systems represented in the physicochemical model are closed and all thermodynamic and transport properties as well as fluxes and source terms are represented by corresponding submodels. All listed data are given for the high-temperature nitrogen. For simulations of high-temperature oxygen or air, appropriate data can be taken from Dunn and Kang [25], Park [14], Gupta *et al.* [23], and Yos [22].

The physicochemical model is not only suitable for the simulation of high-pressure gas discharges, but generally for the modelling of high-temperature gases regardless of the field of application and irrespective of whether the gas is exposed to external electromagnetic fields or not. Thus, it could be used to simulate, for example, flows in a DC plasma torch as well as to simulate high-speed and high-enthalpy flows, as long as the MHD approximation is valid, the magnetostatic assumption is true, and the continuum conditions are met. The model is based on the one-fluid approximation and takes into account the chemical and thermal nonequilibria in the gas mixture. However, special attention should be paid to the validity of all assumptions and simplifications used in the model. This applies in particular to the assumption of the harmonic oscillator for calculating the vibrational energy. Furthermore, it should not be forgotten that turbulence modelling is not yet included in the model. Further, since rotational nonequilibrium may become significant under certain conditions, the assumption of the translational-rotational temperature must be considered with caution. The same applies to the assumption of the electron-electric temperature.

Chapter 4

Numerical Realization

This chapter is devoted to the numerical realization of the physicochemical model defined in Chapter 3. In Sec. 4.1 the software used for numerical implementation is introduced. Sec. 4.2 briefly explains the numerical implementation procedure. Since the software used is based on the finite volume method (FVM), Sec. 4.4 first gives a brief overview of FVM. Subsequently, in Sec. 4.4, the finite volume discretization techniques are explained in detail using the example of the generic conservation equation and the software used. Only the discretization and interpolation techniques used in this work are discussed. Finally, in Sec. 4.5, the solver developed in this work is described in detail.

4.1 Software Description

OpenFOAM is a finite volume based software package developed for numerical simulations of continuum mechanics problems [60]. This tool can be considered primarily as a collection of precompiled C++ libraries, from which executable files are created [61]. The OpenFOAM libraries are grouped into several subdirectories according to their scope of tasks. For example, there are libraries that provide the classes needed for finite volume discretization, libraries with memory management tools and with interpolation schemes, as well as mesh manipulation and post-processing libraries [61]. In the context of this thesis it is important to draw attention to the so-called model libraries which specify physical models. These libraries provide, for example, models for the calculation of thermodynamic and transport properties as well as radiation and turbulence calculation models.

The object classes contained in the OpenFOAM libraries can be regarded as building blocks from which executable files, so-called applications, are created. OpenFOAM already contains a large number of ready-made official applications that can be used directly. These applications can be divided into two main categories, namely utilities and solvers [61]. Utilities are designed to perform pre- and post-processing tasks. As far as numerical solvers are concerned, OpenFOAM does not have a generic solver capable of solving all classes of continuum mechanical problems, but rather a set of predefined solvers, each for a specific class of problems [61].

The object oriented C++ frame work of OpenFOAM allows to design new customized libraries, utilities and solvers [60]. This fact, together with the free availability of the software, are two main reasons for choosing this CFD tool for the present work.

4.2 Numerical Implementation Procedure

In the present work, a new numerical solver is developed together with the associated model library based on the OpenFOAM C++ libraries. In the following, the model library and the solver are discussed in more detail.

4.2.1 Development of the Model Library

The new model library is developed in the spirit of the ready-made official thermophysical OpenFOAM libraries. It consists of several object classes which can be divided into three modules:

- module containing classes for finite-rate chemical kinetics,
- module for the calculation of thermodynamic and transport variables,
- module with classes for complementary electrodynamic calculations.

Finite-Rate Chemical Kinetics Module

The classes contained in this module are, in principle, an extension of the original OpenFOAM classes from single-temperature to multi-temperature chemical kinetics. With their help, the contribution of chemistry in each control volume is represented via an independent matrix-vector system of ordinary differential equations (ODE). Each system of equations is solved iteratively by means of an ordinary differential equation solver (ODE solver). For this purpose, several variants of ODE solvers are available in OpenFOAM. The theory of the chemical kinetics module is described in Sec. 3.1. The numerical calculation of species production rates is based on the following equations: Eqs. 3.5, 3.6, 3.7, and 3.8. The coefficients required in Eq. 3.8 (see Tab. B.1) must be listed by the user in a particular file so that they can be read out during the calculation. The same applies to the data listed in Tab. 3.1.

Module for Calculation of Thermodynamic and Transport Variables

These classes are used to declare and initialize all variables required for thermo- and fluid dynamic calculations. Furthermore, the classes of the thermodynamic module contain calculation models for all necessary thermodynamic and transport properties as well as all energy exchange models. The implemented calculation models can be divided into three groups:

- **Models for thermodynamic relations**: These models relate changes in energies e_e, e_vib, and e, to changes in temperatures T_e, T_vib, and T, respectively.

Their numerical implementation is based on Eqs. 3.23 - 3.31, discussed in Sec. 3.2.2.

- **Calculation models for transport variables**: These models are used for the calculation of transport properties μ, σ, κ'_{vib}, κ'_{e}, κ_{tr}, κ_{rot}, and $\mathcal{D}_s$, as well as diffusion fluxes $\rho \mathbf{V}_s c_s$ and heat fluxes $\mathbf{q}_{\mathrm{vib}}$, $\mathbf{q}_{\mathrm{e}}$, and $\mathbf{q}$. The numerical implementation of these quantities is based on Eqs. 3.32 - 3.53, given in Sec. 3.2.3.
- **Calculation models for energy exchange**: These models are required for the calculation of all internal energy exchange processes that are summarized in Eqs. 3.80 and 3.81 under $\left(\frac{\partial E_{\mathrm{vib}}}{\partial t}\right)_{\mathrm{int}}$ and $\left(\frac{\partial E_{\mathrm{e}}}{\partial t}\right)_{\mathrm{int}}$ (see Sec. 3.2.5) as well as radiation losses $\dot{Q}_{\mathrm{rad}}$. The corresponding equations are Eqs. 3.60 - 3.79.

Module for Electrodynamic Calculations

The declaration and initialization of electrodynamic variables is executed with these classes. In addition, they provide calculation models for the Lorentz force $\mathbf{F}_{\mathrm{Lorentz}}$ and the Joule heating $\dot{Q}_{\mathrm{Joule}}$. The numerical implementation of these two physical phenomena is based on Eqs. 3.141 and 3.137.

The relations between the fields $\mathbf{E}$ and $\mathbf{B}$ and the potentials Φ and $\mathbf{A}$ are also defined in the electrodynamic module. They are given by Eqs. 3.132 and 3.133.

4.2.2 Development of the Solver

The new solver is based in part on two official OpenFOAM solvers, namely *reactingFoam* and *sonicFoam*. The solver *reactingFoam* is a multi-species solver developed for calculations of combustion with chemical reactions. The solver *sonicFoam* belongs to the compressible family of OpenFOAM solvers and is developed for the simulation of transient, subsonic, transonic, supersonic and turbulent flows [62]. It is a pressure-based, compressible solver which solves governing equations in a segregated manner.

For the development of the new solver, basic chemical features were first implemented in *sonicFoam* by incorporating parts of *reactingFoam* into it. This modification extended the capabilities of *sonicFoam* to simulations of chemically-reacting multi-species flows. In the next step, the thermodynamic part of *sonicFoam* was extended to multi-temperature approach to account for thermodynamic nonequilibrium in the gas. Finally, the new solver was extended by equations of magnetostatics to account for plasma responses to electric and magnetic fields.

4.3 General Comments on Finite Volume Method

Finite Volume Method (FVM) is a discretization method that approximates partial differential equations representing conservation laws by a system of algebraic equations for a set of discrete places in space and time [51, 60]. Other important

discretization methods are, for example, the finite difference method (FDM) and the finite element method (FEM).

The application of FVM requires a temporal discretization over the time axis as well as a spatial discretization of the solution area into finite volumes. Afterwards, the partial differential equations are transformed into algebraic equations by integrating them over a time interval and over each finite volume [60]. This procedure results in a large nonlinear algebraic equation system [51]. To obtain the solution, after discretization and linearisation, the system of linear equations is solved using an iterative technique (linear solver). In this way, the variables in the conservation laws are calculated in each discrete point of the solution area.

4.3.1 Spatial Discretization: Computational Grid

To spatially discretize the geometric region of interest, a numerical grid is created which divides the solution region into a limited number of discrete elements referred to as control volumes (CV). The centroids of each CV represent the computational nodes in which the variable values are calculated [51]. The geometry of the grid (also called computational mesh) defines the location of these discrete points. Some of the possible grid geometry options are: structured grids, block-structured grids, and unstructured grids. The finite volume method can be applied to any type of computational grids, which makes it suitable for complex geometries (for more information on this topic see Ferziger and Perić [51]).

4.3.2 Discretization of Partial Differential Equations

FVM uses the integral form of the conservation equations as a starting point [51]. The conservation equations are applied to each control volume and transformed into a set of algebraic equations by integrating them over each CV [60]. According to Moukalled *et al.* [60], this transformation involves two basic steps:

1. The partial differential equation is integrated over the CV and Gauss theorem is applied to transform the volume integrals of the convection and diffusion terms into surface integrals. Then, the integrated equation is transformed into a balance equation over a control volume by applying quadrature formulas, such as a Gaussian quadrature rule [51, 60]. The result is the so-called semi-discretized equation, which means that the equation is discretized in space, but not in time. The subsequent temporal discretization yields a discrete equation.

2. An interpolation procedure is used to approximate the variation of the variables within the control volume and on the CV's surfaces by the values in the CV centroids [60].

The result is a set of algebraic equations, each for one CV, where each equation contains the value of the dependent variable from its own control volume centroid and values from the centroids of adjacent or neighbouring CVs [51].

4.3.3 Solution of Linear Equation System

For the solution of the algebraic equation system, iterative solution algorithms are usually used. An iterative method starts with an estimated solution and uses the equation to systematically improve this solution [51]. If the differential equation to be discretized is nonlinear, its algebraic form will also contain some nonlinear terms. In such a case, successive linearisation of the algebraic equations is performed followed by the iterative solution of the linear equation system.

Explicit and Implicit Numerical Solution Schemes

It is generally possible to distinguish between explicit and implicit numerical solution schemes. A numerical method is said to be explicit when the dependent variable in each algebraic equation is computed via already known variable values from the last available solution. In an implicit method, however, all dependent variables are treated as unknowns and calculated via an iterative solution algorithm in a coupled set of equations for the current time step [60].

Simultaneous and Separate Solution Methods

The governing equations of fluid dynamics represent a system of coupled equations in which the dependent variable in one equation also occurs in some other equations. There are two types of solvers for such problems. In the first type, all equations for all variables are solved simultaneously. In the second type, each equation is solved separately for its own variable, assuming the other variables as known. The two methods are referred to as simultaneous and separate solution methods [51].

4.4 Finite Volume Discretization

Conservation equations of fluid dynamics contain terms that represent different physical processes. For example, the advectional process represented by the convective terms is highly directional, while the diffusion terms represent non-directional phenomena. For this reason, the individual terms in the conservation equations are discretized by using different methods in order to best mimic the underlying physics of each term.

This section explains the discretization process of the governing equations of fluid and electrodynamics using the example of the general conservation equation. For this purpose, the general conservation equation is first derived in Sec. 4.4.1. Afterwards, in Sec. 4.4.2 - 4.4.8, all the discretization schemes used in this work are presented and then applied to the general conservation equation to obtain an algebraic equation.

4.4.1 General Conservation Equation

All governing equations of fluid dynamics described in Sec. 3.2.1 are of the same structure. They all are given in their conservation and differential form and are

written in terms of intensive properties. By replacing these intensive properties with a generic intensive scalar/vector property ϕ, all of these governing equations may be described by the following general conservation equation [51]:

$$\frac{\partial \rho\phi}{\partial t} + \boldsymbol{\nabla} \cdot \underbrace{(\rho \mathbf{u} \phi)}_{\boldsymbol{\mathcal{F}}_{\phi}^{\mathrm{C}}} = \mathcal{T}_{\phi} \ . \tag{4.1}$$

The generic variable ϕ stands in the governing equations of fluid dynamics for the following intensive properties:

- $\phi = 1$ in the mass conservation equation,
- $\phi = \mathbf{u} = (u_x, u_y, u_z)^{\mathrm{T}}$ in the momentum conservation equation,
- $\phi = c_1, c_2, ..., c_n$ in the species conservation equation,
- $\phi = e_{\mathrm{e}}$ in the electron-electronic energy conservation equation,
- $\phi = e_{\mathrm{vib}}$ in the vibrational energy conservation equation,
- $\phi = e$ in the overall energy conservation equation.

The quantity $\mathcal{T}_{\phi}$ in Eq. 4.1 denotes all the transport mechanisms of ϕ, except the transport due to convection flux $\boldsymbol{\mathcal{F}}_{\phi}^{\mathrm{C}}$, as well as all sources and sinks [51]. The diffusive transport mechanisms are always present in a fluid. They can be represented by means of the diffusion flux as follows: $\mathcal{T}_{\phi}^{\mathrm{D}} = \boldsymbol{\nabla} \cdot \boldsymbol{\mathcal{F}}_{\phi}^{\mathrm{D}}$. The diffusion fluxes are usually described by the spatial gradient of the transport variable and the corresponding diffusion coefficient Γ^{ϕ} as follows: $\boldsymbol{\mathcal{F}}_{\phi}^{\mathrm{D}} = \Gamma^{\phi} \boldsymbol{\nabla} \phi$ [51]. Thus, Eq. 4.1 can be rewritten as [52, 60, 51]:

$$\underbrace{\frac{\partial \rho\phi}{\partial t}}_{\substack{\text{unsteady} \\ \text{term}}} + \underbrace{\boldsymbol{\nabla} \cdot (\rho \mathbf{u} \phi)}_{\substack{\text{convection} \\ \text{term}}} = \underbrace{\boldsymbol{\nabla} \cdot \left(\Gamma^{\phi} \boldsymbol{\nabla} \phi \right)}_{\substack{\text{diffusion} \\ \text{term}}} + \underbrace{\dot{Q}^{\phi}}_{\substack{\text{source} \\ \text{term}}} \ . \tag{4.2}$$

In the species conservation equation the diffusion term is described by the Fick's law as $\boldsymbol{\nabla} \cdot (\rho \mathrm{D}_s \boldsymbol{\nabla} c_s)$. In the momentum conservation equation, the transport mechanisms, denoted in Eq. 4.1 by $\mathcal{T}_{\phi}$, include pressure forces and forces due to viscous normal and shear stress and the Lorentz force (see Eqs. 3.13 and 3.14):

$$\mathcal{T}_{\mathbf{u}} = \boldsymbol{\nabla} \cdot \left[-p\boldsymbol{I} - \mu \frac{2}{3} \left(\boldsymbol{\nabla} \cdot \mathbf{u} \right) \boldsymbol{I} + \mu \boldsymbol{\nabla} \otimes \mathbf{u} + \mu \left(\boldsymbol{\nabla} \otimes \mathbf{u} \right)^{\mathrm{T}} \right] + \mathbf{F}_{\mathrm{Lorentz}} \ .$$

The diffusion term is then: $\mathcal{T}_{\mathbf{u}}^{\mathrm{D}} = \boldsymbol{\nabla} \cdot (\mu \boldsymbol{\nabla} \otimes \mathbf{u})$, where $\Gamma^{\mathbf{u}} = \mu$. The rest of the mechanisms may be assigned to the source term $\dot{Q}^{\mathbf{u}}$ [60]. The same procedure can be performed for each of the three energy conservation equations (Eqs. 3.17, 3.18, and 3.19), where the transport mechanisms denoted in Eq. 4.1 by $\mathcal{T}_{\phi}$ include, besides source terms, the rate of work due to surface forces. The thermal diffusion can be then described by the Fourier's law as follows [51]: $\mathcal{T}_{e}^{\mathrm{D}} = \boldsymbol{\nabla} \cdot (\kappa \boldsymbol{\nabla} T)$.

In the magnetostatic part of the solver the general conservation equation is reduced to Laplace and Poisson equations in which the generic variable stands for the following variables:

- $\phi = \Phi$ in the Laplace's equation,
- $\phi = \mathbf{A} = (A_x, A_y, A_z)^{\mathrm{T}}$ in the Poisson's equation.

The partial differential equation, Eq. 4.2, can be derived in several ways. One of the possibilities is to derive it from its integral form by allowing the control volume V to become infinitely small. The integral form of Eq. 4.2 is [60, 51]:

$$\int_V \left[\frac{\partial \rho\phi}{\partial t} + \boldsymbol{\nabla} \cdot (\rho \mathbf{u} \phi) - \boldsymbol{\nabla} \cdot \left(\Gamma^{\phi} \boldsymbol{\nabla} \phi \right) - Q^{\phi} \right] dV = 0 \ . \tag{4.3}$$

By rearranging Eq. 4.3 and applying the Gauss' theorem to its convection and diffusion terms the following expression is obtained [51]:

$$\int_V \frac{\partial \left(\rho\phi \right)}{\partial t} dV + \int_S \left(\rho\phi\mathbf{u} \right) \cdot \mathbf{n} \ dS = \int_S \left(\Gamma^{\phi} \boldsymbol{\nabla} \phi \right) \cdot \mathbf{n} \ dS + \int_V Q^{\phi} dV \ . \tag{4.4}$$

This is the integral form of the general conservation equation used in the FVM. It may be derived by applying the fundamental physical principle of conservation of ϕ to a finite control volume which is fixed in space. This finite control volume has a volume V and a surface that bounds it ∂V (called control surface). The fluid moves through this fixed control volume across its control surface [52]. Thus, the physical meaning of Eq. 4.4 may be interpreted as follows [60, 52]:

Rate of change of ϕ inside the control volume	+	Net flux of ϕ into the control volume via advective flux	=	Net flux of ϕ into the control volume via diffusive flux	+	Source/sink of ϕ within the control volume

For more information on the derivation of Eq. 4.4 Anderson's book [52] is recommended.

4.4.2 Gradient Evaluation at Cell Centroids

Gradient Operator in the Conservation Equations

The evaluation of gradients at cell centroids is crucial for the discretization of the governing equations. For example, the gradient operators directly appear as pressure gradients in the momentum conservation equations and as mass fraction gradients in the species conservation equations. It will be shown in later sections that gradients at cell centres are also needed for the calculation of gradients at cell faces, which, in turn, occur during discretization of the diffusion terms. Furthermore, in unstructured meshes the gradients are used for the calculation of the so-called virtual upwind nodes, since defining upwind nodes directly is not straightforward in unstructured grid systems [60]. These virtual nodes are used, for example, in the high-resolution interpolation schemes utilized for the discretization of convection terms. At this point it should be mentioned that the software used in this work is based on an unstructured grid platform with the so-called face-addressing storage [60].

Gradient Scheme Used

There are various techniques for discretization of gradients at cell centroids, such as the least-squares or the Green-Gauss method. In the present work, the Green-Gauss method (or just Gauss method) is used for the gradient evaluation, which requires the interpolation of values from cell centres to face centres of the CV (see Eq. 4.5). For this interpolation procedure, linear interpolation (or central differentiation) is chosen in the present work. For the interpolation of the energy and temperature gradients an additional limiting scheme (the `cellLimited` scheme) is switched on. According to [61], this scheme limits the gradients in such a way that when extrapolating cell centroid values to cell faces using the calculated gradient, the cell face values are not outside the limits of the values in the surrounding cells. The corresponding keywords in the OpenFOAM directory `fvSchemes` in which all the numerical schemes used are defined, are entered in the sub-directory `gradSchemes` and read as follows: `Gauss linear` and `cellLimited Gauss linear 1` for the energy and temperature gradients, where the entry `1` activates the limiting.

Green-Gauss Gradient Evaluation Method

The discretization of the gradient at cell centroid by using the Green-Gauss method is defined as follows [60]:

$$(\boldsymbol{\nabla}\phi)_C = \frac{1}{V_C} \sum_{f}^{\mathrm{nb}(C)} \phi_f \mathbf{S}_f \ . \tag{4.5}$$

In the following, the variable value at the centroid of the cell C is denoted by ϕ_C and the variable values of all neighbouring cell centroids F by ϕ_F. The corresponding computational molecule is shown in Fig. 4.1 left. OpenFOAM uses the cell-centred and collocated variable arrangement, where all variables are stored at the centroids of discrete elements. That is, the variable values at the face centroids ϕ_f in Eq. 4.5 must be evaluated by using ϕ_C and ϕ_F.

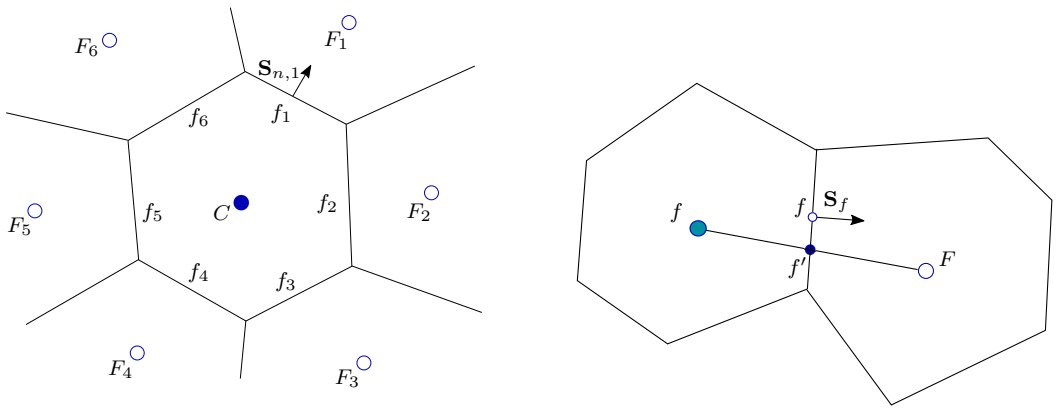

Figure 4.1: left: Computational molecule of the spatial element C; right: Two discrete elements in a skewed numerical grid (adapted from Moukalled *et al.* [60]).

Linear Variable Interpolation

The computational grid used in this work is of a low skewness, which is why the linear interpolation scheme provides a sufficiently accurate evaluation of the values at the face centroids. Linear interpolation of any variable between the cell points C and F is given by the following generic formulation [60]:

$$\square_f = g_f \square_C + (1 - g_f) \square_F \ , \tag{4.6}$$

where the weighting function g_f is calculated as:

$$g_f = \frac{d_{Ff}}{d_{Ff} + d_{fC}} = \frac{d_{Ff}}{d_{CF}} \ . \tag{4.7}$$

Thus, the value of the generic variable ϕ_f may be calculated as follows:

$$\phi_f = g_f \phi_C + (1 - g_f) \phi_F \ . \tag{4.8}$$

In unstructured non-orthogonal grids with strong skewness, however, the point of intersection f' of the surface S_f with the line connecting the centroids C and F does not usually coincide with the face centroid f (see Fig. 4.1 right). For this reason, the variable can not be approximated by linear interpolation alone, but requires an additional correction term. For more information on the correction procedure the book of Moukalled *et al.* [60] is recommended.

4.4.3 Divergence Operator Evaluation

The evaluation of the divergence operators is not only required for the discretization of convective terms that describe a highly directional processes. It is also used, for example, for the discretization of the components of the viscous stress tensor (see Eq. 3.13) which describe diffusive phenomena. Therefore, depending on the type of physical phenomenon, the divergence operators must be discretized by different schemes [61].

Divergence Schemes Used

Following numerical schemes are used for the evaluation of the divergence operators:

- Convection terms of the momentum conservation equations:

  `Gauss limitedLinearV 1`.

- Convection terms of the energy and species conservation equations:

  `Gauss limitedLinear 1`.

- Viscous stress tensor terms in the momentum equation as well as terms of the rate of work due to the surface forces in the energy conservation equation:

  `Gauss linear`.

The keyword `Gauss` means that for all discretization schemes the Gaussian integration rule is used. The keyword `limitedLinear 1` stands for a particular High Resolution (HR) interpolation scheme which is based on the Total Variation Diminishing[1] (TVD) formulation and uses the Sweby limiter for the bounding of convective fluxes [61]. The entry `1` denotes the strongest limiting. The `limitedLinearV 1` scheme is a special version of the `limitedLinear 1` scheme designed for vector fields [61]. The `Gauss linear` scheme uses the linear profile approximation (see Eq. 4.6) which is a physically reasonable scheme for diffusive phenomena.

Gaussian Quadrature Integration: Convection Term

The Gaussian quadrature integration for the flux $\boldsymbol{\mathcal{F}}_\phi$ of variable ϕ through the surface of face f is given such that [60]:

$$\int_f \boldsymbol{\mathcal{F}}_\phi \cdot d\mathbf{S} = \int_f (\boldsymbol{\mathcal{F}}_\phi \cdot \mathbf{n}_f)\, dS = \sum_{ip}^{\mathrm{nip}(f)} (\boldsymbol{\mathcal{F}}_\phi \cdot \mathbf{n}_f)_{ip}\, \omega_{ip} S_f \ , \tag{4.9}$$

where the flux $\boldsymbol{\mathcal{F}}_\phi$ for a convective process is defined as: $\boldsymbol{\mathcal{F}}_\phi^C = \rho \mathbf{u} \phi$. In Eq. 4.9 the subscript ip denotes the integration point on the surface f and $\mathrm{nip}(f)$ is the number of integration points along surface f. Further, the quantity ω_{ip} denotes the weighting function of the integration point and S_f is the area of the surface f.

In the finite volume method, it is customary to use one integration point located at the centroid of the discrete element, which is why the following applies: $ip = \omega_{ip} = 1$. This assumption results in a discretization accuracy of the second order [60].

The discretized convection term can be obtained by replacing the surface integral in Eq. 4.4 by a summation over all discrete element faces and applying the Gauss quadrature rule to each face of the CV [60]:

$$\int_{S_C} (\rho \phi \mathbf{u}) \cdot \mathbf{n}\ dS = \sum_f^{\mathrm{nb}(C)} \left(\int_f (\rho \mathbf{u} \phi) \cdot d\mathbf{S} \right) = \sum_f^{\mathrm{nb}(C)} (\rho \phi \mathbf{u})_f \cdot \mathbf{S}_f = \sum_f^{\mathrm{nb}(C)} F_f \phi_f \ , \tag{4.10}$$

where the mass flux through the cell face f is defined as: $F_f = \rho_f \mathbf{u}_f \cdot \mathbf{S}_f$.

High Resolution Interpolation Scheme: Convection Term

The next step in the discretization of the convection term consists in expressing the face values ϕ_f in Eq. 4.10 in terms of the cell centroid values ϕ_C and ϕ_F.

High-resolution methods are used because general methods are subject to severe limitations. For example, the first-order upwind scheme (UD) is characterized by being able to correctly mimic the basic physics of the advection process, since the cell face value ϕ_f depends on the value of the upwind node. This scheme is stable and gives

[1] Total Variation Diminishing (TVD) framework represents an approach for developing High Resolution (HR) convective schemes [60].

physically plausible results. However, the UD scheme introduces strong numerical diffusion to the solution, resulting in the smearing of sharp gradients of the transport variable. To minimize numerical diffusion, the so-called upwind-biased higher-order schemes have been developed, such as SOU, QUICK or FROMM schemes. These high-order schemes significantly increase the accuracy while remaining stable, but show strong unboundedness, resulting in oscillations near sudden jumps or steep gradients. This type of error is known as dispersion error [60]. These limitations led to the development of the high-resolution schemes.

According to Ferziger and Perić [51], the idea behind a higher-resolution scheme is always to produce a sharp discontinuity in the right place without falsifying the solution in the smooth area. One possible technique to achieve this, is the so-called flux limiter approach. The function of a flux limiter consists in limiting the flux of the transport variable (here ϕ) into a control volume in such a way that no local maximum or minimum of the profile of this quantity in the considered CV arises [51]. The formation of these local maxima and minima results from the above-mentioned numerical dispersion which is typical for higher-order schemes. To achieve the boundedness of the interpolation profile, the limiter function reduces the order of approximation near the discontinuity from the high-order scheme towards the first-order upwind scheme. At the discontinuity itself, the order of approximation becomes first order. In this way high-resolution, high-order, oscillation free (TVD) difference schemes are obtained.

According to Jasak [63], a HR scheme can be expressed as a linear combination of the first-order differencing scheme and a higher order correction as follows:

$$\phi_f = (\phi)_{UD} + \psi(r)\left[(\phi)_{HO} - (\phi)_{UD}\right] \ , \tag{4.11}$$

where $(\phi)_{UD}$ and $(\phi)_{HO}$ denote the face values of ϕ obtained by the first-order upwind scheme and the higher-order (HO) scheme, respectively. The quantity $\psi(r)$ denotes the flux limiter which is a function of consecutive gradients of ϕ given as [63]:

$$r = \frac{\phi_C - \phi_U}{\phi_D - \phi_C} \ . \tag{4.12}$$

Nodes D and U are the neighbouring nodes of C lying downwind and upwind from C, respectively. In the present work, these nodes and all other neighbouring nodes of C are generally denoted by the subscript F. The cell face f lies between the nodes D and C. This means that for the face f the nodes D, C and U represent downwind, upwind and far upwind nodes, respectively (see Fig. 4.2 left). In unstructured grids with face-addressing storage no information is available about U which is required for the calculation of r. Only the information about the owner (C) and the neighbour (D) of the face f is available. This hurdle is overcome by creating a virtual node U as follows [60]:

$$\phi_U = \phi_D - 2\boldsymbol{\nabla}\phi_C \cdot \mathbf{d}_{CD} \ . \tag{4.13}$$

In this particular method it is assumed that U lies at the line joining the nodes C and D such that C represents the midpoint of the segment UD [60].

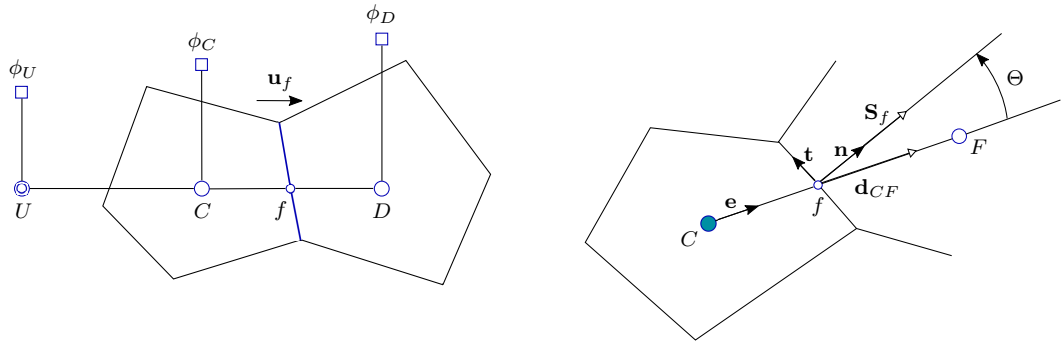

Figure 4.2: left: Schematic representation of the U, C and D node locations in an unstructured grid; right: Discrete element in a non-orthogonal computational grid (adapted from Moukalled *et al.* [60]).

The HR scheme used in this work uses the second-order central differencing scheme (CD) as a HO scheme and limits it towards the first-order upwind scheme in regions of rapidly changing gradients by using the limiter proposed by Sweby [61, 64].

The first-order UD scheme is defined as follows [60]:

$$\phi_f = \phi_C \text{ if } F_f > 0 \text{ and } \phi_f = \phi_F \text{ if } F_f < 0 \ . \tag{4.14}$$

By introducing an operator $||a, b||$ that represents the maximum of a and b, the convective flow calculated by the upwind scheme is such that [60]:

$$F_f \phi_f = ||F_f, 0||\, \phi_C - ||-F_f, 0||\, \phi_F \ . \tag{4.15}$$

The second-order central differencing scheme is given in Eq. 4.8. By substituting Eqs. 4.8 and 4.14 into Eq. 4.11, the following expression is obtained for a positive flux direction ($F_f > 0$) [60]:

$$\phi_f = \phi_C + \underbrace{(g_f \psi + 1 - \psi)}_{\overline{\omega}} (\phi_C - \phi_F) = \underbrace{\phi_C}_{\text{upwind}} + \underbrace{(\overline{\omega} - 1)\,(\phi_F - \phi_C)}_{\text{anti-diffusive flux}} \ . \tag{4.16}$$

The approach described in Eq. 4.16 for the derivation of a HR scheme can be understood as adding a limited anti-diffusive flow to the highly diffusive first-order upwind scheme. The quantity $\overline{\omega}$ is the so-called downwind weighting factor (DWF). The DWF method is implemented in OpenFOAM [60]. The complete expression for the discretized convective term is:

$$F_f \phi_f = ||F_f, 0|| \left[\overline{\omega}^+ \phi_C + \left(1 - \overline{\omega}^+\right) \phi_F\right] - ||-F_f, 0|| \left[\overline{\omega}^- \phi_F + \left(1 - \overline{\omega}^-\right) \phi_C\right] \ . \tag{4.17}$$

The values $\overline{\omega}^+$ and $\overline{\omega}^-$ must be calculated for positive and negative flow directions. As far as the flow through the cell surface, F_f, is concerned, the quantity $(\rho \mathbf{u})_f$ is calculated in this work by means of linear interpolation (see Eq. 4.6), which is acceptable because of a low mesh non-orthogonality. For this, values from the last available solution are used for the velocity vector. In this way, the nonlinear

convective term of the momentum equation can be linearised: $F_f u_f = (\rho_f^\circ \mathbf{u}_f^\circ \cdot \mathbf{S}_f)\mathbf{u}_f^*$, where the superscripts $^\circ$ and * denote the values of the last available solution and instantaneous values, respectively. The face surface vectors $\mathbf{S}_f$ are calculated from the computational grid geometry.

The original Sweby limiter is defined as [64]:

$$\psi(r) = max\left\{0, min\left(\beta r, 1\right), min\left(r, \beta\right)\right\} \text{ , where } 1 \leq \beta \leq 2 \text{ .} \tag{4.18}$$

In OpenFOAM the Sweby limiter is implemented as follows:

$$\psi(r) = max\left\{0, min\left(2r/k, 1\right)\right\} \text{ ,} \tag{4.19}$$

where $k = 1$ in the present work (the entry `1` in the keyword: `limitedLinear 1`).

4.4.4 Gradient Evaluation at Cell Faces

The evaluation of spatial gradients $(\boldsymbol{\nabla}\phi)_f$ on the cell faces in the direction normal to the cell surface is needed for the discretization of the diffusion terms (Laplacian terms), discussed in the following section.

The gradient evaluation procedure is complicated by the fact that most computational grids for real-world engineering applications are nonorthogonal. The gradient evaluation procedure is divided into three steps:

- calculation of the non-orthogonal contribution to the gradient,
- approximation of the gradient at the CV face via gradients at CV centroids,
- evaluation of the gradients at the CV centroids (see Sec. 4.4.2).

Non-Orthogonal Contribution

In an orthogonal computational grid the gradient at the face f with the surface vector $\mathbf{S}_f$ may be evaluated by using the nodal values of two neighbouring computational cells C and F as follows [60]:

$$(\boldsymbol{\nabla}\phi)_f \cdot \mathbf{S}_f = (\boldsymbol{\nabla}\phi \cdot \mathbf{n})_f S_f = \left(\frac{\partial \phi}{\partial n}\right) S_f = \frac{\phi_C - \phi_F}{d_{CF}} S_f \text{ ,} \tag{4.20}$$

where d_{CF} is the distance between the nodes C and F. However, in unstructured grids the non-orthogonality is the rule rather than the exception. For this reason, the surface normal gradient term is split into an orthogonal and a non-orthogonal part as follows [60]:

$$\underbrace{(\boldsymbol{\nabla}\phi)_f \cdot \mathbf{S}_f}_{\substack{\text{surface normal} \\ \text{gradient}}} = (\boldsymbol{\nabla}\phi)_f^* \cdot \underbrace{\mathbf{E}_f}_{E_f \mathbf{e}} + (\boldsymbol{\nabla}\phi)_f^\circ \cdot \mathbf{T}_f = \underbrace{\left(\frac{\partial \phi}{\partial e}\right)_f^* E_f}_{\substack{\text{orthogonal-like} \\ \text{contribution}}} + \underbrace{(\boldsymbol{\nabla}\phi)_f^\circ \cdot \mathbf{T}_f}_{\substack{\text{non-orthogonal like} \\ \text{contribution}}} \text{ ,} \tag{4.21}$$

where $\mathbf{E}_f$ represents the surface vector, which is collinear with the vector $\mathbf{d}_{CF}$ joining the centroids of the elements C and F (see Fig. 4.2 right). Vector $\mathbf{e}$ is the unit vector of $\mathbf{E}_f$. Surface vector $\mathbf{T}_f$ is orthogonal to the cell face f. There exist several approaches for calculating $\mathbf{E}_f$ and $\mathbf{T}_f$, such as minimum correction approach, orthogonal correction approach, and over-relaxed approach (for more information see Moukalled *et al.* [60]). The minimum correction approach, for example, is defined as follows:

$$(\boldsymbol{\nabla}\phi)_f \cdot \mathbf{E}_f = (\boldsymbol{\nabla}\phi)_f \cdot (\mathbf{e} \cdot \mathbf{S}_f)\,\mathbf{e} = (\boldsymbol{\nabla}\phi)_f \cdot (S_f \cos\Theta)\,\mathbf{e}\ , \tag{4.22}$$

$$(\boldsymbol{\nabla}\phi)_f \cdot \mathbf{T}_f = (\boldsymbol{\nabla}\phi)_f \cdot (\mathbf{S}_f - \mathbf{E}_f) = (\boldsymbol{\nabla}\phi)_f \cdot (\mathbf{n} - \cos\Theta\mathbf{e})\,S_f\ . \tag{4.23}$$

The non-orthogonal contribution in Eq. 4.21 contains the gradient on the control volume surface, which according to [60] can be evaluated as follows:

$$(\boldsymbol{\nabla}\phi)_f = \overline{(\boldsymbol{\nabla}\phi)}_f + \left[\frac{\phi_F - \phi_C}{d_{CF}} + \left(\overline{(\boldsymbol{\nabla}\phi)}_f \cdot \mathbf{e}_{CF}\right)\right]\mathbf{e}_{CF} \quad \text{with } \mathbf{e}_{CF} = \frac{\mathbf{d}_{CF}}{d_{CF}}\ . \tag{4.24}$$

The orthogonal contribution in Eq. 4.21 can be calculated analogous to Eq. 4.20 by using the linear profile of ϕ along the $\mathbf{e}$ direction. Thus, the surface normal gradient can be calculated by the following expression:

$$(\boldsymbol{\nabla}\phi)_f \cdot \mathbf{S}_f = \underbrace{\frac{\phi_C^* - \phi_F^*}{d_{CF}} E_f}_{\substack{\text{implicit ortho-}\\ \text{gonal contribution}}} + \underbrace{\left(\overline{(\boldsymbol{\nabla}\phi)}_f + \left[\frac{\phi_C - \phi_F}{d_{CF}} - \left(\overline{(\boldsymbol{\nabla}\phi)}_f \cdot \mathbf{e}_{CF}\right)\right]\mathbf{e}_{CF}\right)^{\circ} \cdot \mathbf{T}_f}_{\text{explicit non-orthogonal contribution}}\ . \tag{4.25}$$

In Eq. 4.25, the orthogonal part is treated implicitly. The non-orthogonal correction, however, is calculated explicitly, meaning it is treated in a deferred correction manner by using the values currently available.

Gradient Interpolation

The interpolated gradient at the face, $\overline{(\boldsymbol{\nabla}\phi)}_f$, in Eq. 4.25 is obtained by linear interpolation between the values at points C and F given by Eq. 4.6, which leads to the following formulation:

$$\overline{(\boldsymbol{\nabla}\phi)}_f = g_f\,(\boldsymbol{\nabla}\phi)_C + (1 - g_f)\,(\boldsymbol{\nabla}\phi)_F\ . \tag{4.26}$$

The evaluation of the surface gradients is completed by the calculation of the gradients at the centroids $(\boldsymbol{\nabla}\phi)_C$ and $(\boldsymbol{\nabla}\phi)_F$, as discussed in Sec. 4.4.2.

4.4.5 Laplacian Operator Evaluation

The evaluation of the Laplacian operator is required for the discretization of the diffusion term in Eq. 4.2.

Laplacian Scheme Used

The Laplacian scheme used in the frame of this work is defined in the OpenFOAM's directory `fvSchemes` by the keyword: `Gauss linear limited 1.0`.

The keyword `Gauss` means that the Gaussian integration rule is used for the evaluation of the surface integral in the diffusion term. This is the only available scheme for the diffusion term evaluation in OpenFOAM [61]. Further, the keyword `linear` denotes that linear interpolation scheme given in Eq. 4.6 is used for the surface interpolation of the diffusivity Γ^{ϕ}. Finally, the keyword `limited 1.0` means that the explicit non-orthogonality correction is performed in the evaluation of the surface gradient (see Sec. 4.4.4). This explicit non-orthogonal contribution is added to the orthogonal component (see Eq. 4.25). With high non-orthogonality of the computational grid, this explicit part can become very large, which leads to instabilities during the solution process. The stabilization is achieved by limiting the non-orthogonal contribution over a coefficient ζ, which can have values of $0 \leq \zeta \leq 1$ [61]. The coefficient `0.5` in the entry `limited 0.5` would mean that the non-orthogonal contribution can be smaller or equal to the orthogonal part. Since the computational grid used in the present work has a low non-orthogonality, the non-orthogonal correction is added to the orthogonal component without limitations (that is $\zeta = 1.0$).

Gaussian Quadrature Integration: Diffusion Term

The discretization of the diffusion term is carried out analogous to the convection term, whereby $\boldsymbol{\mathcal{F}}_{\phi}$ in Eq. 4.9 represents in this case the diffusive flux given as follows: $\boldsymbol{\mathcal{F}}_{\phi}^{D} = \Gamma^{\phi}\boldsymbol{\nabla}\phi$. This results in the following relation for the diffusion term when one integration point is used [60]:

$$\int_{S_C} \left(\Gamma^{\phi}\boldsymbol{\nabla}\phi\right) \cdot \mathbf{n}\, dS = \sum_{f}^{\mathrm{nb}(C)} \left(\Gamma^{\phi}\boldsymbol{\nabla}\phi\right)_f \cdot \mathbf{S}_f \ . \tag{4.27}$$

The evaluation of the surface gradient $(\boldsymbol{\nabla}\phi)_f$ is carried out as described in Sec. 4.4.4.

4.4.6 Source Term: Linearisation and Spatial Discretization

Source terms are used in the transport equations not only for modelling such effects as radiation losses or body forces. Another task of the source terms is to treat all those terms that cannot be written as convection, diffusion or unsteady terms [63].

Linearisation of the Source Term

The linearisation (or implicit treatment) of the source term plays an essential role in the solution process, because this enhances the solution robustness of the algebraic system of equations [63, 60]. It is therefore recommended to treat the source terms as implicitly as possible.

The source term Q^{ϕ} can be a function of ϕ. As described in [60], $Q(\phi)$ can be treated purely explicitly by using the last available solution of the generic variable (ϕ°), or implicitly by linearising it using the Taylor-like series expansion:

$$Q\left(\phi_C\right) = Q\left(\phi_C^{\circ}\right) + \left(\frac{\partial Q}{\partial \phi}\right)^{\circ}\left(\phi_C - \phi_C^{\circ}\right) = \underbrace{\left(\frac{\partial Q}{\partial \phi}\right)^{\circ}\phi_C}_{\substack{\text{implicit part} \\ = Q_{\text{im}}^{\phi}\phi_C}} + \underbrace{Q\left(\phi_C^{\circ}\right) - \left(\frac{\partial Q}{\partial \phi}\right)^{\circ}\phi_C^{\circ}}_{\text{explicit part } = Q_{\text{ex}}^{\phi}} \ . \quad (4.28)$$

For the sake of convenience, the coefficient of the implicit part of the linearised source term is in the following denoted by Q_{im}^{ϕ} and the explicit part by Q_{ex}^{ϕ}. More information on this topic can be found in Moukalled *et al.* [60] and Patankar [65].

Spatial Discretization of the Source Term

By applying the Gaussian quadrature integration to the control volume and using the relation in Eq. 4.28, the discretized source term is obtained as follows [60]:

$$\int_{V_C} Q^{\phi} dV = \sum_{ip}^{\text{nip}(V_C)} \left(\omega_{ip} Q_{ip}^{\phi} V_C\right) = \sum_{ip}^{\text{nip}(V_C)} \omega_{ip} \left(Q_{\text{im}}^{\phi}\phi_C + Q_{\text{ex}}^{\phi}\right)_{ip} V_C \ . \quad (4.29)$$

In Eq. 4.29, the upper bound of summation $\text{nip}(V_C)$ stands for the number of integration points in the volume of the discrete element C. By using only one integration point for the discretization (e.g. cell centroid) the following expression for the source term is obtained:

$$\int_{V_C} Q^{\phi} dV = \left(Q_{\text{im}}^{\phi}\phi_C + Q_{\text{ex}}^{\phi}\right) V_C \ . \quad (4.30)$$

4.4.7 Spatial Discretization of the Transient Term

According to Moukalled *et al.* [60], for fixed grids in which the volume and the surface area of each discrete element are constant in time, the transient (unsteady) term can be integrated as follows:

$$\int_{V_C} \frac{\partial\left(\rho\phi\right)}{\partial t} dV = \frac{\partial}{\partial t}\left(\int_{V_C} \rho\phi \ dV\right) = \frac{\partial\left(\overline{\rho\phi}\right)_C}{\partial t} V_C = \frac{\partial\left(\rho\phi\right)_C}{\partial t} V_C \ , \quad (4.31)$$

where:

$$\overline{\rho\phi}_C = \frac{1}{V_C}\int_{V_C} \rho\phi \ dV = \left(\rho\phi\right)_C + \mathcal{O}\left(\Delta^2\right) \ . \quad (4.32)$$

In Eq. 4.32 the symbol $\mathcal{O}\left(\Delta^2\right)$ denotes the truncation error, meaning that the numerical scheme is of the second order accuracy.

4.4.8 Temporal Discretization

Temporal Discretization Scheme Used

The temporal discretization is required for the evaluation of the time derivative appearing in the unsteady term of the general conservation equation. In the context of the present work, the implicit Euler scheme, which is a first-order scheme, is used for temporal discretization.

Semi-Discretized Equation

By inserting Eqs. 4.10, 4.27, 4.30, and 4.31 into the general conservation equation, Eq. 4.4, the following relation is obtained:

$$\frac{\partial \left(\rho\phi\right)_C}{\partial t} V_C + \sum_f^{\mathrm{nb}(C)} \left(\rho\phi\mathbf{u} - \Gamma^\phi \boldsymbol{\nabla}\phi\right)_f \cdot \mathbf{S}_f = \left(Q^\phi_{\mathrm{im}}\phi_C + Q^\phi_{\mathrm{ex}}\right) V_C \ . \tag{4.33}$$

This is the so-called semi-discretized conservation equation. The expressions of face values $\square_f$ in Eq. 4.33 in terms of the nodal values $\square_C$ and $\square_F$ are described in the previous sections. In the following, the integration over time is performed in order to obtain a discrete equation.

Temporal Discretization Procedure

As described in Moukalled *et al.* [60], in the FV method the temporal discretization is performed in a manner similar to spatial discretization, with the difference that integration is carried out over a temporal rather than a spatial element. The centroid of the temporal element in the transient domain is situated in t, the faces of the element are at $t - \frac{\Delta t}{2}$ and $t + \frac{\Delta t}{2}$, and Δt can be thought of as the volume of the temporal element. By introducing a spatial operator $\mathcal{L}(\phi_C)$ that includes all non-transient terms and integrating over the time interval from $t - \frac{\Delta t}{2}$ to $t + \frac{\Delta t}{2}$, Eq. 4.33 becomes [60]:

$$\int_{t-\Delta t/2}^{t+\Delta t/2} \left[\frac{\partial \left(\rho\phi\right)_C}{\partial t} V_C\right] dt + \int_{t-\Delta t/2}^{t+\Delta t/2} \mathcal{L}(\phi_C) dt = 0 \ . \tag{4.34}$$

The integration yields a transient discrete finite volume equation for the discrete element C [60]:

$$\frac{\left(\rho_C\phi_C\right)^{t+\Delta t/2} - \left(\rho_C\phi_C\right)^{t-\Delta t/2}}{\Delta t} V_C + L(\phi_C^t) = 0 \ . \tag{4.35}$$

The implicit first-order Euler scheme is obtained by using a first-order interpolation profile analogous to the spatial upwind scheme. Thus, the values at the faces of temporal element are set to be equal to the values at the centroids of the temporal elements $t - \Delta t$ and t yielding [60]:

$$\left(\rho_C\phi_C\right)^{t+\Delta t/2} = \left(\rho_C\phi_C\right)^t \quad \text{and} \quad \left(\rho_C\phi_C\right)^{t-\Delta t/2} = \left(\rho_C\phi_C\right)^{t-\Delta t} \ . \tag{4.36}$$

4.4.9 Discretized Equation

Applying Eq. 4.35 to Eq. 4.36 and evaluating the spatial operator $L(\phi_C^t)$ yields the following expression for the transient discrete equation:

$$\underbrace{\frac{(\rho_C\phi_C)^t-(\rho_C\phi_C)^{t-\Delta t}}{\Delta t}V_C}_{\text{transient term}}+\underbrace{\sum_f^{\text{nb}(C)}F_f\phi_f^t}_{\text{convection term}} \\ \underbrace{-\sum_f^{\text{nb}(C)}\Gamma_f^\phi\left(\boldsymbol{\nabla}\phi\right)_f^t\cdot\mathbf{S}_f}_{\text{diffusion term}}=\underbrace{\dot{Q}_{\text{im}}^\phi\phi_C^tV_C+\dot{Q}_{\text{ex}}^\phi V_C}_{\text{source term}}\ . \quad (4.37)$$

Eq. 4.37 is the balance equation of the generic variable ϕ over the discrete element C. In the following the individual terms are considered in more detail, whereby all surface values are represented in terms of variable values at cell centroids. To simplify the notation, the values from the last available solution or the previous time step are in the following marked with the superscript $^\circ$ ($\square^{t-\Delta t}\rightarrow\square^\circ$). For the values from the current time step or iteration the superscript * is used ($\square^t\rightarrow\square^*$).

Transient Term

$$\frac{(\rho_C\phi_C)^t-(\rho_C\phi_C)^{t-\Delta t}}{\Delta t}V_C=\frac{\rho_C^*V_C}{\Delta t}\phi_C^*-\frac{\rho_C^\circ V_C}{\Delta t}\phi_C^\circ\ . \quad (4.38)$$

Convection Term

$$\sum_f^{\text{nb}(C)}F_f\phi_f^t=\sum_F^{\text{NB}(C)}\left\{||F_f,0||\left[\overline{\omega}^+\phi_C^*+\left(1-\overline{\omega}^+\right)\phi_F^*\right]\right. \\ \left.-||-F_f,0||\left[\overline{\omega}^-\phi_F^*+\left(1-\overline{\omega}^-\right)\phi_C^*\right]\right\}\ , \quad (4.39)$$

where:

$$F_f=\left[g_f\rho_C^*+(1-g_f)\rho_F^*\right]\left[g_f\mathbf{u}_C^\circ+(1-g_f)\mathbf{u}_F^\circ\right]\cdot\mathbf{S}_f\ . \quad (4.40)$$

Diffusion Term

$$\sum_f^{\text{nb}(C)}\Gamma_f^\phi\left(\boldsymbol{\nabla}\phi\right)_f^t\cdot\mathbf{S}_f=\sum_F^{\text{NB}(C)}\left[g_f\Gamma_C^\phi+(1-g_f)\Gamma_F^\phi\right]\left\{\frac{\phi_C^*-\phi_F^*}{d_{CF}}E_f\right. \\ \left.+\left(\left(\overline{\boldsymbol{\nabla}\phi}\right)_f^\circ+\left[\frac{\phi_C^\circ-\phi_F^\circ}{d_{CF}}-\left(\left(\overline{\boldsymbol{\nabla}\phi}\right)_f^\circ\cdot\mathbf{e}_{CF}\right)\right]\mathbf{e}_{CF}\right)\cdot\mathbf{T}_f\right\}\ , \quad (4.41)$$

where:

$$\left(\overline{\boldsymbol{\nabla}\phi}\right)_f^\circ=g_f\left(\overline{\boldsymbol{\nabla}\phi}\right)_C^\circ+(1-g_f)\left(\overline{\boldsymbol{\nabla}\phi}\right)_F^\circ\ . \quad (4.42)$$

The gradient $\left(\overline{\boldsymbol{\nabla}\phi}\right)_C^\circ$ is calculated as follows:

$$\left(\overline{\boldsymbol{\nabla}\phi}\right)_C^\circ = \frac{1}{V_C}\sum_f^{\mathrm{nb}(C)} \phi_f^\circ \mathbf{S}_f \text{ , where } \phi_f^\circ = g_f\phi_C^\circ + (1-g_f)\phi_F^\circ \text{ .} \tag{4.43}$$

The gradient $\left(\overline{\boldsymbol{\nabla}\phi}\right)_F^\circ$ is calculated analogous, but for the computational molecule with the node F in the centre.

4.4.10 Algebraic Equation

Inserting Eqs. 4.38, 4.39, and 4.41 into Eq. 4.37 yields a balance equation that contains only values from the control volume centroids. By rearranging the terms according to the transport variables ϕ_C^* and ϕ_F^*, the algebraic equation for the control volume C is obtained [60]:

$$a_C\phi_C^* + \sum_F^{\mathrm{NB}(C)} a_F^*\phi_F = b_C \text{ ,} \tag{4.44}$$

where the source term b_C includes the explicit part of the source term, Q_{ex}^ϕ, as well as all terms calculated explicitly from the currently available solution (denoted by $^\circ$).

4.4.11 System of Algebraic Equations

The discretization of the generic conservation equation and its subsequent transformation into the algebraic form is performed for each CV in the solution domain. The result is a set of algebraic equations that can be summarized into a matrix equation as follows [51, 60]:

$$\begin{bmatrix} a_{11} & a_{12} & \cdots & a_{1N-1} & a_{1N} \\ a_{21} & a_{22} & \cdots & a_{2N-1} & a_{2N} \\ \vdots & \vdots & \cdots & \vdots & \vdots \\ a_{N1} & a_{N2} & \cdots & a_{NN-1} & a_{NN} \end{bmatrix} \begin{bmatrix} \phi_1 \\ \phi_2 \\ \vdots \\ \vdots \\ \phi_N \end{bmatrix} = \begin{bmatrix} b_1 \\ b_2 \\ \vdots \\ \vdots \\ b_N \end{bmatrix} \text{ .} \tag{4.45}$$

Eq. 4.45 can be written in matrix notation as follows [60]:

$$\mathbf{A}\boldsymbol{\phi} = \mathbf{b} \text{ .} \tag{4.46}$$

In Eq. 4.46, the vector $\boldsymbol{\phi}$ contains the sought-after variable values in the cell centroids (unknowns), and $\mathbf{b}$ is the vector containing all source terms as well as all explicitly calculated terms and boundary conditions. The matrix $\mathbf{A}$ is a sparse quadratic coefficient matrix, which may be symmetric or asymmetric depending on the governing equation to be discretized. According to [61], the transient and Laplacian (e.g. diffusion) terms form coefficients of a symmetric matrix, whereas the discretization of advective derivatives introduces asymmetry.

The equation system in Eq. 4.45 can be linear or nonlinear, depending on governing equation to be solved. If the equation system is nonlinear, a linearisation of the algebraic equations is performed during the solution process, resulting in a linear system of equations. The solution techniques for linear systems of equations are generally grouped into direct and iterative methods. In the field of CFD, iterative techniques are usually preferred for the solution of linear systems of equations. The reasons are, for example, the lower computational costs and a lower memory requirement. In addition, if the equation system is not linear, the linearisation of the algebraic equations is performed during the iterative solution process [51, 60].

The iterative techniques for the solution of linear systems of algebraic equations are not explained in detail in this work. In the following it is mentioned only briefly which class of linear solvers is used in the present work. It is the class of gradient methods that includes the Steepest Descent methods and the Conjugate Gradient methods (CG). The latter method is relevant to the present work. The CG method belongs to the category of Krylov-space methods and is developed for solving linear equation systems whose coefficient matrix is symmetric. However, in CFD applications coefficient matrices resulting from the discretization of conservation equations are usually asymmetric. To solve linear systems with asymmetric matrices with the CG method, the Bi-Conjugate Gradient method (BiCG) was developed. However, this method has a low stability, which is why modifications such as the Bi-CGSTAB method of Van Der Vorst [66] are usually used, which are more stable and robust [60]. More information about the solution of algebraic systems of equations can be found, for example, in Moukalled *et al.* [60].

4.5 New Numerical Solver

The numerical solver developed in the frame of this work is segregated and pressure-based. The individual conservation equations are solved implicitly. As mentioned above, the solver is used with the flux-limited schemes. The PIMPLE algorithm is utilized in the numerical solver for the calculation of velocity and pressure fields. PIMPLE is a combination of SIMPLE[2] and PISO[3] algorithms belonging to a family of pressure-momentum coupling algorithms used in pressure-based solvers for calculating velocity and pressure fields that satisfy mass conservation. More information about pressure-momentum coupling algorithms can be found in Moukalled *et al.* [60].

In the following the functionality of the new solver is explained in detail. All conservation equations are listed in their discretized form. However, for reasons of clarity, the variable values on the cell faces, ϕ_f, are not represented by corresponding interpolation schemes in terms of nodal values. All interpolation methods used in this work have been discussed extensively in the previous sections.

The following notation is used for the algorithm description:

- Superscript $\square^{IC}$ denotes the initial condition values.

[2]Semi-Implicit-Method-of-Pressure-Linked-Equations.
[3]Pressure-Implicit-Split-Operator.

- Superscript $\square^{\circ}$ denotes the values currently available.
- Superscripts $\square^{*}$, $\square^{**}$, and $\square^{***}$ are intermediate values of the current iteration.

4.5.1 Preliminary Remarks

Reformulation of the Heat Flux Vectors

For the numerical implementation, the heat flux vectors $\mathbf{q}_{\mathrm{e}}$ and $\mathbf{q}_{\mathrm{vib}}$ given in Eqs. 3.51 and 3.52, respectively, are reformulated and renamed as follows:

$$\mathbf{q}_{\mathrm{e}} = -\kappa_{\mathrm{el}}\boldsymbol{\nabla}T_{\mathrm{e}} - \kappa'_{\mathrm{e,tr}}\boldsymbol{\nabla}T_{\mathrm{e}} + \underbrace{\sum_{\substack{s=1\\ s\neq \mathrm{e}}}^{n} \rho c_s \mathbf{V}_s e_{\mathrm{e},s}}_{\boldsymbol{\alpha}'_{\mathrm{e}}} = \\ - \kappa_{\mathrm{el}}\boldsymbol{\nabla}T^{\circ}_{\mathrm{e}} - \kappa'_{\mathrm{e,tr}}\boldsymbol{\nabla}T^{\circ}_{\mathrm{e}} + \underbrace{\frac{\boldsymbol{\alpha}'_{\mathrm{e}}}{e^{\circ}_{\mathrm{e}}}}_{\boldsymbol{\alpha}_{\mathrm{e}}} e^{*}_{\mathrm{e}} = -\left(\kappa_{\mathrm{el}} + \kappa'_{\mathrm{e,tr}}\right)\boldsymbol{\nabla}T^{\circ}_{\mathrm{e}} + \boldsymbol{\alpha}_{\mathrm{e}} e^{*}_{\mathrm{e}} \quad (4.47)$$

and

$$\mathbf{q}_{\mathrm{vib}} = -\kappa'_{\mathrm{vib}}\boldsymbol{\nabla}T_{\mathrm{vib}} + \underbrace{\sum_{s=m} \rho c_s \mathbf{V}_s e_{\mathrm{vib},s}}_{\boldsymbol{\alpha}'_{\mathrm{vib}}} = \\ - \kappa'_{\mathrm{vib}}\boldsymbol{\nabla}T^{\circ}_{\mathrm{vib}} + \frac{\boldsymbol{\alpha}'_{\mathrm{vib}}}{e^{\circ}_{\mathrm{vib}}} e^{*}_{\mathrm{vib}} = -\kappa'_{\mathrm{vib}}\boldsymbol{\nabla}T^{\circ}_{\mathrm{vib}} + \boldsymbol{\alpha}_{\mathrm{vib}} e^{*}_{\mathrm{vib}} \ . \quad (4.48)$$

The overall heat flux $\mathbf{q}$, given in Eq. 3.53 is reformulated analogue to $\mathbf{q}_{\mathrm{e}}$ and $\mathbf{q}_{\mathrm{vib}}$ such that:

$$\mathbf{q} = -\left(\kappa_{\mathrm{el}} + \kappa'_{\mathrm{e,tr}}\right)\boldsymbol{\nabla}T_{\mathrm{e}} - \kappa'_{\mathrm{vib}}\boldsymbol{\nabla}T_{\mathrm{vib}} - \kappa\boldsymbol{\nabla}T + \sum_{s=1}^{n} \rho c_s \mathbf{V}_s e_s = \\ - \left(\kappa_{\mathrm{el}} + \kappa'_{\mathrm{e,tr}}\right)\boldsymbol{\nabla}T^{\circ}_{\mathrm{e}} - \kappa'_{\mathrm{vib}}\boldsymbol{\nabla}T^{\circ}_{\mathrm{vib}} - \kappa\boldsymbol{\nabla}T^{\circ} + \boldsymbol{\alpha} e^{*} \ . \quad (4.49)$$

Initial Condition Values Calculation

Variables p^{IC}, T^{IC}, $\mathbf{u}^{\mathrm{IC}}$, and c_s^{IC} are predefined and are read from the corresponding files. The following variables are automatically initialized by starting the solver:

$$\psi^{\mathrm{IC}} = \frac{1}{RT^{\mathrm{IC}}} \ , \ \ \rho^{\mathrm{IC}} = \frac{p^{\mathrm{IC}}}{\psi^{\mathrm{IC}}} \ , \ \ F_f^{\mathrm{IC}} = \rho_f^{\mathrm{IC}} \mathbf{u}_f^{\mathrm{IC}} \cdot \mathbf{S}_f \ , \ \ T_{\mathrm{e}}^{\mathrm{IC}} = T_{\mathrm{vib}}^{\mathrm{IC}} = T^{\mathrm{IC}} \ , \text{ and } \ \tilde{\psi}^{\mathrm{IC}} = \frac{\psi^{\mathrm{IC}}}{\gamma^{\mathrm{IC}}} \ ,$$

where the heat capacity ratio is $\gamma = c_p/c_v$. The electron pressure is initialized by the expression: $p_{\mathrm{e}}^{\mathrm{IC}} = T_{\mathrm{e}}^{\mathrm{IC}} n_{\mathrm{e}}^{\mathrm{IC}} k_{\mathrm{B}}$. The quantities ψ and $\tilde{\psi}$ denote the compressibility and the isentropic compression/expansion coefficient, respectively. The initial energies $e_{\mathrm{e}}^{\mathrm{IC}}$, $e_{\mathrm{vib}}^{\mathrm{IC}}$, and e^{IC} are calculated from the corresponding initial temperatures.

Derivation of the Compressible Pressure Equation

The algebraic form of the momentum conservation equation can be written as follows:

$$a_C^{\mathbf{u}}\mathbf{u}_C^* + \sum_F^{\mathrm{NB}(C)} a_F^{\mathbf{u}}\mathbf{u}_F^* = \mathbf{r} - \boldsymbol{\nabla} p \ . \tag{4.50}$$

By introducing a new operator

$$\mathbf{H}(\mathbf{u}) = \mathbf{r} - \sum_F^{\mathrm{NB}(C)} a_F^{\mathbf{u}}\mathbf{u}_F^* \ , \tag{4.51}$$

where $\mathbf{r}$ denotes all source terms, Eq. 4.50 can be rewritten so that [63]:

$$\mathbf{u}_C^* = \left(a_C^{\mathbf{u}}\right)^{-1} \left(\mathbf{H}(\mathbf{u}) - \boldsymbol{\nabla} p\right) \ . \tag{4.52}$$

The pressure term in Eq. 4.52 is left for better clarity in vector notation (not discretized). By substituting Eq. 4.52 into the convection term of the compressible continuity equation, Eq. 3.10, the following equation is obtained [67]:

$$\frac{\partial \rho}{\partial t} + \boldsymbol{\nabla} \cdot (\rho \mathbf{u}) = \frac{\partial \rho}{\partial t} + \boldsymbol{\nabla} \cdot \left[\rho \left(a_C^{\mathbf{u}}\right)^{-1} \mathbf{H}\left(\mathbf{u}\right)\right] - \boldsymbol{\nabla} \cdot \left[\rho \left(a_C^{\mathbf{u}}\right)^{-1} \boldsymbol{\nabla} p\right] = 0 \ . \tag{4.53}$$

For the derivation of the pressure equation the equation of state for ideal gases is usually used: $\rho = \frac{p}{RT} = \psi p$. Replacing ρ in Eq. 4.53 with ψp yields the compressible pressure equation, for which an isothermal compression/expansion is assumed [67]:

$$\frac{\partial \left(\psi p\right)}{\partial t} + \boldsymbol{\nabla} \cdot \left[\psi \left(a_C^{\mathbf{u}}\right)^{-1} \mathbf{H}\left(\mathbf{u}\right) p\right] - \boldsymbol{\nabla} \cdot \left[\rho^{\circ} \left(a_C^{\mathbf{u}}\right)^{-1} \boldsymbol{\nabla} p\right] = 0 \ . \tag{4.54}$$

The second term on the left hand side of Eq. 4.54 may be reformulated as [67]:

$$\boldsymbol{\nabla} \cdot \left[\psi \left(a_C^{\mathbf{u}}\right)^{-1} \mathbf{H}(\mathbf{u}) p\right] = \boldsymbol{\nabla} \cdot \left(F_{\mathrm{p}} p\right) \ , \tag{4.55}$$

where F_p is the convective flux for the pressure. According to Uroić, Jasak, and Rusche [67], this term is the one which is responsible for the appearance of shocks.

The problem with this technique is that as the compressibility ψ approaches zero, the compressible formulation of the pressure equation, Eq. 4.54, will not reduce to the incompressible formulation of pressure equation. This problem is discussed in detail in Uroić, Jasak and Rusche [67]. This behaviour would adversely affect the stability of the algorithm if there are zones in the simulation domain where the effective Mach number approaches zero. In order to obtain a pressure equation which reduces to the incompressible formulation at $\psi \to 0$, [67] propose an alternative technique based on the isentropic compression/expansion assumption. By using this technique the following expression is obtained for the density [67]:

$$\rho^* = \rho^{\circ} + \tilde{\psi} \left(p^* - p^{\circ}\right) \ . \tag{4.56}$$

Substituting this expression into the convective term in Eq. 4.53 yields the following formulation for the new convection term [67]:

$$\boldsymbol{\nabla} \cdot \left[\rho^* \left(a_C^{\mathbf{u}}\right)^{-1} \mathbf{H}(\mathbf{u})\right] = \underbrace{\boldsymbol{\nabla} \cdot \left[\tilde{\psi} \left(a_C^{\mathbf{u}}\right)^{-1} \mathbf{H}(\mathbf{u}) p^*\right]}_{\text{implicit part}} + \underbrace{\boldsymbol{\nabla} \cdot \left[\left(\rho^\circ - \tilde{\psi} p^\circ\right) \left(a_C^{\mathbf{u}}\right)^{-1} \mathbf{H}(\mathbf{u})\right]}_{\text{explicit part}} , \quad (4.57)$$

where the isentropic compression coefficient $\tilde{\psi} = \frac{1}{RT\gamma}$. Using Eq. 4.57 yields a compressible pressure equation that reduces to the incompressible form at $\psi \to 0$:

$$\frac{\partial \left(\tilde{\psi} p\right)}{\partial t} + \boldsymbol{\nabla} \cdot \left[\tilde{\psi} \left(a_C^{\mathbf{u}}\right)^{-1} \mathbf{H}(\mathbf{u}) p^*\right] + \boldsymbol{\nabla} \cdot \left[\left(\rho^\circ - \tilde{\psi} p^\circ\right) \left(a_C^{\mathbf{u}}\right)^{-1} \mathbf{H}(\mathbf{u})\right] - \boldsymbol{\nabla} \cdot \left[\rho^\circ \left(a_C^{\mathbf{u}}\right)^{-1} \boldsymbol{\nabla} p\right] = 0 . \quad (4.58)$$

As already mentioned, the new solver is partially based on the pressure-based solver *sonicFoam* from the software package foam-extend-4.0. This solver uses Eq. 4.58 proposed by Uroić, Jasak and Rusche for pressure correction.

4.5.2 Solver Algorithm

The sequence of events during the solution procedure of the new solver is schematically represented in Fig. 4.3 and contains the following steps:

1. Initialize all the variables as well as all transport properties and source terms used in the solver.
2. Start of the time loop: $t = t_{\text{start}}$.
3. Use the values from the converged solution of the last time step or initial condition values as initial guess for the current time step t: $x^\circ = x^{t+\Delta t}$ or $x^\circ = x^{\text{IC}}$.
4. Activate chemistry solver: The finite-rate chemistry solver calculates the mass production rates $(\dot{\omega}_1, \dot{\omega}_2, \cdots, \dot{\omega}_n)$ of all species participating in the gas mixture for the current time step t by means of the following quantities: c_1°, c_2°, $\cdots$, c_n°, ρ°, T_{e}°, T_{vib}°, and T°. The calculation of the production rates is carried out by means of the Euler-implicit ODE solver.
5. Start PIMPLE loop: The number of PIMPLE loops can be defined in the OpenFOAM directory `fvSchemes` under the keyword `nOuterCorrectors`. If the PIMPLE loop is executed only once, the solution algorithm is analogue to the PISO algorithm [61]. In the present work the number of outer correctors is set to one, which is why the PIMPLE loop is executed only once per each time step and thus the solver operates in the PISO mode.
6. Solve mass conservation equation explicitly for density ρ_C^*:

$$\frac{V_C}{\Delta t} \left(\rho_C^* - \rho_C^\circ\right) + \sum_f^{\text{nb}(C)} F_f^\circ = 0 . \quad (4.59)$$

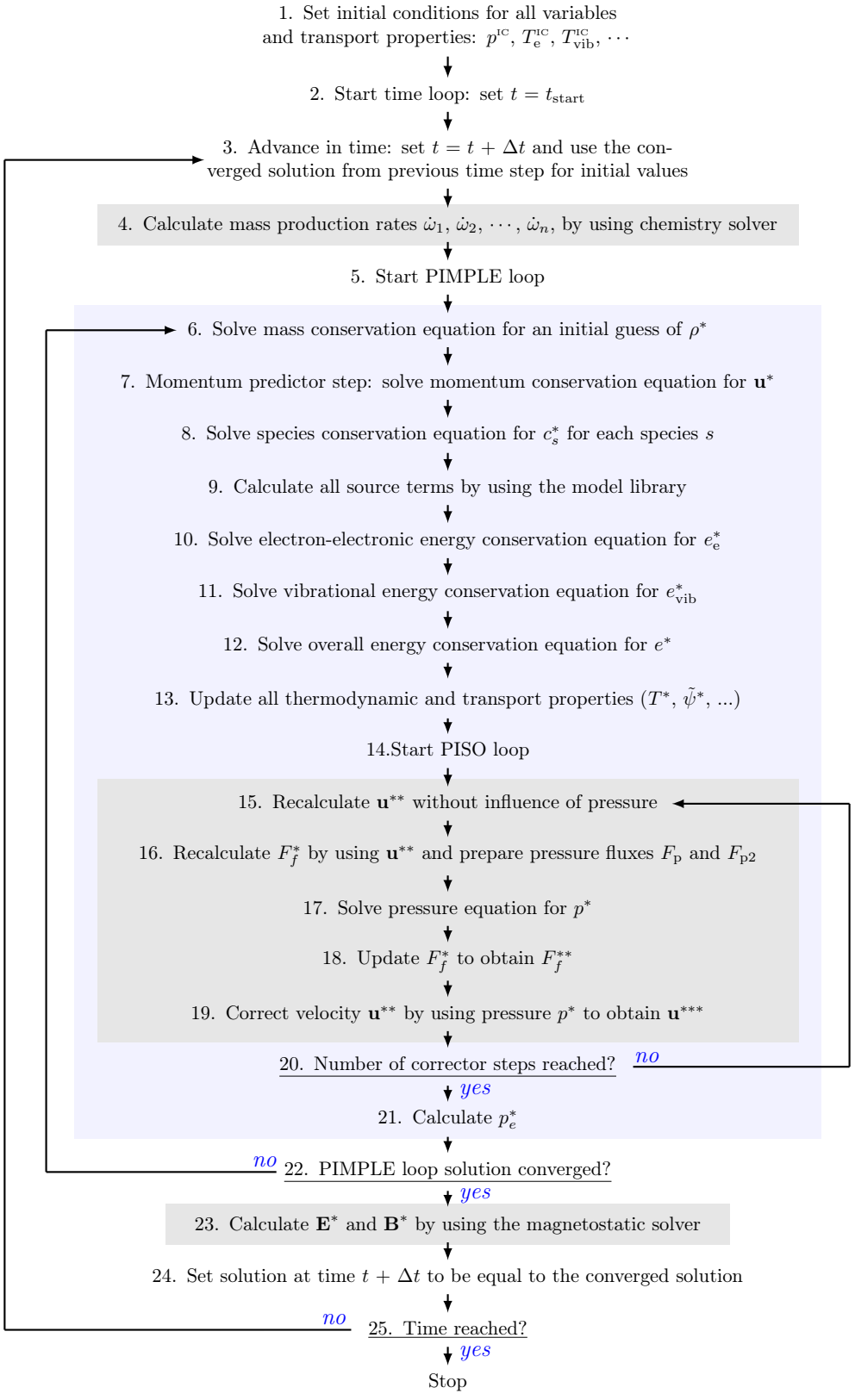

Figure 4.3: Flow chart of the numerical solver.

7. Momentum predictor step: Solve momentum conservation equation implicitly for velocity field $\mathbf{u}_C^*$ using pressure values p° from the previous corrector step or previous time-step:

$$\frac{V_C}{\Delta t}\left(\rho_C^*\mathbf{u}_C^* - \rho_C^\circ\mathbf{u}_C^\circ\right) + \sum_f^{\mathrm{nb}(C)} F_f^\circ \mathbf{u}_f^* - \underbrace{\sum_f^{\mathrm{nb}(C)} \mu_f^\circ \mathbf{S}_f \cdot (\boldsymbol{\nabla}\otimes\mathbf{u})_f^*}_{\substack{\text{implicit part of } \boldsymbol{\nabla}\cdot\boldsymbol{\tau} \\ \text{treated as laplacian term}}} - \underbrace{\sum_f^{\mathrm{nb}(C)} \mu_f^\circ \mathbf{S}_f \cdot \left[(\boldsymbol{\nabla}\otimes\mathbf{u})^{\circ T} - \frac{2}{3} tr\left((\boldsymbol{\nabla}\otimes\mathbf{u})^{\circ T}\right)\mathbf{I}\right]_f}_{\text{explicit part of } \boldsymbol{\nabla}\cdot\boldsymbol{\tau} \text{ treated as source term}} = -\sum_f^{\mathrm{nb}(C)} \mathbf{S}_f p_f^\circ + F_{\mathrm{Lorentz}}^\circ \ . \quad (4.60)$$

8. Solve species conservation equation implicitly for each species s to obtain c_1^*, c_2^*, $\cdots$, and c_n^*:

$$\frac{V_C}{\Delta t}\left(\rho_C^* c_{s,C}^* - \rho_C^\circ c_{s,C}^\circ\right) + \sum_f^{\mathrm{nb}(C)} F_f^\circ c_{s,f}^* - \sum_f^{\mathrm{nb}(C)} \rho_f^* \mathcal{D}_{s,f}^\circ \mathbf{S}_f \cdot (\boldsymbol{\nabla} c_s)_f^* = \dot{\omega}_s \ . \quad (4.61)$$

9. Perform the following operations by using the new model library:

   I. If necessary, correct mass fractions such that: $\sum_{s=0}^{n} c_s^* = 1$.

   II. Calculate mole fractions: y_1^*, y_2^*, $\cdots$, y_n^*, as well as particle numbers: n_1^*, n_2^*, $\cdots$, n_n^*.

   III. Calculate $\mathbf{B}^\circ$, $\mathbf{E}^\circ$, and $\mathbf{J}^\circ$, based on potentials $\mathbf{A}^\circ$ and Φ°.

   IV. Calculate the following quantities:

   - Source terms: $\dot{Q}_{\mathrm{rad}}$, $\dot{Q}_{\text{vib-rot}}$, $\dot{Q}_{\mathrm{vib}}^{\mathrm{R}}$, $\dot{Q}_{\mathrm{el}}^{\mathrm{R}}$, $\dot{Q}_{\mathrm{e,tr}}^{\mathrm{R}}$, $\dot{Q}_{\mathrm{e,tr}}^{\mathrm{I}}$, $\dot{Q}_{\mathrm{e,tr}}^{\mathrm{D}}$, $\dot{Q}_{\mathrm{Joule}}$, F_{Lorentz}.
   - Coefficient $q_{\text{tr,rot-e}}^\circ$ for calculating source terms $\dot{Q}_{\text{tr-e}}$ and $\dot{Q}_{\text{rot-e}}$.
   - Relaxation times $\tau_{\text{vib-tr}}^\circ$ and $\tau_{\text{vib-e}}^\circ$ for vibrational-translational and electron-impact vibrational-relaxation source terms.

   V. Calculate the electric potential on the cathode surface Φ_c, to be used in the next time step as cathode boundary condition.

10. Calculate the electron-electronic heat flux over the cell face due to species diffusion: $\mathcal{F}_{\mathrm{e},f}^{\alpha} = \boldsymbol{\alpha}_{\mathrm{e},f} \cdot \mathbf{S}_f$. Solve electron-electronic energy conservation equation

implicitly for $e^*_{\mathrm{e},C}$:

$$\frac{V_C}{\Delta t}\left(\rho^*_C e^*_{\mathrm{e},C} - \rho^\circ_C e^\circ_{\mathrm{e},C}\right) + \sum_f^{\mathrm{nb}(C)} F^\circ_f e^*_{\mathrm{e},f} + \sum_f^{\mathrm{nb}(C)} \mathcal{F}^{\alpha\circ}_{\mathrm{e},f} e^*_{\mathrm{e},f} - \sum_f^{\mathrm{nb}(C)} \left(\kappa^\circ_{\mathrm{el}} + \kappa'^\circ_{\mathrm{e,tr}}\right)_f (\boldsymbol{\nabla} T_{\mathrm{e}})^\circ_f$$
$$+ \sum_f^{\mathrm{nb}(C)} \frac{F^\circ_f}{\rho^*_f} p^\circ_{e,f} + \underbrace{\frac{q^\circ_{\mathrm{tr,rot\text{-}e}} T^\circ_{\mathrm{e}}}{e^\circ_{\mathrm{e},C}} e^*_{\mathrm{e},C}}_{\substack{\text{implicit part of} \\ \dot{Q}_{\mathrm{tr\text{-}e}} \text{ and } \dot{Q}_{\mathrm{rot\text{-}e}}}} = \underbrace{q^\circ_{\mathrm{tr,rot\text{-}e}} T^\circ}_{\substack{\text{explicit part of} \\ \dot{Q}_{\mathrm{tr\text{-}e}} \text{ and } \dot{Q}_{\mathrm{rot\text{-}e}}}} + \dot{Q}^{\mathrm{I}}_{\mathrm{e,tr}} + \dot{Q}^{\mathrm{D}}_{\mathrm{e,tr}}$$
$$+ \dot{Q}^{\mathrm{R}}_{\mathrm{e,tr}} + \dot{Q}^{\mathrm{R}}_{\mathrm{el}} + \dot{Q}_{\mathrm{Joule}} - \dot{Q}_{\mathrm{rad}} + \frac{\rho^*_C}{\tau^\circ_{\mathrm{vib\text{-}e}}}\left(e^\circ_{\mathrm{vib},C} - e_{\mathrm{vib},C}\left(T^\circ_{\mathrm{e}}\right)\right) . \quad (4.62)$$

11. Calculate the vibrational heat flux over the cell face due to species diffusion: $\mathcal{F}^\alpha_{\mathrm{vib},f} = \boldsymbol{\alpha}_{\mathrm{vib},f} \cdot \mathbf{S}_f$. Solve vibrational energy conservation equation implicitly for obtaining $e^*_{\mathrm{vib},C}$:

$$\frac{V_C}{\Delta t}\left(\rho^*_C e^*_{\mathrm{vib},C} - \rho^\circ_C e^\circ_{\mathrm{vib},C}\right) + \sum_f^{\mathrm{nb}(C)} F^\circ_f e^*_{\mathrm{vib},f} + \sum_f^{\mathrm{nb}(C)} \mathcal{F}^{\alpha\circ}_{\mathrm{vib},f} e^*_{\mathrm{vib},f} - \sum_f^{\mathrm{nb}(C)} \kappa'^\circ_{\mathrm{vib},f} \mathbf{S}_f \cdot (\boldsymbol{\nabla} T_{\mathrm{vib}})^\circ_f$$
$$+ \underbrace{\frac{1.4\rho^*_C}{\tau^\circ_{\mathrm{vib\text{-}tr,rot}}} e^*_{\mathrm{vib},C}}_{\substack{\text{implicit part of} \\ \dot{Q}_{\mathrm{vib\text{-}tr}} \text{ and } \dot{Q}_{\mathrm{vib\text{-}rot}}}} + \underbrace{\frac{\rho^*_C}{\tau^\circ_{\mathrm{vib\text{-}e}}} e^*_{\mathrm{vib},C}}_{\substack{\text{implicit part} \\ \text{of } \dot{Q}_{\mathrm{vib\text{-}e}}}} = \underbrace{\frac{1.4\rho^*_C}{\tau^\circ_{\mathrm{vib\text{-}tr,rot}}} e_{\mathrm{vib},C}(T^\circ)}_{\substack{\text{explicit part of} \\ \dot{Q}_{\mathrm{vib\text{-}tr}} \text{ and } \dot{Q}_{\mathrm{vib\text{-}rot}}}} + \underbrace{\frac{\rho^*_C}{\tau^\circ_{\mathrm{vib\text{-}e}}} e_{\mathrm{vib},C}(T^\circ_{\mathrm{e}})}_{\substack{\text{explicit part} \\ \text{of } \dot{Q}_{\mathrm{vib\text{-}e}}}} + \dot{Q}^{\mathrm{R}}_{\mathrm{vib}} . \quad (4.63)$$

12. Calculate the total heat flux over the cell face due to species diffusion: $\mathcal{F}^\alpha_f = \boldsymbol{\alpha}_f \cdot \mathbf{S}_f$. Solve total energy conservation equation implicitly for obtaining e^*_C:

$$\frac{V_C}{\Delta t}\left(\rho^*_C e^*_C - \rho^\circ_C e^\circ_C\right) + \sum_f^{\mathrm{nb}(C)} F^\circ_f e^*_f + \sum_f^{\mathrm{nb}(C)} \mathcal{F}^{\alpha\circ}_f e^*_{\mathrm{vib},f} - \sum_f^{\mathrm{nb}(C)} \kappa^\circ_f \mathbf{S}_f \cdot (\boldsymbol{\nabla} T)^\circ_f$$
$$- \sum_f^{\mathrm{nb}(C)} \left(\kappa^\circ_{\mathrm{el}} + \kappa'^\circ_{\mathrm{e,tr}}\right)_f \mathbf{S}_f \cdot (\boldsymbol{\nabla} T_{\mathrm{e}})^\circ_f - \sum_f^{\mathrm{nb}(C)} \kappa'^\circ_{\mathrm{vib},f} \mathbf{S}_f \cdot (\boldsymbol{\nabla} T_{\mathrm{vib}})^\circ_f + \sum_f^{\mathrm{nb}(C)} \frac{F^\circ_f}{\rho^*_f} p^\circ_f$$
$$\underbrace{- \sum_f^{\mathrm{nb}(C)} \mu^\circ_f \mathbf{S}_f \cdot \left[\left\{(\boldsymbol{\nabla} \otimes \mathbf{u})^*_f + (\boldsymbol{\nabla} \otimes \mathbf{u})^{*T} - \frac{1}{3} tr\left[(\boldsymbol{\nabla} \otimes \mathbf{u})^* + (\boldsymbol{\nabla} \otimes \mathbf{u})^{*T}\right] \mathbf{I}\right\} \cdot \mathbf{u}^*\right]_f}_{\boldsymbol{\nabla}(\boldsymbol{\tau} \cdot \mathbf{u})}$$
$$= \dot{Q}_{\mathrm{Joule}} - \dot{Q}_{\mathrm{rad}} . \quad (4.64)$$

13. Perform the following operations by using the new model library:

    I. Calculate T^*_{e}, T^*_{vib}, and T^* from e^*_{e}, e^*_{vib}, and e^*, respectively.

II. Recalculate transport properties: $\mathcal{D}_s^*$, $\mathbf{V}_s^*$, μ^*, σ^*, $\kappa_{\mathrm{vib}}'^*$, κ_{el}^*, $\kappa_{\mathrm{e,tr}}'^*$, κ^*, $\boldsymbol{\alpha}_{\mathrm{e}}^*$, $\boldsymbol{\alpha}_{\mathrm{vib}}^*$, $\boldsymbol{\alpha}^*$, ψ^*, and γ^*.

III. Recalculate isentropic compression coefficient and density: $\tilde{\psi}^* = \psi^*/\gamma^*$, $\rho^{**} = p^\circ \psi^*$.

14. Start PISO loop. In the PISO loop the pressure correction is performed. The user may define the execution number of PISO loops (number of pressure corrections) in the OpenFOAM directory `fvSchemes` under the keyword `nCorrectors`. The settings in the present work are `nCorrectors 2`, which is why the steps 15 - 19 are executed twice per each time step.

    Before starting PISO loop calculate the following quantity outside of the loop:

$$\rho_{\mathrm{ref}} = \rho_f^{**} - \tilde{\psi}_f^* p_f^\circ \ , \tag{4.65}$$

    which is necessary for assembling the pressure equation.

15. Calculate the velocity field $\mathbf{u}^{**}$ without any influence of pressure gradient by using $\mathbf{u}$ in the $\mathbf{H}$ operator (for $\mathbf{H}$ operator see Eq. 4.51) [68]:

$$\mathbf{u}_C^{**} = \left(a_C^{\mathbf{u}}\right)^{-1} \mathbf{H}(\mathbf{u}^*) \ . \tag{4.66}$$

16. Perform the following calculations:

I. Recalculate the mass flux: $F_f^* = \rho_f^{**} \mathbf{u}_f^{**} \cdot \mathbf{S}_f$.

II. Calculate the convective pressure flux for the implicit term in Eq. 4.58:

$$F_{\mathrm{p}} = \frac{\tilde{\psi}_f^*}{\rho_f^{**}} F_f^* \ . \tag{4.67}$$

III. Calculate the convective pressure flux for the explicit term in Eq. 4.58 by using the quantity ρ_{ref} calculated outside of the PISO loop in Eq. 4.65:

$$F_{\mathrm{p2}} = \frac{\rho_{\mathrm{ref}}}{\rho_f^{**}} F_f^* = \left(\rho_f^{**} - \tilde{\psi}_f^* p_f^\circ\right) \mathbf{u}_f^{**} \cdot \mathbf{S}_f \ . \tag{4.68}$$

    The derivative of F_{p2} with respect to pressure is needed for the linearisation (or implicit treatment) of the explicit convective term in the pressure equation. The derivation yields the following expression:

$$\frac{dF_{\mathrm{p2}}}{dp} = \frac{\tilde{\psi}_f^*}{\rho_f^{**}} F_f^* \ . \tag{4.69}$$

17. Solve the pressure equation for obtaining p^* (pressure correction step):

$$\frac{V_C}{\Delta t}\left(\tilde{\psi}_C^* p_C^* - \tilde{\psi}_C^\circ p_C^\circ\right) + \underbrace{\sum_f^{\mathrm{nb}(C)} F_f p_f^*}_{\substack{\text{implicit}\\ \text{convection term}}} \underbrace{\underbrace{-\underbrace{\left(\sum_f^{\mathrm{nb}(C)} F_\mathrm{p}\right) p_C^*}_{\text{implicit part}} + \underbrace{\left(\sum_f^{\mathrm{nb}(C)} F_\mathrm{p}\right) p_C^\circ + \sum_f^{\mathrm{nb}(C)} F_\mathrm{p2}}_{\text{explicit part}}}_{\text{linearised explicit convection term}} \underbrace{- \sum_f^{\mathrm{nb}(C)} \rho_f^{**} \left(a_C^{\mathbf{u}}\right)^{-1} \mathbf{S}_f \cdot (\boldsymbol{\nabla} p)_f^*}_{\text{Laplacian term}} = 0 \ . \quad (4.70)$$

This equation is a discretized compressible pressure equation (see Eq. 4.58) for the control volume C.

18. Update the face flux F_f^*:

$$F_f^{**} = F_\mathrm{p2} - \underbrace{\rho_f^{**} \left(a_C^{\mathbf{u}}\right)^{-1} \mathbf{S}_f \cdot (\boldsymbol{\nabla} p)_f^*}_{\text{pressure Laplacian in Eq. 4.70}} \ . \quad (4.71)$$

19. Update the velocity field by using the corrected pressure p^*:

$$\mathbf{u}_C^{***} = \mathbf{u}_C^{**} - (\boldsymbol{\nabla} p)_C^* \left(a_C^{\mathbf{u}}\right)^{-1} \ . \quad (4.72)$$

The pressure gradient in Eq. 4.72 is evaluated at the centroid of CV by using the face values of p^* as follows: $(\boldsymbol{\nabla} p)_C^* = \sum_f^{\mathrm{nb}(C)} \mathbf{S}_f p_f^*$. PISO loop ends with this step.

20. If the number of pressure correction steps (PISO loops) is reached, go to the next step, if not go back to step 15 and execute the pressure correction again.

21. Recalculate electron pressure required in the electron-electronic energy equation:

$$p_e^* = T_\mathrm{e}^* n_e^* k_\mathrm{B} \ . \quad (4.73)$$

22. If the PIMPLE mode is used, in this step it is reviewed whether the solution has converged. If not, the algorithm returns back to step 6 and repeats the PIMPLE loop. Since PISO mode is used in this work, this step is not performed.

23. Magnetostatic solver: The magnetostatic solver is activated at the end of each time step to update the electric and magnetic potential fields, Φ and $\mathbf{A}$, in the simulation domain. To avoid computational stiffness, a stationary solver is used for this purpose. The number of executed iterations is variable and depends on the user-defined residual values to be achieved.

    I. Manipulate the electrical conductivity σ to avoid the division by zero:

    $$\sigma = max\left(\sigma\ ,\ \ 1 \times 10^{-15}\right) \text{ for each computational cell.} \tag{4.74}$$

    This step is necessary for the numerical solution of the Laplace equation.

    II. Start the iterative solution.

    III. Solve the Laplace equation for Φ:

    $$\sum_{f}^{\mathrm{nb}(C)} \sigma_f^* \mathbf{S}_f \cdot (\boldsymbol{\nabla}\Phi)_f^* = 0\ . \tag{4.75}$$

    IV. Solve the Poisson equation for $\mathbf{A}$:

    $$\sum_{f}^{\mathrm{nb}(C)} \mathbf{S}_f \cdot (\boldsymbol{\nabla} \otimes \mathbf{A})_f^* = \sigma_C^* \mu_C \underbrace{\sum_{f}^{\mathrm{nb}(C)} \mathbf{S}_f \Phi_f^*}_{(\boldsymbol{\nabla}\Phi)_C^*}\ . \tag{4.76}$$

    The quantity μ in Eq. 4.76 denotes the magnetic permeability.

    V. Check if the solution has converged. If not, go back to step $23 - III$.

    VI. Recalculate σ to remove the manipulation in step $23 - I$.

24. Set solution at current time step to the converged solution.

25. End of time loop: If the simulation time is reached, stop the algorithm. If not, go back to step 3 and repeat the time loop.

4.5.3 Two Operational Modes of the Magnetostatic Solver

The magnetostatic solver has two different operating modes regarding the calculation of the electric-potential boundary condition at the cathode Φ_c. The anode-potential boundary condition is always set to zero: $\Phi_a = 0$. The potential difference across the electrodes (electrode voltage drop) is calculated as follows: $\Delta\Phi = \Phi_a - \Phi_c$.

Magnetostatic Solver: Mode 1

The electrical potential at the cathode, Φ_c, is not predefined by the user but calculated by the solver at each time step. The only quantities given by the user are the maximum power of the arc discharge $P_{\max}$, the internal resistance of the electrical

circuit R_i (but not of the plasma arc), and the maximum potential difference across the terminals of the power supply $\Delta\Phi_\mathrm{max}$. The cathode potential for the current time step is calculated as follows:

$$\Phi_c^* = max\left[-\frac{P_\mathrm{max}}{I_c^\circ},\quad (-\Delta\Phi_\mathrm{max} + I_c^\circ R_\mathrm{i})\right]\ . \tag{4.77}$$

The cathode current is calculated by the relation: $I_c^\circ = \mathbf{J}_c^\circ \cdot \mathbf{S}_c$, where $\mathbf{S}_c$ denotes the cathode-surface vector. The cathode-surface current density $\mathbf{J}_c$ is obtained by the generalized Ohm's law given in Eq. 3.125. The electrical conductivity σ in Eq. 3.125 is taken from the cathode surface where it is obtained by interpolation from the first cell layer (zero-gradient boundary condition).

The calculated boundary condition Φ_c is used for computing the fields Φ and $\mathbf{A}$ in the simulation domain. From these values the fields $\mathbf{E}$, $\mathbf{B}$ and $\mathbf{J}$ are calculated. The advantage of this procedure is that the unknown value of Φ_c is calculated directly by the solver. The drawback of this operational mode lies in very long calculation times, because even small changes in σ on the cathode surface lead to changes in $\mathbf{J}_\mathrm{c}$. Therefore Φ and $\mathbf{A}$ have to be recalculated at each time step, which increases the computation effort considerably.

Magnetostatic Solver: Mode 2

The value of Φ_c is not modelled, but is defined by the user. This reduces the calculation effort enormously, since the recalculation of the fields Φ and $\mathbf{A}$ is associated with minimal effort. However, this reduces the modelling depth.

It is therefore recommended to use the solver in mode 1 until the quasi-stationary state in the gas discharge is reached. After that, the modelled average of Φ_c calculated by the solver in mode 1 can be used as the user defined value in mode 2 to reduce the computation time.

Chapter 5

Solver Validation and Simulation Results

This chapter deals with the validation of the new numerical solver and the evaluation of the simulation results. The validation is carried out by comparing the simulation results of the system under investigation - a surface discharge in a supersonic flow - with experimental measurements and analytically calculated values.

5.1 General Information on Solver Verification and Validation

The solver verification and validation are structured as follows: a one-dimensional analysis, which is presented in Appendix C, and a three-dimensional analysis, which is discussed in this chapter. The 1-D analysis is carried out for the verification of the chemical module of the solver as well as all submodels for the calculation of transport and thermodynamic properties. For the 3-D analysis, the test case defined in Chapter 2 is used, because it exemplarily represents the field of application of the new solver. During the 3-D validation, the simulation results are compared with analytical calculations from Chapter 2 and the experimental measurements presented in Appendix D.

5.1.1 One-Dimensional Solver Verification

In the frame of the 1-D analysis, a total of 12 numerical calculations are carried out for a temperature range from 2000 K to 24,000 K with temperature increments of 2000 K. The results of this analysis are presented in Appendix C. Physically, the 1-D test case may be interpreted as a thin tube in a constant temperature heat bath. Since the new solver is transient, the simulations are transient as well. Each of the twelve simulations is carried out until the thermal and chemical equilibria are reached, that is: $T \approx T_\mathrm{e} \approx T_\mathrm{vib}$ and $c_s \approx const$, where s stands for each species.

The results of the 1-D analysis for the kinetic and thermodynamic properties

generally show very good agreement with the analytically calculated data, with the exception of the specific heat capacity, which drops in the temperature range between 12,000 K and 20,000 K up to 6.7 % below the analytical data. From 20,000 K, however, the deviation reduces to $2-3$ %.

The verification of the transport properties shows that at temperatures below the characteristic temperature of the system under investigation (T_c = 12,000 K), all models show a good agreement with other research works, except for the viscosity model, which delivers significantly higher values already at $T > 10{,}000$ K. At temperatures above T_c, the radiation model used provides overestimated values, while the electrical and thermal conductivities are underestimated by $8-12$ %.

5.1.2 Three-Dimensional Solver Validation

The multidimensional analysis is performed by means of a 3-D simulation. An attempt to simulate this system in two dimensions would not consider the energy losses in the arc column due to lateral heat diffusion, which would affect the energy balance in the system. During this multi-dimensional analysis, the validation of the fluid dynamic and electrodynamic modules of the numerical solver is carried out.

5.1.3 Experimental Measurements

The experimental measurements discussed in Appendix D are performed to obtain the temperature and pressure distributions in the arc discharge and in its vicinity.

All temperature measurements are conducted with a constant arc input power of 10 kW. For the surface pressure distribution, however, only experimental results of plasma arcs with uncontrolled capacitor discharge are available. Nonetheless, in the present work, an attempt is made to use these data for validation as well.

5.2 Data for Three-Dimensional Solver Validation

Two types of information sources are generally used for the 3-D solver validation:

- Analytical calculations of the system under investigation in Sec. 2.1 - 2.3.
- Data obtained from the experimental measurements described in Appendix D.

In the following, all data available for solver validation are summarized in Tab. 5.1 – 5.4. In addition, following two conclusions can be made:

- In the centre line of the electric discharge, thermal equilibrium is expected. At the gas discharge periphery, however, nonequilibrium may occur, since a deviation between $\overline{T}_{vib}$ and $\overline{T}_{rot}$ is experimentally measured.
- Quasineutrality in the system may not be guaranteed because the ambipolar diffusion model used does not include calculation of polarization fields and the resulting restoring forces in the case of charge separation (see Sec. 3.2.3).

Table 5.1: Data obtained from analytical calculations in Sec. 2.1.

quantity	description	value
p_∞	free-stream pressure	0.34 bar
p_2	pressure behind the shock wave	1.4866 bar
T_∞	free-stream translational-rotational temperature	234 K
T_2	translational-rotational temperature behind the shock wave	389 K
u_∞	free-stream velocity magnitude	1452.44 $\mathrm{m \cdot s^{-1}}$
u_2	velocity magnitude behind the shock wave	1335 $\mathrm{m \cdot s^{-1}}$
ρ_∞	free-stream density	0.4893 $\mathrm{kg \cdot m^{-3}}$
ρ_2	density behind the shock wave	1.2855 $\mathrm{kg \cdot m^{-3}}$
β	oblique shock wave angle	25.1°

Table 5.2: Data obtained from the calculation of characteristic values for a 10 kW nitrogen gas discharge at 1 atm in Sec. 2.3.1.

quantity	description	value
E_c	electric field magnitude in the positive column	2.0×10^4 $\mathrm{V \cdot m^{-1}}$
B_c	induced magnetic field magnitude in the positive column at a distance of 1 mm from the centre line	1.6×10^{-2} T
T_c	translational-rotational temperature in the centreline of the positive column	12,000 K

Table 5.3: Data obtained from time-resolved emission spectroscopy.

quantity	description	value
$\overline{T}_\mathrm{rot}$	mean rotational temperature from exp. 1 and 3 only	7017 K
$\overline{T}_\mathrm{vib}$	mean vibrational temperature from exp. 1 and 3 only	8306 K
$\overline{T}_\mathrm{el}$	mean electronic-excitation temperature from exp. 4	10,672 K
$\overline{U}$	electrical voltage at the electrodes during the discharge	$120 - 128$ V
$\overline{I}$	electric current in the electrical circuit during the discharge	$79 - 80$ A

Table 5.4: Data obtained from pressure measurements.

quantity	description	value
p	pressure in the discharge between the electrodes b and c	$\approx 1.85 \pm 0.05$ bar
p_s	surface pressure on the wedge outside the gas discharge	$\approx 1.45 \pm 0.05$ bar

5.3 Three-Dimensional Test Case

5.3.1 Computational Grid

In the frame of the 3-D analysis, the symmetry of the aerodynamic model is exploited in order to reduce the size of the computational domain (see Fig. 5.1). Only a quarter of the wedge surface is considered, namely the electrode side of the wedge, of which only one half is modelled due to the symmetry.

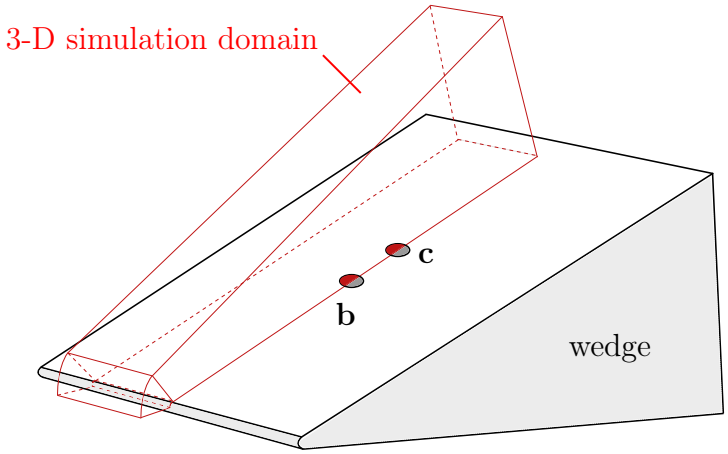

Figure 5.1: Location of the 3-D simulation domain on the wedge.

The computational grid used for the three-dimensional analysis is shown in Fig. 5.2. The overall domain bounding box has a length of 0.29 m, a height of 0.18 m and a depth of 0.03 m. The grid is created using the mesh generation utility, *blockMesh*, supplied with OpenFOAM. It is a three-dimensional block structured computational grid consisting of 1.88 million hexahedral cells. The mesh density is increased at the leading edge of the wedge, towards the wedge surface, and in the vicinity of the electrodes (see Fig. 5.2). The thickness of the first computational cell layer on the wedge surface amounts to ≈ 32 μm. This grid density at the surface is sufficient for the resolution of a laminar boundary layer profile (as a reminder: in the present work the laminar assumption is used for the flow).

In the following, using the equations for the flat-plate boundary layer theory given in Schlichting [69], it is examined which near-wall mesh density would be necessary for resolving a turbulent boundary layer. The equations are as follows:

$$y = \frac{y^+ \mu}{\rho u_*} \ , \tag{5.1}$$

$$u_* = \frac{\tau_\mathrm{w}}{\rho} \ , \tag{5.2}$$

$$\tau_\mathrm{w} = C_\mathrm{f} \frac{1}{2} \rho u_\infty^2 \ , \tag{5.3}$$

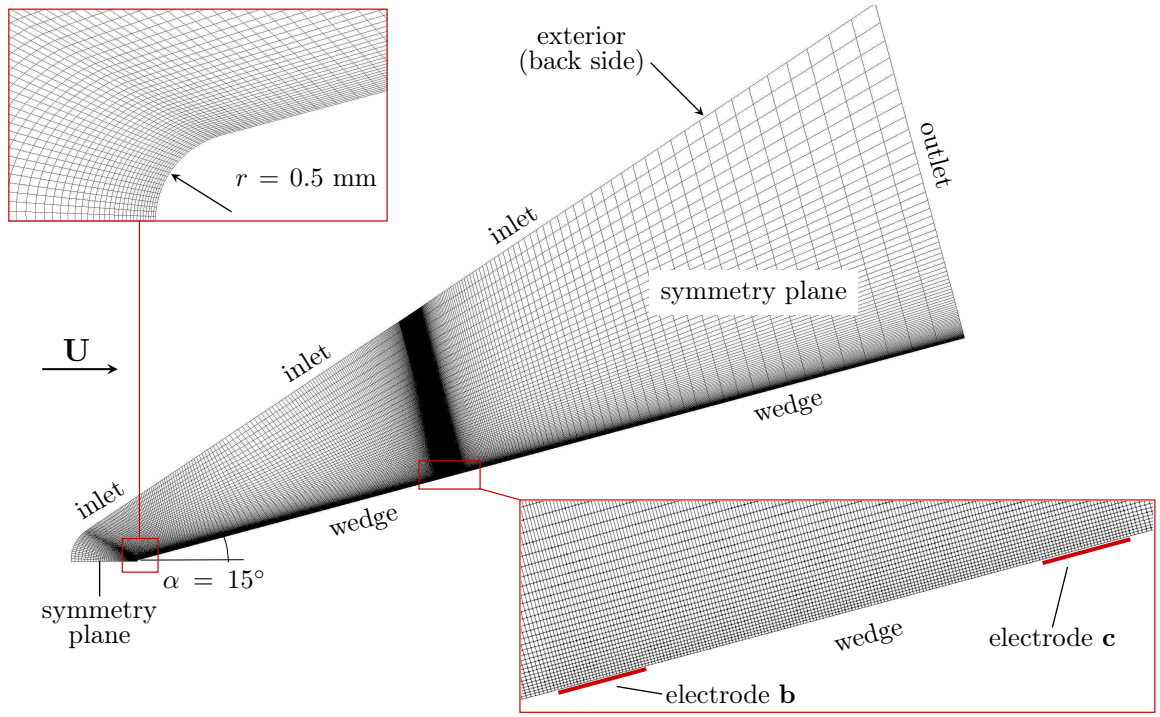

Figure 5.2: Computational grid for the 3-D analysis.

$$C_f = (2\ log_{10}(Re_x) - 0.65)^{-2.3} \quad \text{for } Re_x < 10^9\ , \tag{5.4}$$

$$Re_x = \frac{\rho u_\infty x}{\mu}\ . \tag{5.5}$$

The quantities y^+, y, u_*, τ_w, and C_f denote the so-called dimensionless wall distance, the absolute distance from the wall, the friction velocity, the wall shear stress and the skin-friction correlation, respectively. Re_x is the Reynolds number based on the current length x, which is chosen as the distance from the leading edge of the wedge to the electrode b. For a correct resolution of a turbulent boundary layer, the first cell centre must be placed in the viscous sublayer, that is y^+ must be approximately 1 (the value of 5 must not be exceeded). When inserting the stream-flow properties that prevail behind the oblique shock wave ($u_\infty = 1334\ \mathrm{m \cdot s^{-1}}$, $\mu = 2 \times 10^{-5}\ \mathrm{kg \cdot m^{-1} \cdot s^{-1}}$, $\rho = 1.27\ \mathrm{kg \cdot m^{-3}}$, $x = 0.1$ m), the following value is obtained: $y = 3.2 \times 10^{-7}$ m $= 0.32\ \mu$m. That means for a good resolution of the turbulent boundary layer, the thickness of the first cell layer should be $\approx 0.7\ \mu$m. This means that the grid spacing at the wedge surface in the 3-D mesh used in the present work would not suffice for a turbulent flow. Although the computational grid used is sufficiently dense for the resolution the laminar velocity and temperature profiles at the wall, it is assumed that a higher grid density in the near-wall zone is required in order to resolve the physicochemical processes at the cold surface more precisely.

5.3.2 Boundary Conditions

The boundary conditions used in the 3-D simulations are listed in Tab. 5.5.

Table 5.5: 3-D test case boundary conditions.

variable	inlet	outlet	wedge	cathode	anode	exterior
$\mathbf{u}\ \left[\frac{\mathrm{m}}{\mathrm{s}}\right]$	(1443, 0, 0)	$\frac{\partial u_i}{\partial n}=0$	(0, 0, 0)	(0, 0, 0)	(0, 0, 0)	$\frac{\partial u_i}{\partial n}=0$
$T\ [K]$	234	$\frac{\partial T}{\partial n}=0$	calculated[a]	calculated[a]	calculated[a]	$\frac{\partial T}{\partial n}=0$
$T_{\mathrm{vib}}\ [K]$	$T_{vib}=T$	$\frac{\partial T_{vib}}{\partial n}=0$	calculated[a]	calculated[a]	calculated[a]	$\frac{\partial T_{vib}}{\partial n}=0$
$T_{\mathrm{el}}\ [K]$	$T_{el}=T$	$\frac{\partial T_{el}}{\partial n}=0$	calculated[a]	$\frac{\partial T_{el}}{\partial n}=0$	$\frac{\partial T_{el}}{\partial n}=0$	$\frac{\partial T_{el}}{\partial n}=0$
$p\ [bar]$	0.34	$\frac{\partial p}{\partial n}=0$	$\frac{\partial p}{\partial n}=0$	$\frac{\partial p}{\partial n}=0$	$\frac{\partial p}{\partial n}=0$	$\frac{\partial p}{\partial n}=0$
$c_{\mathrm{N_2}}\ [-]$	1.0	$\frac{\partial c}{\partial n}=0$	$\frac{\partial c}{\partial n}=0$	$\frac{\partial c}{\partial n}=0$	$\frac{\partial c}{\partial n}=0$	$\frac{\partial c}{\partial n}=0$
$c_{\mathrm{N,N_2^+,N^+,}e}\ [-]$	0.0	$\frac{\partial c}{\partial n}=0$	$\frac{\partial c}{\partial n}=0$	$\frac{\partial c}{\partial n}=0$	$\frac{\partial c}{\partial n}=0$	$\frac{\partial c}{\partial n}=0$
$\mathbf{A}\ \left[\frac{\mathrm{kg\ m}}{\mathrm{s^2\ A}}\right]$	(0, 0, 0)	(0, 0, 0)	$\frac{\partial A_i}{\partial n}=0$	$\frac{\partial A_i}{\partial n}=0$	$\frac{\partial A_i}{\partial n}=0$	(0, 0, 0)
$\Phi\ \left[\frac{\mathrm{kg\ m^2}}{\mathrm{s^3\ A}}\right]$	$\frac{\partial \Phi}{\partial n}=0$	$\frac{\partial \Phi}{\partial n}=0$	$\frac{\partial \Phi}{\partial n}=0$	calculated[b]	0.0	$\frac{\partial \Phi}{\partial n}=0$

[a] If for the temperature value in the first cell on the wedge surface the following applies: $T < T_{\max}$, then $\frac{\partial T}{\partial n}=0$, otherwise $T_{\max}$, which is 2900 K for the electrodes, 1000 K for T and T_{vib} and 5000 K for T_{e} for the wedge surface.
[b] Φ-value on the cathode surface is calculated via mode 1 (see Sec. 4.5.3).

According to Wendelstorf [20], near the electrode surfaces, the electron temperature decouples from the heavy particles temperature. Wendelstorf states that while the heavy particles equilibrate with the electrode solid, a thermal isolation of the electron gas occurs at the electrode surface due to sheath effects. For this reason, the zero gradient boundary condition is used for the electron-electronic temperature at the electrode surface, while for T and T_{vib}, the temperature is limited to the copper evaporation temperature of 2900 K. Further, for T and T_{vib}, the temperature at the wedge surface is limited to a maximum of 1000 K to model the cold wall. The electron-electronic surface temperature is limited to a maximum of 5000 K, because only from this temperature the electronic excitation and the presence of free electrons, including all associated transport processes, become noticeable. Physical phenomena on the cold wall have not been investigated in the present work (e.g. no finite-catalytic wall model). That is, chemical and thermodynamic properties, such as electronic and vibrational thermal conductivities on the surface are currently unknown. For this reason, the wall-surface values of the following quantities are obtained by the interpolation from the first cell layer (zero-gradient boundary condition): κ_{vib}, $\kappa_{\mathrm{e,tr}}$, κ_{el}, κ_{tr}, κ_{rot}.

5.3.3 Solver Settings

Spatial and Temporal Discretization

For spatial discretization of the convection terms, a high-resolution scheme is used in which the second-order central differencing scheme and the Sweby limiter are utilized for the higher-order correction. The diffusion terms are evaluated using the Green-Gauss method for gradient evaluation and the central-differencing interpolation scheme with an explicit non-orthogonality correction. All other gradient-containing terms are evaluated via the Green-Gauss method using linear interpolation. For the interpolation of the energy and temperature gradients an additional limiting scheme is switched on. The methods mentioned are discussed in detail in Sec. 4.4. For the temporal discretization the implicit first-order Euler scheme is used.

Computational Time Step

Based on the experience gained in the present work, it can be stated that the size of the maximum possible simulation time step decreases with increasing gas temperature. Exceeding this time step leads to oscillations of the source terms in the governing conservation equations for e_e, e_vib and e, since all three energy equations are solved in a segregated manner and thus their source terms can only be implemented semi-implicitly or explicitly. The oscillations would eventually result in the crash of the chemical solver. While a time step of $\Delta t = 1 \times 10^{-6}$ s is absolutely sufficient at 4000 K, a time step of $\sim 10^{-9}$ s has to be used at gas temperatures of 24,000 K. At temperatures that significantly exceed the 30,000 K mark, an even smaller time step may be required. In the present work the temperature at the edge of the cathode approaches 30,000 K and the time step used amounts to 2.0×10^{-10} s.

Linear Solver Settings

The following iterative methods (linear solvers) are used for the solution of linear algebraic equation systems:

- The variable ρ is obtained by explicitly solving the mass conservation equation, Eq. 4.59, by means of the diagonal solver, which is a direct method for solving linear algebraic systems of equations [60].
- The variables $\mathbf{A}$, p, $\mathbf{u}$, e_e, e_vib, e, and c_s are calculated by using the stabilised Bi-Conjugate Gradient solver (*BiCGStab*). The preconditioning of the coefficient matrices is carried out with the diagonal incomplete-LU preconditioner (*DILU*) developed for asymmetric matrices.
- For the calculation of Φ *smoothSolver* is used, which is an iterative solver that uses a smoother. The smoother used is *DICGaussSeidel*, which is a diagonal-based incomplete Cholesky smoother for symmetric matrices where smoothing is carried out by a Gauss-Seidel solver to ensure that any "spikes" created by the DIC sweeps are smoothed out [60].

5.3.4 Simulation Procedure

The simulation procedure is as follows:

1. The electrodynamic module of the new solver is switched to mode 1. The maximal power $P_{\max}$ is set to 10 kW. The maximal voltage at the terminals of the power supply $\Phi_{\max}$ and the internal resistance of the electrical circuit R_{i} are set to 450 V and 0.5 Ω, respectively.
2. After 1.4 ms of the simulated time, a quasi-stationary flow stream is formed past the wedge and the gas discharge can be ignited.
3. With the help of additional ignition source terms in the energy conservation equations, the gas is locally heated between the electrodes to a temperature of over 5000 K. As a result, the gas becomes electrically conductive and the Joule heating between the electrodes builds up.
4. The Joule heating leads to a further increase in the temperature and consequently to a more intensive ionization of the gas eventually resulting in a self-sustaining gas discharge.
5. After a quasi-steady state is reached in the electric arc, the electrodynamic module is switched from mode 1 to mode 2.
6. The simulation is executed until the desired time. If necessary, the solver is repeatedly switched from mode 2 to mode 1 in order to verify the Φ_{c} value.

For the simulation, parallel computing is used. The computational mesh and the associated field data are decomposed into 32 parts using the *decomposePar* utility provided with OpenFOAM. The parallel calculation is carried out via the openMPI implementation (an open source Message Passing Interface). For the calculation a server equipped with 2 Intel Xeon Gold 6130 processors is used with 16 cores each.

In Appendix E, computational costs are discussed. All values and calculations presented are given first only for the system under investigation. Subsequently, possibilities for enhancing the speed of numerical calculations are discussed.

5.4 Flow Conditions across the Oblique Shock

Fig. 5.3, left, shows the simulation results for the static pressure field around the wedge. The oblique shock formed on the leading edge is clearly recognizable. The simulation results yield a wave angle value of approximately 25°. This value is in a good correlation with the analytically calculated value of 25.1° in Sec. 2.1 (see Tab. 5.1). Thus, it can be stated that the numerical solver correctly reproduces the shock-wave theory at least for the system to be analysed.

Fig. 5.3, right, shows the line of data capturing across the oblique shock for the pre- and post-shock validation of the flow variables p, T, ρ and the velocity magnitude u. In Fig. 5.4, the simulation results of the pressure profile across the oblique

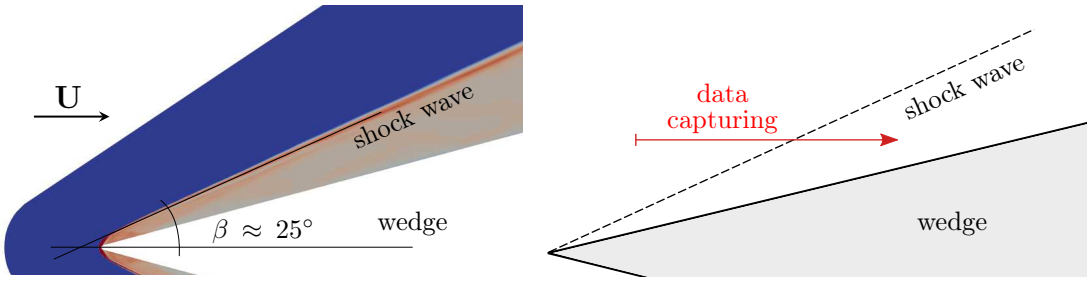

Figure 5.3: Shock wave angle measurement by using the static pressure field (left). Data capturing across the shock wave (right).

shock together with the analytical calculations are presented. It can be seen that the shock wave resolution is rather poor, which is due to the low computational grid density in the zone of shock propagation (see Fig. 5.2). An excellent agreement is observed between the simulation results and the analytical calculations of pressure. Furthermore, the simulated pressure values are in a good correlation with the experimentally obtained results: 0.34 bar for the pre-shock and 1.45 ± 0.05 bar for the post-shock pressure (see Tab. 5.4).

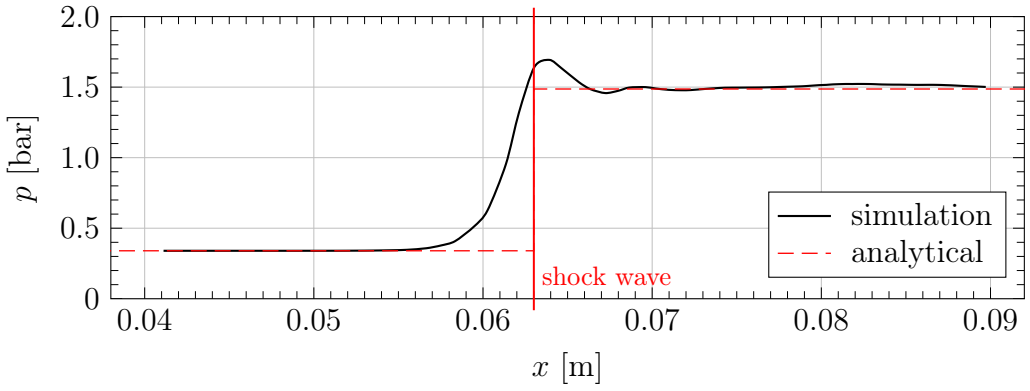

Figure 5.4: Static-pressure profile across the oblique shock at $M_\infty = 4.5$.

Fig. 5.5 and 5.6 show the temperature and mass density profiles across the shock wave. In Fig. 5.7 the velocity magnitude u parallel to the free-stream velocity $\mathbf{u}_\infty$ is plotted across the oblique shock. For all three flow variables, an excellent agreement of the simulation results with the analytical calculations is found.

Overall, it can be stated that the numerical solver correctly reproduces both the flow pattern and the thermodynamic conditions in front of the shock and behind it in a nitrogen flow at Mach 4.5.

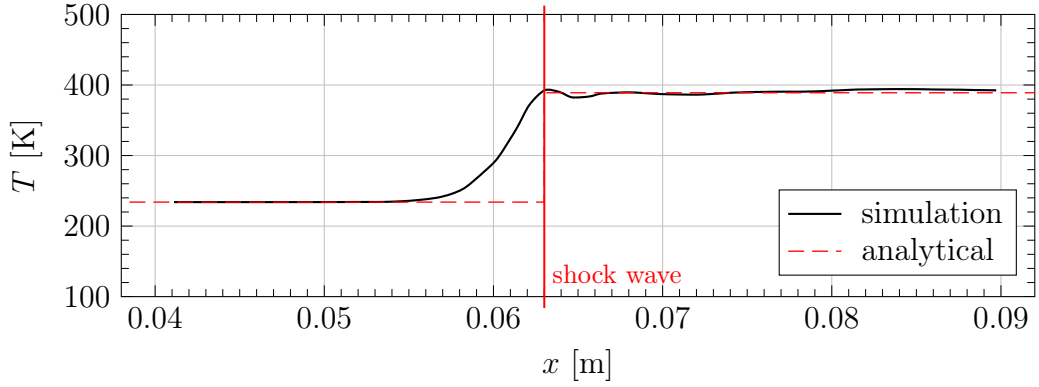

Figure 5.5: Translational-rotational temperature profile across the oblique shock in a nitrogen flow at $M_\infty = 4.5$.

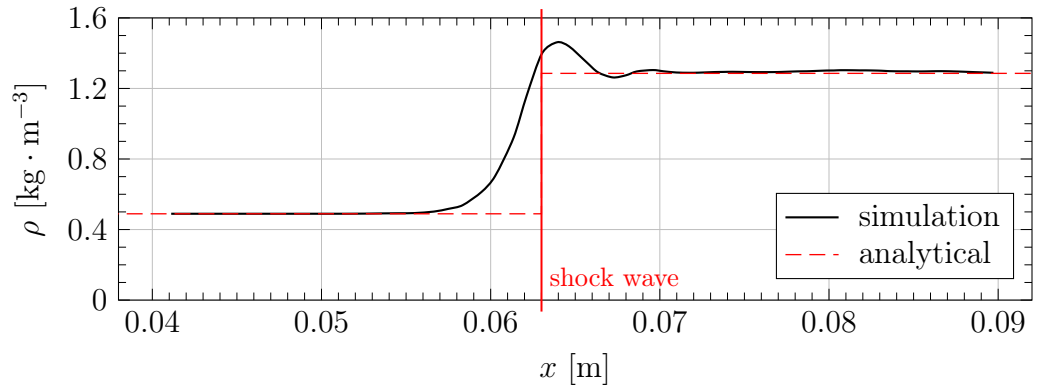

Figure 5.6: Mass-density profile across the oblique shock at $M_\infty = 4.5$.

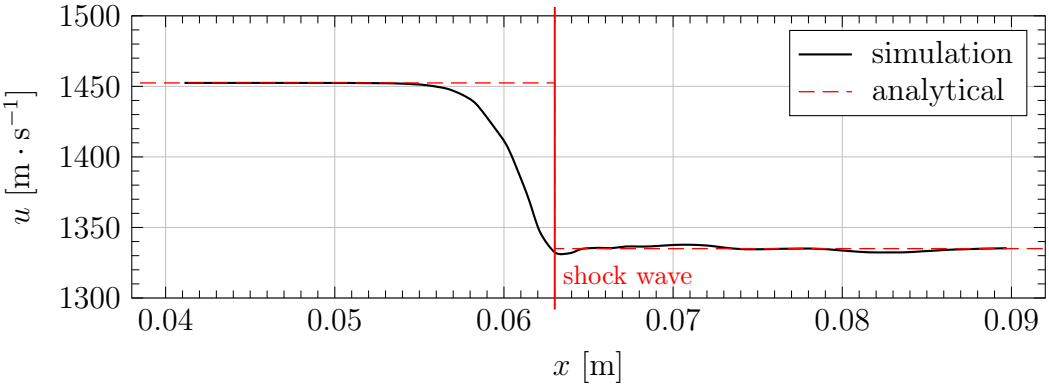

Figure 5.7: Velocity-magnitude profile parallel to the free stream velocity $\mathbf{u}_\infty$ across the oblique shock at $M_\infty = 4.5$.

5.5 Gas Discharge Geometry and Impact on the Flow

5.5.1 Impact of the Gas Discharge on the Flow

In the present analysis, only a very short operating time of the gas discharge of approx. 75 μs is simulated due to the high computational effort and limited computing resources. Nevertheless, this simulation time is sufficient to reach a quasi-steady state in the gas discharge and its vicinity. Due to the electric arc, a shock wave builds up and eventually interacts with the oblique shock, as shown in Fig. 5.8. This shock wave is rather unsharp due to the low computational grid density in the regions further away from the discharge (see Fig. 5.2). Physically, this shock wave is caused by the rapid local temperature increase due to the strong energy input associated with the gas discharge. As a result of the temperature increase, the flow stagnates and a local high-pressure zone is created, which acts as an obstacle on the flow.

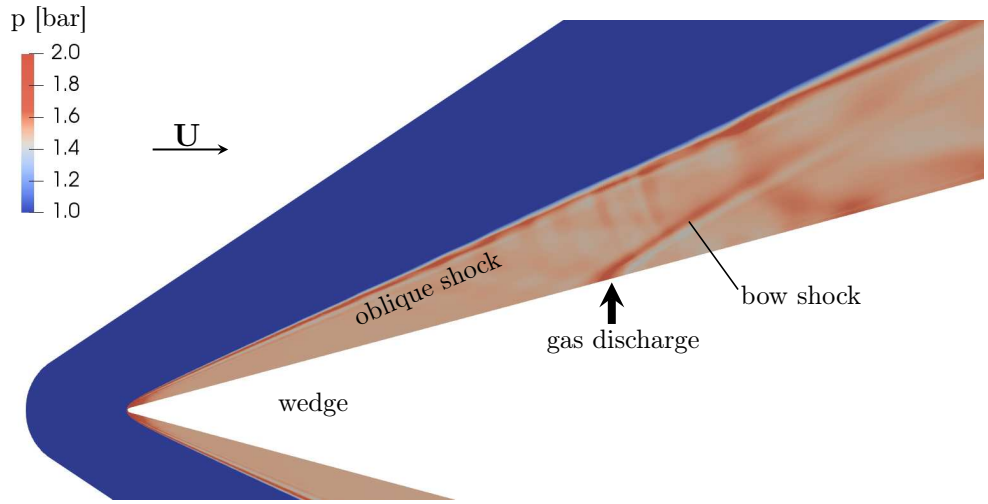

Figure 5.8: Static pressure field around the wedge at Mach 4.5. The location of the electric discharge is marked with an arrow.

5.5.2 Gas Discharge Geometry

Fig. 5.9 shows the three-dimensional view of the gas discharge under investigation. The peripheral temperature of the arc column T_R is set to 5000 K, that is all control volumes in the simulation domain with $T < 5000$ K are blanked out. The distance between the symmetry axes of the electrodes amounts to 6 mm. The fact that the electric discharge is stretched by the supersonic flow and pressed against the surface leads to a rather flat and wide shape of the arc column.

In Fig. 5.10, the cross-section through the gas discharge direct above the wedge surface is presented. It can be seen that the translational-rotational temperature at the cathode edge facing the anode reaches 30,000 K, while the temperature of the rest of the cathode surface is significantly lower. In contrast, the anode surface

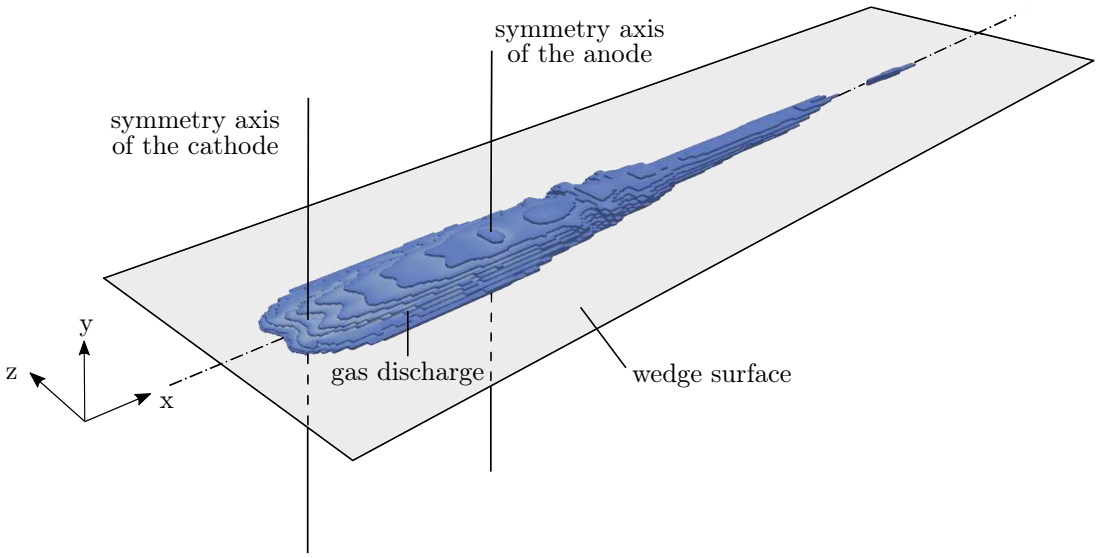

Figure 5.9: 3-D view of the gas discharge at the wedge surface. Peripheral temperature of the arc column is set to $T_{\mathrm{R}} = 5000$ K.

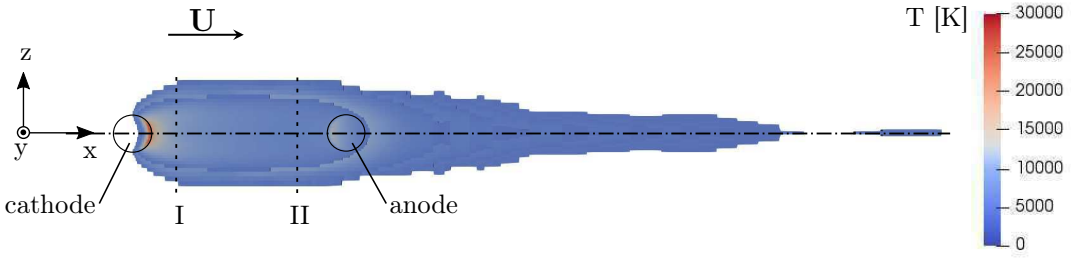

Figure 5.10: Cross-section through the gas discharge above the wedge surface.

is completely covered by the hot tail of the gas discharge in which temperatures of approximately 10,000 K to 15,000 K prevail. This is consistent with the erosion traces on the electrode surfaces shown in Fig. 2.6 where the electrode erosion is limited to the right edge of the cathode and is distributed over the entire anode surface.

As can be observed in Fig. 5.11, the gas discharge downstream of the anode lifts off slightly from the surface and forms a tail. Fig. 5.12 shows two cross-sections of the gas discharge: one at 1 mm behind the cathode and another at 1 mm in front of the anode. The width of the gas discharge is in both cases approximately 2.8 mm. The heights of the arc column at these two points are approx. 0.3 mm and 0.5 mm, respectively. According to Wells [35], an axially-symmetrical uniform arc column with $\mathcal{P} = 10$ kW $\cdot$ cm^{-1} and $\mathcal{E} > 40$ V $\cdot$ cm^{-1} has an arc radius of ≈ 1.75 mm. At higher electric fields and input power this diameter would further decrease with a strongly declining tendency. In the present work, $\mathcal{E} \approx 200$ V $\cdot$ cm^{-1} and the input power per centimetre amounts to 20 kW $\cdot$ cm^{-1}. Furthermore, the electric arc to be examined is a surface discharge and thus its radius is not constant. Nonetheless, the

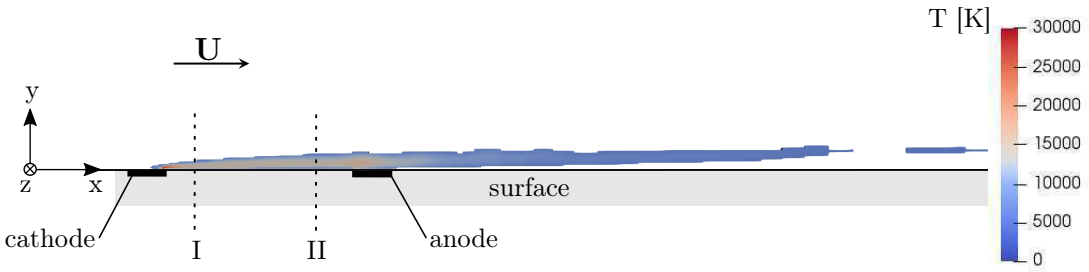

Figure 5.11: Cross-section through the symmetry plane of the arc (x-y-plane).

width of the gas discharge of 2.8 mm correlates well with the estimations of Wells near the wedge surface, where the flow velocity is low. In addition, it can be stated that the radius of the positive column $r_{\mathrm{pc}} = 1 \times 10^{-3}$ m chosen in Sec. 2.3.1 for the characteristic length of the system represents a reasonable estimate.

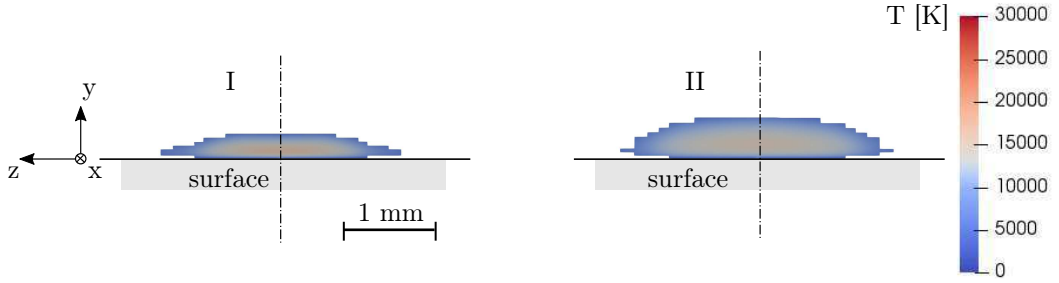

Figure 5.12: Cross-sections through the arc column 1 mm downstream of the cathode (left) and 1 mm upstream of the anode (right).

5.6 Flow Variables across the Gas Discharge

In this section, the impact of the gas discharge on the flow variables T, T_{vib}, T_{e}, p, ρ and $\mathbf{u}$ in its vicinity is discussed.

5.6.1 Data Acquisition from 3-D Simulation Results

For the qualitative evaluation of the 3-D simulation results, the two planes shown in Fig. 5.13 are used. The x-y-plane is the symmetry plane of the gas discharge. The y-z-plane is placed perpendicular to the flow in the middle between the electrodes.

For the quantitative evaluation, data are collected along the following lines:

- Data along the centre line of the gas discharge: x-line (see Fig. 5.14 left). This line is located 0.1 mm above the surface.
- Data acquisition along the y- and z-axes in the middle between the electrodes in the y-z-plane: y1- and z1-lines (Fig. 5.14 right). The z1-line passes the

locations of the pressure transducers P15, P30, and P45. The z1-line is located 0.1 mm above the surface.

- Data acquisition along the y- and z-axes in the middle of the imaged volume V_M – the measuring point used in the time-resolving emission spectroscopy for temperature measurements: y2- and z2-lines (see Fig. 5.14 right).

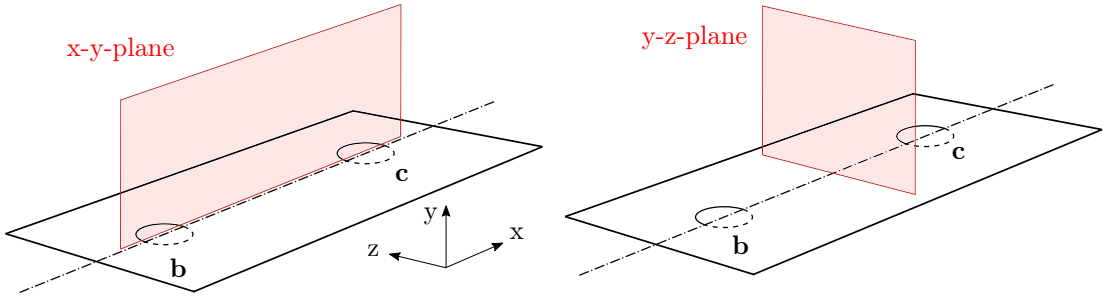

Figure 5.13: Data acquisition from 3-D simulations: x-y-plane crossing the electrodes b and c (left), y-z-plane perpendicular to the arc centre line (right).

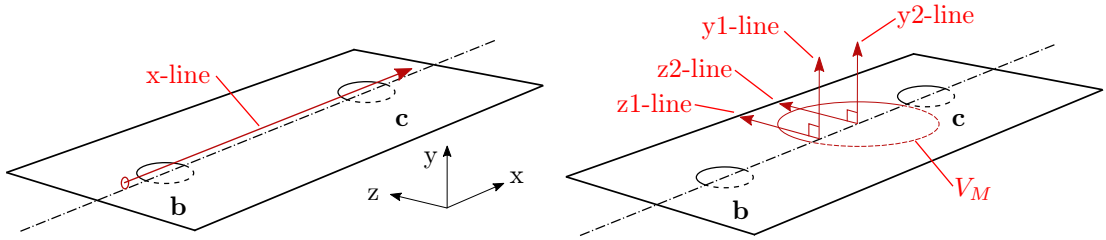

Figure 5.14: Data capturing along the x-axis between the electrodes b and c (left). Data capturing along the y- and z-axes (right). Location of the image volume of the spectroscopic measurements V_M is marked with a circle.

5.6.2 Gas Discharge Impact on the Flow Variables

Gas Discharge Impact on Temperature Field

In Fig. 5.15 the translational-rotational temperature field in the gas discharge is depicted. Fig. 5.16 shows the distributions of T, T_{vib}, and T_e along the x-line. This line runs 0.1 mm above the surface and therefore does not capture the hottest zones at the edges of the electrodes. For this reason, in Fig. 5.16 the highest temperatures in the near-electrode constriction zones are additionally indicated by markers. It can be seen that the temperature profiles in the positive column have a nearly linear distribution, while temperature peaks occur near the electrode edges in the near-electrode zones. This temperature pattern is consistent with the theoretical temperature distribution in the centre line of a free burning axially-symmetrical electric arc shown in Fig. 2.10. The temperature peaks, especially at the cathode, result from the electric

field peaks and the associated increased Joule heating in the near-electrode constricted zones. The temperature in the gas column, where the experimental temperature measurements were carried out, is on average 15,000 K.

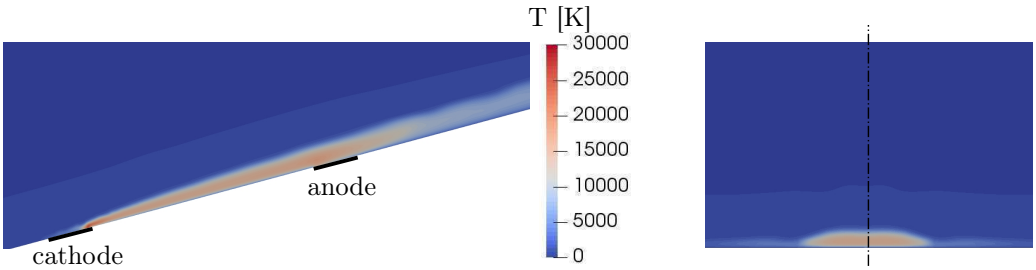

Figure 5.15: Simulation results of the translational-rotational temperature field: x-y-plane (left), y-z-plane (right).

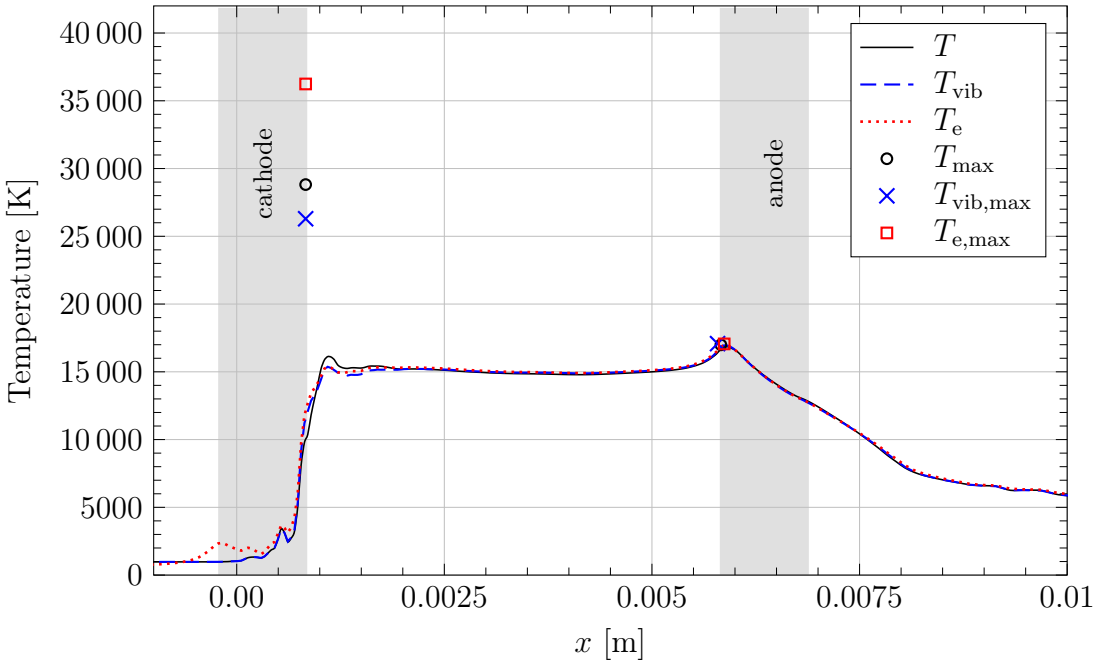

Figure 5.16: Simulation results of T, T_{vib} and T_{e} along the x-line plotted 100 μm above the wedge surface. The highest temperatures in the near-electrode constriction zones are indicated by markers.

In Figs. 5.17 and 5.18, temperature profiles together with the corresponding percentage deviations of T_{vib} and T_{e} from T along the y- and z-axes 1.5 mm upstream of the anode (y2- and z2-lines) are shown. It may be observed that significant deviations from LTE occur in the areas with temperatures below 11,000 K, that is at the wall and towards the arc periphery. They reach $5-7$ % for T_{vib} and >10 % for T_{e}. In the centreline of the plasma column, the deviations of T_{vib} and T_{e} from T are only $1-2$ %.

Therefore, in the centreline the plasma is close to local thermodynamic equilibrium. This is to be expected for collision-dominated high-pressure ($p > 0.1$ bar) thermal arcs, such as the system under investigation.

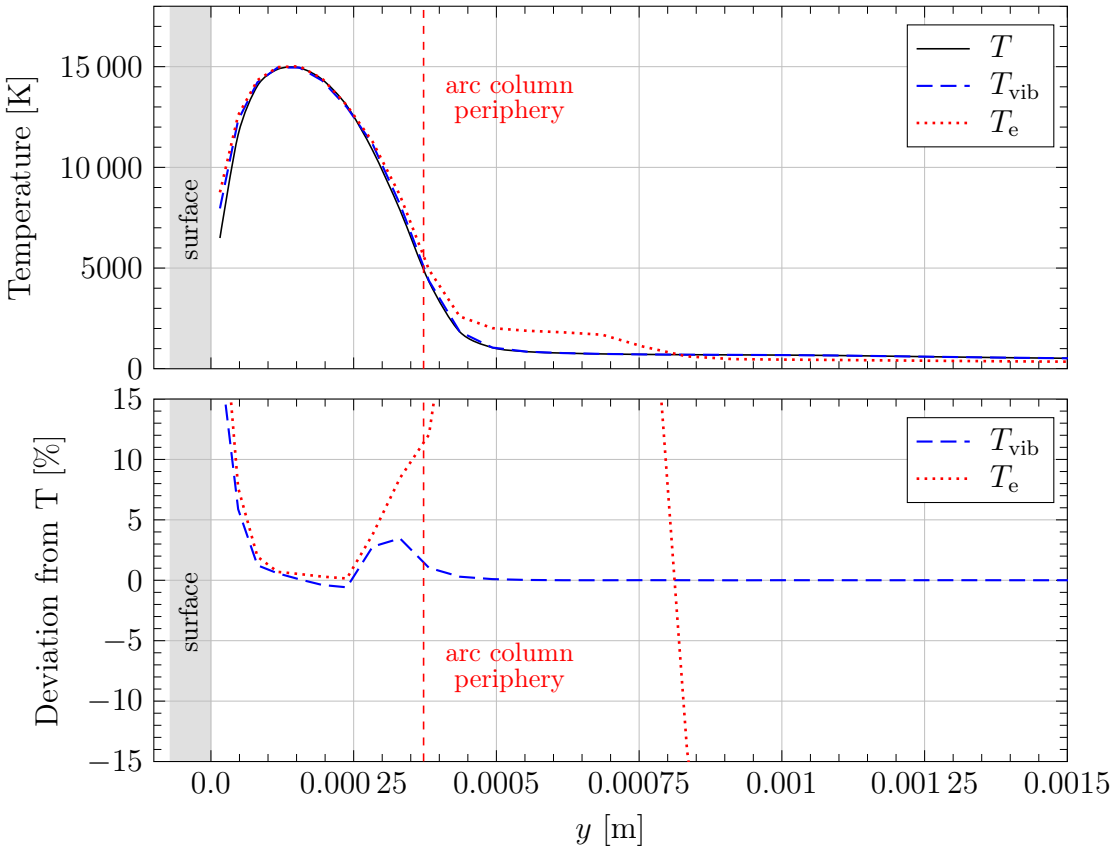

Figure 5.17: Simulation results of T, T_{vib} and T_e along the y2-line (top) and the corresponding percentage deviations of T_{vib} and T_e from T (bottom).

When analysing the relaxation times along the z2-line in Fig. 5.19 and comparing them with the temperature curves in Fig. 5.18, the reasons for the temperature decoupling can be recognized. Approximately 1.1 mm away from the centre line where the temperature drops below 11,000 K, the electron-impact vibrational relaxation time τ_{vib-e} increases extensively. This leads to a decreasing energy exchange between the electron-electronic and the vibrational energy modes resulting in a decoupling of T_e from T_{vib}. From Eq. 3.67 for the calculation of τ_{vib-e}, it can be seen that τ_{vib-e} increases with decreasing electronic pressure. Later it will be shown that p_e decreases considerably at this zone (see Fig. 5.25). In addition, an increasing nonequilibrium between the energy modes $e_{tr,rot}$ and e_e is observed in Fig. 5.18 from 1.0 mm onwards. This correlates well with the increasing relaxation time $\tau_{tr,rot-e}$ in this region.

In summary, it can be said that at $T < 11{,}000$ K nonequilibrium occurs between all three energy modes ($e_{tr,rot}$, e_{vib}, e_e) and at $T > 11{,}000$ K the LTE state is largely reached. At $T < 5000$ K, T and T_{vib} approach equilibrium while the deviation

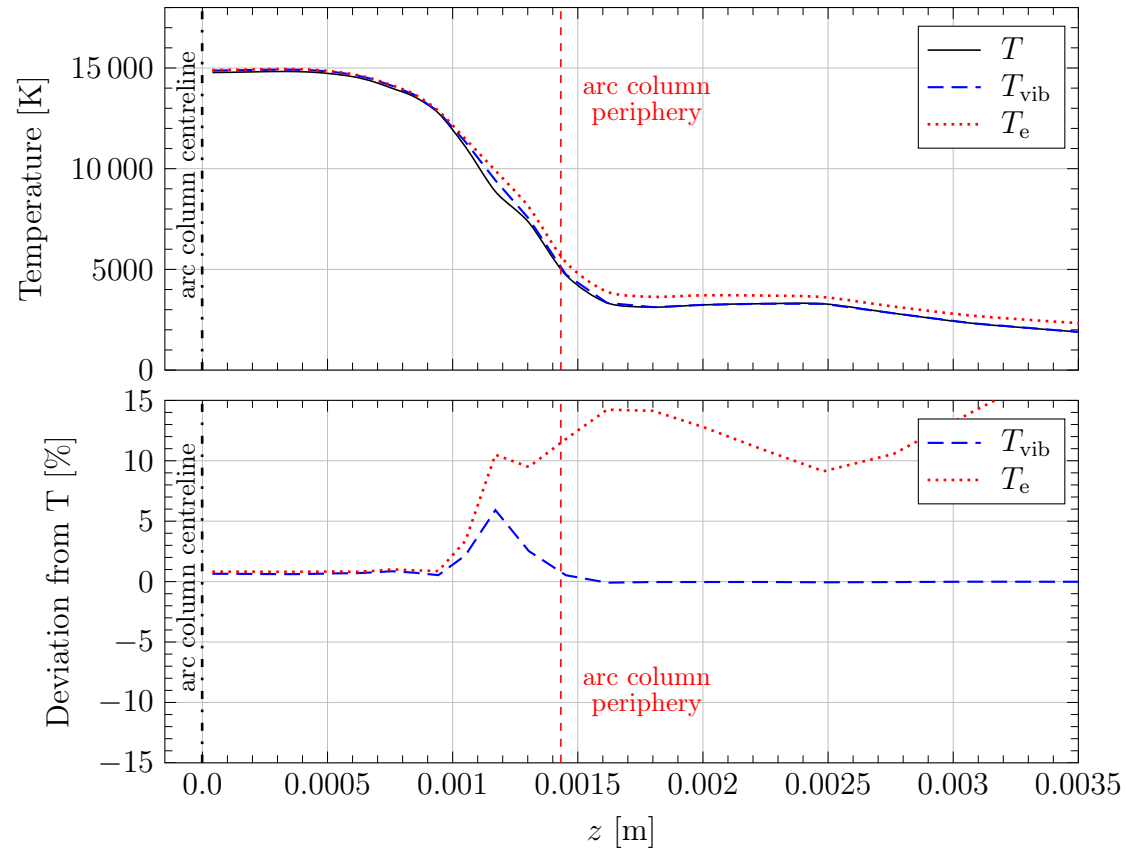

Figure 5.18: Simulation results of T, T_{vib} and T_e along the z2-line (top) and the corresponding percentage deviations of T_{vib} and T_e from T (bottom).

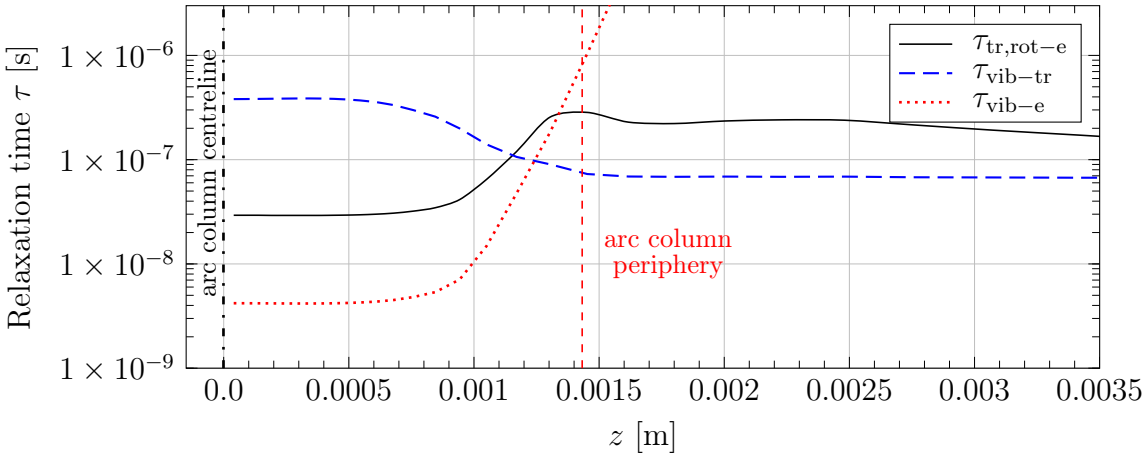

Figure 5.19: Relaxation times along the z2-line.

between T_e and T further increases. It should be mentioned that the temperature distribution in the positive column may vary due to dynamic effects. For example, at a high free-stream velocity, hydrodynamic instabilities may occur due to density

gradients between the hot and cold gas regions. Such effects lead to a continuous change in the cross-sectional area of the plasma channel over its length and, as a result, its temperature [30].

From the results shown in Fig. 5.16 it is recognizable that the highest temperatures in the electric discharge occur at the cathode edge. In addition, a strong thermal nonequilibrium prevails in that zone. In the present work it is assumed that the electron-electronic temperature there is overpredicted, since no doubly-charged ions are taken into account. By considering N^{++} in the calculations, the required second ionization energy would be extracted from the gas, leading to a lower plasma temperature at the cathode edge.

Validation of Temperature Field via Analytical Calculations

In the following, the simulation results of the maximum temperature in the arc column are validated. The numerical results yield for all three temperatures T, T_e and T_{vib} an approximately equal value of around 15,000 K (see Figs. 5.17 and 5.18). According to calculations of Wells [35], the central temperature in an axially-symmetrical uniform arc column generated in nitrogen with 10 kW input power amounts to 12,000 K (see Tab. 5.2). This temperature is 20 % lower compared to the numerically calculated value. The following factors may generally lead to this deviation:

- Wells' calculations have been performed for magnetically propelled discharges, which are electrodeless in contrast to the investigated system. Therefore, they have no hot constricted zones in the vicinity of the electrodes. These zones might cause additional heating of the gas.
- Wells analyses axially symmetric arcs while the plasma arc to be investigated is generated on a surface. In the present study no information about the temperature profile on the wedge surface is available. The surface temperature is limited to a maximum value of 1000 K. The influence of this assumption on the calculated plasma temperature is currently unclear.
- Wells considers only energy losses due to diffusion and radiation in his calculations. However, the gas discharge to be examined is exposed to a strong advection which reduces the residence time of the gas in the electric discharge. This might lead to additional cooling of the plasma.
- Wells studies systems at atmospheric pressure, while the gas discharge under investigation is generated in a flow under a static pressure of 1.4 bar. This could lead to a higher temperature of the gas.

Validation of Temperature Field via Experimental Measurements

The experimentally obtained average electronic-excitation temperature of the copper atoms amounts to $\overline{T}_{el} \approx 10{,}670$ K (see Tab. 5.3). This value is 28.26 % below the numerically calculated maximum temperature of 15,000 K. However, it should be

noted that the experimental values do not necessarily provide the maximum temperature in the plasma column due a large imaged volume used in the measurements (see Fig. D.3). Fig. 5.20 shows the experimentally determined electronic-excitation temperature of copper atoms compared to analytically calculated and numerically obtained maximum temperature of nitrogen in the plasma column.

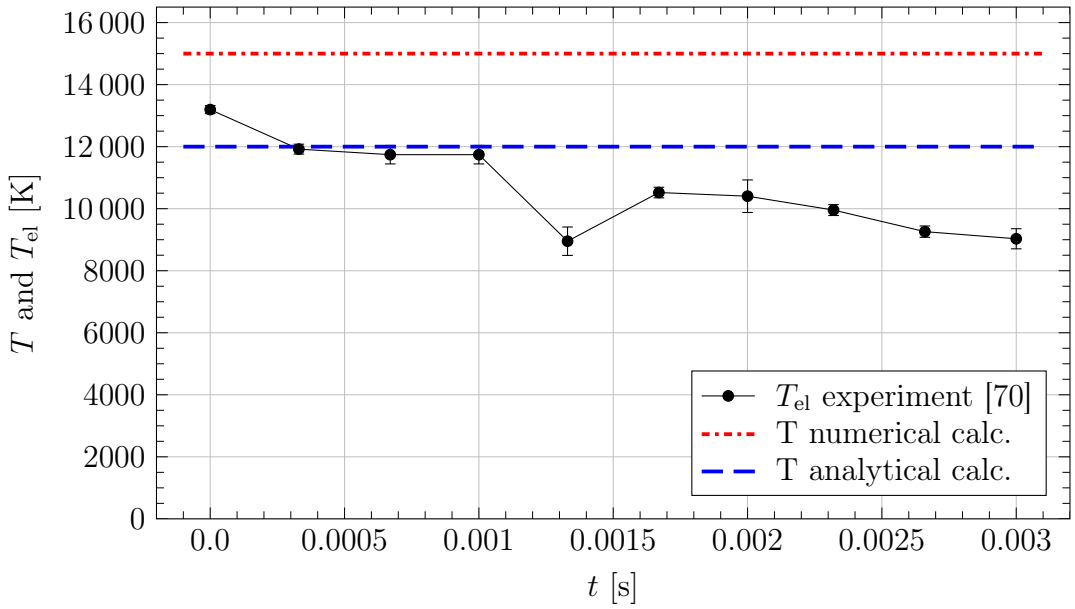

Figure 5.20: Electronic-excitation temperature T_{el} of copper atoms obtained by emission spectroscopy vs. analytical and numerical calculations of T.

Following factors may lead to the discrepancy between the experimentally obtained and the numerically calculated maximum temperature:

- From the experimental measurements it can be observed that the experimentally obtained T_{el} does not reach a quasi steady state, but decreases from 13.000 K to 9000 K during the arc discharge. Since only one experiment for the measurement of T_{el} could be evaluated in the frame of the present work, the value of $\overline{T}_{el} \approx 10{,}670$ K should be treated with caution.
- In addition, the value of 10,670 K is representative for the entire measuring volume. For this reason and due to the fact that plasma has a certain opacity, the value of 10,670 K is affected by averaging and screening phenomena. It is therefore reassuring that this value is below the numerically calculated maximum temperature of 15,000 K.
- For the experiments a contamination of the nitrogen plasma by copper is assumed due to the significant erosion of the electrode material. In the present work, however, a pure nitrogen plasma is modelled. The presence of copper vapour can have a considerable influence on the transport properties of the nitrogen plasma in regions with temperatures below 12,000 K (see Fig. 2.7).

The use of experimentally obtained rotational and vibrational temperatures of the cyano radical for validation proves difficult. This species was not modelled and it is unclear whether the CN molecule equilibrates with N_2 and N_2^+. The experimental measurements yield for the arc column zones with the highest CN number densities $T_{\mathrm{rot}} \approx 7000$ K and $T_{\mathrm{vib}} \approx 8300$ K. That is, T_{vib} deviates by 18.5 % from the rotational temperature. In the present work the maximum deviation between T and T_{vib} occurs in the plasma column regions with $T \approx 9000$ K, showing values of approx. 7.0 % (see Fig. 5.18). Both experiment and numerical calculations thus confirm that thermal nonequilibrium occurs in the peripheral areas of the plasma column.

Parameters of the Physicochemical Model Influencing the Temperature

As far as the physicochemical model is concerned, the following main factors may affect the temperature in the gas discharge:

- The 1-D analysis in Sec. 5.1.1 has shown that at $T > 15{,}000$ K the thermal conductivity model used provides values that are $\approx 6 - 7$ % below the results of Capitelli and Devoto [71] and Murphy and Arundell [72] which are generally considered accurate. The resulting underprediction of thermal conductivity may lead to higher temperature values.
- Further, the 1-D analysis has demonstrated that the radiation model used delivers overestimated values. Nonetheless, the radiation losses in high-pressure gas discharges have a rather insignificant effect on the overall energy balance.
- In the present work, an attempt has been made to estimate the value of the Joule heating efficiency coefficient η. The calculations in Sec. 2.4.6 yield a value of $\eta = 0.5$. Whether this value is sufficiently accurate for the electric arc to be modelled remains the subject of future investigations.
- Less intensive mixing of the gas and a laminar boundary layer profile due to the absence of turbulence (laminar flow assumption is currently used).

Gas Discharge Impact on Pressure Field

As shown in Fig. 5.21 and 5.22, the temperature rise in the arc discharge is accompanied by an increase in pressure and a decrease in mass density. The shock wave induced by the gas discharge can be clearly recognized in Fig. 5.21.

Fig. 5.23 shows the simulation results of pressure distribution on the wedge surface near the electrodes. The zone of increased pressure near the cathode is clearly visible. It is assumed that exactly this effect and the associated resulting force can be used to steer a projectile, as mentioned at the very beginning of this thesis (see Sec. 1.1).

The results in Fig. 5.24 show the static and electron pressure along the x-line. It can be seen that the static pressure in the vicinity of the hot cathode edge reaches a value of 1.8 bar and then drops almost linearly downstream in the direction of the anode to approximately 1.5 bar.

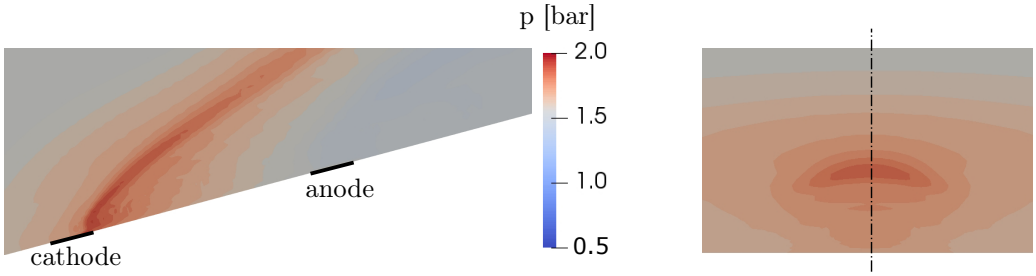

Figure 5.21: Static pressure field: x-y-plane (left), y-z-plane (right).

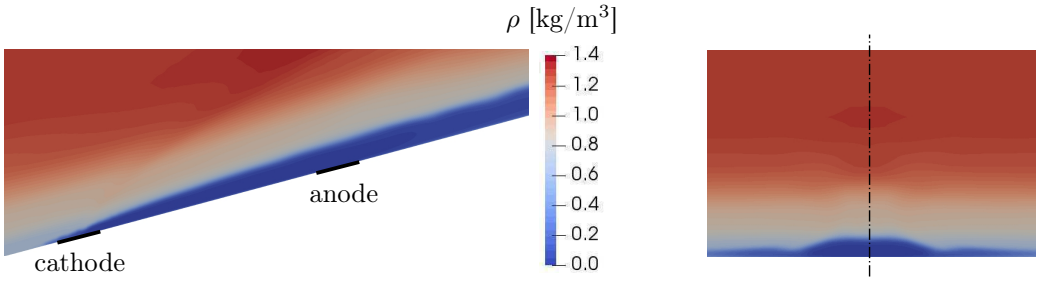

Figure 5.22: Mass density field: x-y-plane (left), y-z-plane (right).

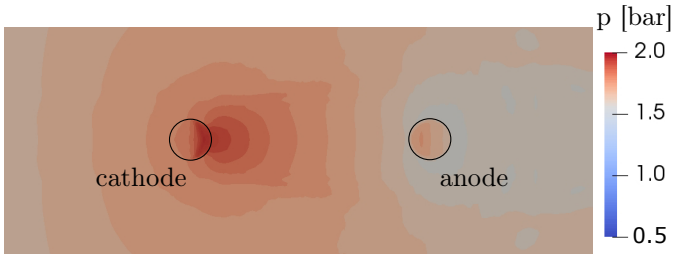

Figure 5.23: Static pressure field on the wedge surface near the electrodes.

In Fig. 5.25, the pressure distribution along the z1-line is shown. The z1-profile runs 0.1 mm above the mounting locations of the P15, P30 and P45 pressure transducers (see Fig. D.12). From the results in Fig. 5.25 it can be observed that the static pressure increases towards the arc column centreline to approximately $1.6 - 1.65$ bar. The pressure measurements yield for the surface pressure outside the gas discharge 1.45 ± 0.05 bar and in the discharge of 1.85 ± 0.05 bar (see Fig D.14 time period of performance decrease at $t \approx 1.1$ ms). That is, the experimentally measured value near the P15, P30 and P45 pressure transducers exceeds the numerical calculated value. However, this value is in good agreement with the simulated maximum pressure at the cathode (see Fig. 5.24). Overall, however, it is assumed that the available pressure measurements are rather less suitable for validation due to uncontrolled capacitor discharge and peak powers of up to 70 kW. Therefore, further surface pressure measurements have to be carried out, where the gas discharge is operated with a constant input power of 10 kW.

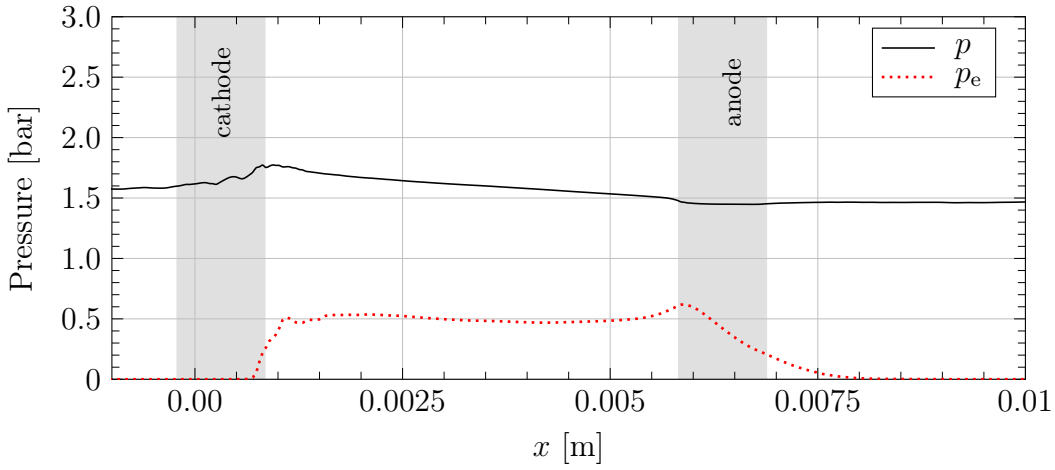

Figure 5.24: Static pressure and electron-pressure profiles along the x-line.

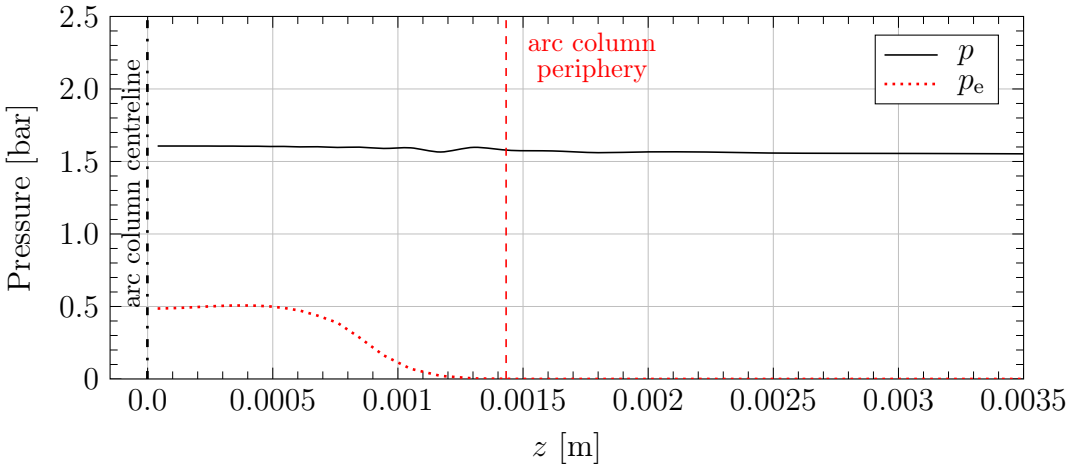

Figure 5.25: Static pressure and electron-pressure distribution along the z1-line.

Gas Discharge Impact on Velocity Field

In Fig. 5.26 the velocity magnitude in the gas discharge is presented and in Fig. 5.27 the components u_x, u_y and u_z and the magnitude u_{mag} along the x-line are shown.

The velocity curves in Fig. 5.27 are plotted 0.1 mm above the wedge surface. It is recognizable that u_z is nearly zero along the whole measuring distance. The velocity component u_y contributes noticeably to the velocity only in the near-electrode zones. The x-component provides the largest contribution to the overall velocity. Further, the gas discharge acts on the flow as an obstacle because the gas tends to expand in all directions as it heats up. This creates a stagnation point above the cathode. Behind the cathode, the gas is accelerated in the direction of flow and its velocity increases to $\approx 800\ \mathrm{m \cdot s^{-1}}$. At the anode, the gas undergoes a further acceleration (see Fig. 5.27). It can be concluded that the characteristic velocity $u_c = 1000\ \mathrm{m \cdot s^{-1}}$

obtained in Sec. 2.3 is somewhat overestimated, but presents an acceptable guess.

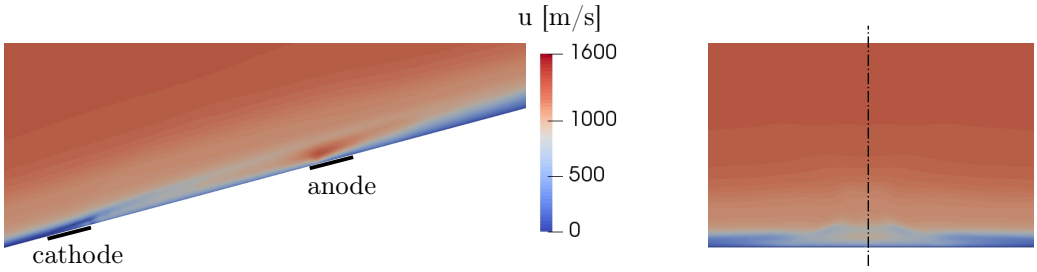

Figure 5.26: Velocity magnitude field: x-y-plane (left), y-z-plane (right).

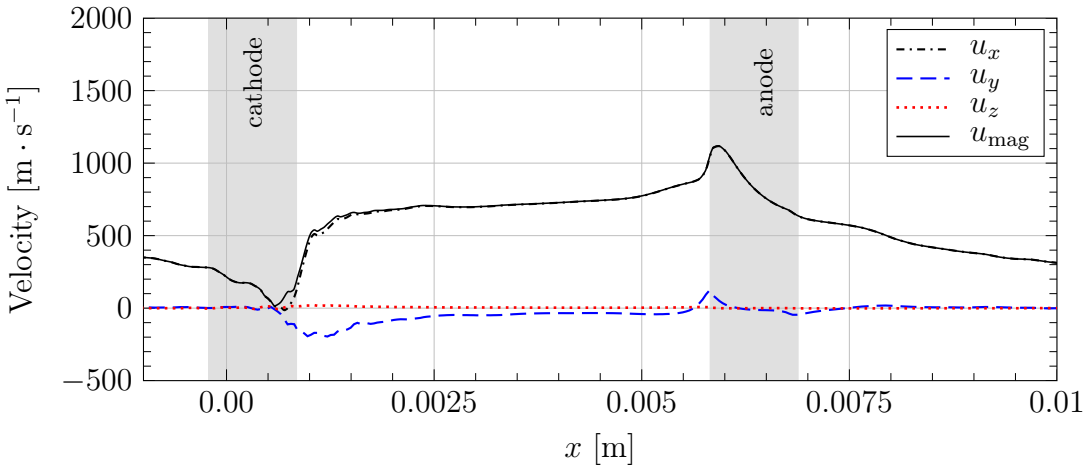

Figure 5.27: Velocity components u_x, u_y, u_z and magnitude u_{mag} along the x-line.

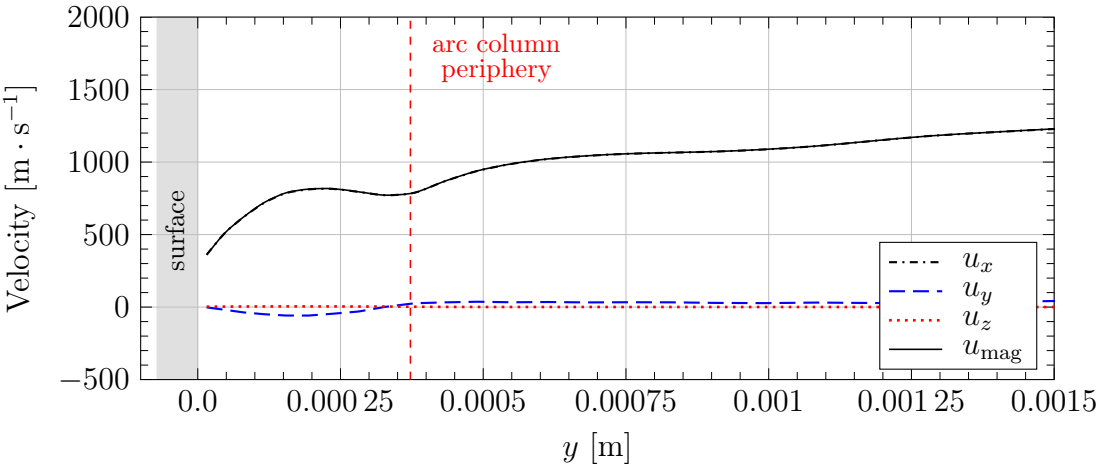

Figure 5.28: Velocity components u_x, u_y, u_z and magnitude u_{mag} along the y1-line.

In Figs. 5.28 and 5.29, the velocity profiles along the y1- and z1-lines are shown. The relatively high contribution of the z-component to the total velocity in Fig. 5.29 indicates the lateral escape of the gas from the arc column.

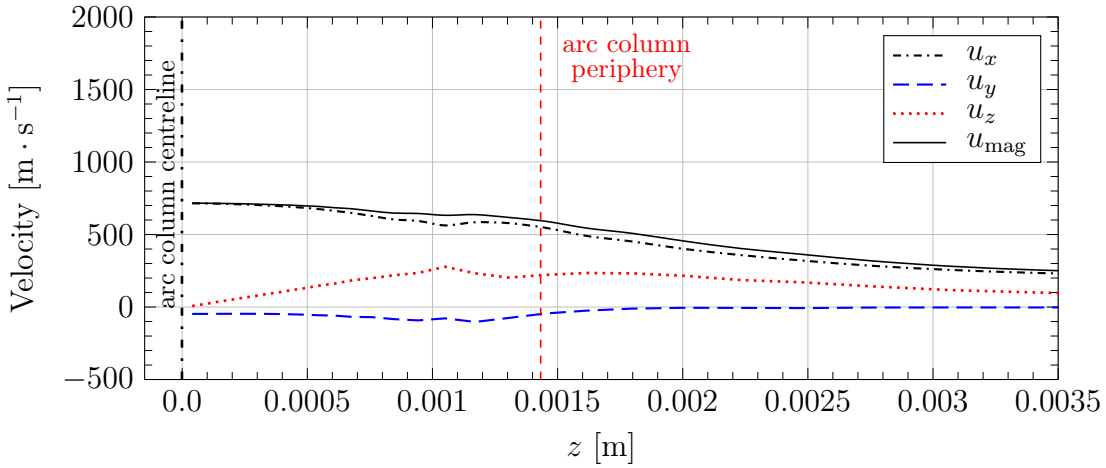

Figure 5.29: Velocity components u_x, u_y, u_z and magnitude u_{mag} along the z1-line.

With the above data, the available flow residence time inside the arc discharge can now be estimated. The residence time in the positive column for $\mathbf{u} = 800\ \mathrm{m \cdot s^{-1}}$ and a column length of 5.0 mm is approx. 6.25×10^{-6} s. In the cathode area, the residence time is about 3.3×10^{-6} s at $\approx 300\ \mathrm{m \cdot s^{-1}}$ and a distance covered of 1.0 mm. The relatively long residence time of the gas in the cathode zone combined with the high Joule heating leads to a temperature peak in this area. It can be stated that 1.0×10^{-6} s chosen for the characteristic time t_{c} in Sec. 2.3 is a reasonable estimate.

5.6.3 Species Number Densities across the Gas Discharge

Spatial Structure of Plasma Constituents in the Gas Discharge

It can be seen from Fig. 5.30 and 5.31 how the molecular nitrogen partially dissociates to atomic nitrogen due to high temperatures prevailing in the gas discharge. The atomic nitrogen forms a kind of shell, in which its number density n_{N} reaches the maximum values. A similar shell structure is also observed for the molecular ions shown in Fig. 5.32. Both N and $\mathrm{N_2^+}$ reach maximum number densities in the zones with $T \approx 8000$ K. This can be seen when comparing the temperature distributions along the y2- and the z2-lines in Figs. 5.17 and 5.18 with the number density profiles in Fig. 5.36 and 5.37. In the core of the gas discharge, where the temperature is the highest, atomic nitrogen ions are increasingly generated (see Fig. 5.33). The number densities of N, $\mathrm{N^+}$ and e in the core of the arc column are approximately equal and amount to around $3 \times 10^{23}\ \mathrm{m^{-3}}$ (see Fig. 5.35). In the cold near-wall region, partial electron recombination as well as recombination of neutral atoms to molecules occur (see Fig. 5.36). However, in order to take these effects more precisely into account, the computational grid density must be increased in the vicinity of the wall.

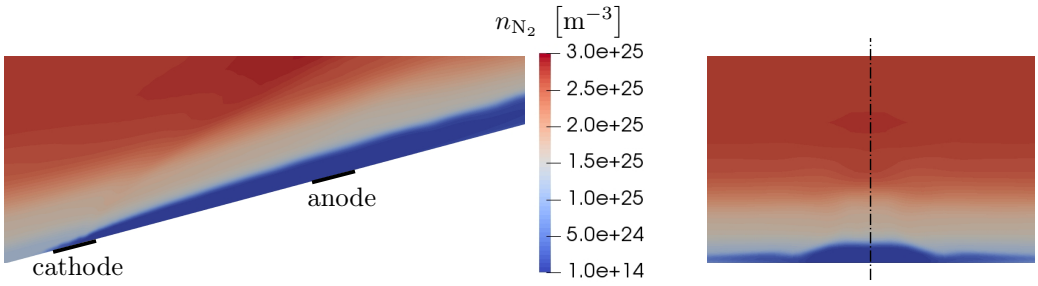

Figure 5.30: Number density field of N_2: x-y-plane (left), y-z-plane (right).

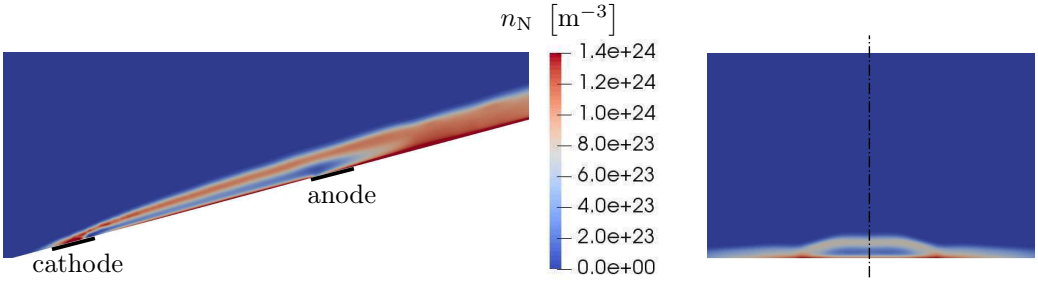

Figure 5.31: Number density field of N: x-y-plane (left), y-z-plane (right).

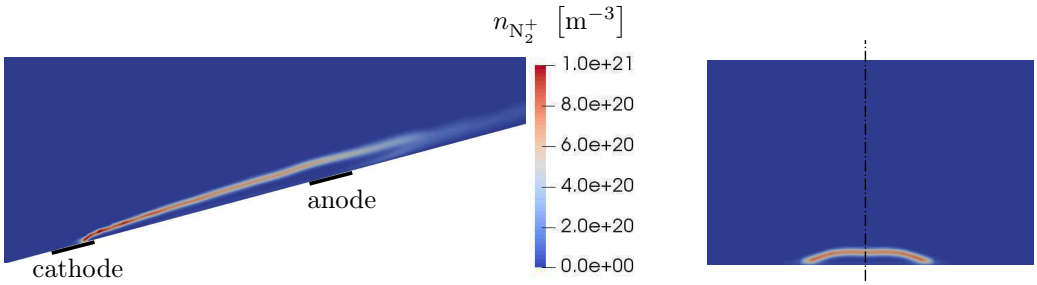

Figure 5.32: Number density field of N_2^+: x-y-plane (left), y-z-plane (right).

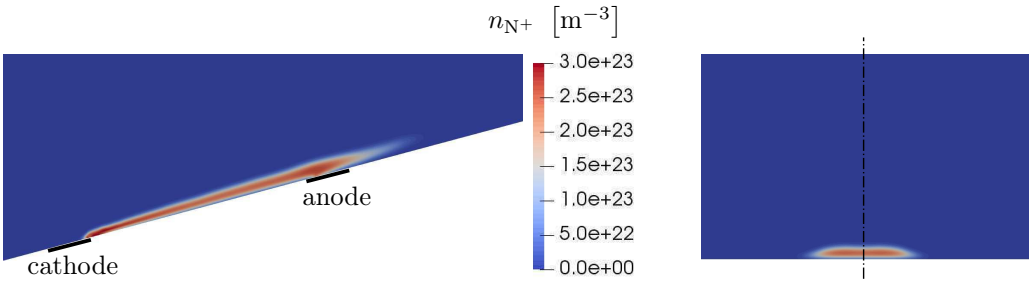

Figure 5.33: Number density field of N^+: x-y-plane (left), y-z-plane (right).

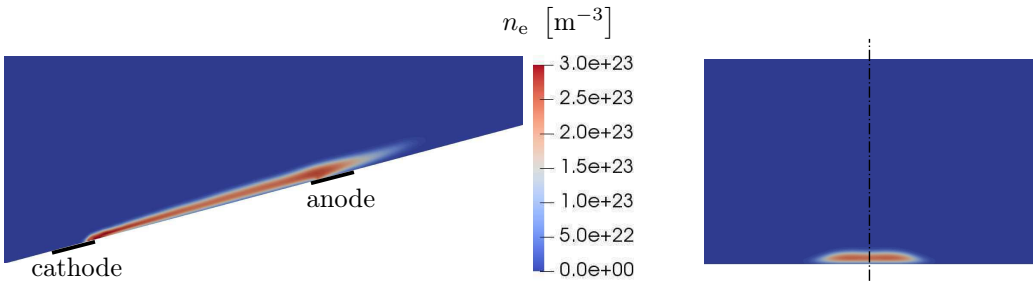

Figure 5.34: Number density field of e: x-y-plane (left), y-z-plane (right).

Preservation of Quasineutrality in the Gas Discharge

The results in Fig. 5.35, 5.36 and 5.37 show that inside the arc discharge at temperatures above 4000 K, the quasineutrality is preserved ($n_e \approx n_i$). At lower temperatures, however, the number densities of electrons and ions differ considerably. It follows that charge separation takes place outside the plasma and thus quasineutrality is not maintained in colder regions. This presents a problem because, firstly, the assumption of quasineutrality serves as a basis for several further assumptions of the physicochemical model and, secondly, the charge separation occurring without the restoring forces is unphysical.

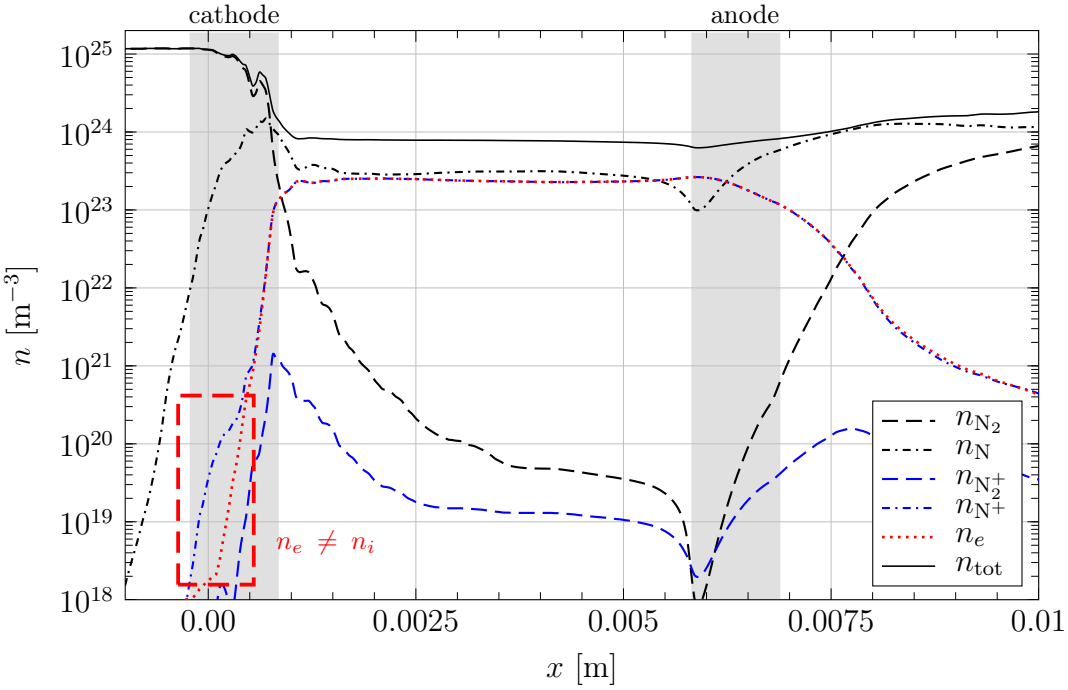

Figure 5.35: Number densities of nitrogen plasma constituents along the x-line.

The species conservation equation shown in Eq. 3.15 is responsible for changes in species concentration due to advection, diffusion, and production/destruction caused

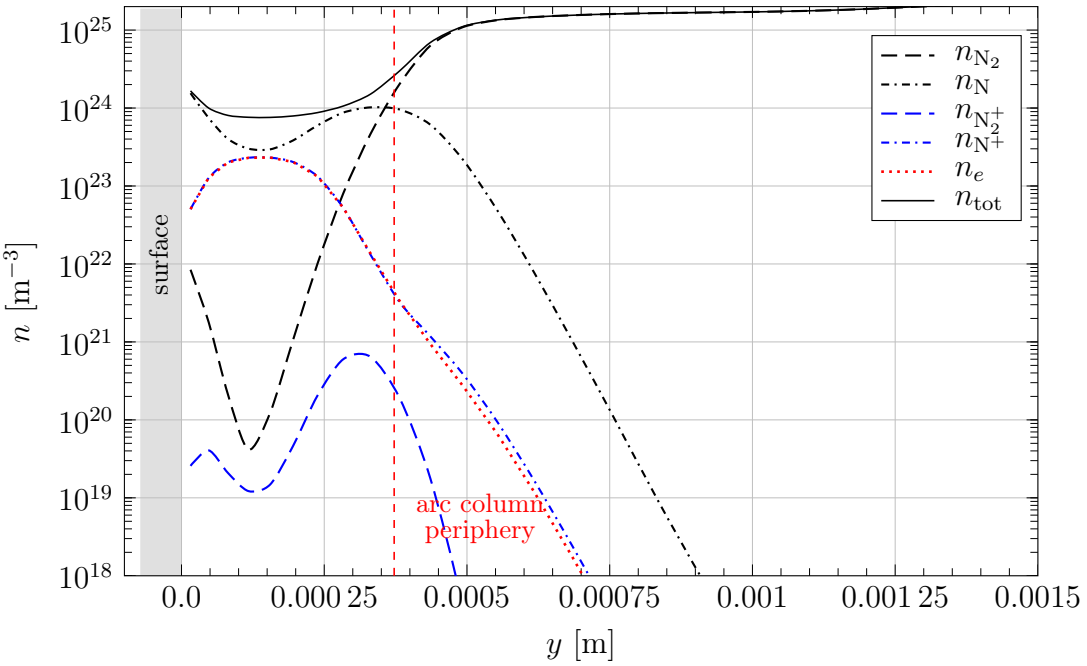

Figure 5.36: Number densities of nitrogen plasma constituents along the y2-line.

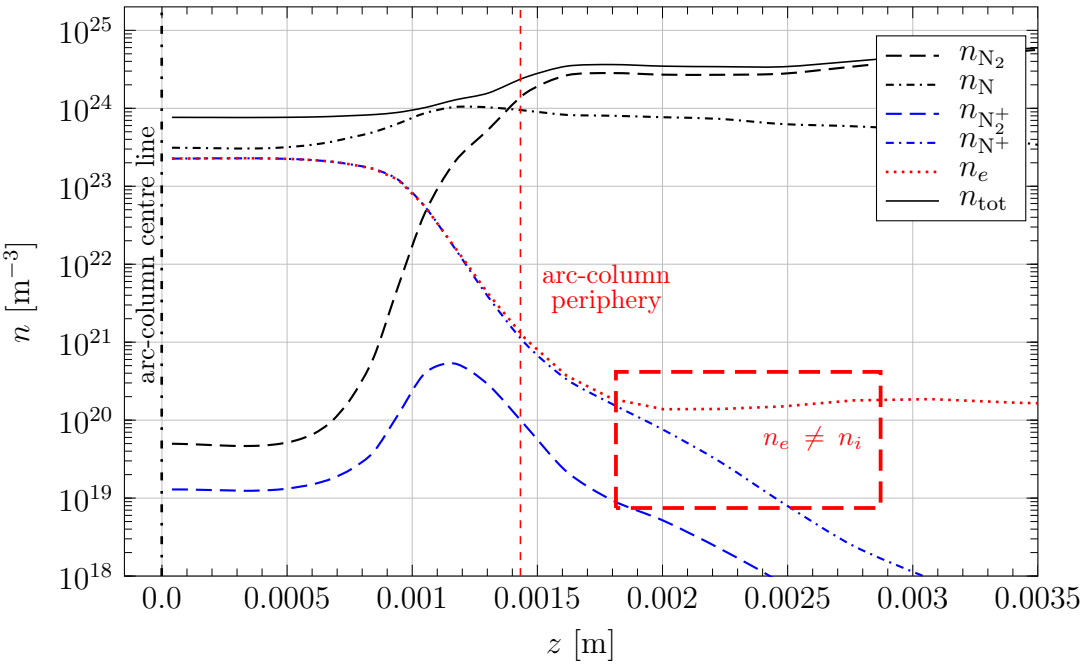

Figure 5.37: Number densities of nitrogen plasma constituents along the z2-line.

by chemical reactions. Since the one-fluid assumption is used in the physicochemical model, the convection term does not contribute to the charge separation. Furthermore, it is assumed that the source terms $\dot{\omega}_s$ for species production/destruction op-

erate correctly. Thus, only the diffusion term, or more specifically the diffusion flux $\rho \mathbf{V}_s c_s$, remains as the possible cause of charge separation. In the present work, the diffusion velocity $\mathbf{V}_s$ given in Eq. 3.50 only accounts for the fluid diffusion due to gradients in species concentration. According to Park [14], however, there exist also thermal and pressure diffusion effects in the fluid, which are relatively weak, and a considerable diffusion of charged particles due to electrostatic forces. For reasons of time, the latter effect has not yet been considered in the present work and will be investigated in further research. This effect arises in the case of slight nonuniformity in number densities of ions and electrons (charge separation), whereby polarization fields and the resulting restoring forces between the charged particles are induced. It is assumed that, due to the neglect of this effect in the diffusion term of the species conservation equation, nothing counteracts a possible emerging charge separation.

Apart from the fact that the charge separation in the simulation results is unphysical, the plasma, which cools down downstream, cannot recombine completely due to differences in ion and electron concentrations. As a result, areas with cool electrons or ions are formed behind the gas discharge. This leads to incorrect calculations of transport properties that negatively affect the stability of the calculation.

5.6.4 Electromagnetic Properties in the Gas Discharge

Electric Potential and Electric Field in the Gas Discharge

Fig. 5.38 shows the electric potential distribution along the x-line. It can be seen that the voltage drop in the positive column of the arc is nearly linear, which is consistent with a theoretical electric potential distribution in the centre line of a free burning axially-symmetrical electric arc shown in Fig. 2.10.

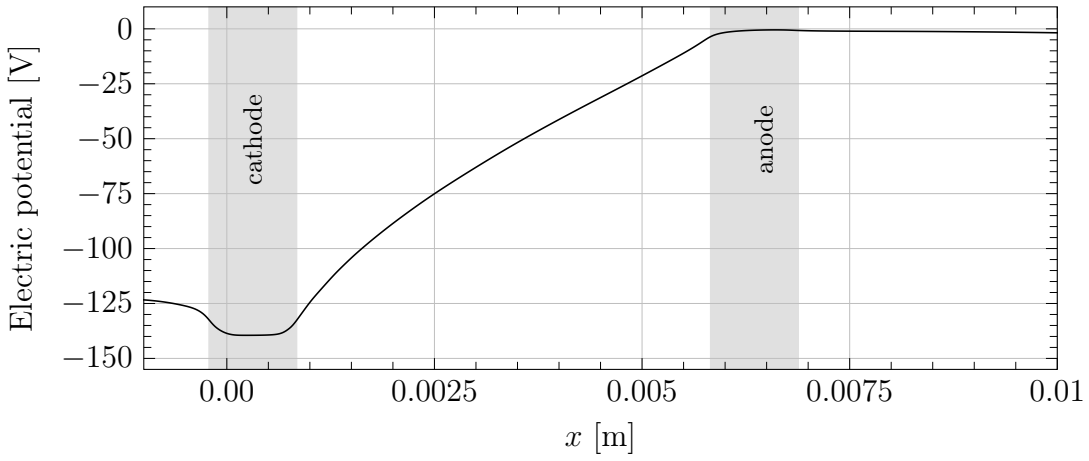

Figure 5.38: Electric potential Φ along the centre line of the gas discharge (x-line).

The time-averaged voltage drop at the electrodes of $\Delta\Phi \approx 139.5$ V calculated with solver mode 1 (see Sec. 4.5.3) is in fair agreement with the voltage measurements

performed during the time-resolving emission spectroscopy experiments where time averaged values between 120 V and 128 V were measured (see Appendix D). Further, the numerical simulation yields for the electric current I at the cathode a value of 70.690 A and at the anode 70.694 A. The deviation of I_a from I_c is 0.004 A, which is very low. The values of I_a and I_c are approximately 9 A below the the characteristic electric current of 80 A and the experimentally measured values ranging from 79.3 A to 80 A listed in Tab. 5.3. However, it was to be expected since the numerically determined time averaged voltage drop at the electrodes of $\Delta\Phi \approx 139.5$ V exceeds slightly the values measured at the power supply terminals. At this point, it must be recalled that electrode voltage drops are not modelled in the present work. Whether and to what extent the consideration of U_{cr} and U_{ar} in the model would affect the arc current I is currently unclear. The comparison of the experimental and the numerically calculated values of I and U is shown in Fig. 5.39.

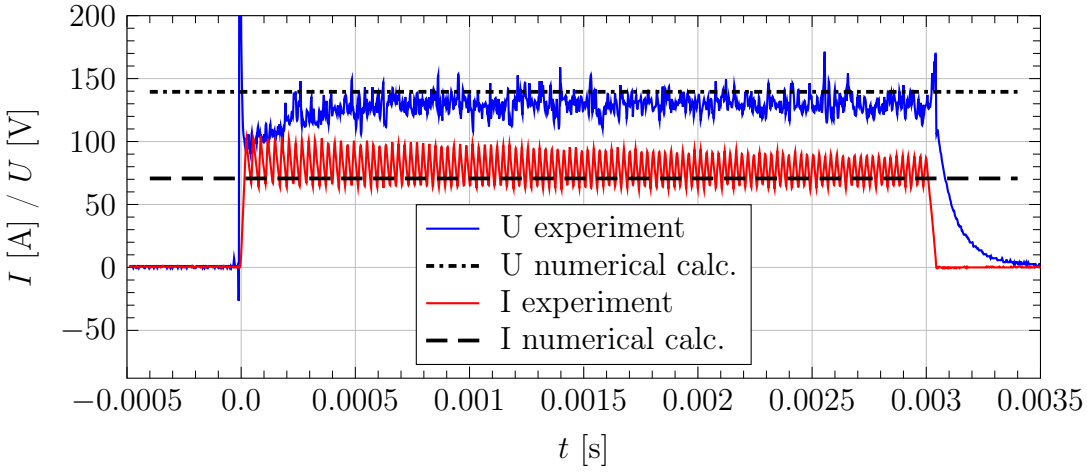

Figure 5.39: Voltage and current measured at the electrodes compared to numerically calculated values.

The potential difference at the electrodes creates an electrostatic field in the gas discharge area. Due to the electrical conductivity of plasma (see Fig. 5.40), the electric field strength is reduced in the conducting area. This results in a discontinuity in the electric field distribution, which is visible over the anode in Fig. 5.41. Physically, this discontinuity may be explained by the fact that due to free charge carriers in the plasma, a partial charge redistribution takes place within the conducting area, which leads to a voltage reduction in that zone (electrostatic induction).

The maximum electrical conductivity in the core of the plasma column is approx. 7500 $\mathrm{S \cdot m^{-1}}$. This value exceeds the characteristic electrical conductivity σ_c considerably (see Tab. 2.2). However, it is to be expected since the numerically obtained maximum temperature in the plasma column of $T = 15{,}000$ K is higher than the analytically calculated characteristic temperature T_c.

It must again be pointed out that electrode voltage drops are not modelled. By considering U_{cr} and U_{ar}, the curve in Fig. 5.38 would have a flatter slope (smaller

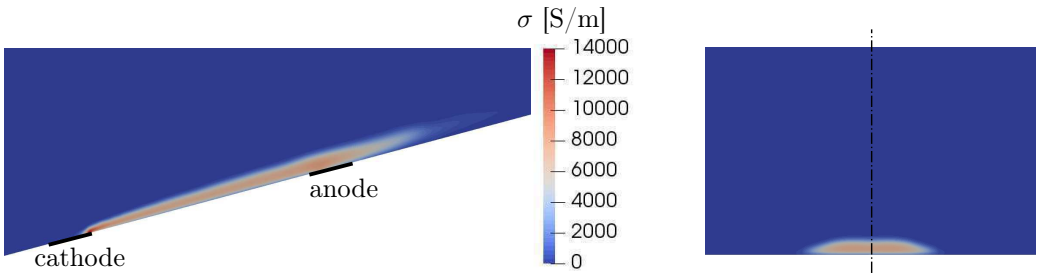

Figure 5.40: Electrical conductivity: x-y-plane (left), y-z-plane (right).

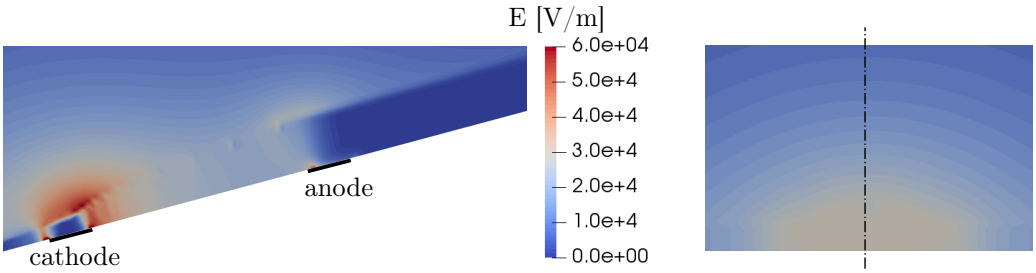

Figure 5.41: Electric field magnitude: x-y-plane (left), y-z-plane (right).

gradient value in x-direction, as schematically shown Fig. 2.10). As a result, **E** directly at the electrodes would increase while decreasing in the positive column. The electric field influences the current density **J** and consequently the induced magnetic field **B** (see the Ampère's and the Ohm's laws in Eqs. 3.123 and 3.125, respectively). The fact that the electric and magnetic fields are slightly overestimated should not be forgotten in the following analysis. In the present work, this fact is taken into account by means of the efficiency coefficient $\eta = 0.5$ (see Sec. 2.4.6). This coefficient is implemented in the calculation of $\dot{Q}_{\text{Joule}}$ and $\mathbf{F}_{\text{Lorentz}}$ (see Sec. 3.3.6).

Fig. 5.42 shows the electric field components E_x, E_y and E_z and the magnitude E_{mag} along the x-line. It can be seen that the electric field in the positive column tends to have an approximately linear and horizontal distribution, while peaks occur near the electrode edges. This pattern is consistent with the theoretical distribution of **E** in the centreline of a free burning electric arc shown in Fig. 2.10. The approximately horizontal distribution of **E** between the electrodes results from the nearly constant spatial electric potential gradient shown in Fig. 5.38.

The characteristic field E_c calculated in Sec. 2.3.1 is 20,000 $\text{V} \cdot \text{m}^{-1}$. This value is obtained by assuming a plasma column voltage drop of 100 V, which results from the subtraction of the cathodic and anodic voltage drops of 30 V from the total voltage drop over the arc of 130 V. Without subtracting 30 V, the characteristic field in the arc column would have the following value: 130 V voltage drop divided by 0.005 m electrode gap yields 26,000 $\text{V} \cdot \text{m}^{-1}$. This value is in a good agreement with the numerically obtained electric field magnitude between the electrodes in Fig. 5.42.

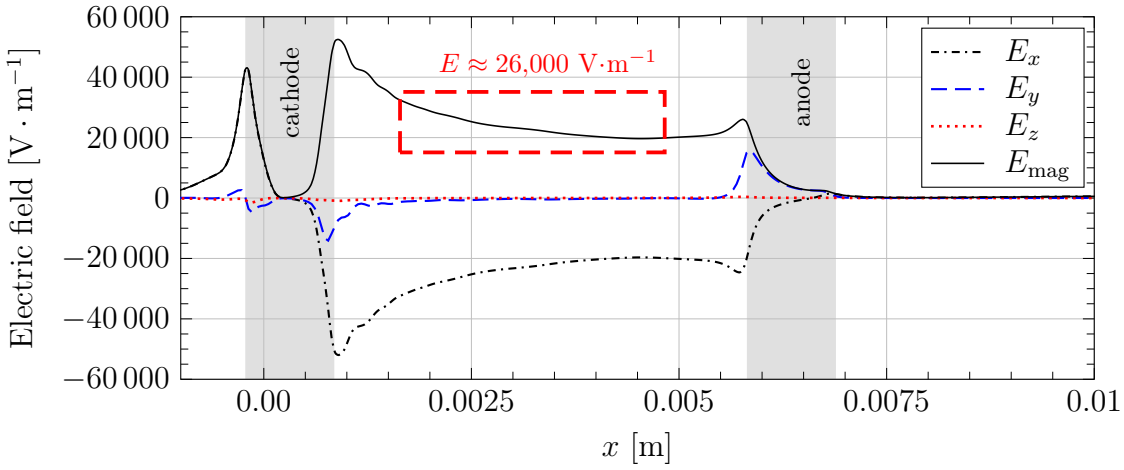

Figure 5.42: Electric field components E_x, E_y and E_z and the corresponding magnitude E_{mag} along the x-line.

Electric Current Density and Magnetic Field in the Gas Discharge

Fig. 5.43 shows the electric current density **J** between the electrodes. The electric current is caused by the electrostatic field and the free charge carriers in the plasma. In addition, the partially ionized gas is transported along with the flow and forms a tail behind the anode (not visible in Fig. 5.43 due to the colour scale used). The electric current thus flows not only between the anode and cathode, but also a certain distance downstream, forming a tail that eventually recombines to a neutral gas.

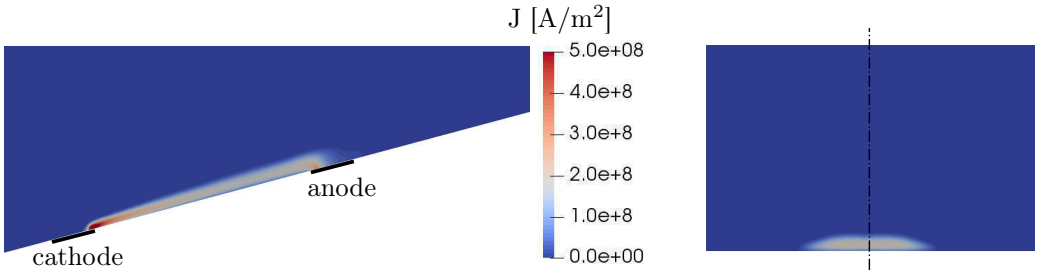

Figure 5.43: Electric current density magnitude: x-y-plane (left), y-z-plane (right).

The constant arc current between the electrodes induces a static magnetic field **B** shown in Fig 5.44. In Figs. 5.45 and 5.46 the magnetic field components B_x, B_y and B_z and the magnitude B_{mag} are plotted along the x-line and the y1-line, respectively. The magnetic field along the x-line 100 μm above the wedge surface varies from 0.027 T to 0.008 T. Above the cathode it reaches peak values of up to 0.05 T (not visible in the diagram). The magnetic field along the y-line shown in Fig. 5.46 amounts at the periphery of the plasma column to 0.021 T and decreases continuously with distance from the discharge. It can be stated that the characteristic value $B_{\text{c}} = 0.016$ T provides a reasonable estimate for the system (see Tab. 2.2).

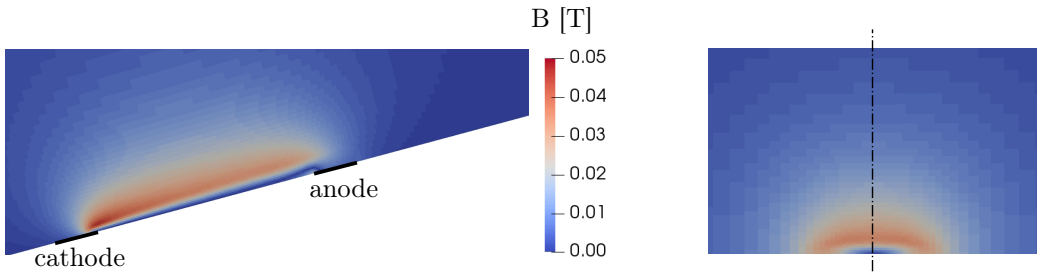

Figure 5.44: Magnetic induction field magnitude: x-y-plane (left), y-z-plane (right).

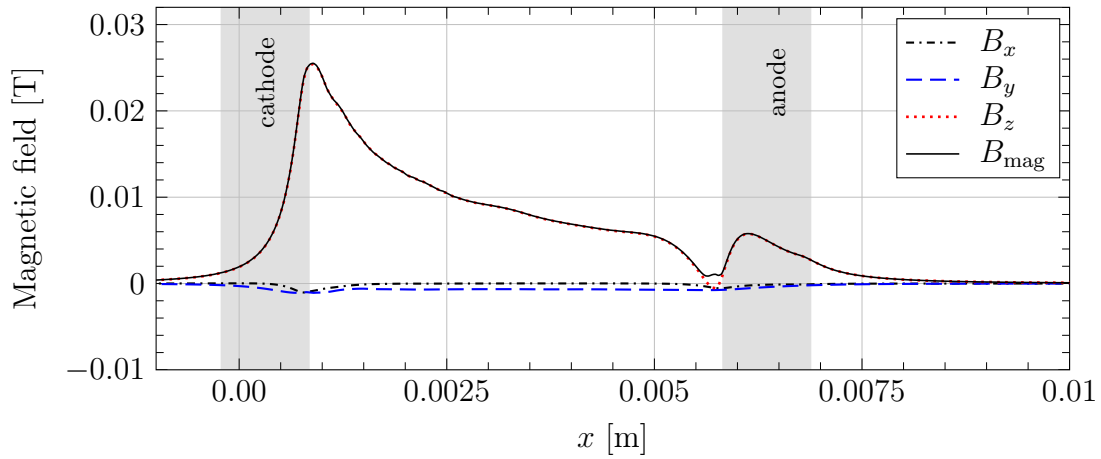

Figure 5.45: Magnetic field components B_x, B_y and B_z and the corresponding magnitude B_{mag} along the x-line.

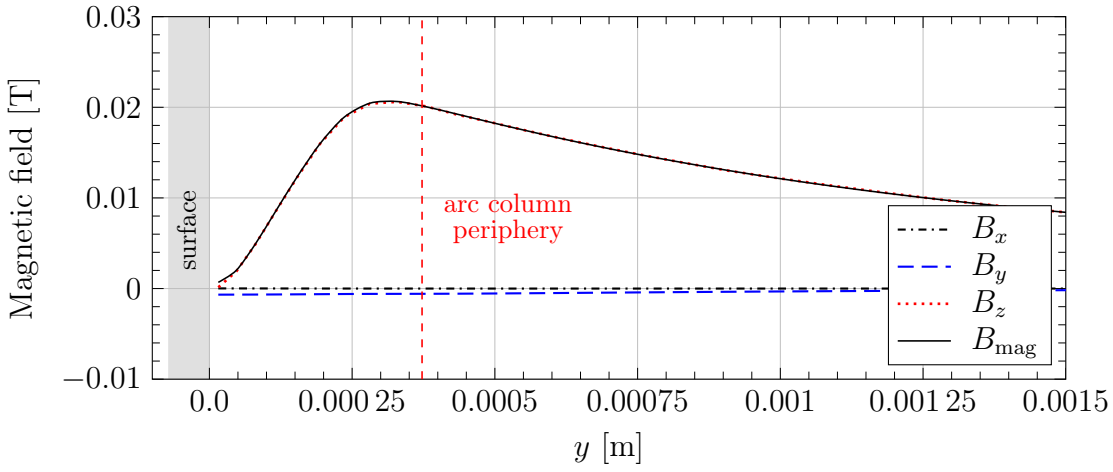

Figure 5.46: Magnetic field components B_x, B_y and B_z and the corresponding magnitude B_{mag} along the y1-line.

At this point it is important to note that the numerically calculated induced mag-

netic field does not take into account induction effects due to the electric circuit wires under the wedge surface. This is explained in detail at the end of this chapter. However, the presented results of **B** are intended to demonstrate the functionality of the new numerical solver and to provide first validation by comparison with characteristic magnetic field magnitude B_c.

In Fig. 5.47, the magnitudes of **E** and **J** in the cross-section through the gas discharge directly above the wedge surface are presented. It can be recognised that both fields occur most strongly at the electrode edges, which is physically correct. The peak values of **E** at the cathode and anode edges facing each other are 8.7×10^4 V·m^{-1} and 7.4×10^4 V · m^{-1}, respectively. The value for the electric field strength in the

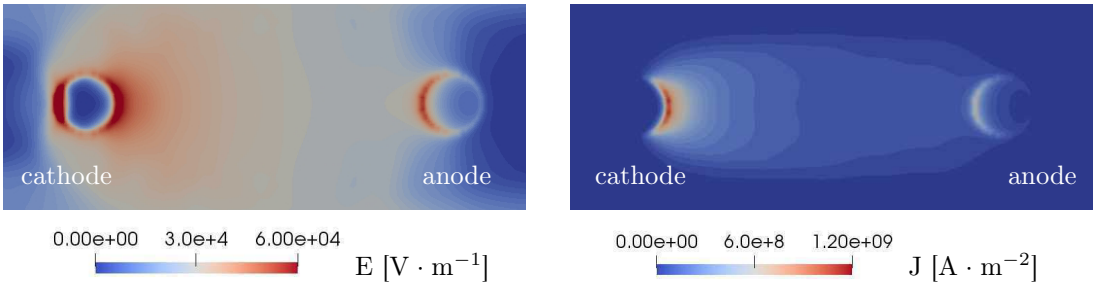

Figure 5.47: Electric current density and electric field magnitude at the electrodes.

cathode sheath estimated analytically in this work in Sec. 2.2 and in Appendix A is $\sim 10^9$ V·m^{-1}. In the present work, however, the electrode nonequilibrium layers (sheath and presheath) are not modelled and the values in Fig. 5.47 are more applicable to the near-electrode constricted zones where the plasma channel becomes wider. This explains why they are much lower than the analytically calculated values. The numerically calculated peak values of **J** at the cathode and anode edges in Fig. 5.47 amount to 1.8×10^9 A·m^{-2} and 0.53×10^9 A·m^{-2}, respectively. The current density in the cathode sheath estimated analytically in Appendix A is $J_c \sim 10^{10}$ A · m^{-2}, which is by one magnitude higher than the numerically calculated value. But again, it should be pointed out that the numerically obtained value of **J** is outside the cathode sheath. For a symmetric and smooth anode, literature provides for $\mathbf{J}_a$ a value in the range of $10^5 - 10^7$ A·m^{-2}. This value is lower than the numerically calculated value, which is probably due to the anode geometry used in the system under investigation.

Plasma Response to Electric and Magnetic Fields

The response of the partially ionized fluid to the electric and magnetic fields is modelled in the present work by the Joule heating and the Lorentz force.

In Fig. 5.48, $\dot{Q}_{\text{Joule}}$ per cubic meter in the electric arc is presented and in Fig. 5.49 its distribution along the x-line is shown. The Joule heating includes the efficiency coefficient $\eta = 0.5$ calculated in Sec. 3.3.6. It can be seen that due to the peaks in the electric field near the electrodes shown in Fig. 5.47, peak values in Joule heating also occur.

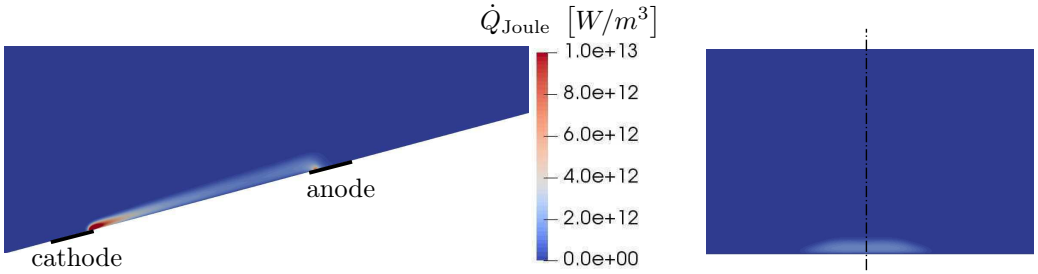

Figure 5.48: Joule heating per cubic meter: x-y-plane (left), y-z-plane (right).

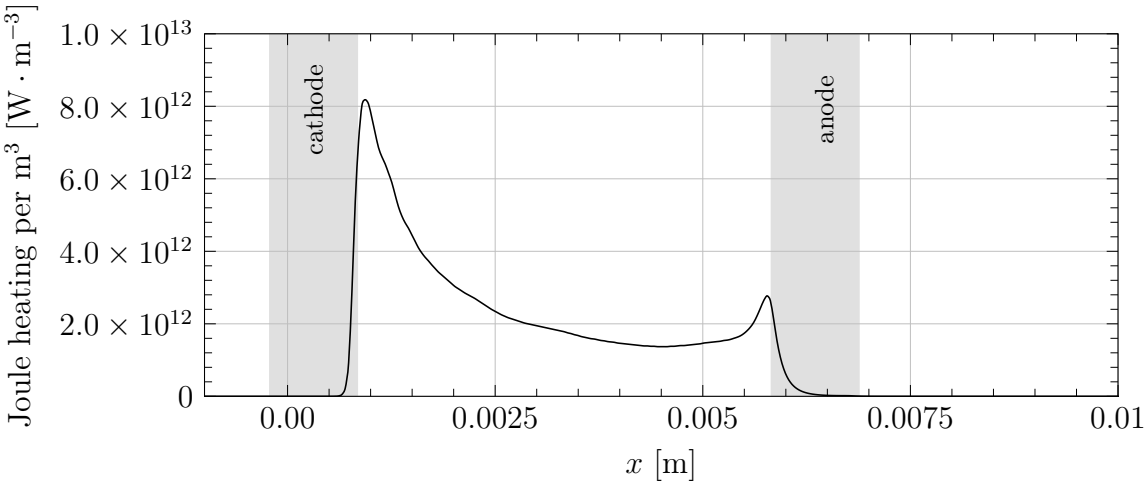

Figure 5.49: Joule heating per cubic meter along the x-line.

Figs. 5.50 and 5.51 show the radiation losses per cubic meter in the discharge. From the comparison of Figs. 5.49 and 5.51 it can be concluded that the radiation losses in the arc column are by two orders of magnitude lower than the Joule heating. This property is typically for thermal high-pressure arcs. In his work, Wells [35] concludes that radiation losses are negligible for arcs created by high electric fields and therefore formed in narrow channels. However, for lower fields, which correspond to arcs in wider channels, the radiation losses have a strong influence on the temperature distribution and thus on the properties of the arc and cannot be neglected.

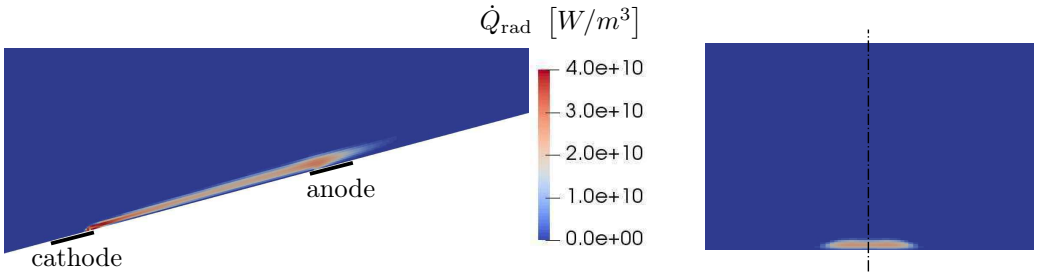

Figure 5.50: Radiation losses per cubic meter: x-y-plane (left), y-z-plane (right).

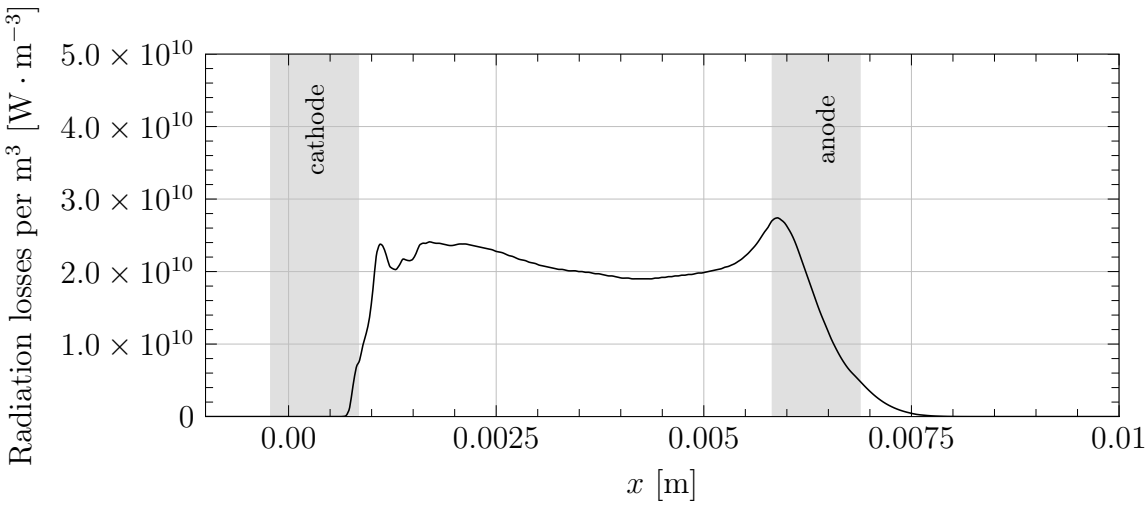

Figure 5.51: Radiation losses per cubic meter along the x-line.

In Fig. 5.52 the Lorentz force magnitude per cubic meter in the gas discharge is presented. In Figs. 5.53 and 5.54 the components F_x, F_y, F_z and the magnitude F_{mag} of Lorentz force per cubic meter along the x-line and the y1-line are shown, respectively. The magnitude of the Lorentz force per cubic meter near the centreline of the positive column is $\approx 1.5 \times 10^6$ N $\cdot$ m^{-3} and reaches values of more than 6.0×10^6 N $\cdot$ m^{-3} in the vicinity of the cathode. Further, as shown in Fig. 5.54, $\mathbf{F}_{\text{Lorentz}}$ reaches 1.7×10^6 N $\cdot$ m^{-3} at a distance 0.2 mm above the wedge surface between the electrodes.

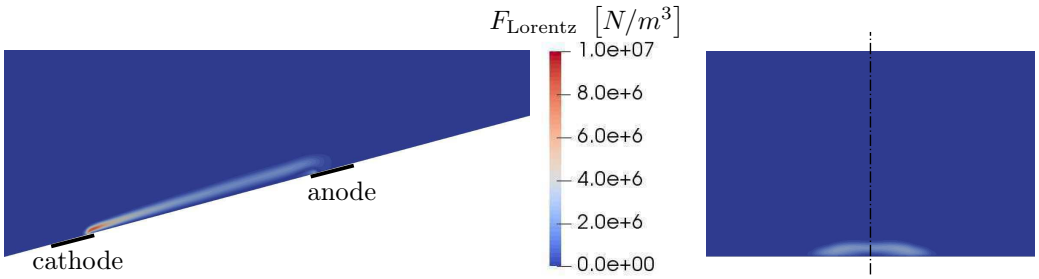

Figure 5.52: Lorentz force magnitude per cubic meter: x-y-plane (left), y-z-plane (right).

When discussing the simulation results of the induced magnetic field, it was mentioned that the numerical calculation does not consider the induction effects due to the electric wiring under the wedge surface. The solid material under the wedge surface, which consists of polyamide and the copper supply lines (see Fig. 2.2), is not considered in the simulation domain. Only the flow around the wedge is modelled (see Fig. 5.1). This results in the following two effects:

First, the static magnetic field induced by the arc current is formed not only in the nitrogen but also in the polyamide plate, as shown schematically in Fig. 5.55 on the

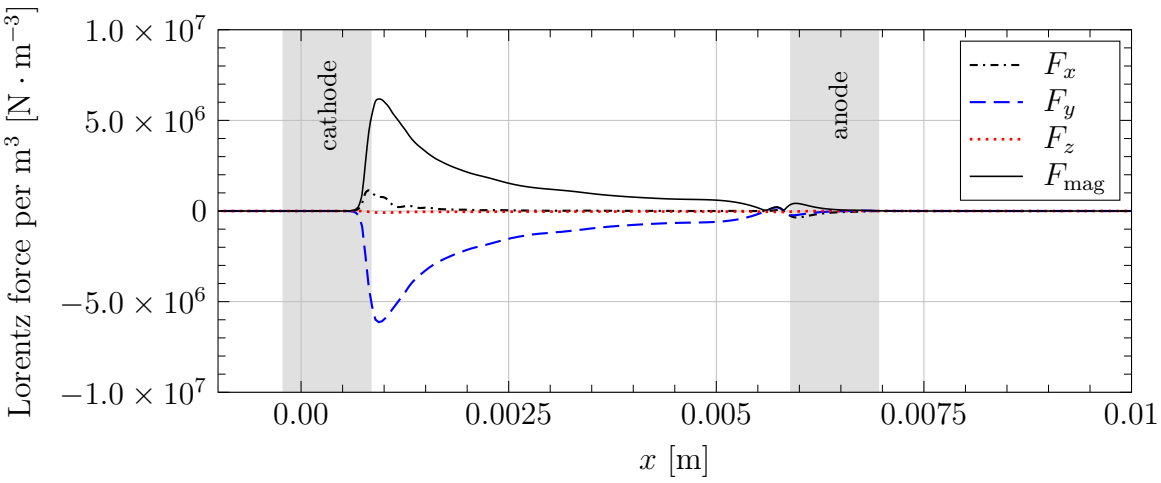

Figure 5.53: Components F_x, F_y, F_y and magnitude F_{mag} of Lorentz force per cubic meter along the x-line.

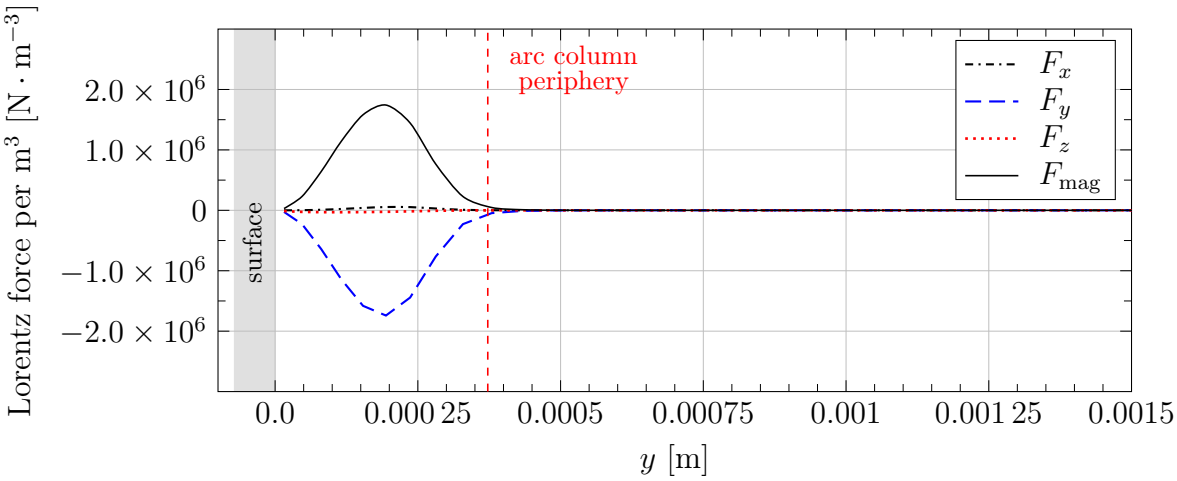

Figure 5.54: Components F_x, F_y, F_y and magnitude F_{mag} of Lorentz force per cubic meter along the y1-line.

left. This means that the magnetic field lines in the solid represented by black dashed lines are missing in the numerical simulation (compare Fig. 5.55 with Figs. 5.44 and 5.46). Consequently, the corresponding Lorentz forces are also missing (depicted by red dashed arrows in Fig. 5.55 on the left). That is, the Lorentz forces acting on the plasma column from above are not compensated by those acting from below. In contrast, the plasma column is laterally stabilized by the corresponding lateral Lorentz forces. It is assumed that due to a rather weakly induced magnetic field in the system under investigation, the generated Lorentz forces have no significant influence on the shape and position of the plasma column.

The sketch in Fig. 5.55 in the middle and the corresponding experimental image on the left demonstrate the influence of the electrode power supply lines on the

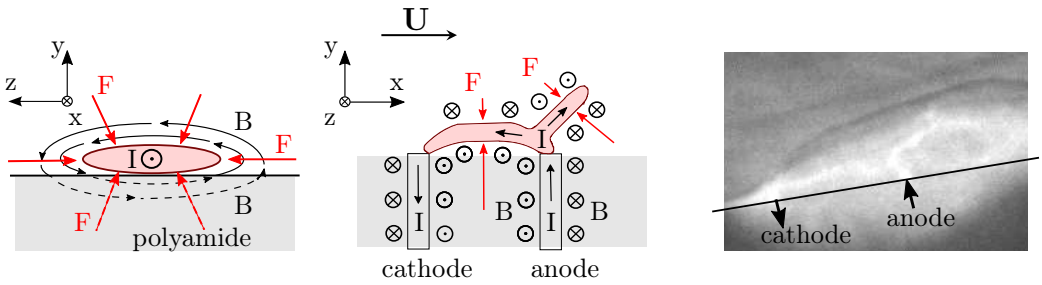

Figure 5.55: Induced magnetic field and corresponding Lorentz forces generated by the arc current in the nitrogen flow and in the polyamide plate (left). Induction effects due to the electric wiring under the wedge surface (middle and right) [1].

magnetic field around the gas discharge. This is the second effect to be discussed, which depends on the position of the power lines in the solid and the material used. In this particular case, the electromagnetic effect shown in Fig. 5.55 is analogous to that of a linear motor (e.g. railgun).

The physical system shown in the photograph in Fig. 5.55 is comparable to the test case under investigation. However, it has a larger electrode distance of 9.5 mm. Furthermore, the electric current of 1200 A and the voltage of 248 V at the time of image recording are substantially higher than in the examined system, where $I \approx 71$ A and $U \approx 139$ V. The magnetic field induced by the high electric current generates strong resulting Lorentz forces acting on the electric arc and its tail. This pushes both the arc and the tail upwards away from the surface (see Fig. 5.55 on the right). Experiments show that while the electric current drops during the capacitor discharge, the plasma column returns to the surface.

In the following, the influence of the Lorentz forces on the system under investigation is briefly examined. The flow velocity in the plasma column is approx. 800 $\mathrm{m \cdot s^{-1}}$ (see Fig. 5.28). As shown in Sec. 3.3.6, the inertial force during a uniform deceleration of a fluid volume over the characteristic length l_c during the time t_c from a velocity magnitude u_c to 0 $\mathrm{m \cdot s^{-1}}$ can be estimated by: $\mathbf{F}_\mathrm{inertial} = \rho \mathbf{a} V \sim \rho V u_\mathrm{c}^2 / 2 l_\mathrm{c}$, where $\mathbf{a}$ is the acceleration in $\mathrm{m \cdot s^{-2}}$ and u_c is the magnitude of the characteristic velocity of the fluid. The mass density of the fluid flow behind the shock wave is approximately 1.28 $\mathrm{kg \cdot m^{-3}}$. For $\rho = 1.28$ $\mathrm{kg \cdot m^{-3}}$, $V = 1.0$ $\mathrm{m^3}$, $u_\mathrm{c} = 800$ $\mathrm{m \cdot s^{-1}}$ and $l_\mathrm{c} = 1$ mm, the inertial force of the fluid is $\approx 4.0 \times 10^8$ $\mathrm{N \cdot m^{-3}}$. The Lorentz force per cubic meter is estimated as follows: $\mathbf{F}_\mathrm{Lorentz} = \eta \left(\mathbf{J} \times \mathbf{B} \right) V \approx \eta J B_c V$, where J is the magnitude of the electric current density. Between the electrodes J has an average value of $\approx 1.5 \times 10^8$ $\mathrm{A \cdot m^{-2}}$ and in the area of the cathode approximately 5×10^8 $\mathrm{A \cdot m^{-2}}$. Since the relative magnetic permeability of polyamide is $\mu_\mathrm{r} \approx 1$, the characteristic magnetic field $B_c = 1.6 \times 10^{-2}$ T is assumed for the field strength around the electrode lines in the insulating plate (the calculation of B_c is given in Sec. 2.3.1). The contributions of Lorentz forces generated by the magnetic field around the arc column would cancel each other out and are therefore not included in the calculation. By using the superposition principle, an approximate value of 0.032 T is obtained for the magnetic field between the electrode supply lines. This results

in an estimated value of $\approx 2.4 \times 10^6$ N $\cdot$ m^{-3} for the resulting Lorentz force in the arc column and $\approx 8.0 \times 10^6$ N $\cdot$ m^{-3} for the cathode region. The resulting Lorentz forces do not necessarily act in the direction opposite to the flow, but rather perpendicular to the surface upwards. Nevertheless, when putting $\mathbf{F}_{\text{Lorentz}}$ in relation to $\mathbf{F}_{\text{inertial}}$, the effects of the Lorentz forces can be approximately predicted. The ratio of the Lorentz force to the inertial force in the arc column between the electrodes amounts to ≈ 0.006 and in the cathode region to approximately 0.02. This means that only near the surface in lower areas of the boundary layer the gas discharge to be investigated could probably counteract the flow due to the low velocity there. It is therefore assumed that in the system under investigation the arc current is rather low to significantly lift the plasma column from the surface.

Chapter 6

Closure

This last chapter summarises the work, draws conclusions from the numerical results and gives suggestions for future work.

6.1 Conclusion

This research work is concerned with the development of a physicochemical model and its subsequent numerical implementation and validation for the simulation of ionized, high-enthalpy and high-speed gas flows in the state of nonequilibrium and in the presence of external electric and magnetic fields.

At the beginning of this work, a physicochemical system, a test case, which exemplarily represents the field of application of the new solver is defined. It is a wedge which is placed without angle of attack in a nitrogen flow with a free-stream Mach number of $M = 4.5$, a static temperature of 234 K and a static pressure of 0.34 bar. A high-intensity direct-current gas discharge with a constant input power of 10 kW is generated on the surface of the wedge between the electrodes installed flush with the surface, which leads to a partial ionisation of the flow and an intensive heating of the gas in that zone.

After defining, the physicochemical system is analysed by first determining the type of gas discharge to be investigated, its structure and physical properties. Then, the system is examined from the point of view of aerothermodynamics and chemical kinetics to determine the necessary modelling depth. During this process, the physicochemical system is analytically evaluated to obtain information on which assumptions and simplifications may be used to construct the physicochemical model as simply as possible, while retaining the most important physical and chemical effects.

After the analytical evaluation of the system, a physicochemical model is developed on the basis of the information obtained. This model is based on the single-fluid assumption and takes the chemical and thermal nonequilibria in the gas mixture into account. Therefore, the assumption of separable modes is used to calculate the energy contents of individual energy modes of the gas and the corresponding temperatures. The response of the partially ionized fluid to the electromagnetic fields is modelled via the Joule heating and the Lorentz force. The radiation losses are

also taken into account in the model. The electrodynamic modelling is simplified by means of the MHD approximation, the magnetostatic assumption and the potential formulation of Maxwell's equations.

Due to the high complexity of the processes within the nonequilibrium regions near the electrodes and their small dimensions compared to the characteristic length of the system, the modelling of the plasma nonequilibrium layers is simplified. Furthermore, the preionization process during the arc ignition is not considered. The ignition is modelled by locally heating the gas between the electrodes until the ionization begins and the gas becomes a conductor.

The numerical implementation of the physicochemical model is carried out using the open-source finite volume based software package OpenFOAM. The numerical solver developed in this thesis is a transient, segregated and pressure-based solver for modelling high-speed flows. The solver is developed together with the corresponding model library, which provides models for calculating the thermodynamic and transport properties as well as the radiation losses and plasma responses to the electric and magnetic fields.

The solver verification and validation consist of a one-dimensional and a three-dimensional analyses. The 1-D analysis is carried out for the verification of the finite-rate chemical module of the solver as well as all submodels for the transport and thermodynamic properties. For the three-dimensional validation, the previously defined and analytically evaluated system – a high-pressure arc discharge generated on the surface of a wedge in a supersonic flow – is numerically calculated. The numerical results are then compared with the experimental measurements and theoretical values obtained from the analytical evaluation of the system.

6.2 Results Summary

The results of the present work have been assessed and discussed in detail in the previous chapters. The most important results and conclusions are summarised in the following:

- The electric arc to be investigated is a surface discharge in a supersonic flow. This causes the arc column of the discharge to be pressed against the surface and severely stretched, giving it a flat shape and forming a long tail downstream. Its height amounts to 0.5 mm on average and its width to 2.8 mm.

- The plasma in the arc column is close to the LTE state. This is to be expected for collision-dominated high-pressure gas discharges to which the system under investigation belongs. At the edges of the gas discharge at temperatures below 11,000 K the thermodynamic nonequilibrium gradually emerges. The deviation of T_e from T exceeds 10 %.

- The maximum numerically calculated temperature in the arc column is approximately 15,000 K. The experimentally determined electronic excitation temperature of the copper atoms decreases during the experiment from 13,000 K

to 9000 K and is on average $\overline{T}_{\mathrm{el}} \approx 10{,}670$ K. This value is representative for the entire measuring volume, which is larger than the plasma column diameter. Because of the resulting averaging effects and due to the opacity of the plasma, the measured value of 10,670 K does not represent the maximum temperature in the arc column. It is therefore reassuring that the measured temperature is below the numerically calculated maximum value of 15,000 K.

- As far as the cathode zone is concerned, no reliable comparative values have been found for this region. It is assumed that the numerically calculated temperatures $T \approx 28{,}000$ K and $T_{\mathrm{e}} \approx 36{,}000$ K near the cathode are exaggerated since no formation of doubly charged nitrogen ions was taken into account. However, these values confirm the assumption of a strong nonequilibrium in the near-cathode region often used for electric discharges.

- The gas discharge acts on the flow as an obstacle, since the gas expands in all directions during rapid heating of the fluid, especially in the cathode area. This creates a stagnation point above the cathode and the static pressure increases. As a result, a shock wave occurs in a supersonic flow due to the gas discharge. The numerical calculations provide a value of approximately 1.8 bar for the static pressure at the cathode, while the pressure in the free-stream flow amounts to 1.45 bar.

- The numerical results show that at temperatures above 4000 K the preservation of quasineutrality is largely ensured. At lower temperatures, however, the concentrations of electrons and ions can decouple considerably. As a result, charge separation takes place in regions with lower temperatures and thus quasineutrality is not preserved. Therefore, the physicochemical model should be extended to ensure quasineutrality.

- The magnetostatic calculations show physically correct behaviour and provide acceptable agreement with the analytically calculated values. As expected, peak values in the electrostatic field and the electric current density occur at the electrode edges, which in turn result in peak values in the Joule heating and as a consequence in the temperature.

- The simulation results confirm the frequently used assumption that in thermal arcs maintained by high electric fields, the radiative cooling effects are negligible. However, according to Wells [35], the radiation losses in less intense gas discharges that form wider arc channels significantly affect the temperature distribution and all related arc properties.

- With regard to the Lorentz forces, the numerical calculation does not take into account the induction effects due to the electric circuit wiring under the wedge surface. However, it has been shown that the Lorentz forces caused by self-induction in the system under investigation have a rather weak influence on the high-speed flow.

In general it can be said that the simulation results provide a very detailed insight into the physical processes in an electric discharge and are generally in a fair agreement to analytical calculations and experimental measurements. For more reliable statements on solver validation, however, further experiments are necessary to determine the plasma temperature, the pressure and the plasma species composition.

6.3 Suggestions for Future Work

6.3.1 Further Development of the Physicochemical Model

The following suggestions represent the lessons learnt from this work.

Inclusion of Doubly-Charged Ions

In a nitrogen plasma, the production of doubly-charged ions in areas with a temperature of over 25,000 K is significant. It not only affects the gas properties there, but also leads to lower temperature values than without consideration of N^{++} due to the extraction of the second ionization energy from the gas. This applies to the gas discharge to be investigated only for the area near the cathode. However, the excessive temperature values there may influence the entire electric discharge. For more accurate calculations it is therefore important to consider the production of doubly charged ions in the kinetic mechanism for high intensity arc discharges.

Individual Treatment of Rotational Excitation as well as Translational Energy of Free Electrons

In the present work it is assumed that the translational and rotational temperatures are equal ($T = T_{\mathrm{tr}} = T_{\mathrm{rot}}$). In case of a strong thermodynamic nonequilibrium, e.g. in an arc-heated wind tunnel at the nozzle exit, the rotational excitation of the expansion flow may differ significantly from the translational temperature. In such a case it would be interesting to calculate T_{tr} and T_{rot} separately.

Furthermore, the present work assumes a common energy pool for the energy contained in the translational mode of the free electrons and the electronic excitation of heavy particles. Thus, both energy fractions are characterized by a common temperature $T_{\mathrm{e}} = T_{\mathrm{e,tr}} = T_{\mathrm{el}}$. Such an assumption might be useful for calculating high-temperature gas dynamics in processes, where free electrons are not exposed to external electric fields. In the work presented here, however, the energy exchange chain starts with the energy of free electrons accelerated by an electrostatic field. That is, the temperature of free electrons $T_{\mathrm{e,tr}}$ would be possibly higher, than the electronic-excitation temperature T_{el}. For further investigations of gas discharges it would therefore be requested to separate both energies from each other.

Turbulence Consideration

The turbulence modelling is not yet included in the physicochemical model due to a tremendous complexity of plasma turbulence. However, it would be useful for the beginning at least to consider the turbulence in the fluid entering the gas discharge area by means of a common turbulence model.

Implementation of More Sophisticated Wall Modelling

In the present work, no information is available about the temperature profile on the wedge surface during the gas discharge. However, it is assumed that the surface acts as a strong heat sink during discharge. For this reason and due to missing information, a maximum temperature of 1000 K is used as a boundary condition for the wall modelling. This simple assumption should be replaced by a more accurate boundary condition.

Additionally, a closer look at the catalytic processes on the wall would increase the modelling accuracy (finite-catalytic wall).

Induction Effects due to the Electric Circuit Wiring under the Surface

The solid material under the wedge surface, which consists of polyamide and the copper supply lines, is not considered in the simulation domain. It would be interesting to include this area in the modelling, because the magnetic field induced by the arc current is not only formed in the flow, but also in the solid below. Additionally, there is an influence of the electrode power supply lines on the magnetic field around the gas discharge, which depends on the position of the power lines in the solid and the material used.

Calculation of Charge Separation for Preservation of Quasineutrality

The numerical results show that in the areas with lower temperatures at the discharge periphery a charge separation may occur and thus the quasineutrality is not preserved. This is an important issue because, firstly, several assumptions of the physicochemical model are based on the assumption of quasi-neutrality and, secondly, that charge separation without restoring forces is unphysical. To preserve quasineutrality, the calculation of diffusion must be extended by an additional term, which calculates polarization fields and the resulting restoring forces in the case of non-uniformity of the number densities of ions and electrons.

6.3.2 Further Development of the Numerical Solver

The numerical tool developed in this thesis is based on a pressure-based compressible OpenFOAM solver that solves governing equations in a segregated manner, making a fully implicit treatment of source terms impossible. The implicit treatment of source terms, however, increases the solution robustness of the algebraic equation system in a numerical solver [63, 60]. In the present work it is particularly topical

for the source terms in the energy conservation equations. In a coupled method, the discretized equations are combined to a block structure and solved simultaneously after linearisation by means of iterative solution methods for coupled systems. The use of a coupled method would not only allow the implicit implementation of the energy source terms, but also the implicit treatment of thermal diffusion terms in the energy equations. This would contribute to the stability of the numerical solver and allow to perform calculations with larger computational time steps, thus reducing the computation time.

6.3.3 Proposals for Further Numerical Investigations

The next step towards a more accurate model would be to consider the contamination of the plasma with the electrode material and the material from the ablating insulating plate. This would help to perform a more accurate validation of the system, as CN (cyano radical) and Cu were used to experimentally determine the temperature in the gas discharge in the frame of this work. Further, the kinetic mechanism for high-temperature nitrogen used in this work can be extended to the mechanism for high-temperature air (11-species air model for chemical and thermal nonequilibrium) by using for example the work of Dunn and Kang [25] and the work of Park [14]. The collision integrals for the thermodynamic and transport properties can be found for example in Gupta *et al.* [23] and Yos [22].

Furthermore, it would be useful to numerically investigate less intensive electric discharges at lower pressures to analyse the equilibration processes in the plasma, since such discharges tend to show stronger thermodynamic nonequilibrium.

Finally, for more reliable statements on solver validation, further simulations on simple two-dimensional geometries are indispensable. In addition, further experimental measurements are required to obtain more data for accurate validation.

Appendix A

Cathode Emission

A.1 Mechanisms of Cathode Emission

The most important factors influencing the cathode emission are: the electric field at the cathode surface E_c, the cathode surface temperature T_c, the accumulation of ions in the cathode region and the cathode material and geometry. In the following, a distinction is made between four different electron emission mechanisms:

- secondary electron emission J_SEE,
- thermoionic emission J_T,
- field emission J_F,
- thermo-field emission J_TF.

Secondary emission (especially secondary ion-electron emission) plays a crucial role in glow discharges. In high-pressure arcs, however, its contribution is rather insignificant [11]. Therefore, secondary ion-electron emission is only briefly discussed here. It occurs due to the bombardment of the cathode by positive ions. This mechanism is not based on the collective effect of ion bombardment, but on individual interactions during which a given positive ion may or may not release an electron from the cathode surface [30]. This probability is given by the ion-electron emission coefficient γ_i that usually has values between 0.01 and 0.1 [11]. The electron current can thus be calculated as follows [20]:

$$J_\mathrm{SEE} = \gamma_i J_i \ . \tag{A.1}$$

Considering that in high-pressure arcs the ionic current accounts for only 10 % to 30 % of the total electric current in the cathode sheath, it becomes evident that secondary emission is not able to provide a sufficient amount of electron current in this electric discharge class.

The electron emission in high-pressure arcs is provided by thermoionic emission, field emission, and thermo-field emission mechanisms. There, the ion bombardment of the cathode surface also plays a key role. However, in contrary to the secondary

emission, this is a collective contribution, leading to the development of a hot spot on the cathode [30]. The T_c and E_c values in the cathode spot are high enough to activate the thermoelectronic and field emission mechanisms or a combined action of the both – the thermo-field emission. In contrary to secondary emission, the electron emission in a high-pressure arc can generate $\gamma_{\text{eff}} = 2 - 9$ electrons per one ion, providing 70 to 90 % of total arc current [11]:

$$S = \frac{\gamma_{\text{eff}}}{\gamma_{\text{eff}} + 1} \approx 0.7 - 0.9 \ . \tag{A.2}$$

A.2 Hot and Cold Cathodes

Cathodes in high-pressure arcs can be classified according to their electron emission mechanisms in hot (thermoionic) and cold (nonthermoionic) cathodes [34].

Hot cathodes are made of refractory materials, like tungsten (W) or carbon (C), and thus can sustain high temperatures without considerable melting or evaporation. Due to high temperature values on the material surface, a sufficient amount of electron current can be provided by a purely thermoionic emission (J_T). The cathode spot on a hot electrode can be both contracted or diffused, depending on cathode geometry and current. The diameter of a diffused spot is usually of several 100 μm, with current densities of about $J_T \sim 10^7 - 10^8$ A $\cdot$ m^{-2} [11, 20]. For a spot diameter of 500 μm and a current density of 1×10^8 A $\cdot$ m^{-2}, an electric current of approximately 20 A would result.

Cold cathodes, like copper (Cu) or silver cathodes (Ag), cannot sustain high temperature values necessary for a sufficiently large thermoionic emission, due to a low melting point of the cathode material. Instead, the electrons are emitted in the thermo-field regime via a very small hot spot, leading to erosion of cathode material [11, 34]. For copper electrodes, the current density ranges between 10^8 and 10^{12} A $\cdot$ m^{-2} [11]. The cathode spot of a cold cathode has a diameter of $\sim$ 10 μm and can reach temperatures of approximately 3000 K and higher. These conditions lead to the electron emission in the thermo-field regime.

A.3 Thermoionic Emission

The thermoionic emission can be calculated by the Richardson-Dushman equation as follows [11, 20, 34]:

$$J_T = \frac{4\pi m_e e k_B^2}{h^3} T_s^2 (1 - R) exp\left(-\frac{\Phi_{\text{eff}}}{k_B T_s}\right) \ , \tag{A.3}$$

where $k_B = 8.617 \times 10^{-5}$ eV $\cdot$ K^{-1}. The quantity R is the quantum mechanical coefficient describing the reflection of the electrons from the potential barrier related to the material surface, which has typical values of $0 - 0.8$ [11]. For the expression $4\pi m_e e k_B^2/h^3$ it is convenient to use a numerical value, which amounts to 1.2×10^6 A $\cdot$

$K^{-2} \cdot m^{-2}$. For a purely thermoionic emission, the value Φ_{eff} is equal to the value of the material's work function Φ_0, which is approximately 4.5 eV for copper. In such a case, only the cathode surface temperature T_c affects the strength of the thermoionic current density J_{T}. If, however, a sufficiently large electric field E_c is established on the cathode surface, a reduction of work function Φ_0 occurs, known as Schottky effect. This work-function decrease is calculated as follows [11, 20, 34]:

$$\Phi_{\text{eff}} = \Phi_0 + \delta\Phi \text{ , where } \delta\Phi = -\left(\frac{eE_{\text{c}}}{4\pi\epsilon_0}\right)^{1/2} . \tag{A.4}$$

It is convenient to use for Eq. A.4 the following numerical form:

$$\delta\Phi = -3.8 \times 10^{-5} E_{\text{c}}^{1/2} . \tag{A.5}$$

When Eq. A.3 is used together with Eq. A.4, the so-called field-enhanced thermoionic emission can be calculated.

A.4 Field Emission

The field emission occurs purely due to the electric field on the cathode surface E_c. It becomes significant at the electric field values of $E_{\text{c}} > 10^9 \text{ V} \cdot \text{m}^{-1}$ [11]. The electric current due to field emission may be estimated by the Fowler-Nordheim equation given as [11, 73]:

$$J_{\text{F}} = \frac{e}{4\pi h\left(\Phi_0 + \epsilon_{\text{F}}\right)} \left(\frac{\epsilon_{\text{F}}}{\Phi_0}\right)^{\frac{1}{2}} E_{\text{c}}^2 \; exp\left(-\frac{4\kappa\Phi_0^{\frac{3}{2}}\xi}{3E_{\text{c}}}\right) , \tag{A.6}$$

where $\kappa^2 = 8\pi^2 m_e/h^2$. The quantity ϵ_{F} is the Fermi energy of the material and ξ is a correction factor which is a function of the ratio $\delta\Phi/\Phi_0$. The numerical form of Eq. A.6 is as follows [11]:

$$J_{\text{F}} = \frac{0.062}{\left(\Phi_0 + \epsilon_{\text{F}}\right)} \left(\frac{\epsilon_{\text{F}}}{\Phi_0}\right)^{\frac{1}{2}} E_{\text{c}}^2 \; exp\left(\frac{-6.8 \times 10^9 \; \Phi_0^{\frac{3}{2}}\xi}{E_{\text{c}}}\right) . \tag{A.7}$$

A.5 Thermo-Field Emission

As described before, the prediction of the emission current via the thermoionic-emission mechanism is sufficiently accurate for hot cathodes with a diffuse cathodic spot and a moderate surface electric field. For cold cathodes, however, this method could lead to an underestimation of electron emission by a factor of several hundreds [34]. The second important emission mechanism – field emission - becomes noticeable only at very high electric fields. However, the combined action of the thermoionic and field emission leads to a non-linear enhancement of the cathode emission, called thermo-field emission. According to Jeanvoine [34], this emission mechanism is the

most effective emission process and can lead to an increase by a factor of more than 500, compared to individual contributions of thermoionic- and field-emission mechanisms together.

The thermo-field emission current density J_{TF} can be predicted most accurately by the equation of Murphy and Good as follows [34]:

$$J_{\mathrm{TF}} = \int_{-W_{\mathrm{a}}}^{\infty} D(E_{\mathrm{c}}, W) \cdot N(W, T_{\mathrm{c}}, \Phi_0) dW \ , \tag{A.8}$$

where $-W_{\mathrm{a}}$ is the effective constant potential of electrons inside the emitter (cathode) surface, and W is the energy of an electron incident on the potential barrier at the metal surface [74]. The function $D(E_{\mathrm{c}}, W)$ is the probability of an electron of energy W to penetrate the barrier. The function $N(W, T_{\mathrm{c}}, \Phi_0)$ is the Fermi-Dirac energy distribution of electrons moving towards the surface [34].

The results of the numerical calculation of the Murphy and Good equation for $\Phi_0 = 4.5$ eV are shown in Fig. A.1. From this diagram, it can be deduced that at low electric-field values the thermo-field emission tends to become independent from E_{c} (purely thermoionic emission), whereas at large E_{c} it becomes temperature independent (pure field emission) [74].

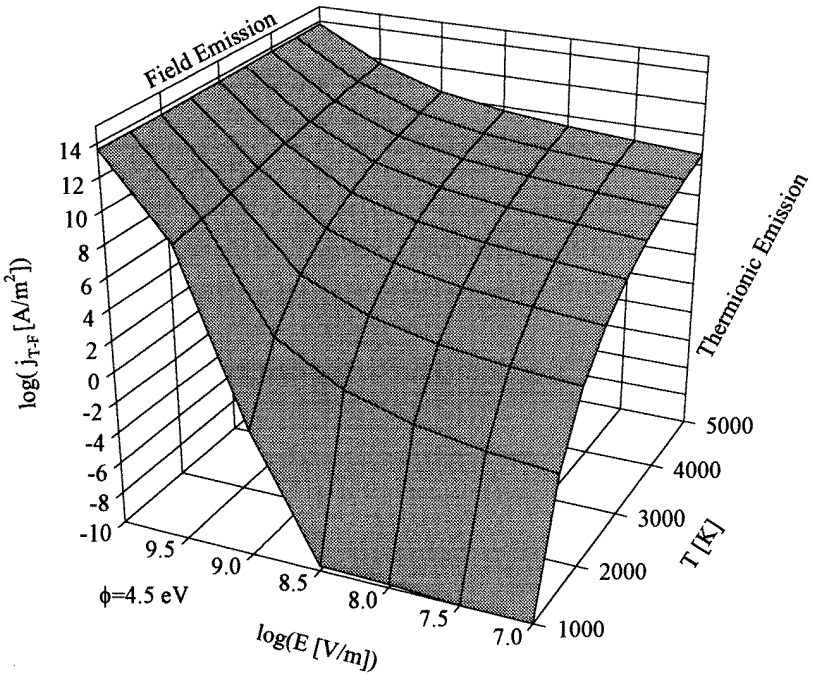

Figure A.1: Thermo-field emission [74].

The results in Fig. A.1 are now used for an estimation of E_{c} in the system under investigation. The amperage in the arc under investigation amounts to 80 A. Assuming a spot diameter of ~ 30 μm (cold cathode), a cathode-spot current density

of $J_{\mathrm{TF}} \approx 2.8 \times 10^{10}$ A $\cdot$ m^{-2} is obtained. The cathode surface temperature in the hot spot is estimated at ≈ 2900 K (evaporation temperature of copper is 2835 K). By using the diagram in Fig. A.1, these values yield an electric field on the cathode of $E_{\mathrm{c}} \approx 2.2 \times 10^{9}$ V $\cdot$ m^{-1}. This value can be verified by an equation, which gives the relation between E_{c}, current density $\mathbf{J}$, and the cathode voltage drop U_{c}. The numerical form of this equation is given as follows [11]:

$$E_{\mathrm{c}} = 5 \cdot 10^{3} \mathcal{M}^{1/4} (1 - S)^{1/2} U_{\mathrm{c}}^{1/4} J_{\mathrm{FT}}^{1/2} \ . \tag{A.9}$$

The derivation of this equation can be found in Fridman and Kennedy [11]. The quantity $\mathcal{M}$ is the molar mass, which is 14 for atomic nitrogen. By assuming a cathodic voltage drop of $U_{\mathrm{c}} = 18$ V [11] and an electric current fraction of $S = 0.8$, Eq. A.9 yields an electric field of $E_{\mathrm{c}} \approx 1.5 \times 10^{9}$ V $\cdot$ m^{-1}. This value is close to the value obtained from the diagram in Fig. A.1. The discrepancy may result from difficulties in reading off the values in Fig. A.1 or from the rather arbitrary chosen diameter of the cathode spot.

In the following, the value calculated above of the thermo-field emission current density J_{TF} is compared with the field-enhanced thermoionic emission current density J_{T} and the field emission current density J_{F}.

By inserting the value calculated above ($E_{\mathrm{c}} \approx 2.2 \times 10^{9}$ V$\cdot$m^{-1}) into Eq. A.5, yields a reduction of the work function of $\delta\Phi = 1.78$. The cathode-surface temperature and the work function of copper are assumed to be of 2900 K and 4.5 eV, respectively. For the quantum mechanical coefficient, the mean value is taken from the typical value range: $R = 0.4$. By inserting these values in Eq. A.3, the field-enhanced thermoionic emission current density amounts to $J_{\mathrm{T}} \approx 1.135 \times 10^{8}$ A $\cdot$ m^{-2}.

The Fermi energy of copper amounts to $\epsilon_{\mathrm{F}} = 7$ eV. The correction factor ξ in Eq. A.9 can be found in Fridman and Kennedy [11] and is 0.85 for the ratio $\delta\Phi/\Phi_0 \approx 0.4$. Using these values together with Eq. A.7, yields a field emission current density of $J_{\mathrm{F}} \approx 6.6 \times 10^{8}$ A $\cdot$ m^{-2}.

The values of J_{T} and J_{F} added give an overall current density of $\approx 7.73 \times 10^{8}$ A $\cdot$ m^{-2}, which is by a factor of nearly 36 less than the thermo-field emission current density, calculated above. This example shows that for cold cathodes the combined action of the thermoionic and field emission leads to a non-linear emission enhancement.

Appendix B

Species Properties

Table B.1: Curve-fit coefficients for equilibrium constant $K_{\text{eq}}{}^{*}$ [14, 23]

reaction r	A_1	A_2	A_3	A_4	A_5
	dissociation of N_2 ($N_2 \rightarrow N + N$)				
1, 2, 3, 4, 6	1.4766	1.6291	1.2153	−11.457	−0.009444
	associative ionization ($N + N \rightarrow N_2^+ + e$)				
5	−2.3644	−5.0704	−4.9885	−5.7332	−0.039703
	electron-impact ionization of N ($N \rightarrow N^+ + e$)				
7	−0.9026	−3.4255	−2.2526	−16.679	−0.008037
	charge exchange between N_2 and N ($N_2 + N^+ \rightarrow N_2^+ + N$)				
8	−0.02208	−0.745209	−2.09774	0.1661	−0.1268

* These curve-fit coefficients are valid only for number densities $n \geq 10^{24}\text{m}^{-3}$.

Table B.2: Species electronic data [14, 46, 26].

	N_2		N		N_2^+		N^+	
level i	g_i	$\Theta_{\text{el},i}$ [K]	g_i	$\Theta_{\text{el},i}$ [K]	g_i	$\Theta_{\text{el},i}$ [K]	g_i	$\Theta_{\text{el},i}$ [K]
ground	1	0.0	4	0.0	2	0.0	1	0.0
1	3	7.223157×10^4	10	2.766470×10^4	4	1.318997×10^4	3	7.006835×10^1
2	6	8.577863×10^4	6	4.149309×10^4	2	3.663323×10^4	5	1.881918×10^2
3	6	8.605027×10^4	12	1.199002×10^5	4	3.668876×10^4	5	2.203657×10^4
4	3	9.535119×10^4	6	1.240142×10^5	8	5.985305×10^4	1	4.703183×10^4
5	1	9.805635×10^4	12	1.268027×10^5	8	6.618366×10^4	5	6.731252×10^4
6	2	9.968267×10^4	02	1.346396×10^5	4	7.598992×10^4	15	1.327190×10^5
7	2	1.048976×10^5	20	1.364503×10^5	4	7.625508×10^4	9	1.571435×10^5

Table B.3: Molar mass values of species in a high-temperature nitrogen [53].

species	N_2	N	N_2^+	N^+	e
$\mathcal{M}_s$ $\left[\mathrm{kg \cdot kmol^{-1}}\right]$	28.01340	14.00670	28.01285	14.006157	5.4858×10^{-4}

Table B.4: Enthalpy of formation $(\Delta h_\mathrm{f})_s^0$ at 0 K in $\mathrm{J \cdot kmol^{-1}}$ [53]

	N_2	N	N_2^+	N^+	e
$(\Delta h_\mathrm{f})_s^0$	-8.67×10^6	4.70818×10^8	1.50331×10^9	1.873149×10^9	-6.197×10^6

Table B.5: Curve-fit constants for collision cross-section $\overline{\Omega}_{ij}^{(1,1)*}$ [23].

pair number	interaction pair (i-j)	$A_{\overline{\Omega}_{ij}^{(1,1)}}$	$B_{\overline{\Omega}_{ij}^{(1,1)}}$	$C_{\overline{\Omega}_{ij}^{(1,1)}}$	$D_{\overline{\Omega}_{ij}^{(1,1)}}$
1	$N_2 - N_2$	0	−0.0112	−0.1182	4.8464
2	$N - N_2$	0	−0.0194	0.0119	4.1055
3	$N - N$	0	−0.0033	−0.0572	5.0452
4	$e - N_2$	0.1147	−2.8945	24.5080	−67.3691
5	$e - N$	0	0	0	1.6094
6	$N^+ - N_2$	0	0	−0.4000	6.8543
7	$N^+ - N$	0	−0.0033	−0.0572	5.0452
8	$N_2^+ - N_2$	0	0	−0.4000	6.8543
9	$N_2^+ - N$	0	0	−0.4000	6.8543

* The collision cross-sections are obtained in $\mathring{A}^2$; 1 $\mathring{A}^2 = 10^{-20}\mathrm{m}^2$.

Table B.6: Curve-fit constants for collision cross-section $\overline{\Omega}_{ij}^{(2,2)*}$ [23].

pair number	interaction pair (i-j)	$A_{\overline{\Omega}_{ij}^{(2,2)}}$	$B_{\overline{\Omega}_{ij}^{(2,2)}}$	$C_{\overline{\Omega}_{ij}^{(2,2)}}$	$D_{\overline{\Omega}_{ij}^{(2,2)}}$
1	$N_2 - N_2$	0	−0.0203	0.0683	4.0900
2	$N - N_2$	0	−0.0190	0.0239	4.1782
3	$N - N$	0	−0.0118	−0.0960	4.3252
4	$e - N_2$	0.1147	−2.8945	24.5080	−67.3691
5	$e - N$	0	0	0	1.6094
6	$N^+ - N_2$	0	0	−0.4000	6.7760
7	$N^+ - N$	0	0	−0.4146	6.9078
8	$N_2^+ - N_2$	0	0	−0.4000	6.7760
9	$N_2^+ - N$	0	0	−0.4000	6.7760

* The collision cross-sections are obtained in $\mathring{A}^2$; 1 $\mathring{A}^2 = 10^{-20}\mathrm{m}^2$.

Appendix C

One-Dimensional Verification

C.1 One-Dimensional Test Case

The computational grid of the test case for 1-D analysis consists of 250 cubic control volumes of equal size with an edge length of 1 mm (see Fig. C.1). The boundary conditions used are listed in Tab. C.1, where $n = 1, 2, ..., 12$. The time steps used in the simulations vary between $\Delta t \sim 10^{-4}$ at low and $\Delta t \sim 10^{-9}$ at high temperatures.

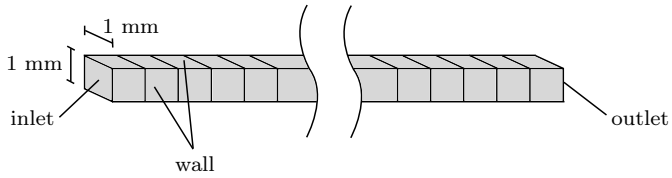

Figure C.1: Schematic diagram of the simulation domain for 1-D analysis.

Table C.1: Boundary conditions for 1-D analysis for n different temperatures*.

boundary	T [K]	p [bar]	U $[\mathrm{m \cdot s^{-1}}]$	$c_{\mathrm{N_2}}$ [−]	$c_{\mathrm{N,N_2^+,N^+,}e}$ [−]
inlet	$2000 \times n$	1.0	1.0×10^{-7}	1.0	0.0
wall	$2000 \times n$	1.0	1.0×10^{-7}	$\frac{\partial c}{\partial n} = 0$	$\frac{\partial c}{\partial n} = 0$
outlet	$\frac{\partial T}{\partial n} = 0$	$\frac{\partial p}{\partial n} = 0$	$\frac{\partial U}{\partial n} = 0$	$\frac{\partial c}{\partial n} = 0$	$\frac{\partial c}{\partial n} = 0$

* $n = 1, 2, ..., 12$.

C.2 Number Densities of Constituents of a Nitrogen Plasma

The focus is now set on the verification of the solver's chemical module and on the kinetic mechanism used in this work (see Tab. 3.1). For the verification, the work of Pflanz and ter Horst [37] is used, which provides particle densities of hydrogen,

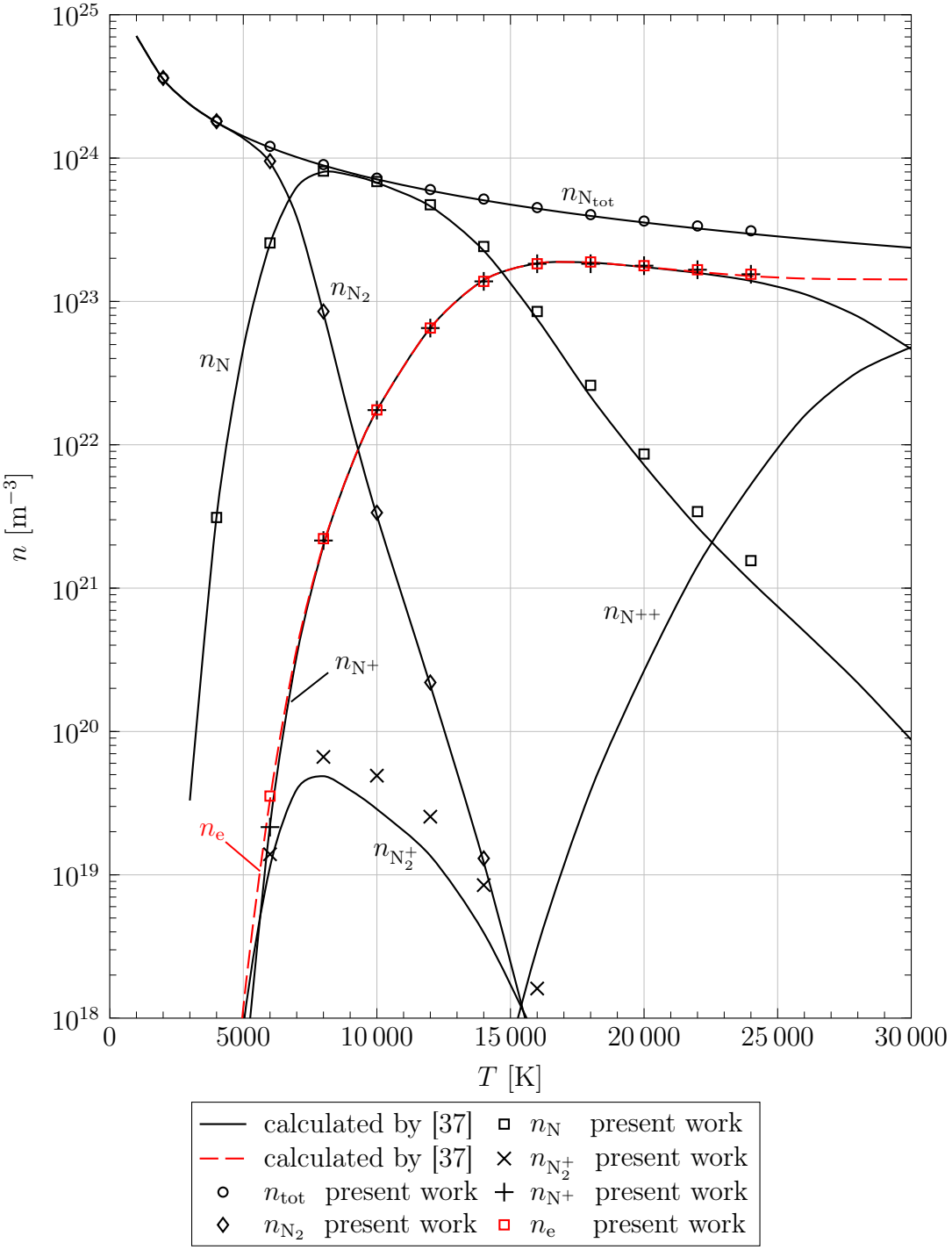

Figure C.2: Number densities of constituents of a nitrogen plasma at 1 bar versus temperature.

nitrogen and oxygen in the state of physicochemical equilibrium for pressures from 1 to 30 bar and temperatures to 50,000 K. The results of the verification are presented in Fig. C.2. The data calculated in [37] are represented by dashed an solid lines.

Results obtained in the present work are indicated by markers.

A good agreement is observed for the number densities of N_2, N^+, and e. The number densities of N_2^+, however, are overestimated. The deviation from the calculations of Pflanz and ter Horst is of a factor 1.36 at 8000 K and of 1.86 at 12,000 K. Although the number density of N_2^+ is very low compared to other species, the overestimation of $n_{N_2^+}$ could noticeably affect the system. This becomes clear when looking at the reaction 8 in the kinetic mechanism in Tab. 3.1. It has been found during the simulations carried out in the present work that taking this reaction into account has a noticeable impact on the whole species composition in the plasma. Furthermore, at temperatures of over 15,000 K, the particle densities of N are slightly overestimated as well. However, no significant influence is expected here since the number densities of N at high temperatures are much lower compared to those of the electrons and ions. The doubly-charged atomic ions, N^{++}, are not considered in the present work.

C.3 Thermodynamic Properties

For the verification of the thermodynamic properties, the specific heat capacity at constant volume c_v and the overall specific energy e for a reference state of 0 K are used. For c_v, the so-called "frozen" specific heat is considered, which does not account for species production or conversion due to chemical reactions. Since the flow velocity in the 1-D test case is very low (see Tab. C.1), the contribution of the kinetic energy per unit mass ($\frac{1}{2}|\mathbf{u}|^2$) to the overall specific energy can be neglected.

In the present work, the comparative values of c_v and e used for the verification are calculated analytically based on the works of Pflanz and ter Horst [37] and Gupta *et al.* [23]. The following two equations are used for the analytical calculation:

$$c_v = \sum_{s=1}^{n} c_s c_{v,s} \text{ and } e = \sum_{s=1}^{n} c_s e_s \ , \tag{C.1}$$

where $c_{v,s}$ and e_s, are calculated by using the curve fits and corresponding tabulated data given in [23]. The mass fractions for each species are calculated as follows:

$$c_s = \frac{n_s \mathcal{M}_s}{\sum_{r=1}^{n} (n_r \mathcal{M}_r)} \ , \tag{C.2}$$

where the number densities n are taken from [37].

C.3.1 Specific Heat Capacity

The verification results of c_v are presented in Fig. C.3. A good correlation is observed between the analytically calculated and numerically obtained data for temperatures below 10,000 K. At higher temperatures, however, the simulation results deliver lower values. The deviation of the simulation results from the analytical values, for example at 14,000 K, is of 6.7 %. Whether and to what extent the deviations

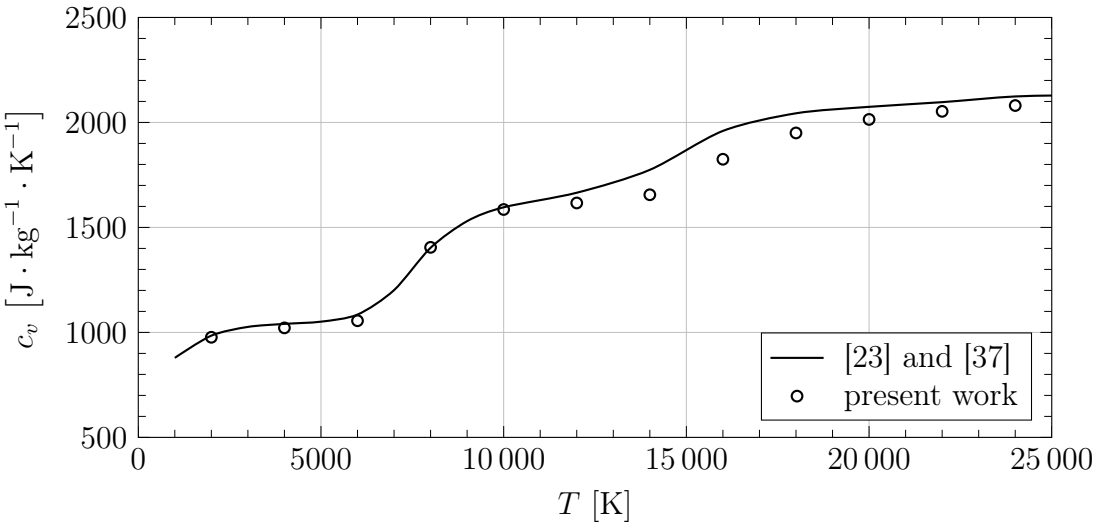

Figure C.3: Specific heat capacity at constant volume of nitrogen plasma at 1 bar versus temperature.

in number densities in Fig. C.2 have an influence on the underestimation of c_v is currently unclear. Furthermore, it has been found during the verification that at temperatures $> 12{,}000$ K the value of c_v is influenced by the number of energy levels used for the calculation of the electronic-excitation specific heat via Eqn. 3.28.

C.3.2 Specific Internal Energy

An excellent agreement is observed between the simulation results and analytically calculated data for the specific energy e (see Fig. C.4).

C.4 Transport and Radiation Properties

For the verification of the transport properties, results from five different research works are used:

i. The work of Yos [22] has already been discussed in the previous chapters.

ii. In the report of Capitelli and Devoto [71], the transport properties are calculated for nitrogen at 1 atm pressure and temperatures from 5000 K to 35,000 K. According to the authors a satisfactory agreement is found between the calculated and measured properties in the arc.

iii. In the work of Wells [35], a detailed study of the axially-symmetrical uniform arc column in nitrogen at 1 atm is undertaken. For the calculations of arc properties, Wells used data regarded as the best available (both experimentally derived and calculated) on the variation of transport properties with temperature. These data are used in the present work for verification.

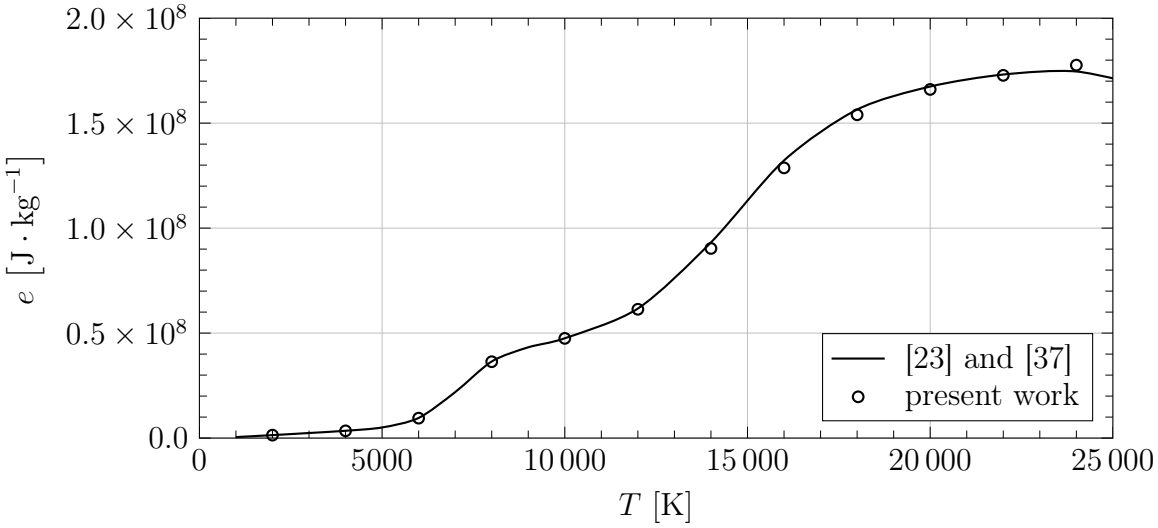

Figure C.4: Specific internal energy of nitrogen at 1 bar versus temperature.

iv. In the research work of Monterde-Garcia [75] a calculation procedure is given for the evaluation of the material functions from the measured electric-field strength and radiated power per unit arc length as functions of current strength. In this way, the material functions of the nitrogen plasma are evaluated from available measurements. The radiation losses are derived from temperature measurements at different electrical currents.

v. Murphy and Arundell [72] calculated transport properties of argon, nitrogen, and oxygen plasmas, and mixtures of argon and nitrogen and of argon and oxygen for atmospheric-pressure plasma. The calculations assume local thermodynamic equilibrium and are performed fo the temperature range from 300 K to 30,000 K. Murphy and Arundell state that a number of the collision integrals used in calculating the transport coefficients are significantly more accurate than values used in previous theoretical studies, resulting in more reliable values of the transport coefficients.

C.4.1 Viscosity

The viscosity verification results are presented in Fig. C.5. A good correlation is found between the data given by Yos [22] and the simulation results for temperatures below 12,000 K. At higher temperatures, the simulated values exceed the values calculated by Yos. At 16,000 K, for example, the deviation from the Yos' data is of 23.5 % and at 20,000 K of 16.05 %. As described in Sec. 3.2.3, the viscosity model used in the present work is a further development of the formula presented by Yos. The improvements consist in the extension of this formula to the multi-temperature approach made by Lee [21] and using more recent collision integrals for neutral-neutral and neutral-charged collisions presented in Gupta *et al.* [23]. Since the 1-D

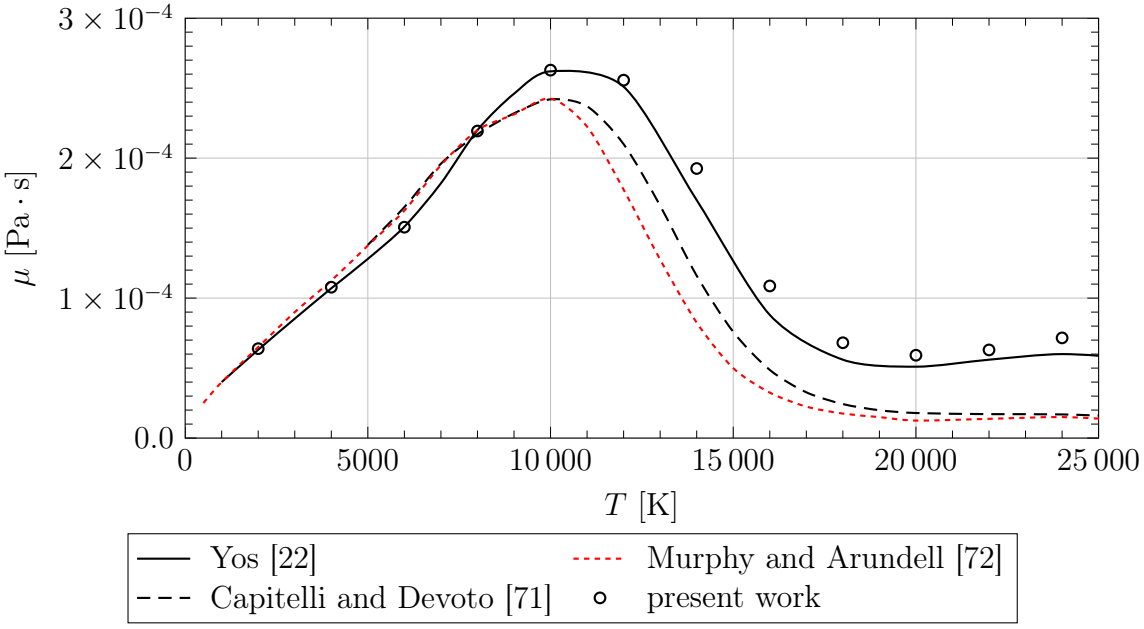

Figure C.5: Viscosity of equilibrium nitrogen at 1 bar versus temperature.

system to be investigated is in thermal equilibrium, it is assumed that the deviations between the numerical simulations and the data calculated by Yos are mainly due to differences in the collision integrals used. Yos' calculations demonstrate a good agreement with the results of other authors at temperatures below 8000 K. However, at higher temperatures, Yos's viscosity model provides a significant overestimation.

C.4.2 Frozen Thermal Conductivity

For the verification of the thermal conductivity the so-called frozen thermal conductivity κ_f is used instead of total thermal conductivity κ_tot. The frozen thermal conductivity is defined as follows [23]:

$$\kappa_\mathrm{f} = \kappa_\mathrm{tot} - \kappa_\mathrm{r} = \kappa_\mathrm{tr} + \kappa_\mathrm{rot} + \kappa_\mathrm{vib} + \kappa_\mathrm{el} + \kappa_\mathrm{e,tr} \ , \tag{C.3}$$

where κ_r denotes the reactive contribution to the thermal conductivity for chemical equilibrium conditions, defined as [23]:

$$\kappa_\mathrm{r} = \rho \sum_{s=1}^{n} \mathcal{D}_s e_s \frac{\partial c_s}{\partial T} \ . \tag{C.4}$$

The consideration of κ_r requires the evaluation of the derivative $\frac{\partial c_s}{\partial T}$, which is associated with a greater computational effort.

In Fig. C.6, the results of κ_f obtained in the present work are compared with the data of other authors. There is a significant divergence, especially at temperatures over 14,000 K, between the Yos' data and the more recent results of Capitelli and

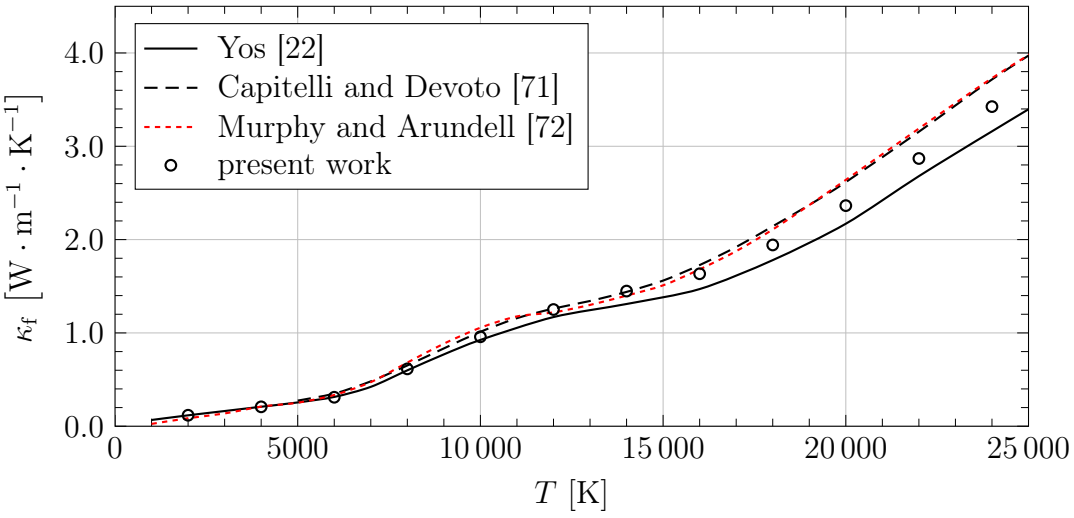

Figure C.6: Frozen thermal conductivity, $\kappa_f = \kappa_{tr} + \kappa_{rot} + \kappa_{vib} + \kappa_{el} + \kappa_{e,tr}$, of nitrogen at 1 bar versus temperature.

Devoto [71] and Murphy and Arundell [72], which in turn are in excellent agreement. The fact that Yos' calculations generally yield significantly lower values of κ compared to other research works is also mentioned in Wells' report [35]. The values of κ_f obtained in the present work correspond well with [71] and [72] up to 16,000 K. At higher temperatures, however, the simulation results are located between the results of [71] and [72] and the data of Yos. The underestimate of the simulation results compared to the calculations of [71] and [72] amounts at 20,000 K to approx. 10 %.

C.4.3 Electrical Conductivity

Fig. C.7 shows simulation results of electrical conductivity versus data of other research works. An excellent agreement is found between the results of Capitelli and Devoto [71] and Murphy and Arundell [72]. Yos' data yield significantly lower values of σ compared to [71] and [72]. The results obtained in the present work deliver values which are between the calculations of [71] and [72] and the data given by Yos. At lower temperatures, they also show good agreement with the data used by Wells.

The model used for the electrical conductivity is taken from the research of Yos, with the difference that in the present work the electron-electronic temperature T_e is used instead of T. Since the simulation model used for the verification is brought into the LTE state, it is assumed that the differences between the simulation results and the data given by Yos stem from different collision integrals used.

C.4.4 Radiated Power

The results of the radiation-losses verification are shown in Fig. C.8. Yos' data show a strong overestimation of the $\dot{Q}_{rad}$ values compared to Monterde-Garcia [75] and Wells [35], which are in a good agreement. The fact that Yos' model tends to provide

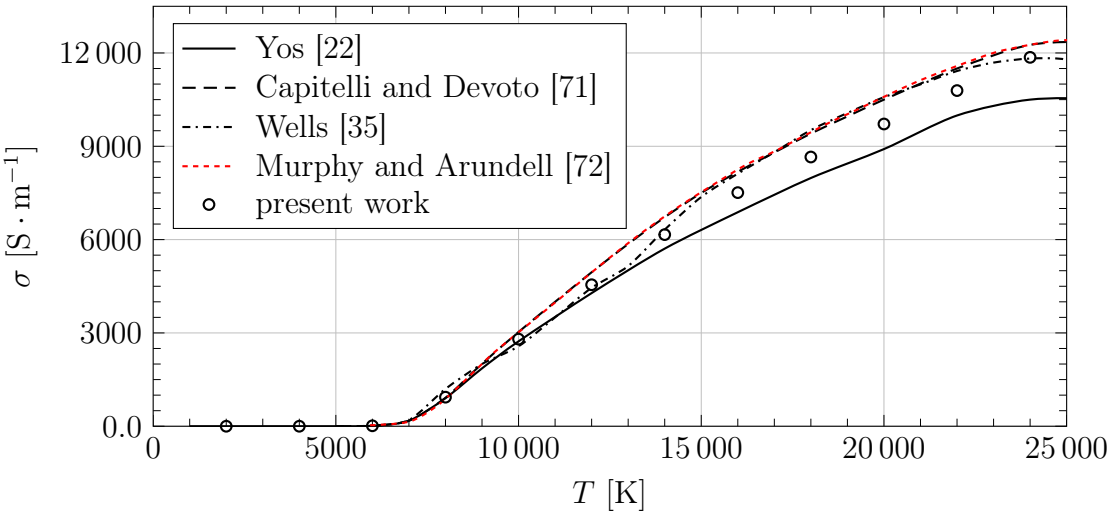

Figure C.7: Electrical conductivity of nitrogen at 1 bar versus temperature.

higher radiation losses is also mentioned in Wells' work. The simulation results obtained in the present work deliver $\dot{Q}_{\mathrm{rad}}$ values above those of Yos at temperatures over 12,000 K. This most likely results from the different collision integrals used.

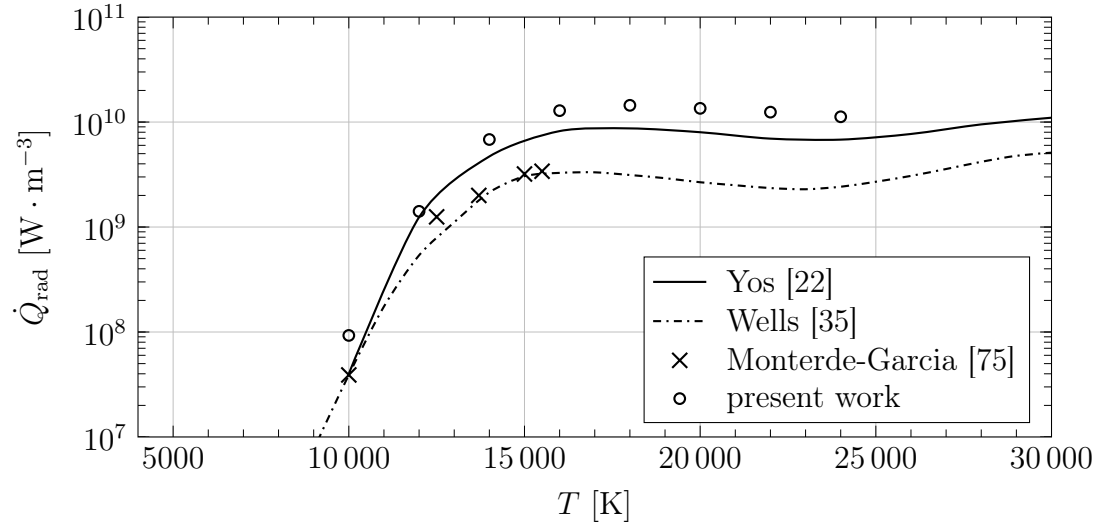

Figure C.8: Continuum radiated power per unit volume from nitrogen at 1 bar versus temperature.

According to Wells, the radiation losses in high-pressure gas discharges have a rather insignificant effect on the overall energy balance. Therefore, it is assumed that the overestimation shown in Fig. C.8 will have no noticeable impact on the simulation results. For less intensive electric discharges in the NLTE state, however, this overestimation could influence simulation results.

Appendix D

Experimental Measurements

As already mentioned, the temperature measurements are conducted with a constant arc input power of 10 kW, while the pressure measurement experiments were carried out at uncontrolled discharge of the capacitor. Another difference between the temperature and the pressure measurements are different diameters of the electrodes used. For pressure measurements, electrodes with a diameter of 1.0 mm are used, while the electrode diameter for temperature measurements is 2.0 mm. The distance between the edges of the electrodes, which is crucial for the electric field strength, is the same for all experiments and is of 5.0 mm.

D.1 Temperature Measurements

D.1.1 General Information

The temperature measurements are carried out by means of time-resolving emission spectroscopy. This technique allows to obtain information about the time evolution of parameters such as rotational, vibrational or electronic-excitation temperature [70].

Several experiments at different operating conditions have been carried out at ISL for measuring the temperature of the plasma formed by an electric discharge actuator in a nitrogen atmosphere. For the present work, only temperature measurements in a discharge with a constant arc input power of 10 kW are considered.

From a total of 22 experiments with a constant input power, 4 experiments are evaluable (see Tab. D.1). It should be noted that further experiments are needed for a more reliable solver validation. The arc input power is controlled by means of the current regulation. Typical time evolutions of current, voltage, and power during the gas discharge operation are presented in Figs. D.1 and D.2.

The measuring point (imaged volume V_{M}) is located between the electrodes directly in front of the anode (electrode c). The height of V_{M} is of a few millimetres and the diameter is around 3.5 mm. The measurements are carried out in two different ways regarding the geometric orientation of the sample beam, namely perpendicularly and horizontally to the wedge surface. In this way, the influence of the sample beam position on the measurements may be investigated. The two different orientations of

Table D.1: Emission spectroscopy experiments for the temperature evaluation.

exp.	exp. number	V_M orientation*	$\overline{I}$ [A]	$\overline{U}$ [V]	$\overline{P}$ [kW]	evaluated quantity
1	141-181204-03	perpendicularly	79.4003	128.0696	10.1426	T_{rot}, T_{vib}
2	143-181204-05	perpendicularly	79.3450	126.9925	10.0560	T_{rot}, T_{vib}
3	144-181211-01	perpendicularly	80.0371	120.7113	9.6366	T_{rot}, T_{vib}
4	150-181213-02	horizontally	79.3768	126.1249	9.9936	T_{el}

* The orientation of the measurement volume V_M with respect to the wedge surface.

the imaged volume are visualized in Fig. D.3 via the backward illumination.

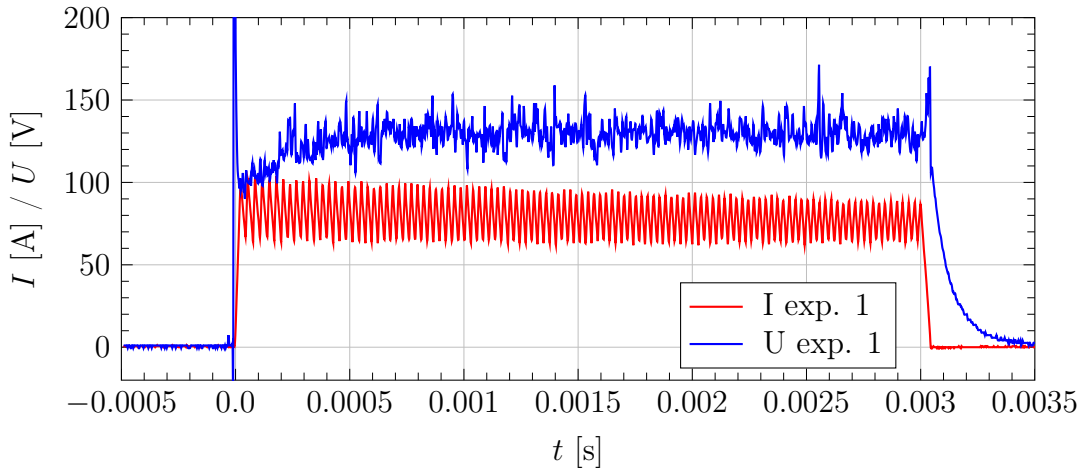

Figure D.1: Voltage and current measured at the electrodes vs. time (exp. 1).

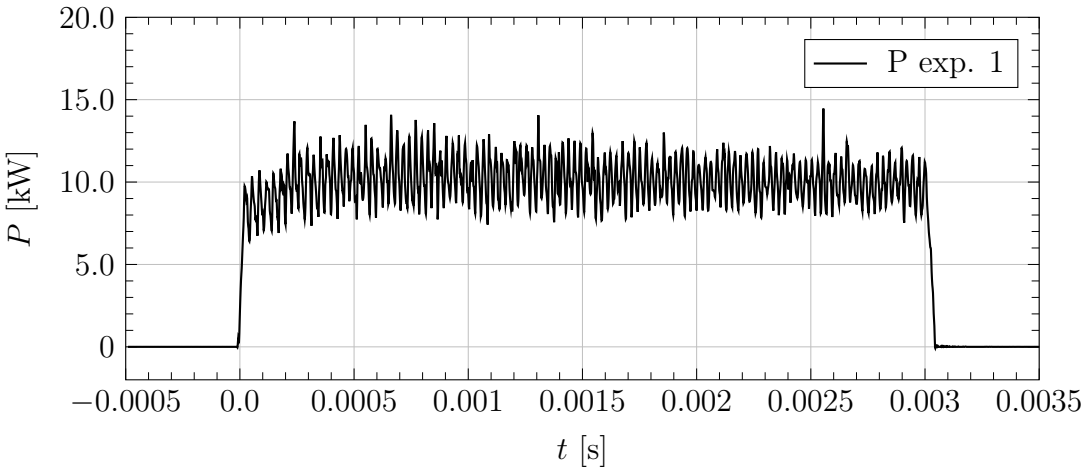

Figure D.2: Power-time curve (exp. 1).

The calculation of T_{rot} and T_{vib} is based on the evaluation of the CN violet system ($B^2\Sigma^+ - X^2\Sigma^+$ system) with the bandhead at approx. 388.34 nm, for the upper

and lower states of vibrational transitions: $\nu' = \nu'' = 0$. For the evaluation of the electronic-excitation temperature, T_{el}, atomic line emission of copper identified in experimentally measured emission spectra at approximately 520.0 nm is utilized [70]. Both species CN (cyano radical) and Cu occur due to the contamination of the nitrogen plasma by the electrode erosion and the ablation of the polyamide insulation plate.

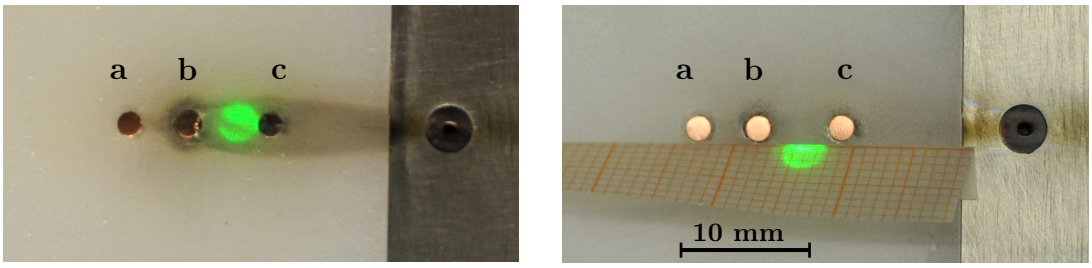

Figure D.3: Temperature measurement with the sample beam oriented perpendicularly (left) and horizontally (right) to the wedge surface.

D.1.2 Experimental Setup and Procedure

For the optical access to the shock-tunnel measurement chamber, a silica window is used, which has a constant transmittance of 0.92 in the wavelength range from 200 nm to approximately 2 μm. This transmittance is taken into account by the calibration of the measurement system with a tungsten-ribbon strip source at known temperature. The optical signal emitted from the measuring point is focused by means of a lens into an optical fibre, as shown in Fig. D.4. The fibre is made of

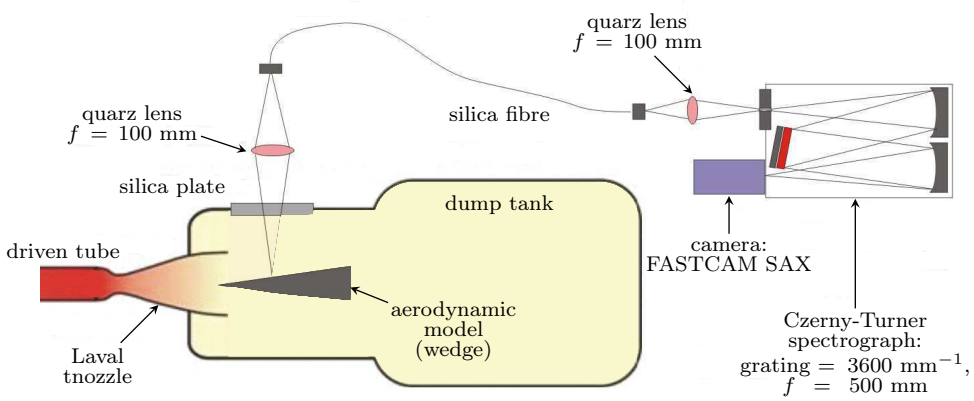

Figure D.4: Experimental setup for time-resolved emission spectroscopy in a shock tube experiment (f denotes the focal length) [70].

high-grade fused silica with a transmittance of 0.55 in the wavelength range from 260 nm to 2.2 μm. Via this silica fibre, the signal is transmitted to the entrance slit of the SPEX-500 Czerny-Turner spectrograph equipped with a 3600 grooves/mm^{-1}

grating. The entrance slit aperture of 25 μm is used for both the measured CN violet system and the copper atomic lines. The function of the entrance slit is to ensure an acceptable spectral resolution of the measured spectra. The signal is recorded by means of a FASTCAM-SAX camera installed in the exit plane of the spectrograph. The camera system is able to work with time frame ranges from 5 ms up to 40 μs [70, 76]. The spectral sensitivity of the system described allows using it for measurements between 330 and 900 nm with good efficiency [70].

The experimental procedure is as follows:

- A capacitor of 330 μF serves as energy source. It is charged under 450 V leading to a stored energy of 33.4 J. The diaphragm of the shock tube bursts and a quasi-stationary flow is formed past the wedge.
- The electric discharge is generated on the wedge's surface between the electrodes b and c. The discharge is triggered at $t = 0.0$ s.
- The streak camera is triggered at $t = 0.0$ s by the signal from a delay generator and a pressure transmitter installed upstream from the test section.
- The operation time of the electric discharge amounts to approximately 3.00 ms. During this time span, the time-spectral picture of the electric-discharge radiation is captured by 10 images, each with an exposure time of 40 μs.

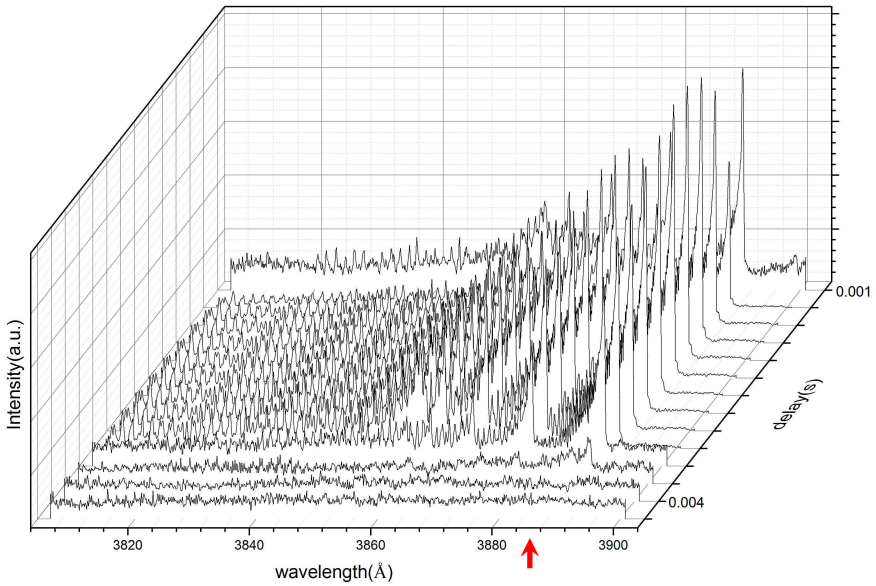

Figure D.5: Time-resolved emission spectra of the CN violet band system with the bandhead at around 3883 $\mathring{A}$ for $\nu' = \nu'' = 0$ transitions (exp. 1) [70].

As an example, Fig. D.5 shows the time-resolved emission spectra of the CN violet-band system recorded in experiment 1 (see Tab. D.1). The band head of the $B^2\Sigma^+ - X^2\Sigma^+$ system is marked with an arrow. In Fig. D.6, the time-resolved atomic copper emission spectra at around 520 nm obtained in experiment 4 are shown.

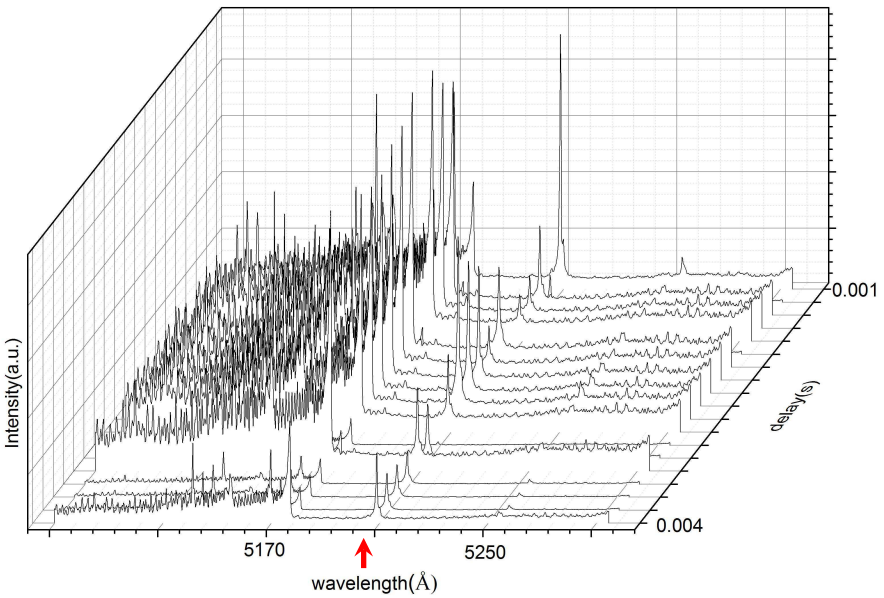

Figure D.6: Time-resolved atomic emission spectra of copper at around 5200 $\AA$ (exp. 4) [70].

D.1.3 Data Processing

For the evaluation of the temperatures, first a numerical technique is used to synthetically generate spectra of the resolved CN violet band emission and atomic copper spectral lines. The intensities of the CN violet-system band head and of the Cu lines

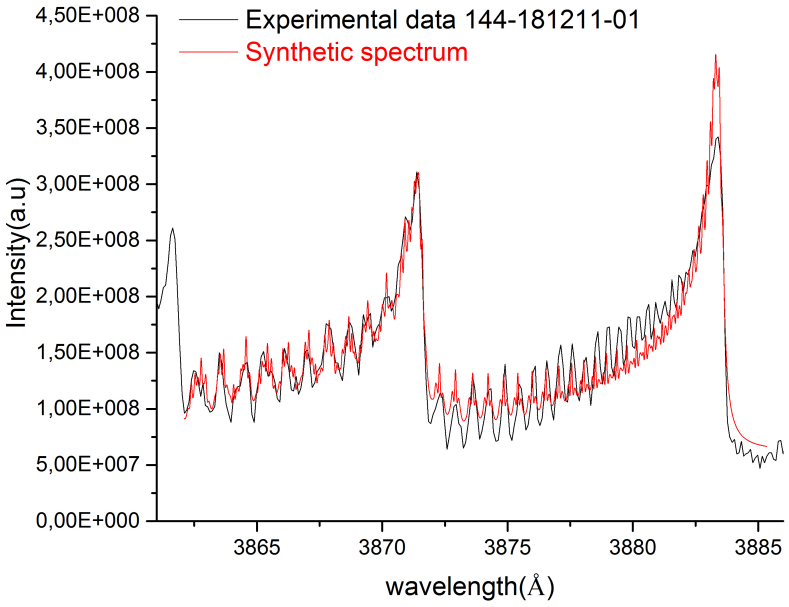

Figure D.7: Synthetically generated CN violet system spectra fitted to experimentally measured spectra (exp. 3) [70].

are then determined by fitting the synthetically generated spectra to the spectra measured in the experiment (see Fig. D.7).

D.1.4 Results

The experimentally obtained temporal variations of T_{rot} and T_{vib} are shown in Figs. D.8 and D.9, respectively. In experiment 3, the first two values at $t = 0.0$ s and $t = 0.0003$ s could not be evaluated. Furthermore, it can be that the temperatures measured in exp. 2 exhibit a strong fluctuation and are significantly higher than in exp. 1 and 3. The reasons of this behaviour are still unclear. The average temperatures, $\overline{T}_{\mathrm{rot}}$ and $\overline{T}_{\mathrm{vib}}$, calculated from the results are shown in Tab. D.2. The experimentally obtained temporal variation of T_{el} is shown in Fig. D.10. The mean temperature value amounts to: $\overline{T}_{\mathrm{el}} = 10{,}672.17$ K.

Table D.2: Mean values of T_{rot} and T_{vib} obtained by emission spectroscopy.

experiment	1	2	3	1, 2, and 3	only 1 and 3
$\overline{T}_{\mathrm{rot}}$ [K]	6860.14	8246.34	7214.79	7456.54	7017.76
$\overline{T}_{\mathrm{vib}}$ [K]	8312.40	11,158.98	8299.33	9325.30	8306.59

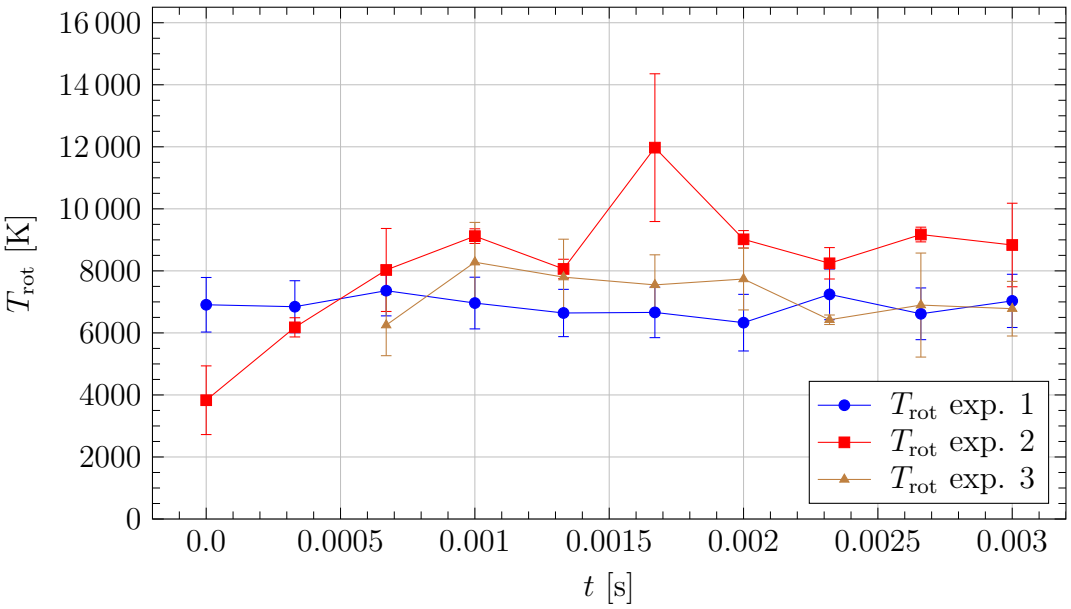

Figure D.8: Rotational temperature T_{rot} of the CN molecule obtained by time-resolved emission spectroscopy [70].

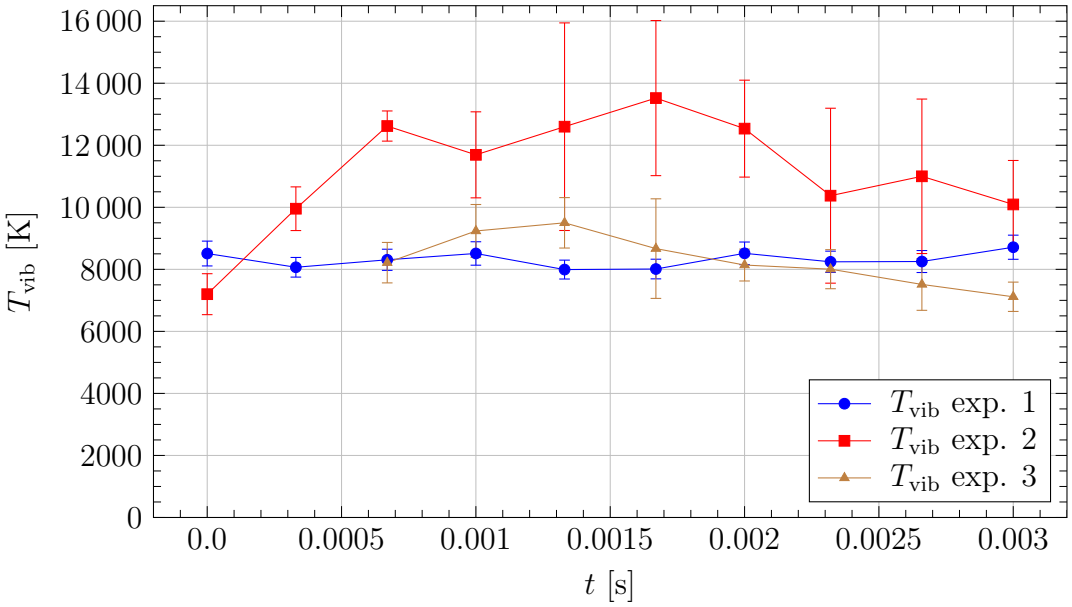

Figure D.9: Vibrational temperature T_{vib} of the CN molecule obtained by time-resolved emission spectroscopy [70].

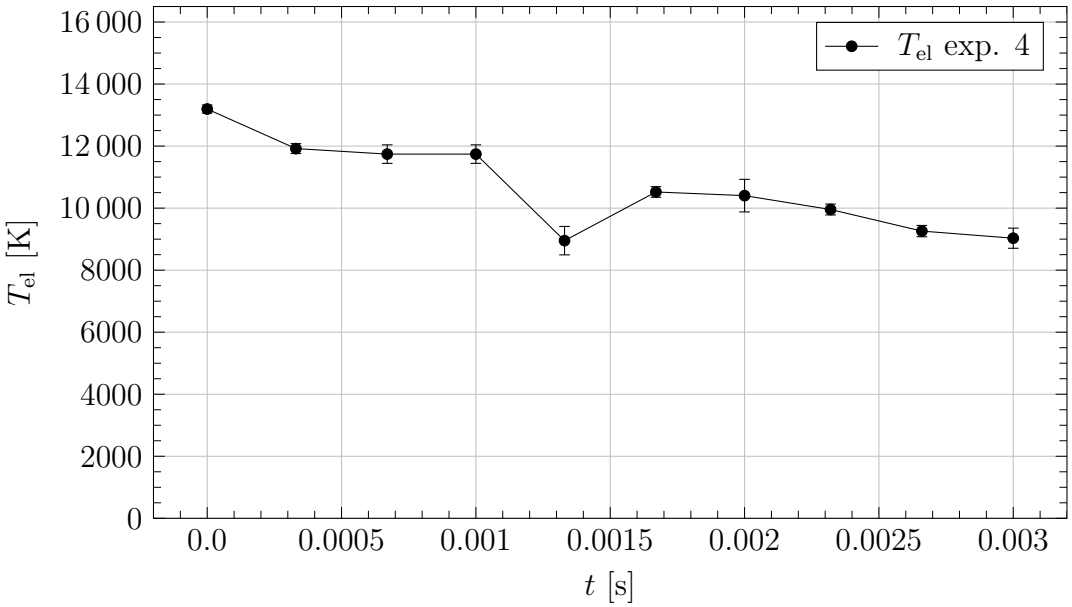

Figure D.10: Electronic-excitation temperature T_{el} of copper atoms obtained by time-resolved emission spectroscopy [70].

D.1.5 Conclusions

For the analysis of the temperature measurements, the mean temperatures of the CN molecule (cyano radical), $\overline{T}_{\mathrm{rot}}$ and $\overline{T}_{\mathrm{vib}}$, calculated only with the data from exp. 1 and 3 are used (see Tab. D.2), since the data from exp. 2 exhibit strong fluctuations.

The results of the temperature measurements don't provide information about the spatial variation of the CN optical emission signals. In the following it is assumed that the received optical signal originates from the areas of the arc column with the highest cyano radical concentrations. For the system under investigation, this would mean that the concentration of CN is highest and consequently the optical signal is strongest in arc regions with $T_{\mathrm{rot}} \approx 7000$ K and $T_{\mathrm{vib}} \approx 8300$ K. Assuming that the temperature in the centre line of the arc column is substantially higher than 7000 K ($T_{\mathrm{max}} = T_{\mathrm{c}} = 12{,}000$ K), then the spatial distribution of cyano radical concentration would form a kind of shell structure in an axisymmetric arc column. Of course, in a surface discharge, such as the system under investigation, this structure would not have a rotationally symmetric shape. In Fig. D.11, an attempt is made to schematically illustrate this shell structure. This figure in no way represents a quantitative analysis and is based on conjecture.

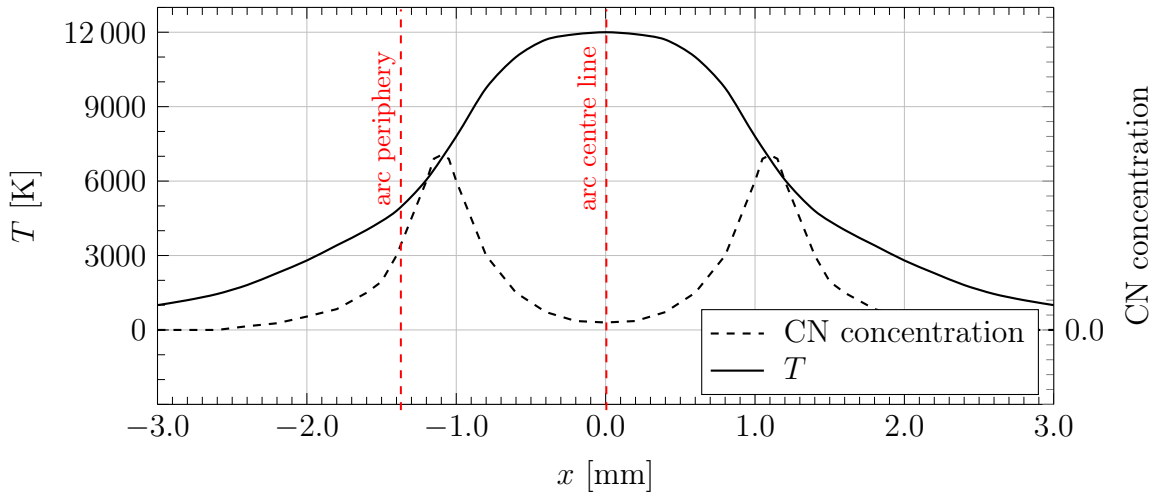

Figure D.11: Schematic representation of CN concentration vs. temperature across the arc column of the gas discharge, CN shows a maximum near 7000 K.

The above analysis can be confirmed by the works of Parigger *et al.* [77] and Colonna [78]. Parigger *et al.* examined the atomic and molecular signatures of hydrogen, cyano radical and carbon in laser-induced plasma by means of temporally-resolved emission spectroscopy. It has been found that for both air and a CO_2-N_2 mixture at atmospheric pressure, the CN molecule shows a maximum concentration at approximately 7000 K. A very similar result can be found in the work of Colonna, where the thermodynamic properties of SiC-seeded air plasma are investigated in wide pressure and temperature ranges. Furthermore, the temperatures experimentally

measured in the present work show that the system under investigation is in the zones of maximum CN concentration in the state of thermal nonequilibrium, because $\overline{T}_{\mathrm{vib}}$ is noticeably higher than $\overline{T}_{\mathrm{rot}}$.

The measured average electronic-excitation temperature of the copper atoms amounts to $\overline{T}_{\mathrm{el}} \approx 10{,}670$ K. At this temperature, the plasma to be examined would probably approach the LTE and hence $T_{\mathrm{el}} \approx T$. Whether the measured electronic-excitation temperature of copper can be assumed as the maximum translational-rotational temperature of the nitrogen-plasma species in the centre line of the arc column is still unclear. In the present work no investigations of the relaxation times between nitrogen species and copper atoms have been carried out. Therefore, this issue remains a subject for future investigations. In addition, Fig. D.10 clearly shows that T_{el} does not reach a steady state, but decreases during the discharge operation from $\approx 13{,}000$ K to approximately 9000 K. Therefore, $\overline{T}_{\mathrm{el}}$ determined from only one experiment should be treated with caution.

D.2 Pressure Measurements

In the present work, three pressure transducers mounted laterally to the electrodes marked with P15, P30, and P45 are used for pressure measurements (see Fig. D.12).

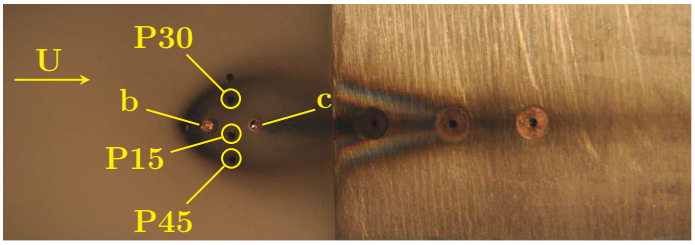

Figure D.12: Electrodes b and c and pressure transducers P15, P30, and P45 in a polyamide plate.

All pressure transducers are from the Kulite-Semiconductor company. Their technical characteristics and their position regarding the distance from the symmetry axis (axis through the centres of the electrodes b and c) are depicted in Tab. D.3. The

Table D.3: Pressure transducers: location and technical characteristics [79]

transducer	distance from the symmetry axis [mm]	model	pressure range [bar]	natural frequency in [kHz]
P15	1.5	XCL-080	3.5	300
P30	3.0	XCQ-080	7.0	380
P45	4.5	XCL-080	7.0	380

accuracy of the measurements is 0.1 % of the rated absolute pressure. The pressure sensing principle is based on the dielectrically isolated piezoresistive technology, which makes these sensors not susceptible to electromagnetic interference [79].

The experimental procedure is as follows:

- A capacitor of 1000 μF serves as energy source. It is charged under 450 V leading to a stored energy of 101 J.
- The diaphragm of the shock tube bursts and a stream flow is formed past the wedge. In Fig. D.14 it can be observed, how at time $t = -0.0005$ s the shock wave passes the sensors P15, P30, and P45.
- The quasi-stationary flow is formed past the model for 2 ms. During this phase, a constant static pressure of $p_\infty \approx 0.310$ bar is established in the flow, whereas the surface pressure on the wedge is of $p \approx 1.45$ bar (see Fig. D.14).
- After a quasi-stationary flow is formed around the model, the electric discharge is generated on the wedge's surface between the electrodes b and c. The gas discharge is triggered at $t = 0.0$ s.
- The operation time of the gas discharge amounts to approximately 1.18 ms. During the experiment, the electrical current and the voltage are measured at the electrodes b and c (see Fig. D.13) in addition to the pressure. The recording of the pressure measurements is shown in Fig. D.14.

To slow down the capacitor discharge, a coil is built into the electrical circuit. As a result, the current peak at the beginning of the discharge is avoided and the current-time curve takes the form of a wave which rises to reach a maximum of 460 A after approximately 380 μs and, after exceeding the maximum, decreases slowly (see Fig. D.13). At the beginning of the discharge the electrical voltage at the electrodes amounts to 450 V. After the arc ignition, it falls to approximately 130 ± 20 V and remains in this value during the whole operational time of the discharge.

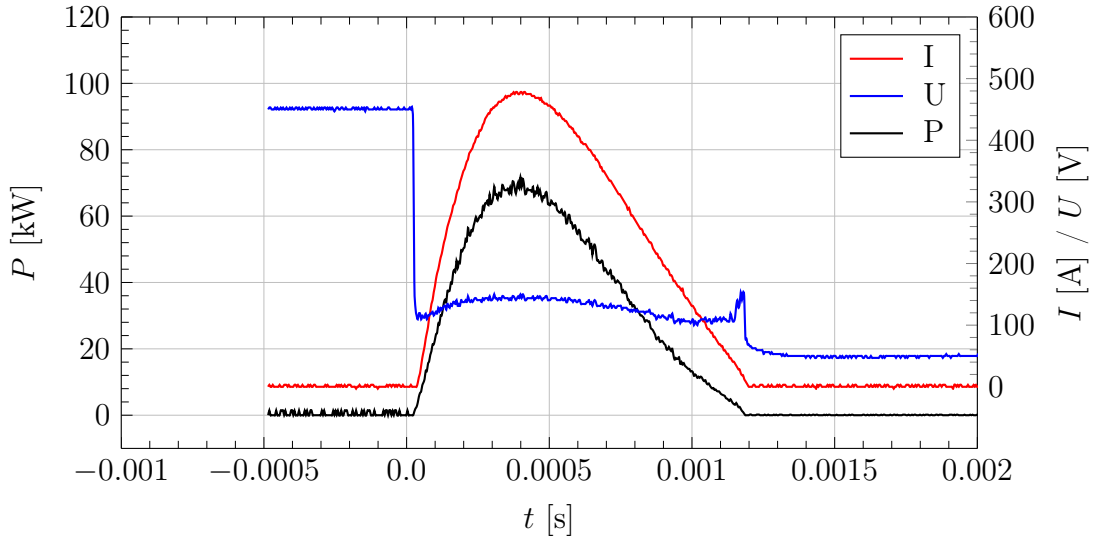

Figure D.13: Voltage and current vs. time measured at the electrodes and the resulting power-time curve [79].

The increase of the electric current I leads to an increase of the Joule heating and thus to a temperature increase in the gas discharge. As a result, the gas pressure in the high-temperature region also rises. Fig. D.14 clearly shows how the pressure values of the three sensors follow over time the power-time curve. The high-temperature region on the wedge surface is recognizable in Fig. D.3 by a darkening of the surface.

For the validation, pressure values at arc input power of 10 kW are needed. These values can only be meaningfully read out during the time period of performance decrease at $t \approx 1.1$ ms. At this time, all three pressure transducers yield approximately of 1.85 ± 0.05 bar. This value is used for the validation. In addition, the surface pressure outside the gas discharge will also be used for the solver validation. This value can be read out from Fig. D.14 at $-0.0004\ \text{s} < t \leq 0.0\ \text{s}$ and is approximately 1.45 bar.

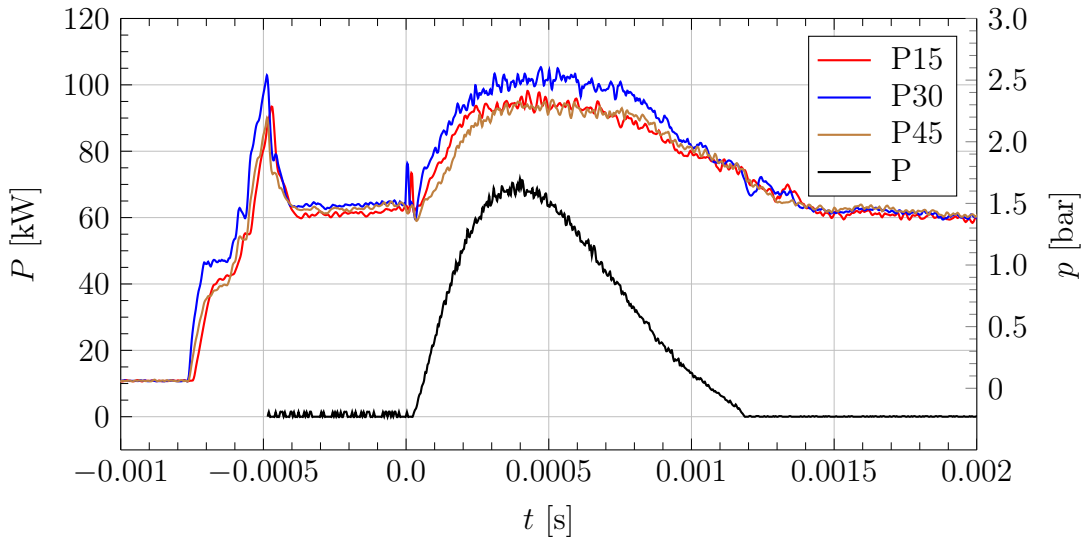

Figure D.14: Pressure vs. time in comparison to power-time curve [79].

Appendix E

Computational Costs

In this Appendix, computational costs are discussed. All values and calculations presented are initially only given for the system under investigation and the computing capacities used in the present work. Afterwards, possibilities for the acceleration of the numerical calculations are discussed.

Using the computational resources (2 Intel Xeon Gold 6130 processors with 16 cores each) and the test case described above, the new solver requires the following computation times per one times step:

- Chemical module: < 1 s.
- Fluid-dynamic module: ≈ 10 s.
- Magnetostatic module in mode 1: $50 - 100$ s.
- Magnetostatic module in mode 2: < 1 s.

That is, in mode 2, a calculation time of ≈ 10 s is required for one time step on the server used, while in mode 1 the same calculation can take up to 110 s. Therefore, it is obvious that mode 1 should be used only at the beginning for obtaining the average value of Φ_c. Thereafter, mode 2 should be utilized.

For the investigation of the gas-discharge impact on the flow variables around the arc and further downstream, a simulation of an operational duration of 1 ms is absolutely sufficient. The quasi-steady state in the gas discharge and in its vicinity is reached even after several tens of microseconds. Assuming a spatial discretization of $\Delta t = 2.0 \times 10^{-10}$ s and a calculation time per one time step of 10 s, the simulation of an operational duration of ≈ 1 ms using the computational resources described above would take $\approx$ 13,900 hours. Increasing the number of computational cores from 32 to 128 or 256 may reduce the computational time by a factor of 3 to 4, which would still result in a computational duration of around 4000 h (165 days).

The solver version used in this work is in its early stage of development and will be further optimized in the future work. Many calculations can be simplified considerably. For example, for the calculation of Coulomb-collision integrals, polynomial equations with tabulated curve-fit coefficients may be used instead of using formulas. It is assumed that the calculation time per time step of the fluid dynamic module can

be reduced by at least a factor of 2 (most likely more). As a result, the calculation time per time step on the server used would reduce to not more than 5 s. Consequence, this would reduce the computing time for the system under investigation from 4000 h (see further above) to 2000 h (83 days). The reduction the operational time of the gas discharge from 1.0 ms to 0.25 ms would reduce the computational time to $\approx$ 500 hours (21 days). By using a more powerful computer and further optimizing the solver, it may be possible to reduce these calculation times even further, approaching a reasonable amount of time.

This simple calculation shows how resource-intensive transient 3-D calculations of high-pressure gas discharges in the state of thermochemical nonequilibrium on computational grids of several million cells can be. For this reason, such calculations are rarely found in the literature. Usually, additional simplifications are made and coarser computational grids are used to reduce the computational effort.

It is important to mention that by reducing the maximum temperature in the simulation domain, larger computational time steps can be used. For this purpose, it has to be investigated whether the consideration of doubly-charged nitrogen ions would significantly contribute to the temperature reduction at the electrode edges. If this should be the case, the formation of N^{++} should definitely be taken into account, even if only to obtain correct temperatures in the near-electrode constricted zones.

According to Wells [35], the maximum temperature in the centre line of an axially-symmetrical arc column of a magnetically propelled discharge with an input power of 20 $kW \cdot cm^{-1}$ amounts to 12,000 K (see Fig. 2.11). For such temperatures, a temporal discretization of the order of $\Delta t \sim 10^{-9}$ s is absolutely sufficient. That is, for the investigation of electrodeless arcs the computation time of $\approx$ 2000 h estimated above for $\Delta t = 2.0 \times 10^{-10}$ would decrease to at least 200 h (8.3 days). This time would be further reduced by using a more powerful computer and further optimizing the solver.

Bibliography

[1] P. Gnemmi and C. Rey. 'Guidance of a Supersonic Projectile by a Plasma Actuator'. In: *23rd International Symposium on Ballistics*. Tarragona, Spain, 2007.

[2] P. Gnemmi, R. Chargon, J. P. Duperoux and A. George. 'Feasibility Study for Steering a Supersonic Projectile by a Plasma Actuator'. In: *AIAA Journal* 46.6 (2008), pp. 1308–1317.

[3] P. Gnemmi and C. Rey. 'Plasma Actuation for the Control of a Supersonic Projectile'. In: *AIAA Journal of Spacecraft and Rockets* 46.5 (2009), pp. 989–998.

[4] P. Gnemmi. Concept of the Steering of a Supersonic Projectile by an Electric Discharge Generating a Plasma, Research Management Accreditation Thesis, University of Paris-Ouest Nanterre La Défense, France. Dec. 2013.

[5] P. Gnemmi, C. Rey and P. Wey. 'Supersonic Projectile Behaviour under Electric Discharges Generating a Plasma'. In: *28th International Symposium on Ballistics*. Atlanta/GA, USA, 2014.

[6] P. Gnemmi and C. Rey. 'Experimental Investigations on a Free-Flying Supersonic Projectile Model Submitted to an Electric Discharge Generating Plasma'. In: *30th International Symposium on Shock Waves (ISSW30)*. Tel Aviv, Israel, 2015.

[7] A. Nekris, P. Gnemmi and Ch. Mundt. 'Modelling of an Electric Arc Discharge Generating a Plasma in Interaction with a Gas Flow'. In: *International Conference on Research and Application of Plasmas (PLASMA-2015)*. Warsaw, Poland, 2015.

[8] A. Nekris, P. Gnemmi and Ch. Mundt. 'Multi-Species Simulations of Plasma Discharges in NLTE State in Supersonic Flows'. In: *51st 3AF International Conference of Applied Aerodynamics*. Strasbourg, France, 2016.

[9] A. Nekris, P. Gnemmi and Ch. Mundt. 'Numerical Simulations of Plasma Discharges in Supersonic Flows'. In: *47th AIAA Fluid Dynamics Conference*. also AIAA 2017–4310. Denver, CO, USA, 2017.

[10] P. Gnemmi, C. Rey, A. Eichhorn, M. Bastide and J. L. Striby. 'Pressure, Temperature and Free-Flight Projectile-Displacement Measurements during a Plasma Discharge generated on a Supersonic Projectile'. In: *International Journal of Aerodynamics* 3.1, 2 and 3 (2013).

[11] A. Fridman and L.A. Kennedy. *Plasma Physics and Engineering*. New-York, USA: Taylor and Francis, 2004.

[12] Y. Takahashi, H. Kihara and K. Abe. 'The effects of radiative heat transfer in arc-heated nonequilibrium flow simulation'. In: *Journal of Physics D: Applied Physics* 43.18 (2010).

[13] S. T. Surzhikov. *Computational Physics of Electric Discharges in Gas Flows*. Walter de Gruyter GmbH, 2013.

[14] C. Park. *Nonequilibrium Hypersonic Aerothermodynamics*. John Wiley and Sons, 1990.

[15] J. D. Jr. Anderson. *Hypersonic and High Temperature Gas Dynamics, Second Edition*. American Institute of Aeronautics and Astronautics, 2006.

[16] M. Mitchner and C. H. Jr. Kruger. *Partially Ionized Gases*. John Wiley and Sons, 1973.

[17] C. Baudry. 'Contribution à la modélisation instationnaire et tridimensionnelle du comportement dynamique de l'arc dans une torche de projection plasma'. PhD thesis. Limoges, France: Université de Limoges, Nov. 2003.

[18] A. Blais. 'Nouvelle méthode de caractérisation des jets de plasma supersoniques en déséquilibre aérodynamique à basse pression'. PhD thesis. Ottawa, Ontario, Canada: Université d'Ottawa, 2008.

[19] J.P. Trelles, J.V.R. Heberlein and E. Pfender. 'Non-equilibrium modelling of arc plasma torches'. In: *Journal of Physics D: Applied Physics* 40 (2009), pp. 5937–5952.

[20] J. Wendelstorf. 'Ab Initio Modelling of Thermal Plasma Gas Discharges (Electric Arcs)'. PhD thesis. Braunschweig, Germany: Technische Universität Carolo-Wilhelmina zu Braunschweig, July 2000.

[21] J. H. Lee. *Basic Governing Equations for the Flight Regimes of Aeroassisted Orbital Transfer Vehicles*. AIAA Paper 84–1729. June 1984.

[22] J. M. Yos. Transport Properties of Nitrogen, Hydrogen, Oxygen, and Air to 30,000 K, AVCO Corp., Technical Memorandum RAD TM-63-7, Wilmington, Massachusetts, U.S. 1963.

[23] R. N. Gupta, J. M. Yos, R.F. Thompson and K.-P. Lee. *Reaction Rates and Thermodynamic and Transport Properties for an 11-Species Air Model for Chemical and Thermal Nonequilibrium Calculations to 30000 K*. NACA Rept. RP-1232. 1990.

[24] M. Yu, Y. Takahashi, H. Kihara, K. Abe, K. Yamada, T. Abe and S. Miyatani. 'Thermochemical Nonequilibrium 2D Modeling of Nitrogen Inductively Coupled Plasma Flow'. In: *Plasma Science and Technology,* 17.9 (2015), pp. 749–760.

[25] M. Dunn and S.-W. Kang. *Theoretical and Experimental Studies of Reentry Plasmas.* NACA Rept. CR-2232. 1973.

[26] V. Casseau. 'An Open-Source CFD Solver for Planetary Entry'. PhD thesis. Glasgow, Scotland, UK: University of Strathclyde, Apr. 2017.

[27] I. D. Boyd. 'Computation of Hypersonic Nonequilibrium Flows using the Direct Simulation Monte Carlo Method'. In: *Thermal Design of Aeroassisted Orbital Transfer Vehicles.* Ed. by E. Josyula. Vol. 247. Atlanta: AIAA, 2015, pp. 45–102.

[28] J. D. Jr. Anderson. *Fundamentals of Aerodynamics, Third Edition.* McGraw-Hill, 2001.

[29] P. J. Shayler and M. T. C. Fang. 'The transport and thermodynamic properties of a copper-nitrogen mixture'. In: *Journal of Physics D: Applied Physics* 10.12 (1977), pp. 1659–1669.

[30] M. F. Hoyaux. *Arc Physics.* New-York, USA: Springer, 1968.

[31] E. Josyula. *Hypersonic Nonequilibrium Flows: Fundamentals and Recent Advances.* American Institute of Aeronautics and Astronautics, 2015.

[32] M. F. Zhukov and I. M. Zasypkin. *Thermal Plasma Torches; Design, Characteristics, Applications.* Cambridge, UK: Cambridge International Science Publishing, 2007.

[33] M. S. Benilov. 'Understanding and Modelling Plasma-Electrode Interaction in High-pressure Arc Discharges: a Reviev'. In: *Journal of Physics D: Applied Physics* 41.14 (2008).

[34] N. Jeanvoine. 'Plasma-Material Interaction and Electrode Degradation in High Voltage Ignition Discharges'. PhD thesis. Saarbrücken, Germany: Universität des Saarlandes, 2009.

[35] A. Wells. *Numerical Calculations of the Properties of Axially Symmetric Arc Columns.* R. and M. No. 3580. Ministry of Technology, Aeronautical Research Council, Reports and Memoranda, 1969.

[36] W. T. Lord. 'Effect of a Radiative Heat Sink an Arc Voltage-Current Characteristics.' In: *Proceedings of a Specialists Meeting on Arc Heaters and M.H.D. Accelerators for Aerodynamic Purposes.* AGARD Fluid Dynamics Institute, Belgium: AGARDograph 84, Part 2, 1964.

[37] H. M. Pflanz and ter Horst D. T. J. *Particle Densities of High Temperature Gases: hydrogen, nitrogen, oxygen. (p = 1, 2, 5, 10, 20, 30 kg/cm2, T = 1000 to 50000 degrees K).* Eindhoven, Netherlands: Technische Hogeschool Eindhoven, 1966.

[38] E. J. Hopkins, D. W. Jillie and V. L. Sorensen. *Charts for Estimating Boundary-Layer Transition on Flat Plates*. NASA TN D-5846. June 1970.

[39] J.D. Callen. *Fundamentals of Plasma Physics*. University Printing House, Cambridge, UK: Cambridge University Press, 2006.

[40] G. Fußmann. 2005/2006, Einführung in die Plasmaphysik, lecture notes, Humboldt Universität zu Berlin.

[41] H. S. Fogler. *Elements of Chemical Reaction Engineering*. Upper Saddle River, NJ, USA: Pearson Education, 2004.

[42] A. F. Okuno and C. Park. Convective Stagnation-Point Heat Transfer in Partially Equilibrium Flow of Highly Ionized Nitrogen, NASA Ames Research Center, Moffet Field, Calif. June 1968.

[43] R. C. Millikan and D. R. White. 'Systematics of Vibrational Relaxation'. In: *The Journal of Chemical Physics* 39.12 (1963), pp. 3209–3212.

[44] J. H. Lee. *Electron-Impact Vibrational Relaxation in High-Temperature Nitrogen*. AIAA Paper 82–0807. Jan. 1992.

[45] T. F. Morse. *Energy and Momentum Exchange between Nonequipartition Gases*. Tech. rep. Princeton, New Jersey: Aeronautical Research Associates of Princeton, Mar. 1963.

[46] L. C. Scalabrin. 'Numerical Simulation of Weakly Ionized Hypersonic Flow over Reentry Capsules'. PhD thesis. University of Michigan, 2007.

[47] P.M. Bellan. *Fundamentals of Plasma Physics*. University of Wisconsin, Madison, USA, 2006.

[48] J. A. Shercliff. *A Textbook of Magnetohydrodynamics*. Pergamon Press, 1965.

[49] D. J. Griffiths. *Introduction to Electrodynamics*. Prentice Hall, 1999.

[50] K. Eisazadeh-Far, H. Meghalchi and J. C. Keck. 'Thermodynamic Properties of Ionized Gases at High Temperatures'. In: *Journal of Energy Resources Technology* 133 (20011).

[51] J. H. Ferziger and M. Perić. *Numerische Strömungsmechanik*. Springer, 2008.

[52] J. D. Jr. Anderson. *Computational Fluid Dynamics, The Basics with Applications*. McGraw-Hill, 1995.

[53] B. J. McBride, M. J. Zehe and S. Gordon. 'NASA Glenn Coefficients for Calculating Thermodynamic Properties of Individual Species'. In: *Journal of Spacecraft and Rockets* (2002). also NASA/TP—2002-211556.

[54] A. C. Yunus and M. A. Boles. *Thermodynamics, An Engineering Approach, Fifth Edition*. McGraw-College, Boston, Massachusetts, 2006.

[55] S. Chapman and T. G. Cowling. *The Mathematical Theory of Non-Uniform Gases: An account of the kinetic theory of viscosity, thermal conduction, and diffusion in gases*. The University Press, 1953.

[56] B. E. Poling, J. M. Prausnitz and J. P. O'Connel. *The Properties of Gases and Liquids, Fifth Edition*. The McGraw-Hill Companies, 2004.

[57] P. A. Gnoffo K. Sutton. *Multi-Component Diffusion with Application to Cumputational Aerothermodynamics*. AIAA Paper 98–2575. 1998.

[58] C. Park. 'Review of Chemical-Kinetic Problems of Future NASA Missions, I: Earth Entries'. In: *Journal of Thermophysics and Heat Transfer* 7.3 (1993), pp. 385–398.

[59] P. A. Davidson. *Introduction to Magnetohydrodynamics, Second Edition*. Cambridge University Press, 2017.

[60] F. Moukalled, L. Mangani and Darwish M. *Fluid Mechanics and Its Application, The Finite Volume Method in Computational Fluid Dynamics, An Advanced Introduction with OpenFOAM and MATLAB*. Springer, 2016.

[61] *OpenFOAM User Guide*. `https://cfd.direct/openfoam/user-guide/`. Accessed: 2019-02-20.

[62] *OpenFOAM Documentation*. `https://www.openfoam.com/documentation/`. Accessed: 2019-02-20.

[63] H. Jasak. 'Error Analysis and Estimation for the Finite Volume Method with Applications to Fluid Flows'. PhD thesis. London, UK: Imperial College London, 1996.

[64] P. K. Sweby. 'High Resolution Schemes Using Flux Limiters for Hyperbolic Conservation Laws'. In: *SIAM Journal on Numerical Analysis* 21.5 (1984), pp. 995–1011.

[65] S. V. Patankar. *Numerical Heat Transfer and Fluid Flow*. Hemisphere Publishing Corporation, 1980.

[66] A. Van Der Sluis and H. Van Der Vorst. 'Numerische Mathematik'. In: *International Journal for Numerical Methods in Fluids* 65 (1986), pp. 543–560.

[67] T. Uroić, H. Jasak and H. Rusche. 'Implicitly Coupled Pressure–Velocity Solver'. In: *OpenFOAM, Sellected Papers of the 11th Workshop*. Cham, Switzerland: Springer Nature Switzerland AG, 2019, pp. 249–267.

[68] I. Asproulias. 'RANS Modelling for Compressible Turbulent Flows Involving Shock Wave Boundary Layer Interactions'. PhD thesis. University of Manchester: School of Mechanical Aerospace and Civil Engineering, 2014.

[69] H. Schlichting. *Boundary-Layer Theory, 7th Edition*. McGraw-Hill Book Company, 1979.

[70] H. Borchert. private communication, French-German Research Institute of Saint-Louis, Saint-Louis, France. June 2019.

[71] M. Capitelli and R. S. Devoto. 'Transport Coefficients of High-Temperature Nitrogen'. In: *The Physics of Fluids* 16.11 (1973), pp. 1835–1841.

[72] A. B. Murphy and C. J. Arundell. 'Transport Coefficients of Argon, Nitrogen, Oxygen, Argon-Nitrogen, and Argon-Oxygen Plasmas'. In: *Plasma Chemistry and Plasma Processing* 14.4 (1994), pp. 451–490.

[73] R. H. Fowler and L. Nordheim. 'Electron Emission in Intense Electric Fields'. In: *Proceedings of the Royal Society of London, Series A* 119.781 (1928), pp. 173–181.

[74] S. Coulombe and J. L. Meunier. 'Thermo-Field Emission: a comparative study'. In: *Journal of Physics D: Applied Physics* 30 (1997), pp. 776–780.

[75] A. Monterde-Garcia. 'Materialfunktionen von Bogenplasmen aus Charakteristikmessungen'. In: *Zeitschrift für Physik* 181 (1964), pp. 317–330.

[76] C. Rond, P. Boubert, J. Félio and A. Chikhaoui. 'Radiation Measurements in a Shock Tube for Titan Mixtures'. In: *Journal of Thermophysics and Heat Transfer* 21.3 (2007), pp. 638–646.

[77] C. G. Parigger, C. M. Helstern and G. Gautam. 'Temporally and Spatially Resolved Emission Spectroscopy of Hydrogen, Cyanide and Carbon in Laser-Induced Plasma'. In: *Atoms* 7.74 (2019).

[78] G. Colonna. 'Thermodynamic properties of air plasma seeded by SiC molecules'. In: *Rendiconti Lincei. Scienze Fisiche e Naturali* 30.3 (2019), pp. 537–547.

[79] P. Gnemmi, C. Rey, B. Sauerwein and M. Bastide. 'Pressure Measurements around an Electric Discharge Produced on a Wedge in a Supersonic Flow'. In: *31st International Symposium on Shock Waves (ISSW31)*. Nagoya, Japan, 2017.